

JYU DISSERTATIONS 803

Anna Önnerstad

Improving Understanding of the QCD Matter Properties with Flow Harmonic Observables at the LHC



UNIVERSITY OF JYVÄSKYLÄ
FACULTY OF MATHEMATICS
AND SCIENCE

JYU DISSERTATIONS 803

Anna Önnerstad

Improving Understanding of the QCD Matter Properties with Flow Harmonic Observables at the LHC

Esitetään Jyväskylän yliopiston matemaattis-luonnontieteellisen tiedekunnan suostumuksella
julkisesti tarkastettavaksi yliopiston Ylistönrinteen salissa FYS1
kesäkuun 19. päivänä 2024 kello 12.

Academic dissertation to be publicly discussed, by permission of
the Faculty of Mathematics and Science of the University of Jyväskylä,
in Ylistönrinne, auditorium FYS1, on June 19, 2024 at 12 o'clock noon.



JYVÄSKYLÄN YLIOPISTO
UNIVERSITY OF JYVÄSKYLÄ

JYVÄSKYLÄ 2024

Editors

Ilari Maasilta

Department of Physics, University of Jyväskylä

Ville Korkiakangas

Open Science Centre, University of Jyväskylä

Cover picture by Caroline Önnerstad.

Copyright © 2024, by author and University of Jyväskylä

This is a printout of the original online publication.

ISBN 978-952-86-0217-0 (PDF)

URN:ISBN:978-952-86-0217-0

ISSN 2489-9003

Permanent link to the online version of this publication: <http://urn.fi/URN:ISBN:978-952-86-0217-0>

Jyväskylä University Printing House, Jyväskylä 2024

ABSTRACT

ÖNNERSTAD, ANNA

IMPROVING UNDERSTANDING OF THE QCD MATTER PROPERTIES WITH
FLOW HARMONIC OBSERVABLES AT THE LHC

This thesis aims to shed light on key aspects of quantum chromodynamics (QCD) by examining recent studies carried out at the Large Hadron Collider (LHC) at CERN. The research focuses on understanding the transport properties of matter created in heavy-ion collisions, specifically the specific shear and bulk viscosity, which provide essential information about QCD. Three primary goals steer this investigation.

The first goal is to accurately estimate these transport properties based on experimental data. This is achieved through the use of Bayesian analysis and additional flow observables that predominantly reflect non-linear hydrodynamic responses. Despite existing uncertainties in model calculations, this approach has shown to reduce these uncertainties significantly.

The second goal is to conduct higher-order multiparticle correlation measurements. Bayesian analysis has allowed for the quantification of the sensitivities of each observable, and it has been found that observables reflecting a hydrodynamic nonlinear response are most sensitive to the transport properties.

Lastly, the third goal is to explore the formation of the Quark-Gluon Plasma (QGP). The thesis investigates the smallest system size necessary for the formation of QGP and also probes whether small and large collision systems exhibit the same underlying mechanism for similar observations.

In summary, this thesis explores the depths of QCD, with the aim of enhancing understanding and reducing uncertainties of the QCD matter properties through precise measurements and analysis.

Keywords: QCD, QGP, FLOW, ALICE, CERN, LHC

TIIVISTELMÄ (ABSTRACT IN FINNISH)

ÖNNERSTAD, ANNA

QCD-AINEEN OMINAISUUKSIEN YMMÄRRYKSEN PARANTAMINEN harmonisen flow:n mittauksin LHC:SSÄ

Tämä väitöskirja pyrkii valaisemaan kvanttiväridynamiikan (QCD) keskeisiä näkökulmia tarkastelemalla hiljattain CERN:in Suuressa hadronitörmäyttimeissä (LHC) suoritettuja mittauksia. Tutkimus keskittyy ymmärtämään raskas-ionitörmäyksissä luodun aineen kineettisiä ominaisuuksia, erityisesti ominaisleikkaus- ja ominaisbolkkiviskositeettia, jotka tarjoavat olennaista tietoa QCD:stä. Kolme ensisijaista tavoitetta ohjaavat tätä tutkimusta.

Ensimmäinen tavoite on arvioida nämä kineettiset ominaisuudet tarkasti kokeellisten tietojen perusteella. Tämä saavutetaan käyttämällä Bayesilaista analyysia ja virtausobservaabeleita, jotka kuvaavat pääasiassa epälineaarista hydrodynaamisia vasteita. Olemassa olevista mallilaskelmien virherajoista huolimatta, tämä lähestymistapa on osoittautunut vähentävän näitä epävarmuuksia merkittävästi.

Toinen tavoite on suorittaa korkeamman kertaluvun monihiukkaskorrelaatiomittauksia. Bayesilainen analyysi on mahdollistanut observaabeleiden herkkyyksien määrittämisen, ja on havaittu, että hydrodynaamista epälineaarista vastetta kuvastavat observaabelit ovat herkimpiä kineettisille ominaisuuksille.

Lopuksi kolmas tavoite on tutkia kvarkkigluoniplasman (QGP) muodostumista. Väitöskirja tutkii pienimmän mahdollisen törmäysjärjestelmän kokoa, jossa QGP:tä muodostuu, sekä tutkii, onko pienissä ja suurissa törmäysjärjestelmissä yhtenevät perustavanlaatuiset mekanismit samanlaisissa havainnoissa.

Yhteenvedon, tämä väitöskirja tutkii QCD:n syvyyksiä, tavoitteenaan parantaa ymmärrystä ja pienentää QCD-aineen ominaisuuksien epävarmuuksia tarkkojen mittausten ja analyysin kautta.

Avainsanat: QCD, QGP, FLOW, ALICE, CERN, LHC

Author	Anna Öennerstad Department of Physics University of Jyväskylä Finland
Supervisor	Adj. Prof. Kim Dong Jo Department of Physics University of Jyväskylä Finland
Supervisor	Adj. Prof. Sami Räsänen Department of Physics University of Jyväskylä Finland
Reviewers	Prof. Julia Velkovska Department of Physics Vanderbilt University Tennessee United States Prof. Maya Shimomura Department of Physics Nara Women's University Nara Japan
Opponent	Prof. Anne Sickles Department of Physics University of Illinois at Urbana Champaign Illinois United States

PREFACE

I started this adventure in the middle of a pandemic, which influenced my experience quite a lot, and made me appreciate my colleagues and friends even more. I therefore want to take this little corner of my thesis to thank everyone.

First and foremost, I want to thank my supervisor Dong Jo Kim. Thank you for pushing me to do my best and for being a supervisor out of the ordinary, I would never have learned as much as I did without you. The second person I want to thank is Sami Räsänen, my co-supervisor. Thank you for going out of your way to make sure of everyone's wellbeing. I am forever grateful for the times you have been there for me.

Jasper Parkkila and Cindy Mordasini, I would not even write this part if it was not for the two of you. Jasper was there when I arrived and was extremely patient with my coding skills. Cindy came along when I was almost halfway through my PhD, and quickly became not only a colleague, but a friend of mine. She taught me everything from how to improve my slides to explain basically every little detail of how it works within a big collaboration such as ALICE. Thank you both for always answering all my questions.

Everyone in the ALICE student office, Oskari Saarimäki, Heidi Rytkönen, Andreas Molander, Laura Huhta, and Maxim Virta, thank you for all the good times and the support. You really are the best, such legends! And the whole Finnish ALICE group, I could not have joined a better group. A huge thank you to my PAG flow coordinators and my conveners in ALICE, I learned a lot from all of our discussions and felt your support.

I also want to thank my follow-up group, Tuomas Lappi and Kari Eskola, for your support, and everyone in the Center of Excellence in Quark Matter group for making such a pleasant and inspiring working environment.

A special thank you to everyone in the "Vappu"-group, you know who you are! You made my experience in Finland to the best experience.

I want to express my gratitude to my reviewers, Prof. Julia Velkovska and Prof. Maya Shimomura, for their time and effort in reviewing this thesis. I also thank Prof. Anne Sickles for agreeing to be my opponent and for her willingness to travel to Jyväskylä. Additionally, I am deeply grateful for the support I received from the Magnus Ehrnrooth Foundation, which funded two years of my thesis work. Finally, I want to acknowledge CSC in Finland, whose extra computing power made the computationally heavy Bayesian analysis possible. I extend a huge thank you to them.

Min familj, ni har betytt och betyder allt för mig. Ni har verkligen stöttat mig i allt, även om ni inte alltid har förstått vägen (vägarna?) jag har tagit. Kära lilla mamma, livet har inte alltid varit lätt, men i kärleken från dig har jag alltid känt mig trygg. Pappa, tack för att du alltid svarat när jag ringt och för att du alltid varit någon att bolla ideer med, stora som små. Min andra familj, mina vänner där hemma, Johanna, Josefine, Lena, Victoria, Lisa, platsen ni har i mitt hjärta är föralltid eran.

The support, love, and inspiration I have gotten from my nowadays "virtual" girl-gang, Katja, Eva, and Trine, has been invaluable. I can't wait for a reunion with all of you. I also want to thank my friend Yiota. Who could have thought that one could find a friend for life in a clean-room during night shifts? Thank you for always being there. Lastly, I want to express my gratitude to Santtu. You will always be a part of my adventures in Finland. Thank you for introducing me to your country.

Jyväskylä, June 2024, Anna Önnestad

LIST OF INCLUDED ARTICLES

- PI Parkkila, J.E. & Onnerstad, A. & Kim, D.J. *Bayesian estimation of the specific shear and bulk viscosity of the quark-gluon plasma with additional flow harmonic observables.* Phys.Rev.C 104(2021).
- PII Parkkila, J.E. & Onnerstad, A. & Taghavi, S.F & Mordasini, C. & Bilandzic, A. & Virta, M. & Kim, D.J. *New constraints for QCD matter from improved Bayesian parameter estimation in heavy-ion collisions at LHC.* Phys. Lett. B 835 (2022).
- PIII S. Acharya et al. (ALICE Collaboration) *Higher-order correlations between different moments of two flow amplitudes in Pb-Pb collisions at $\sqrt{s_{NN}} = 5.02$ TeV.* Phys.Rev.C 108(2023).
- PIV S. Acharya et al. (ALICE Collaboration) *Multiplicity and event-scale dependent flow and jet fragmentation in pp collisions at $\sqrt{s} = 13$ TeV and in p-Pb collisions at $\sqrt{s_{NN}} = 5.02$ TeV.* arXiv:2308.165911, accepted by PLB, final proof here 0(2024).

List of Articles and Contribution

The author contributed to articles [PI] and [PII]. In these articles, which focus on high energy physics phenomenology, the author was responsible for producing model simulations in multidimensional parameter spaces on the CSC cluster and reconstructing experimental observables. Additionally, the author played a leading role in writing the observable and chi-square test of the model to the data.

In experimental articles [PIII] and [PIV], which utilized the ALICE detector at the Large Hadron Collider, the author served as a member of the paper committee in ALICE. Responsibilities included verifying the results, writing the paper, and participating in the review process.

Another contribution of the author is the analysis of higher-order harmonic symmetric cumulant measurements in Pb-Pb collisions at $\sqrt{s_{NN}} = 5.02$ TeV. The author acted as the primary analyst, performing and verifying the results. This analysis includes the first-time measurements of correlations between the 5th and 6th harmonic flow amplitudes. The paper is currently being processed within the ALICE collaboration and will be discussed in Chapter 5 of this thesis.

CONTENTS

ABSTRACT

TIIVISTELMÄ (ABSTRACT IN FINNISH)

PREFACE

LIST OF INCLUDED ARTICLES

CONTENTS

1	INTRODUCTION	11
2	MODELING OF HEAVY-ION PHYSICS	13
2.1	Relativistic hydrodynamics	15
2.1.1	Shear viscosity.....	16
2.1.2	Bulk viscosity	16
2.1.3	Current knowledge on the transport coefficients of QGP ...	17
2.2	Initial states of collisions	18
2.2.1	Initial condition models.....	20
2.2.1.1	MC-Glauber	20
2.2.1.2	MC-KLN.....	23
2.2.1.3	EKRT	23
2.2.1.4	T _R ENTo.....	25
2.2.1.5	IP-Glasma	27
2.2.2	Pre-equilibrium dynamics	29
2.2.3	Particlization	29
2.3	Bayesian parameter estimation	30
2.3.1	Model setup and analysis procedure	31
3	EXPERIMENTAL OBSERVABLES.....	35
3.1	Anisotropic flow.....	35
3.2	Multi-Particle Correlations	37
3.2.1	Two-Particle Correlations	37
3.2.2	Multi-particle correlations and cumulants.....	38
3.3	Linear and non-linear flow modes.....	40
3.3.1	Mode coupling	41
3.4	Generic frameworks of multi-particle correlations	46
3.4.1	Generic formulas	47
3.4.1.1	Multi-particle correlations without η -gap	48
3.4.1.2	Multi-particle correlations with η -gap	48
3.5	Sensitivity of observables	50
4	EXPERIMENTAL SETUP	52
4.1	The Large Hadron Collider.....	53
4.1.1	The experiments at LHC.....	55
4.2	A Large Ion Collider Experiment	56
4.2.1	Tracking detectors.....	58

	4.2.1.1 Time Projection Chamber (TPC)	58
	4.2.1.2 Inner Tracking System (ITS)	60
5	ANALYSIS OF SYMMETRIC CUMULANTS	62
	5.1 Experimental setup and analysis	62
	5.1.1 Event and track selection	62
	5.2 Higher Order Symmetric cumulants	64
	5.2.1 Systematic Uncertainty Evaluation	66
	5.2.1.1 Description of the Barlow test	66
6	RESULTS	69
	6.1 Bayesian parameter estimation in heavy-ion collisions at LHC	69
	6.2 Higher Order Harmonic Symmetric Cumulants	70
	6.3 Asymmetric Cumulants	72
	6.4 Flow signal in small collision systems in LHC	74
7	SUMMARY	76
	REFERENCES	77
	APPENDIX 1 ACCESSING VERY HIGH ORDER FLOW COEFFICIENTS ..	91
2	MULTIPLICITY DEPENDENCE IN SMALL SYSTEMS	94
	APPENDIX 3 TESTING WITH PYTHIA IN PP COLLISIONS AT $\sqrt{s} =$	
	13 TEV	95
	3.1 Results	98
	INCLUDED ARTICLES	

1 INTRODUCTION

It was already predicted in the 70s that at sufficiently high energies or densities, a new state of matter would emerge where quarks and gluons are deconfined [1–3]. In this state of nuclear matter, the constituent quarks and gluons are not confined within the hadrons anymore, and can therefore move freely within the plasma. Today, these extreme conditions can be achieved in high-energy heavy-ion collider experiments. One of the pioneering experiments in this field is the Relativistic Heavy-Ion Collider (RHIC) [4–7] at the Brookhaven National Laboratory (BNL). From its beginnings, this accelerator has been instrumental in advancing our understanding of the behavior of the matter created in heavy-ion collisions.

In the course of their investigation, the researchers made a fascinating observation. They noted that the matter created in heavy-ion collisions expanded in a way that exhibited a specific form of anisotropy [8]. The identification of this anisotropy was of substantial importance, acting as a key turning point in our understanding. It suggested that the expansion of the fluid-like matter was not a random event but was being driven by the action of pressure gradients. This insight held profound implications for our understanding of the fundamental properties of matter. Prompted by these findings [4–7], researchers embarked on a series of extensive studies aimed at exploring this phenomenon in more depth. These investigations have been instrumental in shedding light on the properties of the QGP and its behavior under different collision energies and species in various experiments.

The first indication of the creation of the QGP was observed in 1994 at the Super Proton Synchrotron (SPS) at the European Organization for Nuclear Research (CERN), which was able to accelerate heavier lead ions at 17 GeV per nucleon pair. It was, however, not until 2000 that the first strong indications of creation of QGP were reported from SPS [9], and in 2004 RHIC could confirm that QGP behaves like a near-perfect liquid [10–13].

Recent studies on the QGP have also been conducted at the Large Hadron Collider (LHC) [14–17] at CERN. A significant goal within the heavy-ion community is to constrain the properties of QCD matter, including the transport properties of QGP. However, the uncertainties of these properties remain substantial in

most model calculations [18–21].

The first goal of this thesis is to determine if further constraints can be placed on transport properties using additional flow observables, now available from LHC experiments. Thanks to progress made in Bayesian analysis, two global Bayesian analysis papers [21, 22], that the author was involved in have demonstrated a reduction in the uncertainty of transport properties when additional flow observables from two beam energy data in LHC are used.

Bayesian analysis has also allowed for the quantification of the sensitivities of each observable. These analyses found that observables reflecting hydrodynamic nonlinear response are most sensitive to transport properties. Therefore, the second goal of this thesis is to conduct higher-order multiparticle correlation measurements [23], as they have been shown to be the most sensitive observables studied.

These findings are based on observations in large collision systems. Another important topic is determining the smallest system size needed for QGP to form. Despite initial beliefs that QGP could only be created in heavy-ion collisions, recent measurements have indicated QGP signals in smaller systems, such as pp and p–Pb collisions. The question then arises: do small and large collision systems share the same underlying mechanism for similar observations? The third goal of this thesis is to edge closer to an answer by examining methods where non-flow effects, like jets, are correctly subtracted. This work is published in Ref. [24]. As the experimental work’s details are provided in the paper, they are only discussed in the result and summary sections of the thesis.

The thesis is structured as follows: Chapter 2 introduces the intricate modeling process and the fundamental theoretical concepts that shape our understanding of QGP, as related to Refs. [21, 22]. Chapter 3 explores the experimental observables that play a key role in larger system analyses. Chapter 4 focuses on the experimental setup, specifically highlighting the ALICE detector at CERN. Chapter 5 summarizes the experimental analysis of the higher-order harmonic correlations not discussed in the papers from this thesis work. Chapter 6 summarizes the thesis works. Finally, Chapter 7 provides an overall summary and conclusions.

2 MODELING OF HEAVY-ION PHYSICS

Today, a substantial amount of physics research heavily relies on the utilization of sophisticated computer models. These models and detailed simulations are potent instruments that enable physicists to question assumptions, forecast outcomes, and unveil discoveries in more intricate physical systems. This is particularly critical in scenarios where direct interaction with a real-world system is impractical or entirely unfeasible.

This trend is certainly not an exception in the field of heavy-ion physics. Given that the observations of an event within the fields of particle and nuclear physics are confined to detector read-outs, which are triggered by long-lived final state particles, the only viable approach to comprehend the event in its entirety is to attempt to model it. This modeling is based on our existing understanding of the parameters involved.

By observing how the model mirrors the results of a real-world event, physicists can gain deeper insights into the dynamics at play. This approach not only enriches our understanding of the event and serves to refine and enhance the models themselves, fostering a cycle of continuous learning and improvement.

The most effective methodology for simulating heavy-ion collisions involves segmenting the process of the collision into individual phases. This allows for a complete understanding of the collision by focusing on each individual stage. The stages are typically dictated by several key elements: the initial stage, the QGP phase, the hadronization, and the hadronic scattering. The QGP phase lasts approximately $\tau \sim 5$ to $8 \text{ fm}/c$, and will be discussed later in this chapter. Having a proper description of each of these stages is important in order to overall understand the collision.

An illustration of the collision stages is presented in Fig. 1. The first phase in this process, the initial state, represents the period just before the actual collision takes place. It encompasses information on various aspects, such as the collision geometry, the deposition of energy density, and the dynamics of pre-equilibrium [25–30]. This phase is of utmost importance as it sets the stage for the following processes. The culmination of the initial partonic collisions gives rise to a “fireball”. This fireball signifies a state of high excitation and the partons

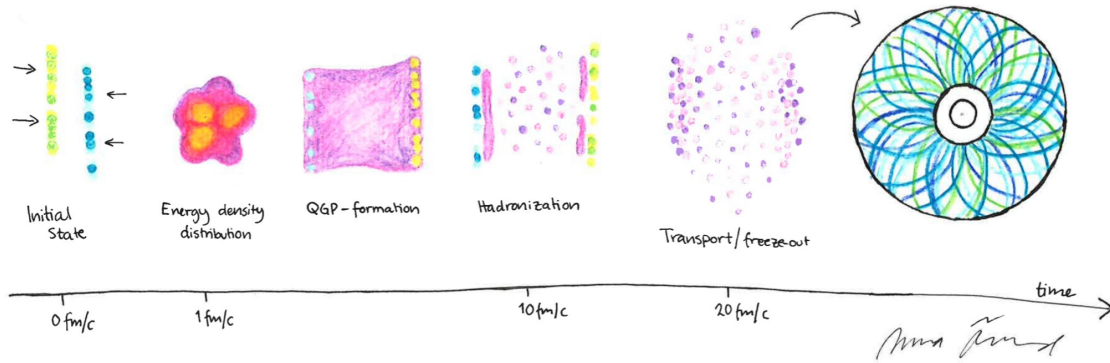


FIGURE 1 Stages of hydrodynamic evolution. 1. Two lead ions approaching each other at $\tau = 0$ (fm/c). 2. The energy density distribution and QGP after initial conditions at $\tau \sim 1$ (fm/c). 3. The process of hadronization and hadronic scattering begins around $\tau \sim 10$ (fm/c). 4. Due to expansion, the collective description does not hold and the freeze-out stage happens at $\tau \sim 20$ (fm/c). 5. The particle tracks recorded in the detector.

within it undergo frequent collisions [31]. However, over time, these continuous collisions actually pave the way for a state of local equilibrium. This state, known as a thermalized state, is where the partons are deconfined. In other words, this is the phase where QGP is formed. The period it takes to achieve a state of balance or equilibrium is commonly referred to as the thermalization time. This is a crucial concept when discussing the formation of QGP. Upon the formation of QGP, a thermal pressure is exerted by the system on the surrounding vacuum, instigating a collective expansion. This collective expansion leads to a decrease in both the temperature and the energy density of the medium. As the temperature descends and eventually falls below a particular critical temperature, denoted as T_c , the previously deconfined partons initiate a process, where the partons recombine into hadrons, known as hadronization. This is the stage where the medium undergoes a rapid expansion over a relatively small temperature interval.

Before the hadrons are detected, they undergo a two-step freeze-out stage — the chemical and the kinetic freeze-out [32]. During the chemical freeze-out phase, the hadrons collide frequently. The continuous collisions cause the medium to persist in its expansion, and hence there is a reduction in temperature. As the expansion continues, the occurrence of inelastic collisions, which allow hadrons to change their type, starts to decline. Eventually, these collisions become too infrequent, leading to a fixed abundance of hadrons. As the system continues to expand, the average separation between hadrons surpasses the reach of the strong interaction. This implies that the rate of hadron collisions will reduce to a level where maintaining a local equilibrium is no longer possible, thus making the collective description of the system inapplicable. This phase is recognized as the kinetic freeze-out stage [32].

The stages involved in the process cannot be measured directly. As such, it is necessary to construct models based on our current understanding and then

compare the predictions from these models to actual data. One method, which has demonstrated its efficacy and is often utilized in the modeling of heavy-ion collisions, is the complex approach of relativistic hydrodynamics [33, 34]. The concept of applying hydrodynamics to the field of particle physics is not a new one. In fact, the origins of which can be traced back to early efforts in the field. These initial endeavors were primarily concentrated on analyzing the collective motion of particles that originated from proton-proton (pp) collisions [33, 34].

In the hydrodynamic model, there is a particular focus on the expansion of the system with transverse anisotropy. This model deviates from the expected isotropic expansion, which is a characteristic of an ideal gas [35]. After the experimental validation of the fluid-like behavior of QGP [9], the hydrodynamics model has gained significance in the heavy-ion physics field. This model, refined continuously over time, has achieved remarkable accuracy in modeling the complex dynamics of QGP. The hydrodynamics model, pivotal in providing insights into the behavior and nature of QGP.

2.1 Relativistic hydrodynamics

This section provides a detailed explanation of the hydrodynamic model based on Ref. [36]. At the core of general hydrodynamics are the principles of the energy-momentum and charge conservation laws, which govern the behavior of fluid dynamics. When these principles are extended to encompass the relativistic scenarios, the energy-momentum conservation takes on the following mathematical representation:

$$\delta_\mu T^{\mu\nu}(x) = 0. \quad (1)$$

The principle of charge conservation, also known as the continuity equation, can be mathematically expressed as follows:

$$\delta_\mu J_i^\mu(x) = 0. \quad (2)$$

In these equations, $T^{\mu\nu}$ refers to the energy-momentum tensor, a concept in the field of general relativity, and J_i^μ denotes the charge current for various conserved quantities, such as baryon number, strangeness, electric charge, among others.

To further expound on this, the local 3-metric can be defined mathematically as:

$$\Delta^{\mu\nu} = g^{\mu\nu} - u^\mu u^\nu. \quad (3)$$

The charge current can now be expressed as follows:

$$J^\mu = nu^\mu + q^\mu, \quad (4)$$

This equation provides a way to represent the charge current in terms of the four-velocity and the charge four-current.

This equation allows for the expression of the energy momentum tensor, as seen in [36]:

$$T^{\mu\nu} = \epsilon u^\mu u^\nu - (P + \Pi)\Delta^{\mu\nu} + \pi^{\mu\nu}. \quad (5)$$

In this equation, ϵ represents the energy density. The equation of state, which is typically denoted as $P = P(\epsilon, n)$, is a central concept in the fields of thermodynamics and statistical mechanics. This equation establishes an important relationship between the variables of a system and the pressure P . By doing so, it allows us to complete the system of equations and describe the physical properties of the system. In relativistic fluid dynamics, two key properties are the shear and the bulk stress. These are represented by the symbols $\pi^{\mu\nu}$ and Π , respectively, in Eq. (5). At this limit, the quantities are reduced to these three expressions:

$$\begin{aligned} \pi^{\mu\nu} &\sim 2\eta\nabla^{(\mu}u^{\nu)} \\ \Pi &\sim -\zeta\partial_\mu u^\mu \end{aligned} \quad (6)$$

where $\nabla^\mu = \Delta^{\mu\nu}\partial_\nu$. From this boundary, the essential transport coefficients can be identified, namely the shear viscosity (η) and bulk viscosity (ζ). In fluid dynamics, one can identify the transport coefficients that play an important role in defining the characteristics of a fluid. These include the shear viscosity, denoted as (η), the bulk viscosity, represented as (ζ). These coefficients are integral to understanding the properties and behavior of the fluid. Alongside these, there is the equation of state $P(\epsilon, n)$, which is an additional factor that helps in predicting how the fluid will respond under various conditions. Collectively, the transport coefficients and the equation of state provide a complete framework to understand and differentiate the characteristics of one fluid from another, thereby playing a pivotal role in fluid dynamics study.

2.1.1 Shear viscosity

Shear viscosity, represented by the symbol η , is an important parameter that quantifies a fluid's resistance to deformation, specifically in response to shear stress, as outlined in Ref. [37]. This property effectively measures how a fluid behaves under varying degrees of pressure, with a "thicker" or more viscous fluid demonstrating a higher shear viscosity and consequently flowing more slowly when subjected to pressure. On the other hand, fluids with lower viscosity are characterized by stronger internal interactions among their constituent particles. This results in these particles covering shorter distances while exchanging momentum with other particles, leading to a faster and more fluid flow in response to external pressures.

2.1.2 Bulk viscosity

Bulk viscosity, denoted by the symbol ζ , is an important concept in fluid dynamics as it measures a fluid's resistance to both expansion and compression [37]. The ability of a medium to expand radially and the degree to which sound can be

attenuated within that medium are both directly impacted by the bulk viscosity. When a fluid undergoes processes of expansion or contraction, a certain amount of energy is invariably required to rearrange the microscopic structure of the fluid in order to adapt to the change in volume. This is where the bulk viscosity plays a crucial role in determining the amount of energy necessary for these processes. In heavy-ion physics, bulk viscosity is usually measured as ζ/s , similar to shear viscosity. This represents a measure of the fluid's internal friction in response to changes in volume.

2.1.3 Current knowledge on the transport coefficients of QGP

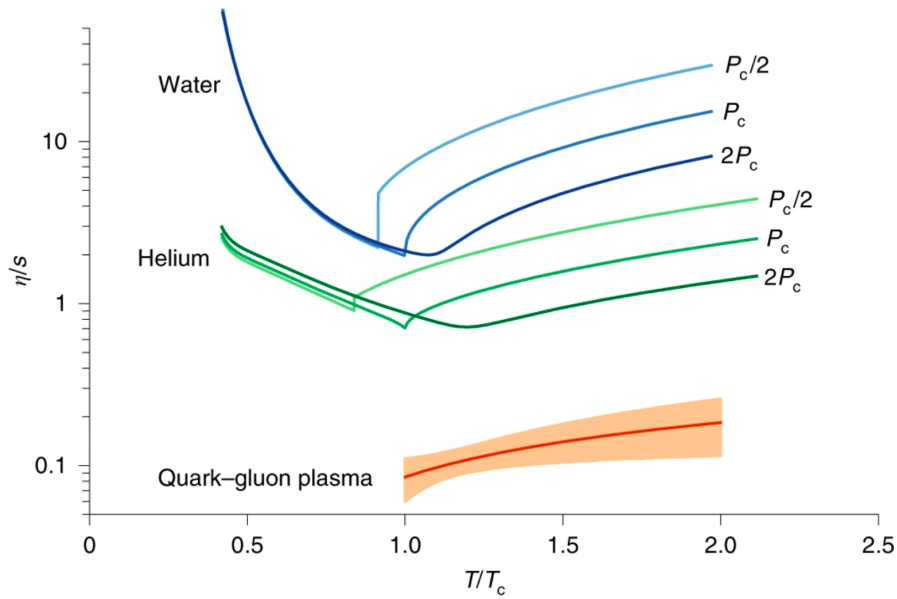


FIGURE 2 The temperature-dependent parameterizations describe the specific shear viscosity $\eta/s(T)$. For comparison, values of $\eta/s(T)$ for various common substances are provided [38]. The lowest value for η/s for the QGP among the substances in nature is estimated based on a Bayesian analysis [39]. Reprinted with permission from Ref. [39], 2019, Nature Physics.

The concept of specific shear viscosity, which is essentially the ratio of shear viscosity to entropy density (η/s), has attracted significant interest in the field of heavy-ion physics. Figure 2 presents a comparison of the specific shear viscosity values for different substances, including the QGP. The currently established measurement for the QGP η/s falls within the approximate range of ~ 0.08 and ~ 0.20 [40, 41]. This range is seen as an accurate representation because the measured ratio is regarded as having the lowest value found in nature. This conclusion aligns with the results derived from computations utilizing the anti-de Sitter/conformal field theory (AdS/CFT). The theory suggests that the universal minimum of the η/s ratio is situated at $1/(4\pi) \approx 0.08$ [42]. Given that the value is infinitesimally small, close to zero, it bears a striking resemblance to what might be considered an ideal "perfect" fluid. This conclusion comes from the observa-

tion that an ideal fluid is defined by having a η/s that is close to zero.

In the case of ordinary fluids, the dependency of the η/s , on thermodynamic conditions, such as temperature, is a well-established concept. It has been observed and studied extensively, and the relationship is widely accepted. In the case of QGP, there are growing indications that a similar relationship might exist [38].

However, despite the evidence and ongoing research, the exact form of the η/s temperature dependence in QGP remains uncertain. Generally, in the case of fluids, the minimum value of $\eta/s(T)$ is found at the critical temperature, denoted as $T = T_c$. Figure 2 presents η/s for various ordinary substances, such as water, nitrogen, and helium [38], and are compared to parameterizations based on a Bayesian analysis [39]. The diverse $\eta/s(T)$ of the QGP candidates correspond to two distinct temperature-dependent parameterizations, both having a minimum, found at the critical temperature, T_c . These parameterizations reflect the phase transition from hadronic matter to the QGP. Additionally, there are three parameterizations with a constant temperature, each presenting an η/s value that falls within the range of 0.08 and 0.2. These parameterizations contribute to our comprehension of the temperature-independent aspects of the QGP.

Each parameterization is meticulously crafted to suit its respective model calculations. These calculations, in turn, are precisely tuned to reproduce quantities that have been measured experimentally in heavy-ion collisions. The quantities encompass a variety of factors, such as the charged hadron multiplicity. Moreover, they also take into consideration the low momentum transverse (p_T) spectra, another pivotal element in this intricate equation of measurements and calculations. Furthermore, several low harmonic flow observables also contribute to these quantities. These measurements are not just numbers on a page; they provide vital constraints on the properties of the QGP.

In the past, the contribution of bulk viscosity, denoted as ζ/s , to the properties of QGP was often overlooked. The common assumption was that its influence was negligible, and as a result, it was frequently omitted from calculations involving QGP. This omission was routine and accepted in the scientific community. However, recent discoveries have shed light on a different perspective. It has been found that the simultaneous reproduction of some specific observables cannot be achieved without incorporating the effect of ζ/s . This revelation has prompted a shift in the previous assumptions. It is now believed necessary to consider a nonzero ζ/s value in the region around the critical temperature, T_c . This has opened up a new avenue of exploration in the studies of QGP and the understanding of its properties.

2.2 Initial states of collisions

Before the complex process of running hydrodynamic models can even begin, one must first secure information regarding the initial conditions of the collision.

This is where the intricacies and importance of the initial state models become apparent. These models are responsible for providing the initial conditions by determining the initial state's energy density. They cover all aspects, from carefully structuring the collision's geometry to accurately placing energy density, and even managing the dynamics before equilibrium. Once these initial state models have completed their task, the hydrodynamic model can then begin its work on the newly generated initial state [36]. This entire process is facilitated through a thoroughly designed lattice equipped with the initial values required. This lattice then sets the initial conditions for the differential equations governing hydrodynamics, thereby setting the stage for the hydrodynamic models to function effectively.

The model for typical initial conditions can be dissected into several unique steps, each of which is characterized by varying degrees of complexity and a variety of underlying physical assumptions. These steps form the backbone of the process of establishing initial conditions and, in most instances, can be outlined in the following manner:

1. The first step involves establishing the initial structure for the collision system. This is a crucial stage as it sets the foundation for the entire process.
2. The second step requires arranging the nucleons based on a specific nuclear density distribution. This ensures that the nucleons are correctly positioned within the system.
3. The third step is establishing nucleon participants based on a binary collision probability. This is a calculation that decides which nucleons will partake in the collision.
4. The fourth step is the assignment of a specific shape and density for each participant nucleon. This is an important step as it helps predict how the nucleons will behave during the collision.
5. The fifth step involves assessing the nuclear thickness and the deposit of energy density within the participant region. This is important for understanding the potential outcomes of the collision.
6. The final step is free streaming and/or pre-equilibrium dynamics. This process allows the system to reach a state of equilibrium before the collision occurs.

Each of these steps plays a vital role in the process of establishing initial conditions for the model and contributes to the accuracy and reliability of the model's predictions.

2.2.1 Initial condition models

2.2.1.1 MC-Glauber

In nuclear physics, a simple model is often used to describe the external geometry of atomic nuclei. This model is based on the assumption of a circular area, with a nuclear radius defined by the equation $R = r_0 A^{1/3}$. In this equation, r_0 is a constant equal to 1.275 fm, and A represents the mass number of the nucleus. This model was originally proposed in Ref. [43].

The model also takes into account the impact parameter, denoted as \vec{b} . This refers to measuring the relative distance between the centers of two nuclei, particularly looking at their placement on the azimuthal plane. The selection of this parameter can be either random or based on the desired centrality of the collision, depending on the specifics of the analysis.

When chosen randomly, the impact parameter may be deduced from the $d\sigma/db = 2\pi b$ distribution, which is a common choice in nuclear physics. This distribution provides a range of possible values for the impact parameter, allowing for a variety of scenarios to be modeled.

In experiments, the orientation of the system is also random. This randomness is a reflection of the inherent uncertainty in quantum mechanical systems. Therefore, it is logical to select a random system orientation between 0 and 2π radians when using this model. This choice ensures that the model can accurately represent the full range of possible orientations, further increasing its versatility and applicability.

The positions of the nucleons within the nucleus are not fixed, but fluctuate, and their distribution is determined in accordance with a nuclear density distribution. As a first step, one would take would be to establish these nucleon positions. These positions, once determined, will later contribute to the calculation of the nuclear energy density, an important aspect in understanding the properties of the nucleus.

The second step of the procedure involves taking samples of the nuclear density for every single nucleon. The nuclear density is in direct proportion to the nucleus's mean field potential, which is determined by the distance, represented as ' r ', from the nucleus's center. When it comes to modeling this mean field potential, the Woods-Saxon potential [44] is the most commonly used one. The mathematical formula for this potential is given by

$$V(r) = -\frac{V_0}{1 + \exp(\frac{r-R}{a})}, \quad (7)$$

In this equation, the variable a is used to ascertain the diffuseness of the nuclear surface, in other words, the thickness of the nucleus surface. This surface thickness is a measure of how quickly the potential falls off towards the edge of the nucleus.

For illustrative purposes, the Woods-Saxon potential for a lead ion, specifically ^{208}Pb , has been plotted in Fig. 3. It should be noted that it is also possible to

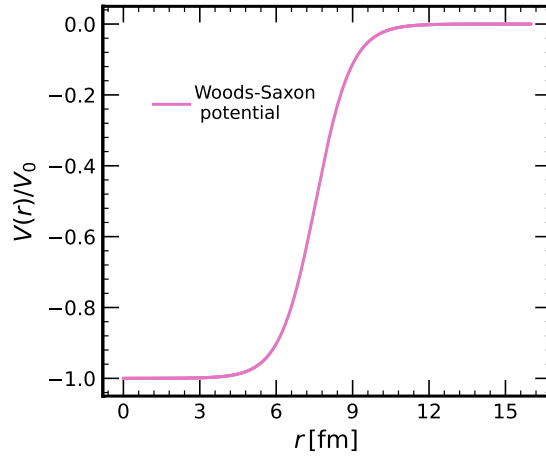


FIGURE 3 The Woods-Saxon potential is applied for the isotope ^{208}Pb . In this specific case, the parameters used are $r_0 = 1.275\text{fm}$ and $a = 0.7\text{fm}$. These parameters represent the radius of the nucleus and the diffuseness respectively. Thus, the Woods-Saxon potential provides an accurate model for the interaction between the nucleons in ^{208}Pb .

utilize the mean field potentials to separate protons and nucleons. This is done in order to more accurately incorporate the Coulomb potential for protons and the skin effect for neutrons into the model.

The nuclear density can be extracted from the Woods-Saxon potential using Eq.(7), which yields $\rho(r) \propto V(r)$. Following this, one samples the radial probability distribution, denoted as $P(r) \propto r^2\rho(r)$, in order to allocate the nucleons for the two nuclei in the collision system. In this particular setup, nucleon positions are assumed to be uncorrelated, meaning that each nucleon's position is independently determined. To prevent an unrealistic degree of nucleon overlap, a minimum distance, usually of the order of $\sim 1\text{fm}$, may be imposed. This enhances the model's authenticity and aligns it more closely with observed nuclear behavior.

Following the distribution process, the next step encompasses the finalization of the geometric configuration of the two incoming nuclei. This stage, along with those that follow, requires an understanding and definition of the intrinsic shape and structure of the nucleons, which includes aspects such as their size and density profile.

Accurate measurements have provided us with valuable information regarding the size and shape of smaller entities, such as the proton. However, the connection or correlation between these individual properties and the initial conditions under which a heavy-ion collision occurs remains uncertain.

This relationship is often measured by considering it as a variable, a free parameter, within the theoretical structure. In essence, this is an unknown constant that is determined through a rigorous process of fitting to empirical data obtained from numerous experiments.

While one can make an educated guess that the shape and spatial arrangement of nucleons adhere to a specific physical distribution, it is far from a con-

firmed fact. The density of a single nucleon is determined by the Fermi distribution [45]. This distribution provides us with a theoretical framework to understand and possibly predict the behavior of such particles.

$$\rho_{\text{nucleon}}(r) = \rho_0 \frac{1 + w \left(\frac{r}{R}\right)^2}{1 + \exp\left(\frac{r-R}{a}\right)}. \quad (8)$$

In the context of this particular equation, the variable w is representative of the width of the nucleon. The remaining parameters in this equation function in a way that is analogous to those found in Eq. (7). Other types of distributions, such as the Gaussian distribution, are also commonly used in these calculations. Occasionally, these distributions are accompanied by certain modifiers that are designed to account for fluctuations in density.

This is a method that allows for the consideration of the fact that densities are not always constant, and can fluctuate based on various factors. The density of individual nucleons, or the basic units of matter, is then combined together to form the overall density $\rho(x, y, z)$. This resultant density is representative of both of the two nuclei in question. Through this process, we are able to get a more accurate representation of the densities and distributions of the nuclei.

After assigning the density, the nuclear thickness can be defined. This nuclear thickness serves as a representation of the transverse profile of nuclei A and B. This is done as follows:

$$T_{A,B}(x, y) = \int dz \rho_{A,B}(x, y, z) = \sum_i^{N_{A,B}} \int dz \rho_{A,B,\text{nucleon}}^{(i)}(x, y, z). \quad (9)$$

In the context of this equation, $N_{A,B}$ represents the count of what are referred to as *participant* nucleons for each nucleus. This term signifies that the contribution to the nuclear thickness, denoted $T_{A,B}$, come only from those nucleons involved in one or more binary collisions.

Furthermore, the probability of a nucleon colliding with another is given by $P_{ij} \sim p(\rho_{A,\text{nucleon}}^{(i)}, \rho_{B,\text{nucleon}}^{(j)})$. This probability is often defined using what is known as a hard disk model, which can be expressed as follows:

$$r \leq \frac{\sigma_{\text{NN}}}{\pi}, \quad (10)$$

This model does not differentiate between a head-on nucleon-nucleon collision and a peripheral nucleon-nucleon collision. Alternatively, a smoother Gaussian or an Eikonal-type overlap function could be used.

The primary objective of the initial condition model is to transform the given nuclear thicknesses, denoted as T_A and T_B , into an energy density, indicated by $\epsilon \sim f(T_A, T_B)$. Distinct predictions arise from different models due to the varying assumptions made about the physical mechanisms of energy production.

In the basic MC-Glauber model [43], the method of energy deposit is rather uncomplicated. It involves both the addition and multiplication of the two thicknesses, which are utilized to model the energy density in the nuclear matter and

the individual nucleon-nucleon collisions, respectively. This can be illustrated as follows:

$$\epsilon \sim T_A + T_B + \alpha T_A T_B, \quad (11)$$

In this equation, α is a phenomenological variable. It has an important role in controlling the relative strength of the energy deposition in nucleon-nucleon collisions.

2.2.1.2 MC-KLN

The MC-KLN model is an initial condition saturation model [46, 47]. This model is based on the Color Glass Condensate (CGC) [48] field theory, which regulates the behavior of gluons at high energy. In the MC-KLN model, a unique saturation picture is proposed. This picture assumes that the number of produced partons reaches a saturation point. Remarkably, this saturation point is directly proportional to the square of the parton transverse momentum, denoted as Q^2 , and the area of the nucleus. The reasoning behind this phenomenon is rooted in the uncertainty principle. According to this principle, as the parton's momentum increases, it will occupy a larger area on the Lorentz contracted nucleus disk. This means that the parton's "footprint" on the nucleus expands as its momentum grows. When a sufficient number of partons are present, they will begin to overlap and interact, which impedes any further increase in parton density. This critical juncture, where the increase in parton density is halted, is known as the saturation scale, represented by Q_s . Furthermore, the energy deposition in such a system is directly related to the density of produced gluons, as shown by the following equation:

$$\epsilon \sim \frac{dN_g}{dyd^2r_\perp} \sim Q_{s,\min}^2 \left[2 + \log \left(\frac{Q_{s,\max}^2}{Q_{s,\min}^2} \right) \right], \quad (12)$$

where $Q_{s,\min}^2 \propto T_{\min(A,B)}$ and $Q_{s,\max}^2 \propto T_{\max(A,B)}$. These relationships provide a mathematical representation of the saturation scale and its dependence on the properties of the interacting partons and the nucleus.

2.2.1.3 EKRT

EKRT is a thorough saturation model, which has been specifically designed to incorporate collinearly factorized perturbative Quantum Chromodynamics (pQCD) in the production of minijets [49, 50]. This model operates on the principle that the energy deposition is primarily driven by the saturated low- p_T partons, in addition to the higher energy partonic jets or minijets that are subsequently produced during this process.

To quantify this, the initial transverse energy density of the minijet in a specific rapidity range, represented as Δy and above a predetermined transverse momentum scale $p_0 \gg \Lambda_{QCD}$, can be calculated using the formula shown below:

$$\frac{dE_T}{d^2\mathbf{x}_*\perp} = T_A(\mathbf{x}_*\perp)T_B(\mathbf{x}_*\perp - \mathbf{b})\sigma\langle E_T \rangle * p_0, \Delta y, \beta. \quad (13)$$

In the context of the equation, the term $\sigma\langle E_T \rangle_{p_0, \Delta y, \beta}$ represents the cross-section of the minijet. This is equivalent to $\sigma\langle E_T \rangle_{p_0, \Delta y, \beta} = \int_0^{\sqrt{s_{NN}}} dE_T E_T \frac{d\sigma}{dE_T}$. Additionally, $\frac{d\sigma}{dE_T}$ is derived from the phase-space integrations of next-to-leading order (NLO) (2 \rightarrow 2) and (2 \rightarrow 3) partonic scattering cross-sections.

In conclusion, it's important to underscore the role that the nuclear thickness $T_{A,B}$ plays in the equation, as it encompasses all the nucleons present in both nuclei. Each nucleon, from both nuclei, contributes to the overall structure and properties of the nuclear system being studied. Therefore, in understanding this equation, one must fully recognize the nature of $T_{A,B}$, and how it encapsulates the collective contribution of every single nucleon from the two nuclei. This signifies that EKRT treats every nucleon as a participant when the initial nuclear thickness is generated, thus ensuring a comprehensive and accurate calculation.

Within the scope of partonic scattering events, at transverse momenta $p_T < p_0$, it's observed that the higher-order processes, such as those involving 3 \rightarrow 2 scattering, start to play a more significant role, overshadowing the contributions from minijets and conventional low-order processes. Within the frame of a saturation condition, this can be expressed as $\frac{dE_T}{d^2\mathbf{x}_\perp dy}(2 \rightarrow 2) \sim \frac{dE_T}{d^2\mathbf{x}_\perp dy}(3 \rightarrow 2)$.

In light of this, a criterion can be formulated for the transverse energy density production of minijets. This is given by the following equation:

$$\frac{dE_T}{d^2\mathbf{x}_\perp dy} = \frac{K_{\text{sat}}}{\pi} p_0^3 \Delta y \quad (14)$$

In this equation, the saturation momentum is denoted by p_{sat} . This is computed using a Monte Carlo (MC) implementation, with fixed values for the parameters K_{sat} and β .

Once the minijet production, as given by equation (13), is connected to the saturation criterion, denoted by equation (14), it is then possible to numerically determine the saturation scale p_0 . By setting $p_{\text{sat}} \equiv p_0$, the formula for the energy density evolves to take the following form:

$$\epsilon \sim \frac{K_{\text{sat}}}{\pi} p_{\text{sat}}^3 (K_{\text{sat}}, \beta; T_A, T_B). \quad (15)$$

In terms of visual representation, the EKRT generated energy density profile can be observed in Fig. 4. Additionally, the parameterized saturation momentums, considered as a function of nuclear thickness, can be viewed in Fig. 5.

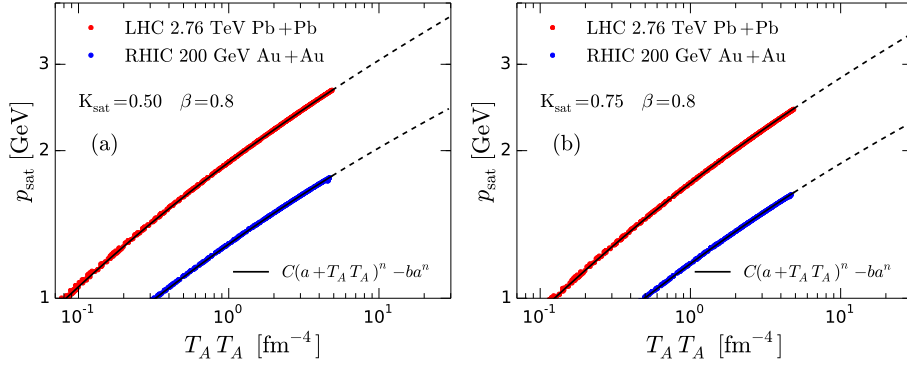


FIGURE 5 Parameterizations of the EKRT saturation momentum p_{sat} are depicted for $K_{\text{sat}} = 0.5$ (left) and $K_{\text{sat}} = 0.75$ (right), as detailed in the work by Niemi et al. [49]. Reprinted with permission from [49], 2016, American Physical Society.

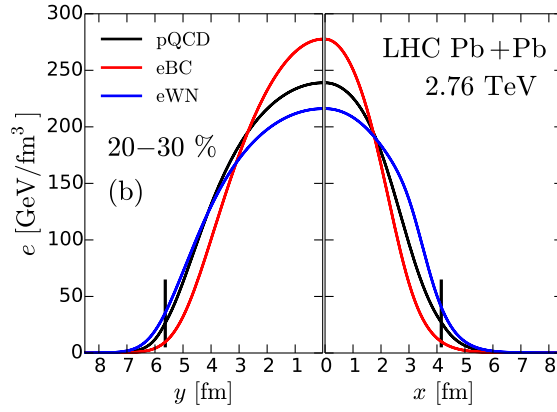


FIGURE 4 The energy density profile is obtained from EKRT with parameters $K_{\text{sat}} = 0.63$ and $\beta = 0.8$ at $\tau_0 = 0.204$ during Bjorken pre-thermal free streaming from Ref. [49]. Reprinted with permission from [49], 2016, American Physical Society.

2.2.1.4 T_RENTo

T_RENTo (Reduced Thickness Event-by-event Nuclear Topology) [51] is an initial condition model that operates differently from its counterparts. In the realm of nuclear physics, there exists a multitude of initial condition models, each generating a unique array of initial states. These initial states, in turn, lead to considerable differences in the predicted values of hydrodynamic transport coefficients by these models. As a result, the inherent complexity of these models and the vast diversity of their outputs make it an challenging task to completely disentangle the variations in initial conditions from the properties of the QGP medium. To navigate this intricate landscape, T_RENTo introduces a novel approach. It employs a parametrized function of the nuclear thickness, a departure from the traditional method that relies heavily on the intrinsic physical assumptions of the energy deposition. This departure consequently simplifies the representation by reduc-

ing its complexity. The usage of such parametrization provides a dual benefit. It not only allows for the simultaneous constraint of initial conditions and medium properties, but it also grants a phenomenological perspective on the actual form of the initial conditions.

The probability of a collision between two nucleons candidates in nuclei A and B is evaluated by

$$P_{ij} = 1 - \exp \left(-\sigma_{gg} \int dx dy \int dz \rho_{A,\text{nucleon}}^{(i)} \int dz \rho_{B,\text{nucleon}}^{(j)} \right). \quad (16)$$

In this context, the term σ_{gg} is used to denote an effective parton-parton interaction cross-section. This cross-section is then normalized by the total nucleon-nucleon cross-section, which is represented by σ_{NN} . Nucleons will contribute to the nuclear thickness only if the collision probability in Eq. 16 is positive.

To determine if the nuclei collides, the probability is sampled once, assuming they do collide, `TRenTo` assigns fluctuations to the nucleon densities, leading to a fluctuating nuclei thickness

$$\tilde{T}_{A,B} = \sum_i^{N_{A,B}} w_{A,B}^{(i)} \int dz \rho_{A,B,\text{nucleon}}^{(i)}(x, y, z). \quad (17)$$

This thickness will in turn model the fluctuating quantity of partons generated in each collision between nucleons. $w_{A,B}^{(i)}$ in Eq. 17 is the weight of participant i and is sampled from a gamma distribution

$$P_{\kappa}(w) = \frac{w^{\kappa-1} \kappa^{\kappa}}{\Gamma(\kappa)} e^{-\kappa w}. \quad (18)$$

With the reduced thickness of the two colliding nuclei, `TRenTo` derives the final energy density

$$\epsilon \sim \left(\frac{\tilde{T}_A^p + \tilde{T}_B^p}{2} \right)^{\frac{1}{p}}. \quad (19)$$

Here, p is introduced, which is a dimensionless phenomenological parameter, also referred to as the energy deposition parameter. This particular parameter holds significant importance in the model because it provides the flexibility to adjust the model's behavior. By simply tweaking the value of p , the `TRenTo` model can reproduce the results of a broad spectrum of other models. This means that `TRenTo` has the inherent capability to mimic the characteristics of various models by just manipulating a single parameter.

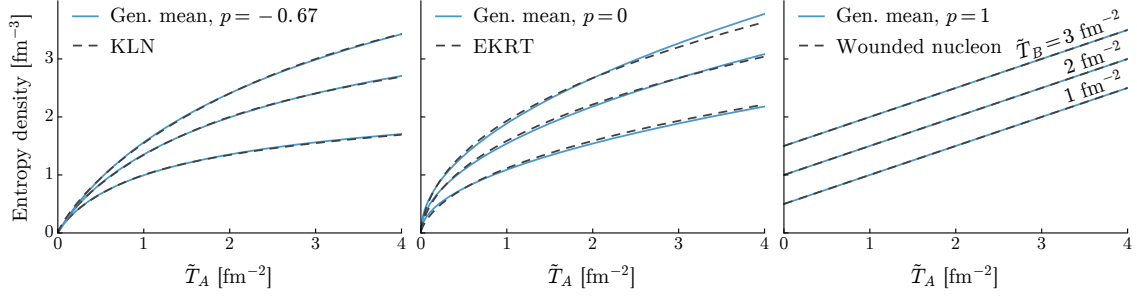


FIGURE 6 The initial entropy density profile is an essential aspect to consider, and three models are often used to predict it: the KLN model, the EKRT model (where $K = 0.64$ and $\beta = 0.8$), and the wounded nucleon model. The figure on the left shows the prediction of the KLN model, the middle figure represents the EKRT model's prediction, and the right figure depicts the wounded nucleon model's prediction. Reprinted with the permission from [52], 2016, the American Physical Society.

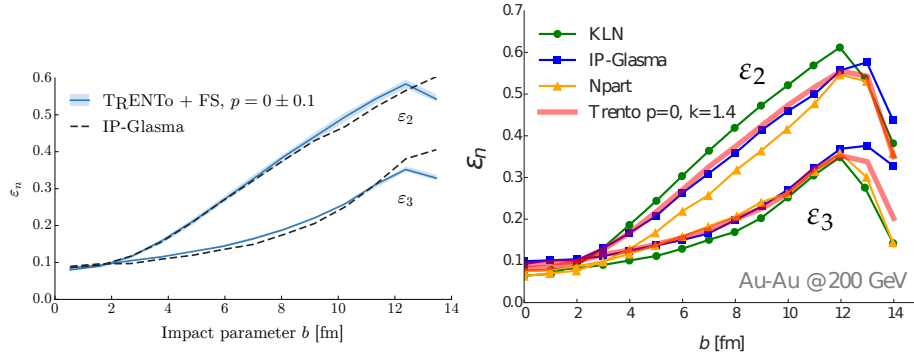


FIGURE 7 This figure presents the eccentricity generated by the T_{RENTo} model with specific parameters, namely $p = 0$, $k = 1.6$, and nucleon width $w = 0.4$ (Gaussian). These results are subsequently compared with those derived from other models. The comparison is meticulously plotted as a function of impact parameter, thereby providing a comprehensive overview of the differences and similarities between the models, and illuminating the unique aspects of the T_{RENTo} model. Further details of this process and the models used can be found in the referenced work [52]. Reprinted with the permission from the American Physical Society, 2016.

2.2.1.5 IP-Glasma

The IP-Glasma model effectively combines the Color Glass Condensate saturation model (IP-Sat), which considers the impact parameter, with a classical Yang-Mills model that focuses on the initial gluon fields. This combination makes the IP-Glasma model a successful model for initial conditions [53]. While all the models discussed so far express the energy density in terms of $T_{A,B}$, the IP-Glasma model deviates from this norm. IP-Glasma requires a few distinct steps before the energy density can be derived, adding to its complexity.

The first step in this process involves obtaining the color charge density,

denoted as $g^2\mu_{A,B}$. This is achieved in a manner that is directly proportional to the summed saturation scales, represented as Q_s^2 , which is a concept provided by the IP-Sat model. It is important to note that each individual nucleon in the system contributes to this saturation scale. After this, the color charges, denoted as ρ^a , are drawn from a Gaussian distribution. This can be represented by the following equation:

$$\langle \rho_{A,B}^a(\vec{x}_\perp) \rho_{A,B}^b(\vec{y}_\perp) \rangle = (g^2\mu_{A,B})^2 \delta^{ab} \delta^{(2)}(\vec{x}_\perp - \vec{y}_\perp), \quad (20)$$

The gluon fields, which are pivotal for our understanding of the strong interactions between quarks and gluons, are then derived by methodically solving the classical Yang-Mills equations:

$$[D_\mu, F_{\mu\nu}] = J^\nu. \quad (21)$$

In equation 21, $J^\nu = \delta^{\nu\pm} \rho_{A,B}(\vec{x}_\perp)$ represents the color current. Through this equation, the gluon fields are finally determined. From these deduced gluon fields, the energy density, denoted as ϵ , is derived and evolves to a starting time of the hydrodynamic model.

In Fig. 8, the energy density profile from the IP-Glasma model is presented alongside two other simpler models. Additionally, the eccentricity generated by the IP-Glasma model is showcased in Fig. 9.

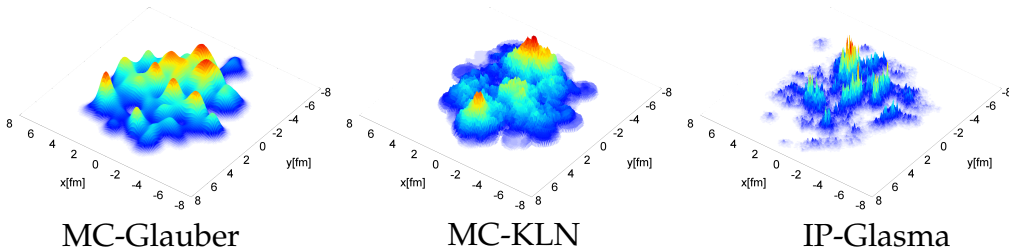


FIGURE 8 This figure presents the visualization of the initial energy density profile of nuclear collisions. Three models are employed in the representation of these profiles: the Monte Carlo Glauber (MC-Glauber), the Monte Carlo Kharzeev-Levin-Nardi (MC-KLN), and the IP-Glasma models [53]. Reprinted with permission from [53], 2012, American Physical Society.

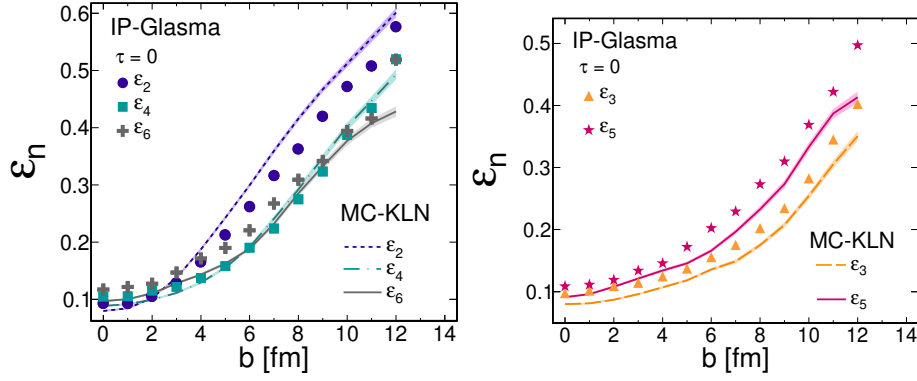


FIGURE 9 The eccentricity derived from the IP-Glasma model is compared to the MC-KLN model, specifically as a function of the impact parameter [54]. Reprinted with the permission from [54], 2012, American Physical Society.

2.2.2 Pre-equilibrium dynamics

In general, hydrodynamic models are based on the assumption that the medium has reached a state of thermal equilibrium. As per our current understanding [55], the QGP achieves this state of thermalization rather quickly, typically within a time span of approximately 1 fm/c. This rapid thermalization implies that the principles of hydrodynamics can be applied very early on, immediately following the initial collision.

However, it is important to note that this thermal equilibrium is not instantaneous. There is a need for a secondary dynamical process to convert the initial energy density profile into a state of thermal equilibrium. This process is not addressed by hydrodynamic models, requiring the development of additional models to account for it.

One such model is the Freestreaming model [55]. This model attempts to simulate this secondary dynamical process. It does so by hypothesizing that the constituents of the QGP in the initial stages of the collision move as free partons, according to the principles of the collisionless Boltzmann equation. As the system expands, collisions are gradually introduced, which helps the system transition towards thermal equilibrium.

2.2.3 Particlization

In the continuously evolving process of the medium's expansion, the system undergoes a cooling down phase. As it cools, it will eventually reach a specified temperature at which the partons can no longer remain in a state of deconfinement. In response to this change in conditions, the partons will start to rebound with each other, leading to the formation of an assortment of hadrons. This process, known as hadronization or particlization, is a phase in the evolution of the medium.

The concept of hadronization is often modeled utilizing the Cooper-Fry description, a well-established paradigm in the field. This model proposes the sam-

pling of particles from the hypersurface of the hydrodynamic evolution, a process that is mathematically represented in equation ??:

$$E_p \frac{dN_n}{d^3p} = \frac{1}{(2\pi\hbar)^3} \int_{\Sigma} p \cdot d^3\sigma(x) f_n(x, p), \quad (22)$$

In this equation, Σ symbolizes the surface of condensation and $f_n(x, p)$ represents the phase-space distribution for a specific type of hadron species.

In the context of these theoretical models, the temperature at which the processes of hadronization and the subsequent freeze-out stage start is often labeled as the specific switching temperature, or T_{switch} . This use of a switching temperature is a common approach in the field, providing a quantifiable point at which these transformative processes begin.

However, while the use of a switching temperature is prevalent, it is not the only approach. Alternative methods that are based on different parameters such as expansion and scattering rates have also been proposed [56, 57].

2.3 Bayesian parameter estimation

A set of parameters is often employed as a tool to encapsulate and represent constants or relations that exist in the natural world. These parameters enable researchers to quantify their observations and provide a structured framework within which these observations can be evaluated and compared. For instance, it was discussed in previous sections that models of initial conditions often utilize parameters that govern the size of the nucleon and the scale of energy deposition. These parameters serve as control factors in these models, offering a means to manipulate and examine different scenarios and their outcomes. Similarly, hydrodynamic models make use of parameters to regulate various transport properties. These include, but are not limited to, $\eta/s(T)$, and the bulk viscosity to entropy density ratio, represented as $\zeta/s(T)$. Through the strategic use of these parameters, researchers can effectively model and predict the behavior of these transport properties under different conditions.

The concept of estimating parameters may initially seem complex, but it essentially refers to the process of model calibration. This is a crucial step in any type of statistical modelling, where the parameters of the model are delicately tuned to achieve the best possible reproduction of experimental results.

In recent years, there has been a significant increase in the use of Bayesian statistics within the scientific community [21, 39, 58–65]. This method of Bayesian parameter estimation is based on Bayes' theorem, which can be expressed mathematically as follows:

$$P(\vec{x}|\vec{y}) \propto P(\vec{y}|\vec{x})P(\vec{x}). \quad (23)$$

In this equation, the 'likelihood' $P(\vec{y}|\vec{x})$ represents the model's accuracy in accurately representing the data, while the 'prior' $P(\vec{x})$ encapsulates our initial understanding or assumptions about the parameters.

This method is iterative and throughout the process, probability distributions for the optimal parameter values are derived. The result is a detailed picture of how the parameters should be set to achieve the closest fit to the experimental data. For those who are interested in learning more about this process, more detailed explanations can be found in Ref. [39, 62].

2.3.1 Model setup and analysis procedure

In this thesis, one of the analyses that is presented is based on the Bayesian parameter estimation framework, as provided by Ref. [39]. This framework is strategically employed to estimate the transport properties of the QGP utilizing the higher harmonic observables as a component of the estimation process.

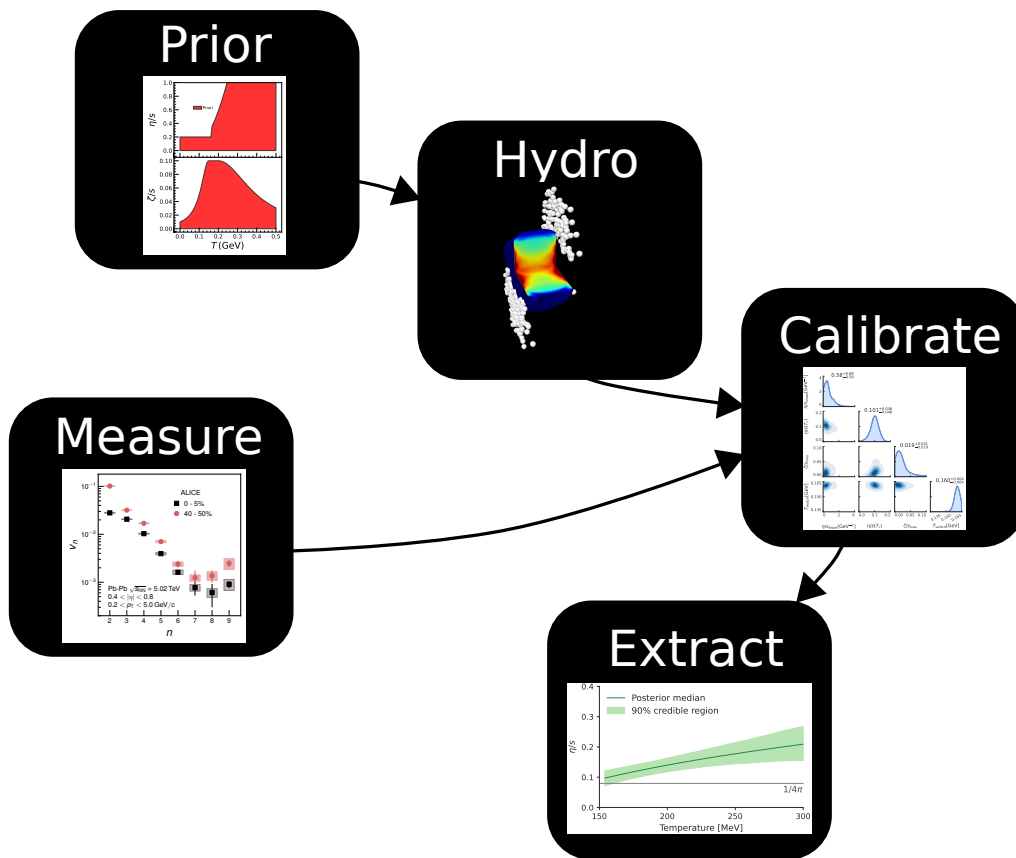


FIGURE 10 A schematic view of the Bayesian Analysis process. The process begins with a prior from the hypothesis, representing a range of feasible parameters. Hydro calculations are then run within these ranges. The aim is to identify the optimal set of model parameters that most accurately reflect the experimental data. Constraints such as flow observables among others are utilized to hone in on the shear and bulk viscosity. This process constitutes the Calibration phase. Figure credits to Jasper Parkkila and Dong Jo Kim.

To perform this analysis, a modified model was constructed, a process overseen and carried out by Dr. Jasper Parkkila. This model comprises of several constituent models, each playing an integral part in the overall analysis. These

models and their specific roles have been detailed below:

- The first component of the model is the TRENTo initial conditions [39, 62]. This model is responsible for determining the initial conditions of the system and its parameters relate to nucleon attributes and energy deposition. It contains 4 parameters that can be fine-tuned to match experimental data.
- The second component is the freestreaming pre-equilibrium dynamics [55, 66], which describes the evolution of the system before thermal equilibrium is reached. This model has a single parameter, which is the time scale of the freestreaming process.
- The third main component is the OSU 2+1D viscous hydrodynamics model (also known as VISHNew) [67, 68]. This model, which contains 8 parameters, is used to simulate the viscous fluid dynamics of the Quark-Gluon Plasma.
- The final component of the model is the UrQMD hadronic afterburner [69, 70]. This model is used to simulate the final stages of the collision, including the transition from the Quark-Gluon Plasma to a gas of hadrons and the subsequent interactions of these hadrons. It does not have any estimated parameters.

The combination of models used in this instance serves as an example and signifies the starting point of this research project. Future plans include the integration of EKRT as an initial state model. But, in the course of this study, presented in this thesis, the total count of parameters that were used were 13. The majority of these parameters were specifically designed to make up the parameterizations for the η/s and ζ/s . The formulation of the viscosities in this study has been expressed using the following equations:

$$(\eta/s)(T) = (\eta/s)_{\min} + (\eta/s)_{\text{slope}}(T - T_c) \left(\frac{T}{T_c} \right)^{(\eta/s)_{\text{crv}}} \quad (24)$$

and

$$(\zeta/s)(T) = \frac{(\zeta/s)_{\max}}{1 + \left(\frac{T - (\zeta/s)_{\text{peak}}}{(\zeta/s)_{\text{width}}} \right)^2} \quad (25)$$

The above equations represent the parameterized form of the viscosities. The details of the analysis and the methodology employed in this research are comprehensively included in Ref. [21]. In addition, a follow-up paper that incorporates new and independent observables as input for the model is extensively summarized in Chapter 6.

The primary objective of this analysis is to uncover an enhanced parameterization method that has the capability to accurately reproduce the newly observed higher harmonic flow patterns along with the pre-existing lower harmonic ones. Moreover, the research seeks to evaluate the sensitivity of these novel observables

to various transport coefficients. A part of the aim is also to evaluate any potential model shortcomings that may be revealed in the process, thereby providing a pathway for future improvements in the model.

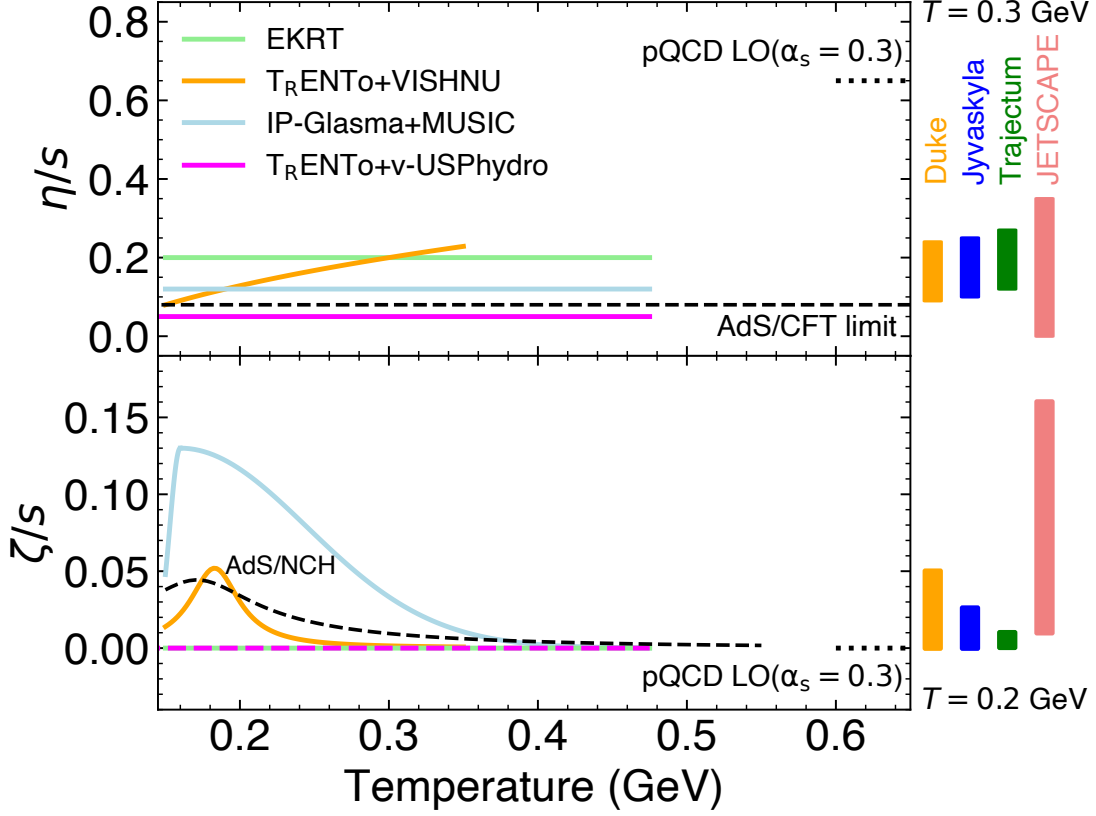


FIGURE 11 The compilation of various estimates of the temperature dependence of the specific shear and bulk viscosity as of 2021 [17] is shown in the top and bottom panels, respectively. The fixed sets of parameterizations from four different hydrodynamical model calculations are shown on the left, and the uncertainty ranges of estimated parameterizations based on Bayesian analysis from four different groups are shown on the right. The ranges on the right represent the 90% credibility region from the Bayesian analysis. Reprinted with permission from [17], 2022, EPJC.

The compilation of various estimates of η/s and ζ/s as of 2021 [17] are shown in Fig. 11. This was done while the ALICE collaboration was summarizing their 20-year journey [17]. Four different hydrodynamical models are presented, along with limits from pQCD [71], AdS/CFT [42], and AdS/Non-Conformal Holographic [72]. The upper panel presents the η/s , where EKRT+hydrodynamics [49], IP-Glasma+MUSIC, and $T_{\text{RENTO}}+v\text{-USPhydro}$ [73] are all temperature-independent, while $T_{\text{RENTO}}+\text{VISHNU}$ displays an increasing η/s value with rising temperature. The lower panel illustrates ζ/s , where EKRT+hydrodynamics and $T_{\text{RENTO}}+v\text{-USPhydro}$ both hold a value of zero, and the two other models have a non-zero value, agreeing better with AdS/CFT.

On the right side of Fig. 11, the Bayesian parameter estimated posterior distributions of η/s and ζ/s are depicted as ranges representing the 90% credibility

region. The four models displayed in Fig. 11, namely Duke [18], Jyväskylä [21], Trajectum [19], and JETSCAPE [20], have all utilized ALICE measurements of anisotropic flow to constrain the temperature-dependent specific shear and bulk viscosity. For η/s , the temperature is $T = 0.3$ GeV, and for ζ/s , it is $T = 0.2$ GeV. The figure shows that JETSCAPE has a broader η/s posterior range than Duke, Jyväskylä and Trajectum. The Jyväskylä group's results included higher-order harmonic flow measurements, like flow amplitudes and Symmetric Cumulants, but only with the higher beam energy data for this study (both observables will be explained in Chapter 3). The ranges for ζ/s vary more between the models than for η/s . JETSCAPE argues that the pre-equilibrium duration significantly influences the extracted transport properties. This can also be seen in TRENTo+v-USPhydro [73], where the hydrodynamic evolution initiates without a pre-equilibrium phase. Therefore, it requires a low η/s value (0.05) and ζ/s to be 0 to represent ALICE data [74]. The extension from Jyväskylä [21] is part of this thesis and was published in [22]. This work incorporated the lower beam energy results and is summarized in Section 6.

3 EXPERIMENTAL OBSERVABLES

In heavy-ion physics, understanding core principles often depends on measuring particle-level observables, allowing a detailed evaluation of theoretical models and enhancing understanding. An important step in this process is the comparison of measured observables, the empirical data gathered from experimental procedures, with those that are predicted by the theoretical calculations of the model. This comparison helps in evaluating and refining the model, resulting in more accurate predictions.

This chapter delves deeper into the concept of anisotropic flow. This concept is a tool for gauging and quantifying the effects of medium expansion in the context of heavy-ion physics, providing valuable insights into the dynamics at play. By utilizing this concept of flow, it becomes possible to observe and understand the intricacies of the collective phenomena occurring within the system.

Further, we will present a derivation of the standard flow observables. These observables are widely used in the field for the characterization of collective phenomena, particularly in the low- p_T region.

3.1 Anisotropic flow

A valuable observable of the QGP is the distribution of the final-state particles that are created in the freeze-out stage. As the medium expands and cools down in this stage, its momentum will be carried over to the produced particles, i.e. the particle distribution reflects the expansion of the medium itself. The anisotropy, or the directional difference, in the distribution of these particles is an integral factor that needs to be quantified to effectively understand the characteristics of the medium in which they are dispersed. This anisotropy provides valuable insights into the nature of the medium. It is also one of the earliest indicators of the formation of QGP.

In the field of anisotropy analysis, a common method employed to describe the anisotropy is through the application of a Fourier decomposition to the az-

imuthal particle distribution [75]. This process can be represented by the following equation:

$$f(\varphi) = \frac{a_0}{2\pi} + \frac{1}{\pi} \left(\sum_{n=1}^{\infty} a_n \cos(n\varphi) + \sum_{n=1}^{\infty} b_n \sin(n\varphi) \right). \quad (26)$$

In this equation, a_n and b_n are defined as:

$$a_n = \int_{-\pi}^{\pi} f(\varphi) \cos(n\varphi) dx = \sum_v f(\varphi_v) \cos(n\varphi_v) \quad (27)$$

and

$$b_n = \int_{-\pi}^{\pi} f(\varphi) \sin(n\varphi) dx = \sum_v f(\varphi_v) \sin(n\varphi_v). \quad (28)$$

The sums in a_n and b_n are limited to a finite number, and the v symbol here represents the index of an individual particle.

To further this analysis, a symmetry-plane angle is introduced, denoted as $-\frac{\pi}{n} < \psi_n < \frac{\pi}{n}$. This results in $\omega_n = \sqrt{a_n^2 + b_n^2}$. Consequently, a_n and b_n can be written in terms of ω_n and ψ_n as follows: $a_n = \omega_n \cos(n\psi_n)$ and $b_n = \omega_n \sin(n\psi_n)$.

With these substitutions, the original equation, Equation (26), can now be expressed in a slightly different form:

$$f(\varphi) = \frac{a_0}{2\pi} + \frac{1}{\pi} \sum_{n=1}^{\infty} \omega_n (\cos(n\psi_n) \cos(n\varphi) + \sin(n\psi_n) \sin(n\varphi)). \quad (29)$$

The trigonometric products, $\cos(n\psi_n) \cos(n\varphi) + \sin(n\psi_n) \sin(n\varphi)$, can be rephrased as $\cos(n(\varphi - \psi_n))$. Also, the total number of particles can be redefined by $a_0 = \omega_0 \cos(0\psi_n) = \omega_0 = \int_{-\pi}^{\pi} \frac{dN}{d\varphi} d\varphi = N$. This simplification allows us to express the equation as follows:

$$f(\varphi) = \frac{N}{2\pi} \left(1 + \sum_{n=1}^{\infty} v_n \cos(n(\varphi - \psi_n)) \right), \quad (30)$$

where the term v_n represents the magnitude of each harmonic contribution.

The v_n , often referred to as flow coefficients, provide detailed insights into the shape and anisotropy of a specific event. These coefficients are to understand the geometry and characteristics of the underlying phenomenon. Starting from v_2 , the flow coefficients incrementally increase to v_3 , v_4 , v_5 , and so forth, each representing a distinct expansion mode. For instance, the v_2 flow coefficient is a representation of the eccentricity of an elliptic distribution. This coefficient is particularly useful as it can describe the ellipse-like anisotropic expansion that occurs during collisions involving a participant region with a highly almond-shaped geometry. Following the same concept, v_3 represents the triangular modes that could be observed in an asymmetric collision system. This is important in order to understand the dynamics of such collisions and the resultant geometrical variations. Furthermore, considering the occurrence of event-by-event collision geometry fluctuations, a large value of v_3 is always expected. This anticipation is

based on the established patterns and empirical studies in the field [76]. This understanding of flow coefficients and their implications can greatly enhance our knowledge of complex collision systems and their behaviors. The value of the flow coefficients helps in determining the behavior of the system at hand. These integral values can be ascertained through the use of the formula as follows [77]:

$$v_n = \langle \cos(n(\varphi - \psi_n)) \rangle. \quad (31)$$

In the formula represented by (31), the $\langle \rangle$ brackets are used to signify an average across all particles in consideration. However, for each event, the flow exhibits a distinct magnitude. In other words, the flow, and by extension the v_n , exhibits fluctuations from event to event. These fluctuations inevitably lead to the experimentally measured values of v_n and other observables being reported as an average computed over a substantial sample of events. This average is reflective of the expectation value for the flow coefficients across a distribution of values specific to each event. It is currently understood that these fluctuations are attributable to the unpredictable spatial arrangement of the nuclear constituents at the very moment of the collision. In Equation (30), the azimuthal distribution is expressed with the use of trigonometric expressions. However, it is also possible to convey the same information using exponential complex quantities. This alternative method of expression is illustrated in Equation (32):

$$f(\varphi) = \frac{N}{2\pi} \sum_{n=-\infty}^{\infty} v_n e^{-in(\varphi - \psi_n)} = \frac{N}{2\pi} \sum_{n=-\infty}^{\infty} V_n e^{-in\varphi}, \quad (32)$$

In the above equation, $V_n \equiv v_n e^{in\psi_n}$. This definition allows us to also express V_n in terms of $V_n = \langle e^{in\phi} \rangle$, as derived from Equation (31). The symbol V_n represents a particularly useful quantity within this context, as it encompasses both the magnitude and direction of the flow harmonic, providing a comprehensive overview of the flow's properties.

3.2 Multi-Particle Correlations

3.2.1 Two-Particle Correlations

Multi-Particle correlations are essential for advanced flow analysis. Multi-Particle correlations means that two, three or more particles from the same event are correlated in the azimuthal plane, which is then used to calculate different flow observables. In theory, it is possible to calculate the flow coefficient with Eq. 31, without multi-particle correlations. However, due to the dependency on the symmetry plane, which is not possible to measure directly, its practical use is very limited. It is only the particle azimuthal angles that are directly measurable in experimental analysis, and the event-plane estimates are generally not up to the accuracy standard to make Eq. (31) applicable [78].

This is where the multi-particle approach is applied. It offers a solution that is focused solely on the azimuthal angles of the particles, avoiding the involvement of any quantities that are either unobtainable or challenging to measure.

The first step in implementing this method involves forming a distribution of pairs. This is achieved by multiplying two single particle distributions together as shown in Eq. (32). The result of this operation is what's known as a pair distribution. This pair distribution can be expressed in the following way [79–81]:

$$\begin{aligned} f_{\Delta}(\varphi) &= \Delta N \left(1 + \sum_{n=1}^{\infty} 2 \underbrace{\langle v_n^a v_n^b \rangle}_{*v * n\Delta} \cos(n(\varphi_a - \varphi_b)) \right) \\ &= \Delta N \sum_{n=-\infty}^{\infty} \underbrace{\langle v_n^a v_n^b \rangle}_{*v * n\Delta} e^{-in(\varphi_a - \varphi_b)}. \end{aligned} \quad (33)$$

Once this pair distribution is determined, the average value of v_n over all the particles involved in an event can be calculated. This does not include the instances when the particle pairs with itself. This average value is obtained by calculating the two particle correlation as shown below:

$$v_n^2 + \delta_2 = \langle 2 \rangle_{n|n} = \langle \cos(n(\varphi_a - \varphi_b)) \rangle = \langle e^{-in(\varphi_a - \varphi_b)} \rangle. \quad (34)$$

This expression is only dependent on the azimuthal angle, hence it can be directly used in an experimental setting. The δ_2 on the left side of the equation is introduced as an additional nonflow contribution that is uncorrelated to v_n and emerges from the azimuthal correlations that has another source than the anisotropic flow. Examples of nonflow contributions are resonance decays and jet contributions and common methods used to remove these contributions will be discussed in this chapter.

The first measurements of v_n up to the 9th order harmonic ($n = 9$) is presented in Ref [82]. Figure 12 is from this analysis and it depicts the values of the different flow coefficients as a function of harmonic order for two centrality percentiles, 0 – 5% and 40 – 50%. This shows how the coefficients depend on the harmonic order, and that for orders up to $n = 7$ there is a decreasing trend that points to a viscous damping [83]. A detailed discussion of the figure can be found in Ref. [82]. A study exploring the potential of exceeding $n > 9$ is discussed in Appendix. 1.

3.2.2 Multi-particle correlations and cumulants

It is possible to go to arbitrarily high orders of particle correlations. A general way of notating multi-particle correlations is

$$\langle m \rangle_{n_1, n_2, \dots, n_m} = \langle \cos(n_1 \varphi_1 + n_2 \varphi_2 + \dots + n_m \varphi_m) \rangle. \quad (35)$$

As mentioned before, it is important to only average over distinct particle combinations, such that a self-correlation can be avoided. Non-zero values will only be present for isotropic correlators, meaning correlators that satisfy the condition $n_1 + n_2 + \dots + n_m = 0$.

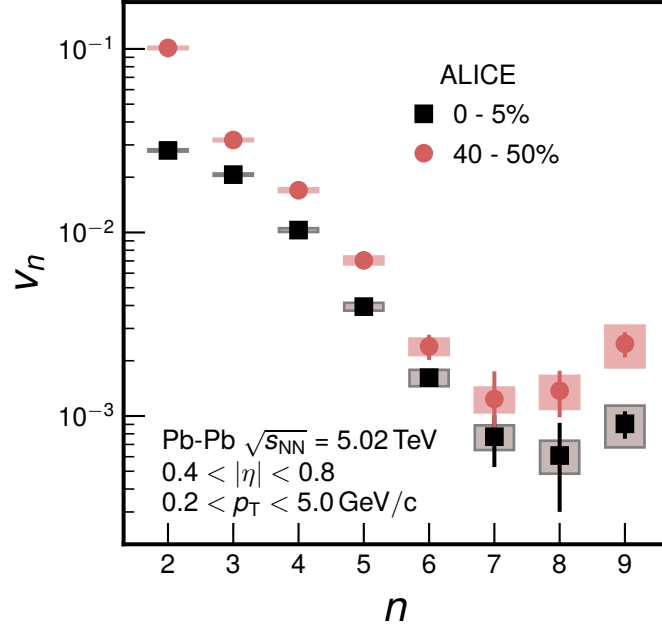


FIGURE 12 The flow amplitude, v_n , as a function of harmonic order in collisions at = 5.02 TeV. Reprinted with permission from [84], 2020, Springer

The non-flow components of lower orders can be minimized by creating correlations between higher and lower orders [85]. This is achieved in the *cumulant method*, where a mix of lower order correlations is subtracted from a higher order correlation. The product of this process, referred to as a cumulant, is a high order correlation that remains insensitive to the non-flow in lower orders. This mechanism is invaluable as it enables the creation of a more streamlined and efficient system.

The equation (36) that follows presents the second to eighth order flow constructed from these cumulants,

$$\begin{aligned}
 v_n\{2\}^2 + \delta_2 &= \langle 2 \rangle_{n|n}, \\
 v_n\{4\}^4 + \delta_4 &= - \left(\langle 4 \rangle_{n,n|n,n} - 2 \langle 2 \rangle_{n|n}^2 \right), \\
 v_n\{6\}^6 + \delta_6 &= \frac{1}{4} \left(\langle 6 \rangle - 9 \langle 4 \rangle \langle 2 \rangle + 12 \langle 2 \rangle^3 \right), \\
 v_n\{8\}^8 + \delta_8 &= - \frac{1}{33} \left(\langle 8 \rangle - 16 \langle 6 \rangle \langle 2 \rangle - 18 \langle 4 \rangle^2 \right. \\
 &\quad \left. + 144 \langle 4 \rangle \langle 2 \rangle^2 - 144 \langle 2 \rangle^4 \right),
 \end{aligned} \tag{36}$$

where the use of curly brackets signifies the order of the cumulant in question. It should be noted, for simplicity and brevity, the harmonics (represented as $n, \dots |n, \dots$) have been purposely left out from the sixth order cumulant as they are always identical.

It is generally observed that the nonflow magnitude tends to be larger for lower orders when compared to higher orders. To clarify how the nonflow is

removed, one can divide the particle correlations into their individual components, a process that is outlined in Ref. [85]. For better understanding, here is an example of the fourth order cumulant

$$\begin{aligned}
& \langle \cos(n(\varphi_1 + \varphi_2 - \varphi_3 - \varphi_4)) \rangle \\
&= \langle \cos(n(\varphi_1 - \varphi_3)) \rangle \langle \cos(n(\varphi_2 - \varphi_4)) \rangle \\
&+ \langle \cos(n(\varphi_1 - \varphi_4)) \rangle \langle \cos(n(\varphi_2 - \varphi_3)) \rangle \\
&+ \langle 4 \rangle_{n,n|n,n} - 2 \langle 2 \rangle_{n|n}^2 + \delta_4.
\end{aligned} \tag{37}$$

The nonflow suppression mechanism serves as the foundational basis for the symmetric cumulants (SC) observable as referenced in the works of [86, 87]. The symmetric cumulants observable is an important measure in this field of study.

The two-harmonic symmetric cumulant is defined by the equation:

$$\begin{aligned}
\text{SC}(m, n) &\equiv \langle v_m^2 v_n^2 \rangle - \langle v_m^2 \rangle \langle v_n^2 \rangle \\
&= \langle \cos(m\varphi_1 + n\varphi_2 - m\varphi_3 - n\varphi_4) \rangle \\
&- \langle \cos(m(\varphi_1 - \varphi_3)) \rangle \langle \cos(n(\varphi_2 - \varphi_4)) \rangle.
\end{aligned} \tag{38}$$

Upon inspection, the equation looks remarkably similar to $v_n\{4\}$ in Eq.(36). Both harmonic symmetric cumulants are used to assess the correlations between the magnitudes of two different flow harmonics. This is a key observable due to its particular sensitivity to the temperature dependence of $\eta/s(T)$ [21, 86].

A large positive value from the SC shows a strong correlation between the two harmonics. On the other hand, if the SC value is negative, it indicates an inverse relationship between the harmonics.

In addition to the symmetric cumulant, there exists the normalized symmetric cumulant (NSC) observable. The NSC observable is a scaled quantity, derived from a correlation of flow coefficients. This approach provides the opportunity to delve into the details of flow harmonic correlations. One of its key advantages is that it does not have a reliance on the magnitude of the flow coefficients. The NSC observable is defined by:

$$\text{NSC}(m, n) = \frac{\text{SC}(m, n)}{\langle v_m^2 \rangle \langle v_n^2 \rangle} = \frac{\langle v_m^2 v_n^2 \rangle}{\langle v_m^2 \rangle \langle v_n^2 \rangle} - 1. \tag{39}$$

Both the measured observables can be seen in Fig. 13 where a comparison to the EKRT model is done.

3.3 Linear and non-linear flow modes

The idea of non-linearity in anisotropic flow has been derived from the observed correlations between initial state eccentricity and flow. As one moves to higher harmonics, the evident linear correlations that were observed in lower harmonics

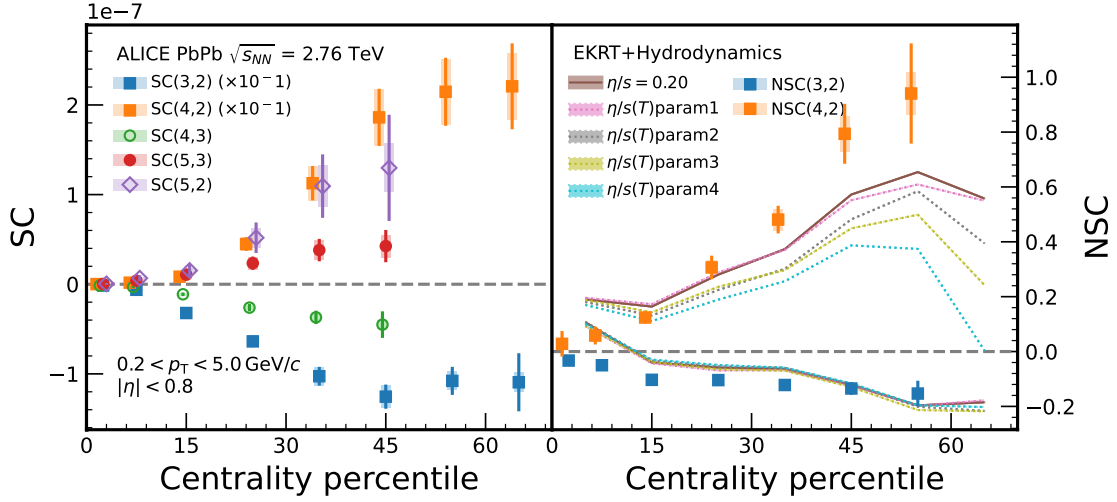


FIGURE 13 The SC and NSC observables presented as a function of centrality percentile in collisions at $\sqrt{s_{NN}} = 2.76$ TeV [86]. Additionally there is a comparison to EKRT+hydrodynamics [88] for the NSC observables.

begin to fade. This change in correlation is clearly depicted by the hydrodynamical calculations presented in Fig.14 [88]. From these calculations, it is clearly seen that the linear correlation denoted as $\varepsilon_n \propto v_n$ begins to break down for the fourth harmonic. This breakdown represents a deviation from what has been observed in the lower harmonics. Furthermore, the evaluation of the symmetric cumulant, SC(4,2), shows a strong and consistent correlation between the fourth and second harmonics. This correlation can be clearly seen in Fig. 13. It's important to note the scaling of one order for both SC(3,2) and SC(4,2). This correlation is likely attributed to the pronounced non-linear relationship that exists between ε_4 and v_4 . In this section, I will delve into the details of a methodology that can be employed to systematically measure non-linear interactions among various flow harmonics. This formalism is not only important for understanding the system but also serves as the foundation for the measurements that are presented in the final chapters of this thesis.

3.3.1 Mode coupling

The connection between v_n and ε_n can be linearly stated as

$$v_n e^{in\psi_n} = k \varepsilon_n e^{in\Phi_n}, \quad (40)$$

with k acting as a scaling factor. This equation is a reasonable approximation when $n < 3$. A more accurate prediction for higher harmonics was discussed in Ref. [89]. This was achieved by quantitatively testing such an estimator for the fourth harmonic. It was found that the fourth and fifth harmonics can be expressed as a combination of $\varepsilon_{4(5)}$ and ε^2 for lower harmonics, i.e.

$$v_4 e^{i4\psi_4} = k \varepsilon_4 e^{4i\Phi_4} + k' \varepsilon_2^2 e^{4i\Phi_2}. \quad (41)$$

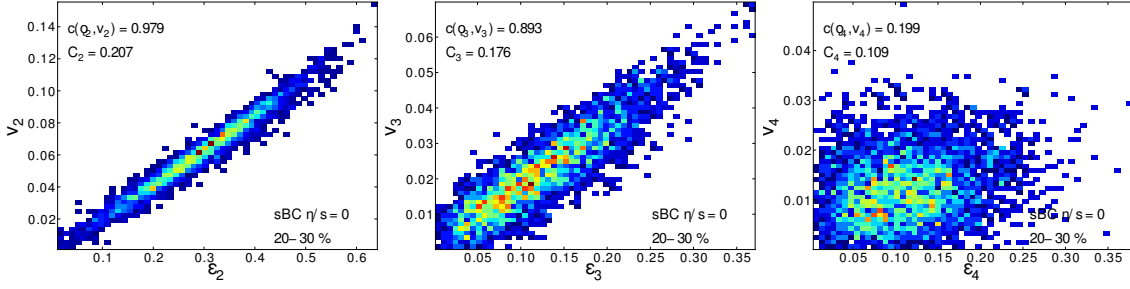


FIGURE 14 The hydrodynamic calculations of v_n are plotted with respect to the corresponding initial state eccentricity ε_n , as per the research conducted by Niemi et al. [88]. In the case of the second and third harmonics, the correlations that emerge from this plotting are approximately linear. This suggests a predictable and direct relationship between these harmonics and the initial state eccentricity. However, when considering the fourth harmonic, this linearity breaks down. It's an interesting deviation that implies the relationship between the fourth harmonic and the initial state eccentricity is more complex, and it may be influenced by additional factors not present or not as significant in the second and third harmonics. Reprinted with permission from [88], 2012, American Physical Society.

$$v_5 e^{i5\psi_5} = k\varepsilon_5 e^{5i\Phi_5} + k'\varepsilon_2 e^{2i\Phi_2} \varepsilon_3 e^{3i\Phi_3}. \quad (42)$$

The relationships between Equation 40 and Equation 41 are instrumental when it comes to estimations. It has been observed that Equation 40 provides an underwhelming estimation in scenarios involving mid-central and peripheral collisions. On the other hand, Equation 41 offers a considerably more accurate estimation, demonstrating its effectiveness across a broad centrality range.

Based on these findings, it can be stated that the higher harmonic flow is effectively a combination of linear and non-linear contributions. The subsequent step in the investigation of these relationships entails representing the estimators (taking Equation 41 as a key example) in terms of the final state flow.

To accomplish this, we start by writing Equation 40 for the second harmonic and then substitute it into Equation 41. This process culminates in the formulation of the following expression:

$$v_4 e^{in\psi_4} = v_{4,L} e^{4i\psi_4} + \frac{k'}{k'^{1/2}} v_2^2 e^{2i\psi_2}. \quad (43)$$

In this equation, $v_{4,L}$ symbolizes the linear contribution to the fourth harmonic. The linear contribution maintains a direct relationship with a cumulant defined initial state anisotropy [90]:

$$v_{4,L} e^{4i\psi_4} \propto \varepsilon_4' e^{i4\Phi_4'} = \varepsilon_4 e^{i4\Phi_4} + \frac{3\langle r^2 \rangle^2}{\langle r^4 \rangle} \varepsilon_2 e^{i4\Phi_2}. \quad (44)$$

However, when contrasted with the total contribution for $n = 2, 3$, it exhibits a linear relationship with the classical definition. As we have previously

established that $V_n \equiv v_n e^{in\psi_n}$, we can therefore rewrite Equation 43 as

$$V_4 = V_{4,L} + \chi_{4,22} V_2^2, \quad (45)$$

Here, $\chi_{4,22}$ represents the quantification of the non-linear response and is referred to as the non-linear flow mode coefficient accordingly. The same decomposition of flow can be further extended to higher harmonics as mentioned in Ref. [91]

$$\begin{aligned} V_5 &= V_{5,L} + \chi_{5,23} V_2 V_3, \\ V_6 &= V_{6,L} + \chi_{6,222} V_2^3 + \chi_{6,33} V_3^2 + \chi_{6,24} V_2 V_{4,L}, \\ V_7 &= V_{7,L} + \chi_{7,223} V_2^2 V_3 + \chi_{7,34} V_3 V_{4,L} + \chi_{7,25} V_2 V_{5,L}, \\ V_8 &= V_{8,L} + \chi_{8,2222} V_2^4 + \chi_{8,233} V_2 V_3^2 + \mathcal{E}(V_{4,L}, V_{5,L}, V_{6,L}). \end{aligned} \quad (46)$$

It is important to note that starting from the sixth harmonic, the contribution from lower harmonics begins to increase. This means that more terms that include the lower linear harmonics contributions are added. The symbol $\mathcal{E}(\dots)$ denotes the many higher harmonic linear contributions for V_8 .

It is possible to separate the linear and non-linear parts under the assumption that these components are uncorrelated [92]. In practical terms, this assumption means that the expression $\langle (V_2^*)^2 V_{4L} \rangle \simeq \langle V_2^2 V_{4L}^* \rangle \simeq 0$ holds true. In this particular expression, the brackets indicate an average taken over a large sample of events, while the * symbol denotes a complex conjugate.

This assumption has been put to the test in numerous experimental settings, with the results documented in various scholarly articles, such as Ref. [93]. The procedure involves taking the mean square of these relations over all events. When the assumption of non-correlation is applied in this context, it allows for the derivation of an expression that specifically describes the linear part.

The expression in question is as follows:

$$\underbrace{\langle |V_{4L}|^2 \rangle^{\frac{1}{2}}}_{*} \langle v_{4,L} \rangle = \left(\underbrace{\langle |V_4|^2 \rangle}_{*} \langle v_4^2 \rangle - \underbrace{\chi_{4,22}^2 \langle |V_2|^4 \rangle}_{*} \langle v_{4,NL}^2 \rangle \right)^{\frac{1}{2}}. \quad (47)$$

In the process of studying the events, it becomes clear that the linear flow component, denoted by $\langle v_{4,L} \rangle$, is something that can be quantified through experimental measurement. In addition to this, there is also the potential to identify the non-linear contribution represented by $\langle v_{4,NL}^2 \rangle \equiv \chi_{4,22}^2 \langle |V_2|^4 \rangle$. This identification is made possible by referring to Eq.(47).

In a further step, we can develop an expression for $\chi_{4,22}^2$. This is achieved by multiplying Eq.(45) by $V_2^{(*2)}$. The following equations provide a detailed break-

down of the derivation process:

$$\begin{aligned}
V_4 &= V_{4,L} + \chi_{4,22} V_2^2 | \cdot V_2^{(*2)} \\
V_4 V_2^{(*2)} &= V_{4,L} V_2^{(*2)} + \chi_{4,22} V_2^2 V_2^{(*2)} \\
\langle V_4 V_2^{(*2)} \rangle &= \chi_{4,22} \langle |V_2|^4 \rangle \\
\chi_{4,22} &= \frac{\langle V_4 V_2^{(*2)} \rangle}{\langle |V_2|^4 \rangle} \\
&= \frac{\langle \langle \cos(4\varphi_1 - 2\varphi_2 - 2\varphi_3) \rangle \rangle}{\langle \langle \cos(2\varphi_1 + 2\varphi_2 - 2\varphi_3 - 2\varphi_4) \rangle \rangle} \\
&= \frac{\langle \langle 3 \rangle_{4,-2,-2} \rangle}{\langle \langle 4 \rangle_{2,2,-2,-2} \rangle}.
\end{aligned} \tag{48}$$

In a similar manner, the higher harmonics can be derived, such as the mode coupling coefficient for the fifth harmonic, which can be expressed as follows:

$$\begin{aligned}
\chi_{5,23} &= \frac{\langle V_5 V_2^* V_3^* \rangle}{\langle |V_2|^2 |V_3|^2 \rangle} \\
&= \frac{\langle \langle \cos(5\varphi_1 - 2\varphi_2 - 3\varphi_3) \rangle \rangle}{\langle \langle \cos(2\varphi_1 + 3\varphi_2 - 2\varphi_3 - 3\varphi_4) \rangle \rangle} \\
&= \frac{\langle \langle 3 \rangle_{5,-2,-3} \rangle}{\langle \langle 4 \rangle_{2,3,-2,-3} \rangle}.
\end{aligned} \tag{49}$$

In conclusion, the magnitude of the fourth harmonic non-linear contribution can be expressed using the notation $v_{4,22} \equiv \chi_{4,22}^2 \langle |V_2|^4 \rangle$. On closer inspection, $v_{4,22}$ serves as a representation of the projection of the fourth harmonic in the direction of the second harmonic. This means that $v_{4,22}$ quantifies the extent to which the fourth harmonic aligns with the direction of the second harmonic. This $v_{4,22}$ measurement is crucial as it offers a numerical depiction, and potentially forecast, of the strength of the non-linear flow contribution. Meanwhile, $\chi_{4,22}$ offers a measure of the strength of the non-linear flow between different harmonics, providing a deeper insight into this complex system.

The magnitudes of all measured non-flow coefficients as a function of centrality percentile are shown in Fig.15. There is a centrality trend of decreasing magnitudes towards more peripheral collisions for observables up to $\chi_{6,222}$. Whereas the higher orders show no clear centrality dependency within the uncertainty. More details discussed in Ref. [82].

In addition to the previously discussed observables, another set of measurements, known as the symmetry plane correlations, are introduced. These particular correlations provide insight into the relationships between the directions of various flow harmonics. Among the symmetry plane correlations, the lowest harmonic is the correlation between the fourth and second harmonic. This corre-

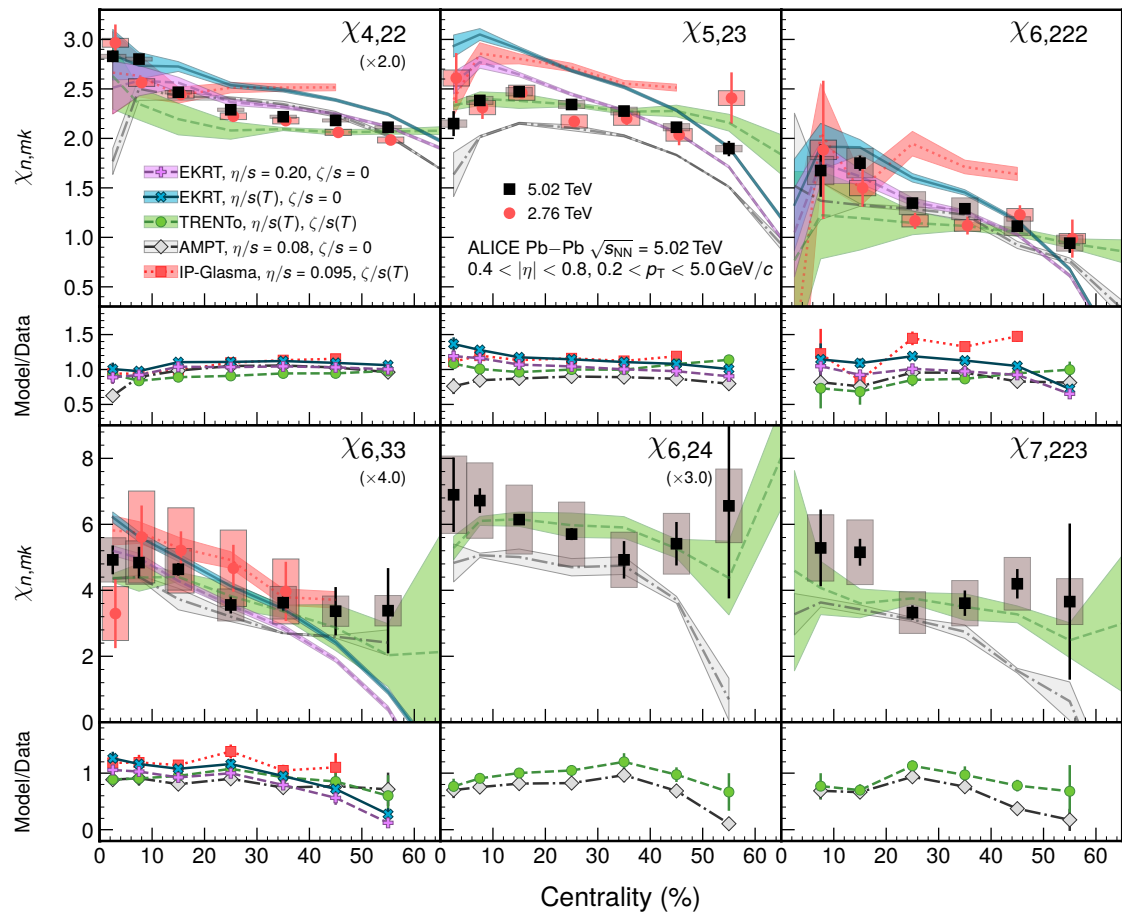


FIGURE 15 Non-linear flow mode contribution as a function of centrality percentile in collisions at $\sqrt{s_{NN}} = 5.02$ TeV. Reprinted with permission from [82], 2020, Springer.

TABLE 1 Exploring the unique characteristics of collective flow observables in high energy physics phenomenology.

Name	Observables	Characteristics	Sensitivity
Flow Coefficient	v_n	System expansion	Average $\langle \eta/s \rangle$ and $\zeta/s(T)$ peak
(Normalized) Symmetric Cumulant [86, 87, 95]	(N)SC(m, n)	Correlation between v_m and v_n	$\eta/s(T)$ temperature dependence
Linear/non-linear flow modes [82]	$v_{n,L}, v_{n,mk}$	linear/non-linear contributions to v_n	(not tested)
Non-linear flow mode coefficients [96]	$\chi_{n,mk}$	non-linear response	$\eta/s(T)$ at the freeze-out temperature
Symmetry plane correlations	$\rho_{n,mk}$	Correlations between the symmetry planes	(not observed)

lation is defined as follows [94]:

$$\rho_{4,22} = \frac{\langle V_4 V_2^{(*2)} \rangle}{\sqrt{\langle |V_4|^2 \rangle \langle |V_2|^4 \rangle}} = \frac{v_{4,22}}{v_4}. \quad (50)$$

The symmetry plane correlations, along with the initial set of observables discussed earlier are all summarized in Table 1 with information of what they measure as well as what they are sensitive to when using a stochastic approach, which means that the model to data comparison is done in a limited parameter space. What is found is that the flow coefficient is sensitive to the average specific shear viscosity and the peak of the temperature dependent bulk viscosity and that the symmetric cumulants are sensitive temperature dependent specific shear viscosity. Additionally, the non-linear flow mode coefficients are sensitive to the temperature dependent specific shear viscosity at the freeze-out temperature. The symmetry plane correlations and the linear and non-linear contributions had not observed any sensitivity or is not tested.

The Bayesian parameter estimation presented in this thesis also includes a sensitivity analysis of the observables included in the analysis, which included a model to data comparison of the full parameter space. More details is found in 3.5.

3.4 Generic frameworks of multi-particle correlations

Over the years of heavy-ion research, many methods have been carefully developed and improved to measure links from particle directional angles. One par-

ticular method, which has gained widespread popularity due to its efficacy, is the application of Eq. (30). This equation is typically used in direct conjunction with either the reaction plane ψ_R or symmetry-planes ψ_n .

Using this method is simple, though detailed. The initial step involves estimating the direction of the symmetry-plane using an event-plane estimation. Following the successful execution of this step, Eq. (30) is then evaluated. The concluding action in this sequence is to rectify the result by computing the event-plane resolution.

This innovative system of measurement is known as the event-plane method [77, 78]. While this method has proven to be highly effective, it is not without its limitations. For example, it is not the most practical choice when it comes to measuring higher order flow observables, as it is prone to various biases. Consequently, our focus will be on examining more efficient techniques for calculating multi-particle correlations in accordance with Eq. (35).

A significant practical challenge associated with Eq.(35) is the computational expense involved in its calculation, unless mitigated through some means. This challenge becomes evident when explicitly expressing the average [97]:

$$\langle m \rangle_{n_1, n_2, \dots, n_m} = \frac{\sum_{\substack{k_1, k_2, \dots, k_m=1 \\ k_1 \neq k_2 \neq \dots \neq k_m}}^M w_{k_1} w_{k_2} \dots w_{k_m} \cos(n_1 \varphi_{k_1} + n_2 \varphi_{k_2} + \dots + n_m \varphi_{k_m})}{\sum_{\substack{k_1, k_2, \dots, k_m=1 \\ k_1 \neq k_2 \neq \dots \neq k_m}}^M w_{k_1} w_{k_2} \dots w_{k_m}} \quad (51)$$

where w_j represents the weights assigned to individual particles to adjust for uneven detector acceptance.

3.4.1 Generic formulas

Another approach to finding the $\langle m \rangle_{n_1, n_2, \dots, n_m}$ expressions is in terms of products of sums in the linear form. To find these expressions, the process begins with the definition of an essential element known as the flow vector, or the Q-vector as it is commonly referred to in literature [98].

The Q-vector is defined using the following equation:

$$Q_{n,p} = \sum_{k=1}^M w_k^p \cos(in \varphi_k), \quad (52)$$

This equation implies that $Q_{-n,p} = Q_{n,p}^*$, establishing an important relationship.

In the next step, these Q-vectors are multiplied together and then normalized to yield an approximate result of a correlation. However, it is crucial to note that these results have a potential bias introduced by autocorrelations. This bias holds significant weight and should be eliminated for the results to be accurate. Moreover, this approach does not fully account for non-uniform detector acceptance in the correct manner, which can also impact the final results. It is for these

reasons that this thesis will focus solely on the complete and unbiased solutions that are used in the analyses, ensuring that the results presented are as accurate and reliable as possible.

3.4.1.1 Multi-particle correlations without η -gap

The solutions that are presented here are derived from the generic framework as discussed by Bilandzic et al. [97]. Within this framework, a two particle correlation is considered. In this case, the autocorrelation has been eliminated and the non-uniform acceptance has been factored in, as indicated by the following expression:

$$\langle 2 \rangle_{n_1, n_2} = \frac{Q_{n_1,1} Q_{n_2,1} - Q_{n_1+n_2,2}}{Q_{0,1}^2 - Q_{0,2}}. \quad (53)$$

Additionally, a three-particle correlator is considered. This is an approach that is used extensively by the non-linear flow mode observables. It can be written as shown in equation 54:

$$\begin{aligned} \langle 3 \rangle_{n_1, n_2, n_3} = & Q_{n_1,1} Q_{n_2,1} Q_{n_3,1} - Q_{n_1+n_2,2} Q_{n_3,1} - Q_{n_2,1} Q_{n_1+n_3,2} \\ & - Q_{n_1,1} Q_{n_2+n_3,2} + 2Q_{n_1+n_2+n_3,3} \\ & / (Q_{0,1}^3 - 3Q_{0,2} Q_{0,1} + 2Q_{0,3}). \end{aligned} \quad (54)$$

Finally, we also examine a four-particle correlation. This approach is often found in symmetric cumulants and also for some high harmonic non-linear flow observables. It is expressed as shown in equation 55:

$$\begin{aligned} \langle 4 \rangle_{n_1, n_2, n_3, n_4} = & Q_{n_1,1} Q_{n_2,1} Q_{n_3,1} Q_{n_4,1} - Q_{n_1+n_2,2} Q_{n_3,1} Q_{n_4,1} - Q_{n_2,1} Q_{n_1+n_3,2} Q_{n_4,1} \\ & - Q_{n_1,1} Q_{n_2+n_3,2} Q_{n_4,1} + 2Q_{n_1+n_2+n_3,3} Q_{n_4,1} - Q_{n_2,1} Q_{n_3,1} Q_{n_1+n_4,2} \\ & + Q_{n_2+n_3,2} Q_{n_1+n_4,2} - Q_{n_1,1} Q_{n_3,1} Q_{n_2+n_4,2} + Q_{n_1+n_3,2} Q_{n_2+n_4,2} \\ & + 2Q_{n_3,1} Q_{n_1+n_2+n_4,3} - Q_{n_1,1} Q_{n_2,1} Q_{n_3+n_4,2} + Q_{n_1+n_2,2} Q_{n_3+n_4,2} \\ & + 2Q_{n_2,1} Q_{n_1+n_3+n_4,3} + 2Q_{n_1,1} Q_{n_2+n_3+n_4,3} - 6Q_{n_1+n_2+n_3+n_4,4} \\ & / (Q_{0,1}^4 - 6Q_{0,1}^2 Q_{0,2} + 3Q_{0,2}^2 + 8Q_{0,1} Q_{0,3} - 6Q_{0,4}). \end{aligned} \quad (55)$$

To calculate all Q-vectors numerically, only one loop over the particle azimuthal angles is used. This ensures that the implementation remains optimal and efficient.

3.4.1.2 Multi-particle correlations with η -gap

The correlators mentioned in the previous discussions are designed to address the autocorrelation and non-uniform acceptance issues. However, these correlators remain vulnerable to nonflow effects in various experimental settings. The

cumulant and symmetric cumulant observables offers a solution to these non-flow issues, having been constructed specifically to address this challenge [99]. However, it is worthwhile to note that this solution is not applicable to all the observables. As a result, these other observables are influenced by the nonflow that is associated with the correlators in Eq. (53)-(55) [99].

Previous research has demonstrated that the majority of the nonflow originates from short-range correlations. These correlations are typically generated through resonance decays and jet contributions, primarily manifesting in the low pseudorapidity (η) region [100]. The issue of these correlations has prompted the proposal of several potential solutions. One such solution that has been proposed to mitigate this issue revolves around making certain that no pairs or higher order combinations are found to be correlated within this low- η region. This is a complex process that requires dividing the events into several distinct subevents. In order to achieve this, these subevents must be separated by one or more η -gaps. This method effectively excludes the nonflow η -region from the analysis, thereby limiting the impact of these correlations on the overall results of the study.

Findings from Ref. [101] suggest that it is generally sufficient to use two subevents in order to eliminate the majority of the nonflow contribution. This is because the majority of potential nonflow sources produce particles within these two subevents only. When the number of subevents is increased, some remaining contribution is removed, but the overall benefit of this approach was found to be minor. As a result, it can be inferred that the nonflow, which will arise from higher order correlations, specifically, elements such as the three-particle correlator, will be negligible.

In scenarios where two subevents are utilized and are separated by one η -gap, two Q-vectors will be calculated using Eq. (52). One Q-vector will correspond to the positive η -region and the other will correspond to the negative η -region. These Q-vectors will be labeled as $Q_{n,p}^A$ and $Q_{n,p}^B$, respectively. The introduction of an η -gap leads to changes in the way we express correlators. In the case of the two-particle correlator specifically, the change brought about by the introduction of the η -gap is reflected in its modified expression, which is as follows:

$$\langle 2 \rangle_{n_1, n_2}^{\text{Gap}} = \frac{Q_{n_1,1}^A Q_{n_2,1}^B}{Q_{0,1}^A Q_{0,1}^B}, \quad (56)$$

where the η -gap takes responsibility for the autocorrelation and hence does not need to be explicitly subtracted. However, it should be noted that the autocorrelation needs to be subtracted for higher correlations. The three-particle correlator where $n_1 = n_2 + n_3$ can be expressed as

$$\langle 3 \rangle_{n_1, n_2, n_3}^{\text{Gap}} = \frac{Q_{n_1,1}^A Q_{n_2,1}^B Q_{n_3,1}^B - Q_{n_1,1}^A Q_{n_2+n_3,2}^B}{Q_{0,1}^A ((Q_{0,1}^B)^2 - Q_{0,2}^B)}, \quad (57)$$

and the four-particle correlator for $n_1 = n_2 + n_3 + n_4$ can be written as

$$\begin{aligned} \langle 4 \rangle_{n_1, n_2, n_3, n_4}^{\text{Gap}} &= Q_{n_1, 1}^A Q_{n_2, 1}^B Q_{n_3, 1}^B Q_{n_4, 1}^B - Q_{n_1, 1}^A Q_{n_2+n_3, 2}^B Q_{n_4, 1}^B \\ &\quad - Q_{n_1, 1}^A Q_{n_3, 1}^B Q_{n_2+n_4, 2}^B - Q_{n_1, 1}^A Q_{n_2, 1}^B Q_{n_3+n_4, 2}^B \\ &\quad + 2Q_{n_1, 1}^A Q_{n_2+n_3+n_4, 3}^B \\ &\quad / (Q_{0, 1}^A ((Q_{0, 1}^B)^3 - 3Q_{0, 2}^B Q_{0, 1}^B + 2Q_{0, 3}^B)). \end{aligned} \quad (58)$$

3.5 Sensitivity of observables

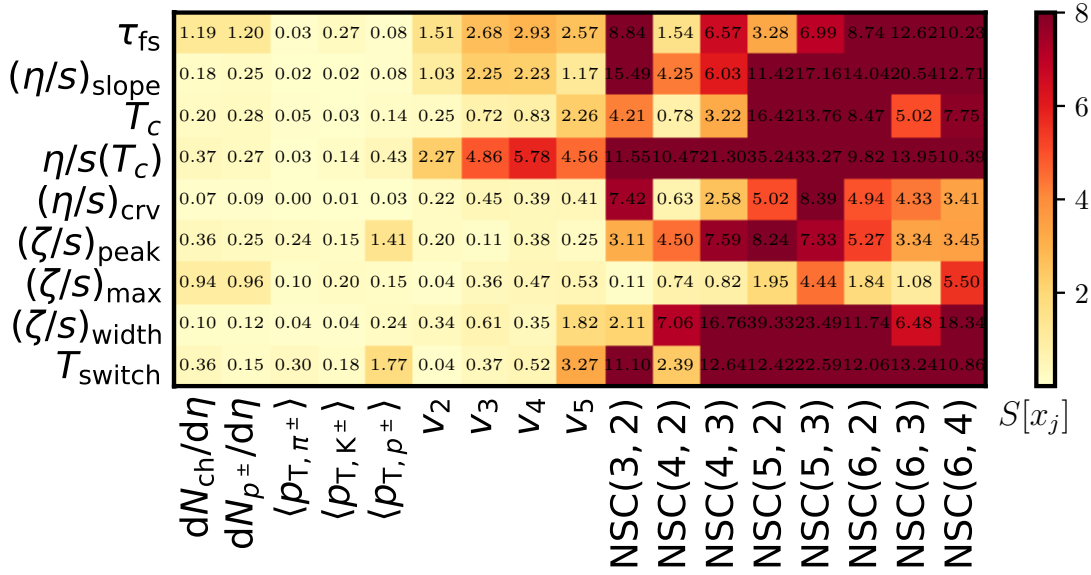


FIGURE 16 Sensitivity of flow observables to the Bayesian model parameters shown as a color map. Different colors are used to represent the varying levels of sensitivity. Light yellow shades are used to depict areas of low or no sensitivity, suggesting that changes in the corresponding model parameter have minimal or no impact on the outcome. On the other hand, orange and darker red colors are used to illustrate moderate or strong sensitivities respectively. This means that any adjustments to the corresponding model parameters can significantly influence the outcome, with orange indicating a moderate level of influence and darker red a strong level of influence.

A way to quantify the independence of an observable is to look at how sensitive that observable is to a model parameter discussed in Chapter 2.3.1. In this analysis, the sensitivity of each observable is evaluated by measuring the relative change in the observable's value, Δ . This change is taken between two distinct points within the parameter space as in the following equation:

$$\Delta = \frac{|\hat{O}(\vec{x}') - \hat{O}(\vec{x})|}{\hat{O}(\vec{x})}, \quad (59)$$

where $\hat{O}(\vec{x})$ and $\hat{O}(\vec{x}')$ denote the observable's values at the parameter positions \vec{x} and \vec{x}' , respectively [20]. The process of measuring this change provides valuable insight into the flexibility and response of the observable to shifts within the parameter space, thus giving a clearer understanding of the observable's behaviour under different conditions.

In the analysis, a particular reference parameter point, denoted as \vec{x} , is selected. This represents the value derived from the analytical work. Another point, labeled as \vec{x}' , is chosen to represent a small percentile change within the parameter space. To elaborate, \vec{x}' is defined as $\vec{x}' = (x_1, x_2, \dots, (1 + \delta)x_j, \dots, x_p)$. In this definition, δ symbolizes the change occurring within the parameter space. In the context of this analysis, the value of δ is set to 0.1, which is a value chosen to ensure a manageable level of change within the parameter space. The actual sensitivity of each observable is then defined as

$$S[x_j] = \Delta/\delta. \quad (60)$$

Figure 16 summarizes the sensitivity measured for some selected observables against the transport properties. From this figure it can be seen that number of charged particles and p_T is not particularly sensitive to the transport properties. However, the flow amplitudes v_n are sensitive to the temperature dependent specific shear viscosity, $\eta/s(T_c)$ and the normalized symmetric cumulants even more sensitive and to more parameters. Hence the sensitivity gives yet another motivation to measure these higher order harmonic flow observables, such that they can be used to reduce the uncertainty of the transport properties.

4 EXPERIMENTAL SETUP

CERN, the European Organization for Nuclear Research, was established in 1954 and is situated near Geneva, on the border of Switzerland and France. CERN, the world's largest laboratory for particle physics acceleration, employs over 2500 staff and receives more than 12000 scientists annually. Currently, it receives support from its 23 member countries, Finland being one of them.

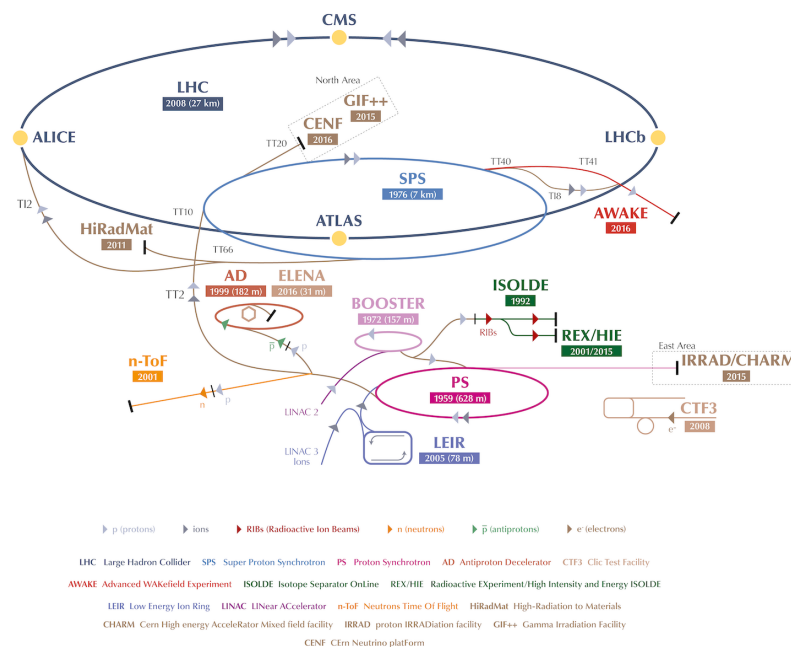


FIGURE 17 A schematic view over the CERN collider infrastructure. Reprinted with permission from [102].

4.1 The Large Hadron Collider

Currently, the world's largest operational particle accelerator is the Large Hadron Collider (LHC) at CERN. With a 26.7 km circumference, it can collide proton and heavy-ion beams at a center-of-mass energy of 14 and 5.02 TeV per nucleon, respectively. Though designed for a luminosity of $10^{32}\text{cm}^{-2}\text{s}^{-1}$, the LHC has often surpassed this, with the highest value nearly doubling the designed one. The LHC's key parameters are found in table 2 [103].

TABLE 2 Some different values of the design parameters of the LHC [103].

Parameters	Values
Circumference of LHC	26.7 km
Dipole operating temperature	1.9 K
Number of magnets	9300
Nominal energy, protons	7 TeV
Momentum at injection to LHC	450 GeV/c
Bunch spacing	25 ns
Design Luminosity	$10^{34}\text{cm}^{-2}\text{s}^{-1}$
Number of bunches / proton beam	2808
Beta function β^*	0.55 m

The capabilities of LHC do not extend to accelerating particles from a state of rest to ultra-relativistic velocities. The process of particle acceleration is complex and multi-staged, and the LHC is only one part of this intricate system. Prior to entering the LHC ring for the final phase of acceleration, the particle beams must undergo several stages of pre-acceleration. Depending on what type of beam they take a slightly different route. The proton beam starts its journey from the proton source to the linear accelerator LINAC2 which accelerates the particles up to 50 MeV and continues to the Proton Synchrotron (PS) booster that accelerates the particles up to 1.4 GeV. For heavy ion beams, the process begins at the heavy ion source, proceeds to the linear accelerator LINAC3, and then to the Low Energy Ion Ring (LEIR). Following that, the beam moves from the PS booster or LEIR to the Proton Synchrotron (PS), where it's accelerated to 25 GeV. The final acceleration step occurs in the Super Proton Synchrotron (SPS), which propels the beam to 450 GeV before it's injected into the LHC.

Acceleration in the LHC is facilitated by Radio Frequency (RF) cavities situated along the ring [104]. The electric field in the RF cavities will oscillate, and when this oscillation is synchronised with the circulating charged particles that are induced in the ring, they will experience a net forward in acceleration. To start acceleration, it's crucial to synchronize the bunches of particles. The RF cavities' oscillation is fine-tuned based on the specific type of particles in use to reach the target energies. As particles approach their intended energy level, the accelera-

tion force decreases. In some instances, particles may acquire excessive energy during certain acceleration phases, leading to their deceleration. Consequently, the LHC accelerates particles in separate bunches, and is able to manage up to 2808 groups at the same time. In theory, the RF cavities in the LHC operate at a frequency of 400.8 MHz, which should result in a separation of 2.5 nanoseconds between bunches. However, in practice, only 10% of the detector's bunch capacity is used, effectively increasing the actual separation to 25 nanoseconds.

The LHC utilizes powerful superconducting electromagnets to guide the beam and maintain its circular path. It requires 1232 dipole magnets, each generating an 8.33 T magnetic field necessary for a 7 TeV proton beam [105]. To focus the beam, 858 quadrupole magnets are used, along with an additional 7210 higher multipole magnets for beam adjustments. This results in a total of 9300 magnets in the LHC.

The term "beam emittance," denoted as ε , is used to describe the confinement of the particle bunch within the beam [106, 107]. A smaller ε indicates smaller distances between the particles, and their energies are more uniform. The emittance is used to define the smallest area that a beam can be squeezed through [107],

$$A = \pi\varepsilon.$$

The greater the confinement of the particle bunch, the easier it navigates through the beam transport system, and the chances of it colliding with the opposing beam at the interaction point are increased. This is also employed to denote an amplitude function:

$$\beta = \frac{\pi\sigma^2}{\varepsilon}, \quad (61)$$

where σ represents the bunch's cross-sectional dimension. At the interaction point, this amplitude function is known as β^* (refer to Figure 18). Every experiment aims to reduce β^* in order to maximize the rate of collisions, which is represented by the term 'luminosity' as follows:

$$\mathcal{L} \sim \frac{fN^2}{4\varepsilon\beta^*}. \quad (62)$$

Therefore, by strategically dispatching large bunches of particles, which are often referred to as N , and ensuring that they have low emittance, we can optimize their performance. This is further improved by maximizing the frequency of their arrival. In doing so, we are able to achieve a state of high luminosity at the interaction point.

Ensuring high luminosity and avoiding major imbalances between experiments necessitates accurate control of β^* . Future methods of operation and advancements to the High Luminosity Large Hadron Collider (HL-LHC) will function at a reduced β of around 0.15 m and accomplish greater luminosities [108].

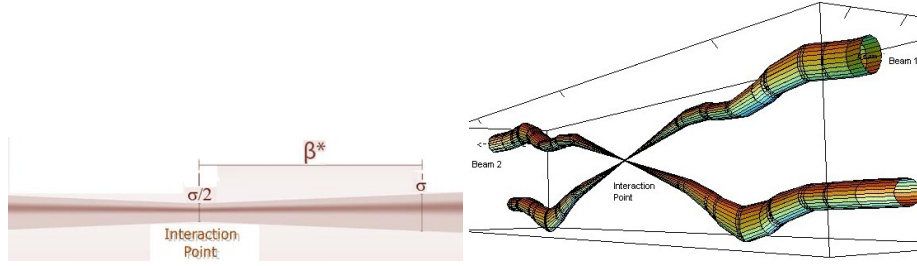


FIGURE 18 The β^* value (shown on the left) and the interaction point (depicted on the right) [109].

4.1.1 The experiments at LHC

Along the LHC accelerator ring are four large experiments; ATLAS [110], ALICE [111, 112], CMS [113], and LHCb [114]. Among these experiments, only ALICE (A Large Ion Collider Experiment) is solely dedicated to heavy ion physics. The most significant work of ALICE includes studying the properties of QGP.

ATLAS (A Toroidal LHC ApparatuS) and CMS (Compact Muon Solenoid), which are the two largest and most comprehensive experiments conducted at CERN, the European Organization for Nuclear Research, are designed with a multifunctional capacity that enables them to conduct a wide array of physics experiments. These experiments range from probing the elementary particles that make up the universe, to the exploration of quantum phenomena and the laws of nature. Among their numerous achievements, the most notable is the discovery of the Higgs boson in 2012 [115, 116]. This groundbreaking discovery, which confirmed the existence of the last unobserved particle predicted by the Standard Model of particle physics, has had an impact on the scientific community and has been a milestone in the field of quantum physics.

LHCb (LHC beauty), an experiment at the LHC, is dedicated to exploring the physics associated with the bottom, or "beauty," quark. The primary focus of this experiment is to investigate CP violation parameters, which is done through detailed analysis of hadron decays that involve the bottom quark. LHCb has, among other things, accomplished the validation of the $B_s^0 \rightarrow \mu^+ \mu^-$ decay [117, 118]. This particular decay is important because it is one of the mechanisms predicted by the Standard Model, the current theoretical framework that describes the fundamental forces and particles in the universe. This validation not only supports the Standard Model but also provides additional insights into the behavior of quarks.

In addition to its primary experiments, the Large Hadron Collider also houses three smaller, yet equally significant, experiments: LHCf, TOTEM, and MoEDAL. Each of these experiments, while being smaller in scale, serves unique and essential purposes in the broad spectrum of particle physics.

The LHCf, or LHC forward, is strategically located right next to the ATLAS experiment. This positioning allows the LHCf to simulate cosmic rays effectively by observing particles that are emitted at ATLAS in the forward direction. This information is invaluable to our understanding of cosmic particles and their be-

havior.

The second experiment, TOTEM, which stands for TOTal Elastic and diffractive cross-section Measurement, shares its location with the CMS experiment. TOTEM's main objective is to concentrate on cross-section measurements at small angles for various productions originating from the CMS interaction point. This experiment provides insights into the production of different particles at varying energy levels.

The third experiment hosted by the LHC is MoEDAL, situated at point 8 near the LHCb experiment. MoEDAL's primary goal is to detect and measure signals from particles that are hypothetically magnetically charged. This experiment could potentially uncover new aspects of particle physics, further expanding our knowledge of the universe.

4.2 A Large Ion Collider Experiment

As previously stated, the ALICE experiment has been specifically designed with the study of heavy-ion physics in mind. This field of study seeks to understand the behavior of these ions and how they interact with each other. To achieve this, the primary objective of ALICE's sub-detector system is to accurately and efficiently read the high number of particles that are produced in each heavy-ion collision. This is an important component in ensuring the success and validity of the experiments conducted. In addition to this, the system is also designed to have a high momentum resolution, even in regions with low- p_T . This feature allows for a more precise and detailed analysis of the collisions and their results. Lastly, the sub-detector system of ALICE boasts an advanced particle identification capability, which further enhances the accuracy and reliability of the experimental data and findings. These features collectively contribute to the robustness and effectiveness of the ALICE experiment in its study of heavy-ion physics [111, 112].

The schematic representation of the ALICE (A Large Ion Collider Experiment) detector is depicted in Figure 19. During the second experimental run, often referred to as Run 2, the ALICE detector was equipped with an array of 24 individual detectors. Each of these detectors was specifically designed and tailored to serve various purposes and facilitate a range of physics analyses.

The structure of the ALICE detector is layered, with different detectors located at varying radial distances from the central interaction point. This thesis will primarily focus on the detectors that are located in the innermost sections of the ALICE detector. These detectors play a pivotal role in tracking and identifying particles produced in the collisions.

The innermost detectors of interest in this thesis are:

- The Inner Tracking System (ITS) [111, 119, 120], which is the detector closest to the interaction point and is responsible for tracking and identifying particles.

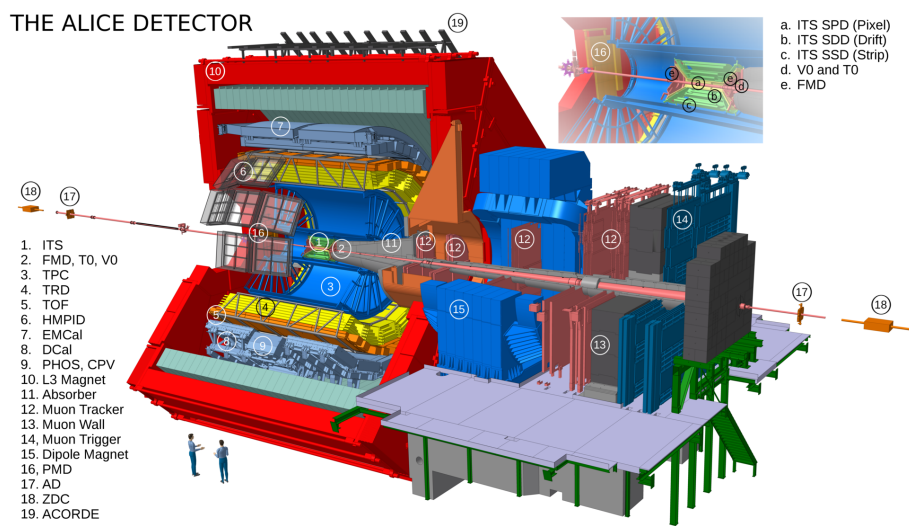


FIGURE 19 This figure provides a detailed schematic view of the ALICE (A Large Ion Collider Experiment) detector as it was configured for its second operational run.

- The V0 detector [121] is used for triggering and event classification.
- The Time Projection Chamber (TPC) [122] serves as the main tracking detector in ALICE.
- The Time of Flight (TOF) [123] detector, which measures the time taken by particles to travel from the interaction point to the detector, thereby providing information on their velocity.

The strategic positioning of detectors, arranged in an extending pattern from the central point near the interaction zone to the farthest boundaries of the structure, ensures an exhaustive accumulation of information from particles produced in a given event. This intricate arrangement is specifically designed to capture the maximum amount of data possible. The placement of tracking detectors closest to the center serves two primary functions: first, to accurately pinpoint the location of the primary interaction vertex and second, to obtain a reliable representation of the paths taken by charged particles. This central placement is intended to reduce particle loss from interactions within the detectors before they reach the outer layers, thereby optimizing the data gathered. Considering the low particle loss in particle identification detectors, it makes sense to place them right after the tracking detectors. This setup ensures that the maximum number of particles are identified and cataloged. Conversely, the calorimeters hold their position in the outer layer of the arrangement. The primary function of the calorimeters is to measure particle energy through a process of absorption, so their outer placement is designed to minimize particle loss and ensure a more accurate energy reading. V0 detectors, play an important role in selecting minimum bias events and determining collision centrality, further enhancing the data collection process. The addition of time-of-flight (TOF) information is a valuable tool in removing background events created from beam interactions with residual gas molecules in the

beam pipe and pileup events. The key roles and features of each of these mentioned detectors are elaborated upon in subsequent sections and in the references attached to this thesis. The upcoming sections offer a more detailed explanation of the operation and importance of the tracking detectors, the TPC and ITS.

4.2.1 Tracking detectors

ALICE is equipped with an array of high-granularity tracking detectors that were specifically designed to handle the unique challenges presented by the exceptionally high particle multiplicities generated in heavy-ion collisions. These dense, high-energy collisions produce a vast number of particles, and the detectors within ALICE were engineered to accurately track and analyze them.

During the initial design and construction phase, a great deal of thought was given to the potential volume of particles that these tracking detectors would need to accommodate. It was estimated that they would need to handle around 8000 charged particles per rapidity unit, an immensely high number that was carefully factored into the construction and configuration of the detectors.

However, once ALICE became operational and began to receive data from heavy-ion collisions, it was revealed that the actual value of particle multiplicity was a lot smaller than initially estimated. In practice, ALICE was dealing with approximately 1600 charged particles per rapidity unit, a number that is much lower than the one anticipated during the design phase. Despite this difference, the high granularity of ALICE's detectors ensures it continues to offer precise and accurate tracking of particles generated in these collisions.

4.2.1.1 Time Projection Chamber (TPC)

ALICE carries a primary tracking detector, known as the Time Projection Chamber (TPC) [122]. This key component has the capacity to offer full azimuthal coverage, and it notably spans the mid-rapidity region of $|\eta| < 0.9$. Working together with other detectors that form part of the central barrel system, the TPC plays a versatile role. Firstly, it delivers accurate momentum measurements, which are crucial for tracking the particles. It also provides effective two-track separation, an essential aspect for distinguishing between particles. Furthermore, it facilitates particle identification, which is an important step in understanding the particles that are examined. Lastly, it assists in vertex determination, which aids in establishing the origin of the particles.

The TPC itself is a hollow cylinder with a large drift volume of approximately 88 m^3 . Its size is substantial, with a radius that stretches from 85 cm at its narrowest point to an outer radius of 250 cm. Along the beam-line, its length extends to 5 m. The TPC holds the distinction of being the world's largest gas-filled TPC, filled with a specific gas mixture to enable its functionalities.

Each end of the TPC features an end-plate. These end-plates are equipped with readout chambers, which are designed to detect signals emanating from the particles. At the center of the TPC cylinder, the Central Electrode (CE) can be

found. Made of mylar foil, this component effectively divides the TPC into two halves, each one mirroring the other.

When a particle that is charged makes its way through the drift volume, it results in the ionization of the gas along its track. This ionization process is significant because it produces electrons along the path that the particle follows. These electrons, once produced, don't remain stationary. They start to drift towards the endplates. This drifting motion of the electrons is caused by an electric field that is generated by an applied voltage difference along the direction of the beam. Therefore, the electric field directs the electrons, produced by the ionization of the gas, towards the endplates along the direction of the beam.

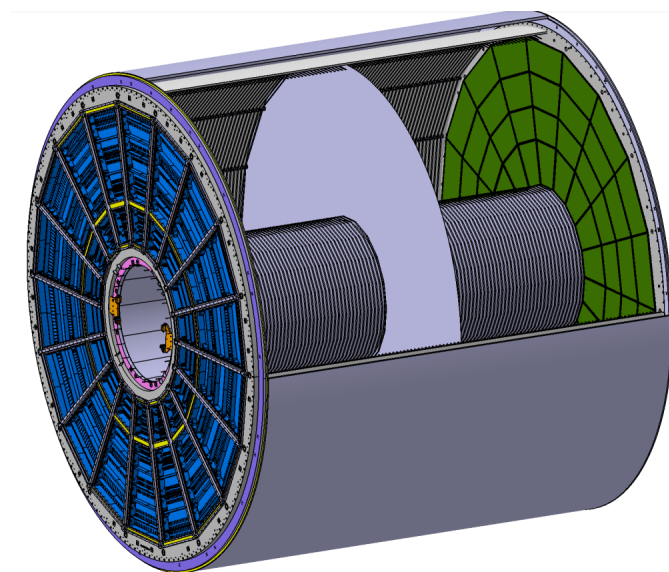


FIGURE 20 This is a schematic view of the Time Projection Chamber (TPC) field cage. Reprinted with permission from [124], 2020, IOP Publishing.

The Multi-Wire Proportional Chambers (MWPCs) [125], which are located at the end-plates, play an important role in detecting the electrons. They amplify the signal by creating an avalanche of ionized particles and electrons. By leveraging the technique of measuring the drift time of the particle, it is possible to reconstruct a detailed three-dimensional image of the ionized particle track. This process is carried out by reading out the MWPC signal and subsequently translating it into the x and y coordinates. Concurrently, the drift time and known drift velocity are used in order to accurately obtain the z component. It's worth noting that the trajectory of the ionized particle will exhibit a curvature as a result of the magnetic field. This curvature is further used to determine the momentum of the particle.

Identification of particles within the Time Projection Chamber (TPC) is performed by measuring three primary factors for each particle that passes through the detector gas. These factors include the specific energy loss (dE/dx), the charge, and the momentum [112]. This method of identifying particles uses the Bethe-Bloch formula, which uses specific particle features to accurately describe energy loss.

The Bethe-Bloch formula is expressed as follows:

$$\left\langle \frac{dE}{dx} \right\rangle = \frac{4N\pi Ne^4}{m_e c^2} \cdot \frac{z^2}{\beta^2} \cdot \left(\ln \frac{2mc^2 \beta^2 \gamma^2}{I^2} - \beta^2 - \frac{\delta(\beta)}{2} \right)$$

In this formula, N represents the electron density of the material, e stands for the elementary charge, and $m_e c^2$ is the rest energy of the electron. Furthermore, z is the charge of the particle traversing the detector, m is the particle mass, and I indicates the mean gas atom excitation potential. $\beta = v/c$ defines the relative velocity, $\gamma = 1/\sqrt{1-\beta^2}$ is identified as the Lorentz factor, and $\beta\gamma = p/mc$ allows the energy loss to function as a momentum, rather than β .

Therefore, diverse types of particles will generate unique bands. These bands will vary depending on both the mass and the charge of the particle. This variation allows for the identification of different particles based on their distinctive characteristics.

4.2.1.2 Inner Tracking System (ITS)

The Inner Tracking System (ITS) [119, 120] is positioned nearest to the interaction point. It encircles the beam-pipe and is fully encapsulated by the Time Projection Chamber (TPC). The ITS is a complex assembly of silicon-based detectors designed to perform a multitude of functions. Among these are the reconstruction of primary and secondary vertices, which gives information on the dynamics of the interaction. The ITS also provides input to the triggering system, a key role in the data acquisition process. Additionally, it is tasked with high-resolution particle tracking within a short distance from the interaction point. This is particularly important for understanding the initial stages of particle interactions. By performing these tasks, the ITS enhances the functionality of the TPC, thereby contributing to an overall improved track reconstruction performance. The ITS and TPC work together to collect and analyze data accurately and efficiently.

The ITS can be further subdivided into three distinct groups. Each group comprises two layers of ITS detectors, with each group having its unique functionality. The innermost group of detectors is the Silicon Pixel Detectors (SPD). The SPD is characterized by its uniquely compact matrix of 8192 silicon diode detector cells. These diode cells, with their compact arrangement, provide a comprehensive two-dimensional resolution. This resolution is capable of accurately resolving the extremely dense particle tracks of heavy ion collisions, a phenomenon regularly seen at a minimum distance of 3.9 cm.

Following the SPD, the next two layers are the Silicon Drift Detectors (SDD). Unlike the SPD, the SDD operates differently. When a particle hits one of the 260 silicon drift cells, its exact position can be determined by calculating the velocity of the resulting charge carrier and the time it takes to drift within that cell. The SDD also offers particle identification (PID) by measuring and analyzing the number of charge carriers that corresponds to a dE/dx of the traversing particle. This feature, combined with its accurate particle tracking capabilities, allows the SDD to resolve high particle track densities, much like the SPD.

The last two layers, the Silicon Strip Detectors (SSD), are constructed differently. The SSD is made up of a mesh of approximately 2.61 million interlaced silicon strips. It identifies a particle hit in a way similar to the silicon pixels. The hit location of a particle is identified at the crosspoint of two overlapping, unaligned silicon strips. The SSD, like the SDD, provides dE/dx information by counting the number of charge carriers.

Together, the SSD and SDD provide four layers of energy loss and PID measurement within the ITS alone. This layered approach ensures a high degree of accuracy and precision in particle tracking. Additionally, an important function of the SSD is to match the particle tracks between SSD and the TPC. This alignment forms the prerequisites for hybrid tracking between the ITS and TPC, further enhancing the system's overall tracking capabilities.

5 ANALYSIS OF SYMMETRIC CUMULANTS

5.1 Experimental setup and analysis

This thesis will detail the datasets used for analysis and provide an overview of the event and track selection for the study of symmetric cumulants. Table 3 provides a succinct summary of the datasets recorded by ALICE. Throughout the first and second runs of the LHC operation, numerous datasets were gathered, which included pp, p–Pb, Pb–Pb, and Xe–Xe collisions at various center-of-mass energies. This analysis will focus solely on the Pb–Pb heavy ion collision datasets recorded in 2015 and 2018.

TABLE 3 A summary of the datasets in Run 1 and Run 2 with the integrated luminosities at ALICE, point 2. Taken from Ref. [126]

Run 1 (2009-2013)			Run 2 (2015-2018)		
0.90	$\sim [200]\mu b^{-1}$		5.02	$\sim [1.3]pb^{-1}$	
2.76	$\sim [100]nb^{-1}$		13.00	$\sim [25]pb^{-1}$	
7.00	$\sim [1.5]pb^{-1}$		5.02	$\sim [3]nb^{-1}$	
8.00	$\sim [2.5]pb^{-1}$		8.16	$\sim [25]nb^{-1}$	
5.02	$\sim [15]nb^{-1}$	Xe–Xe	5.44	$\sim [0.3]\mu b^{-1}$	
2.76	$\sim [75]\mu b^{-1}$		5.02	$\sim [1]nb^{-1}$	

5.1.1 Event and track selection

In total, the data sample consists of $211.92 \cdot 10^6$ minimum bias Pb–Pb collisions at $\sqrt{s_{NN}} = 5.02$ TeV, which were recorded during Run 2 in 2015 and 2018. Each event or collision is triggered by simultaneous signals from two scintillator arrays, V0A and V0C [111, 121]. These arrays cover the pseudorapidity intervals of $2.8 < \eta < 5.1$ and $-3.7 < \eta < -1.7$ respectively. For successful event reconstruction, the primary vertex position must be within 10 cm of the nominal interaction point along the beam axis. During data analysis, certain events that

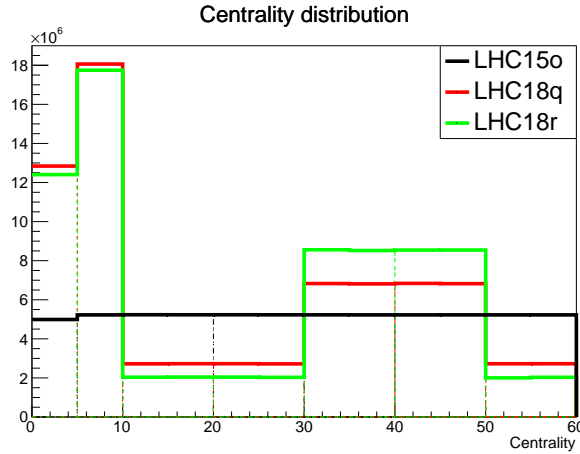


FIGURE 21 The centrality distributions for the datasets in collisions at $\sqrt{s} = 5.02$ TeV in the years 2015 and 2018.

don't fit into the established multiplicity correlation between the V0 detector and the first layer of the Silicon Pixel Detector (SPD) [111, 120] are classified as pile-up and subsequently disregarded. To ensure the accuracy of our results, we need a correlation between the multiplicity estimates provided by the SPD and those imposed with a Time of Flight (TOF) [123] readout. This step is crucial as it aids in the removal of out-of-bunch pile-up, which can otherwise have a significant impact on the data analysis results.

We ascertain collision centrality using data from the V0 detectors. The process of determining centrality in ALICE is detailed in [127]. The analysis only utilizes events within a centrality range of 0% to 60%. The 2015 and 2018 Pb-Pb data's centrality distribution is presented in Fig. 21. The 2015 data show a mostly even distribution. However, due to centrality triggering, the 2018 data reveal a large variation in the number of events per centrality class. This leads to an uneven distribution across centrality classes. To address the 2018 centrality distribution imbalance, we used a centrality flattening method. This method involves the random rejection of events according to a unique inverse distribution for each centrality range.

rack reconstruction leverages combined information from two primary sources. These sources are the TPC [111, 122] and the ITS [111, 120]. These sources work together in a scheme known as "hybrid" tracking. A key consideration in this process is excluding the influence of secondary particles. To ensure this, tracks must maintain a certain minimum distance from the primary vertex. This distance is restricted to less than 3.2 cm longitudinally and less than 2.4 cm transversely. Adhering to these specific limits effectively minimizes interference from secondary particles. Additionally, a loose Distance of Closest Approach (DCA) track cut is selected. This is implemented to improve the uniformity of the φ -distribution, which is an essential aspect for the accurate computation of the Q_n -vector. Furthermore, each track must contain at least 70 out of a possible 159 TPC space points. The average χ^2 per degree of freedom for the track fit, based on these TPC space points, should not exceed 2. This ensures the accuracy

of the track fit. At least two hits in the ITS are required, further corroborating the track fit's validity.

To reduce the influence of track reconstruction efficiency and potential disturbances from secondary particles, a HIJING simulation is implemented, as cited in Ref. [128]. The simulation is integrated with the GEANT3 [129] detector model to provide a comprehensive understanding of the detector's response. A p_T -dependent track weighting correction is constructed by integrating the HIJING simulation with the GEANT3 detector model. This correction is made to ensure that the momentum of the charged particles does not bias our measurements. The efficiency of track reconstruction is approximately 65% for particles with $p_T = 0.2 \text{ GeV}/c$, and it increases to 80% for particles with $p_T > 1.0 \text{ GeV}/c$. This suggests that the efficiency of our track reconstruction increases with the momentum of the particles.

The contamination from secondary sources is controlled, being less than 10% for particles with $p_T = 0.2 \text{ GeV}/c$ and less than 5% for particles with $p_T > 1.0 \text{ GeV}/c$. This demonstrates that our measurements mainly come from primary particles, which ensures the reliability of our results. Fig. 22 illustrates the efficiency, contamination, and the resulting correction factor, all as functions of p_T , for the 20-40% centrality class in the LHC18q + LHC18r data set. The efficiency, in particular, is a key component in determining the effectiveness of the data collection and processing. The contamination factor, on the other hand, provides insights into the level of 'noise' or irrelevant data within the set. Lastly, the correction factor is an essential tool for final data interpretation. In addition to the LHC18q + LHC18r data set, the efficiency was also evaluated independently for the LHC15o dataset. The LHC15o dataset yielded results very similar to those of the LHC18q+LHC18r set, suggesting consistency in the data collection and processing methods across different data sets. In our analysis, we strictly consider particle tracks that lie within the defined transverse momentum interval of $0.2 < p_T < 5.0 \text{ GeV}/c$ and the pseudorapidity range of $0.4 < |\eta| < 0.8$. This specific lower p_T cut-off has been implemented to significantly reduce the impact of a less efficient low- p_T reconstruction process. Conversely, the upper limit has been set to restrict and reduce the influence derived from high-energy jets, which can otherwise skew our results and interpretations. To further refine the data, we use a pseudorapidity gap of $|\Delta\eta| > 0.8$, a strategy effective in dampening non-flow. The observables that we have decided to utilize in this analysis are largely based on multi-particle correlations. This approach, following a standard framework as established and cited in the work of Bilandzic et al. [97], allows us to conduct a robust and comprehensive anisotropic flow analysis.

5.2 Higher Order Symmetric cumulants

This analysis extends the previous results [86, 87] to higher-order harmonic Symmetric Cumulants. Specifically, we achieve good precision in measuring the cor-

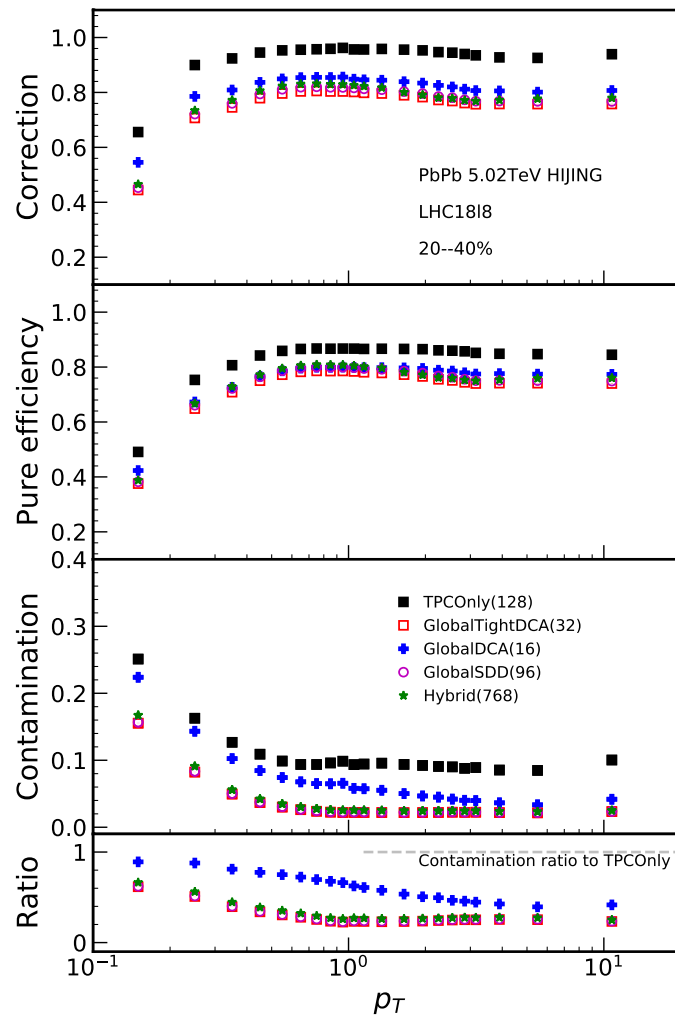


FIGURE 22 In the ALICE simulations, several track selection methods were used. From these methods, certain key factors were derived; these include efficiency, contamination, and the final correction factor. These are the results from the HIJING simulations in collisions at = 5.02 TeV [130, 131].

relations of v_5 and v_6 to the other harmonics by combining the 2015 and 2018 datasets listed in Tab. 3.

TABLE 4 New observables in this analysis are highlighted in red, while previously published observables are displayed in black.

Energy	Observable	Harmonic combinations	published paper
2.76	NSC(m,n)	(3,2),(4,2),(4,3),(5,2),(5,3)	Refs. [86, 132]
5.02	NSC(m,n)	(3,2),(4,2),(4,3),(5,2),(5,3),(5,4),(6,2),(6,3)	Ref. [95]

5.2.1 Systematic Uncertainty Evaluation

The assessment of systematic uncertainties involves the variation and comparison of different selection criteria against the nominal selection. The Barlow test [133] is employed to ascertain the significance of individual trials. If the Barlow σ value of a trial exceeds one, the relative variation of the results is considered significant, beyond mere statistical uncertainties. Such a trial is then classified as a systematic uncertainty. The total systematic uncertainty for each centrality class is computed by summing the significant sources of uncertainty in quadrature.

5.2.1.1 Description of the Barlow test

The Barlow test was used as a method to exclude statistically insignificant contributions for the systematic uncertainties and is defined as,

$$\sigma_{\text{Barlow}} = \frac{|x_{\text{def}} - x_{\text{var}}|}{\sqrt{|\sigma_{\text{def}}^2 \pm \sigma_{\text{var}}^2|}}. \quad (63)$$

The numerator represents the *absolute variation* or *difference* between the results of x obtained with the default (*def*) and with the varied (*var*) selections. The results will have statistical uncertainties σ_x , hence one needs to consider the error in the difference, which is what is done in the denominator. The \pm sign represents the "correlation level" of the data-sets that are compared. The minus sign is used if the data-sets are correlated, while the plus sign is used when the data-sets are fully uncorrelated.

In this analysis, a trial is included in the systematic uncertainty if σ_{Barlow} is larger than 2.0 and the relative variation between the compared results is applied as systematic uncertainty on the corresponding trial, with the relative variation defined as

$$\text{Rel. Var} = \frac{x_{\text{def}} - x_{\text{var}}}{x_{\text{def}}}. \quad (64)$$

For example, the figure 23 summarize the Barlow test conducted for NSC(5,2) and NSC(5,3). The first row displays the measured observables for all

trials, along with the default value and its systematic uncertainty. The second row depicts the absolute or relative variation, depending on the size of the measured values. If these values are too small, the absolute variation is used. The bottom row presents the σ_{Barlow} value for each data point.

- **Magnetic field polarity** The detector operates with either a positive or negative solenoid magnetic field polarity. The polarity impacts the direction of the charged particle's curvature and subjects the detector to two different field conditions. A portion of the dataset was recorded under each configuration. To examine the polarity's effect, these two datasets can be analyzed separately instead of being combined, as is usually done.
- **Centrality determination** An alternate method for determining centrality utilizes data from silicon pixel detectors (SPD). This SPD-based centrality determination is used as a systematic check.
- **Z-vertex cut / Primary vertex position** Typically, only events reassembled within 8 cm of the predefined interaction point are considered. We evaluate the impact of this decision, especially on the η range and φ -distribution, by reducing the rejection cutoff to 7 cm and increasing the cutoff to 9 cm.
- **Pile-up inclusion** The process of event selection involves choosing the primary vertex and removing outliers based on V0 and CL0 multiplicity correlations. Additional pile-up can be eliminated by applying an extra 4σ -cut on the multiplicity correlations and conducting an out-of-bunch pile-up removal using the CL0 multiplicity correlations and time of flight (TOF) information, which also involves another 4σ -cut.
- **Charge combinations** The like-sign method, which only correlates charged particles of the same sign, is used to study the scale of non-flow effects, especially from jets. Usually, an η -gap is applied between correlated sub-events to reduce non-flow effects.
- **Space charge distortion** The multiparticle correlation can be computed by selecting the first particle from the A-side of the detector and the remaining particles from the C-side, or vice versa. By default, both approaches are applied and the outcomes are averaged. The effect of space charge distortion is taken into account by not averaging the results, but instead comparing them individually to the default setup.
- **TPC space points** The criteria for track selection was made more stringent by raising the minimum TPC space points from 70 to 90.
- **Tracking mode** The uncertainty related to track reconstruction, also called tracking mode, was assessed by comparing outcomes from various track types. The function of the ITS, specifically the number of hits in its layers, varies between different configurations (such as hybrid and global tracking).

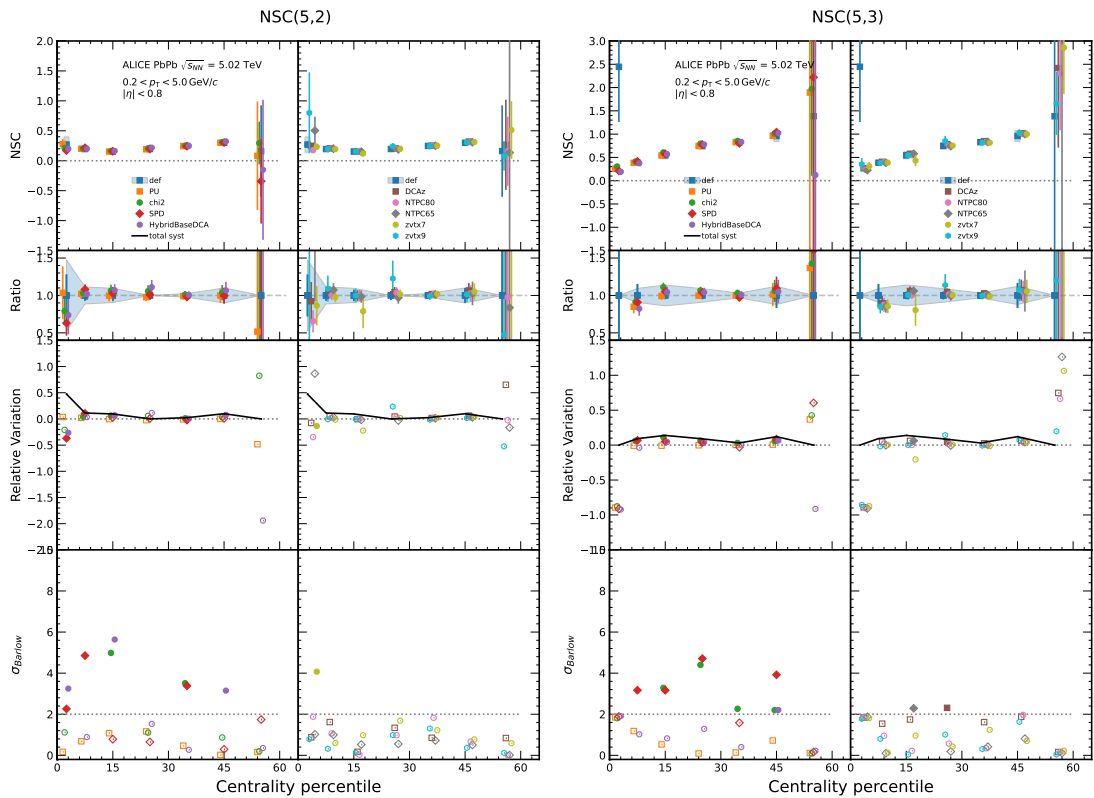


FIGURE 23 Barlow test for NSC(5,2) and NSC(5,3) in collisions at = 5.02 TeV. The first row shows the measured observables for all trials, along with their default value and systematic uncertainty. The second row displays either an absolute or relative variation, depending on the size of the measured values. If these values are small, we use the absolute variation. The last row presents the σ_{Barlow} value for each data point.

6 RESULTS

6.1 Bayesian parameter estimation in heavy-ion collisions at LHC

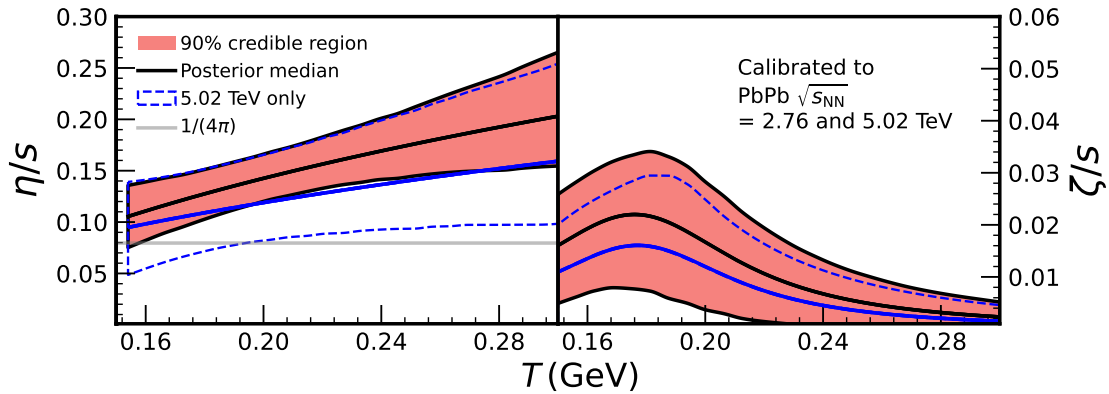


FIGURE 24 The red band represents the 90%-credibility region for the shear (top) and bulk (bottom) viscosity to entropy ratio, with the black line denoting the median within this range. The results are contrasted with the MAP parametrization from Ref. [21], calibrated solely using 5.02 TeV data. Reprinted with permission from [21], 2021, American Physical Society.

This study utilized an enhanced global Bayesian method, a sophisticated approach for probabilistic modeling, to meticulously quantify the transport properties of quark-gluon plasma. More specifically, it focused on the specific η/s and ζ/s using Pb-Pb data at two separate collision energies, $\sqrt{s_{NN}} = 2.76$ and 5.02 TeV. These findings represented a significant advancement in the field, as it was the first time that new, sophisticated collective flow observables from two distinct collision energies were included in the analysis. The inclusion of these new observables served to reduce the uncertainty of the extracted transport coefficients. The reduced uncertainty effectively increased the precision and reliability of the findings, marking a substantial improvement in the methodological approach. The study further revealed that the measurements of higher harmonics

and higher-order flow fluctuation observables are indeed sensitive to the transport coefficients. This finding underscores the importance of measuring these observables with high precision. Doing so ensures that the hydrodynamic transport coefficients, which are important for understanding the behavior of the quark-gluon plasma, are derived accurately and reliably.

Despite the inclusion of new observables as inputs for our model, we still observed discrepancies between our model's predictions and the actual experimental measurements. These discrepancies highlight the need for further refinement in our current modeling process. A clear illustration of this is through examining the NSC(4,2) observable. In this particular observable, our newly revised model does indeed perform better than our previous iteration. However, it's important to note that deviations are still present, particularly at higher centralities, indicating room for further studies.

Our study also struggled to accurately reproduce the sign change of NSC(4,3) at low centralities. This lack of reproduction was not unique to our study, as it was also not reproduced in Ref. [39]. This common challenge underscores the necessity for additional studies focusing on this area to better understand and address this issue.

Furthermore, while our study reveals certain discrepancies, such as poor model-to-data compatibility for the energy scale dependence of $v_2\{2\}$ and particle yields, these results are nonetheless valuable. Rather, they serve as an important indication of the imperative need to continue improving our understanding and modeling of heavy-ion collision models. This will ultimately lead to more accurate and reliable predictions in the future.

6.2 Higher Order Harmonic Symmetric Cumulants

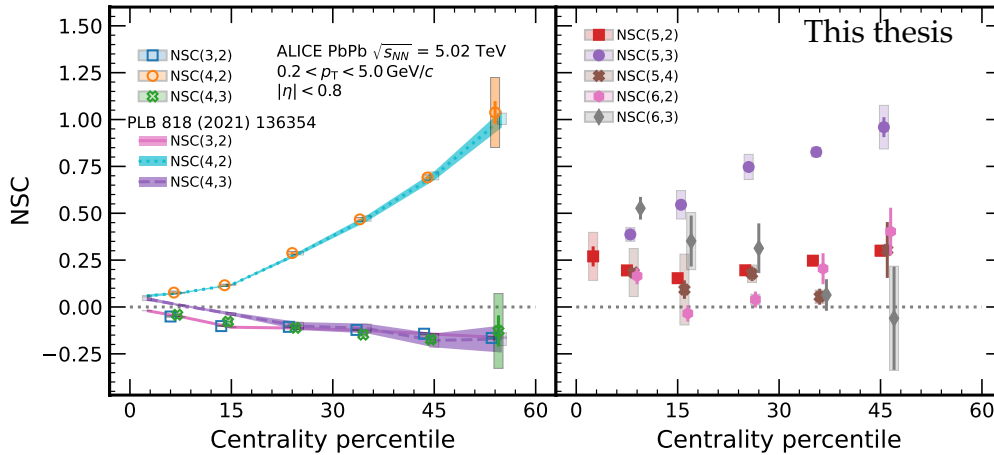


FIGURE 25 **Left panel:** Lower order NSC observables together with published results. **Right Panel:** Higher order harmonic NSC including $n = 5$ and $n = 6$.

The results for higher order harmonic symmetric cumulants are presented

in this section. In Figure 25, the left panel shows the lower orders together with the already published NSC [95], while the right panel showcases the higher orders. The new measurements include the fifth and sixth harmonic amplitudes of the flow. It is observed that all observables are positive except for NSC(3,2) and NSC(4,3). It is also observed that there is a strong centrality dependence for NSC(5,3) and a slight decreasing trend towards peripheral collisions of NSC(6,3). There is no strong centrality dependence for NSC(5,2), NSC(5,4), and NSC(6,2).

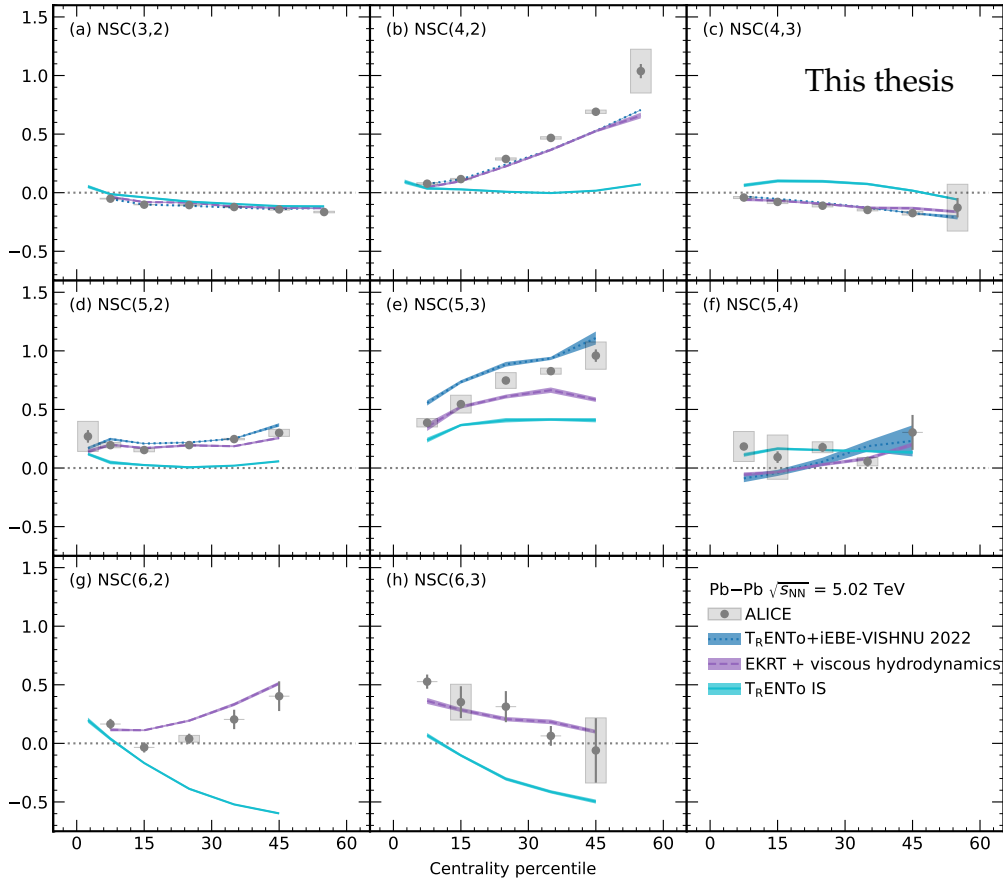


FIGURE 26 A model comparison for the measured NSC observables. The Final State models of $T_{\text{RENTo}}+i\text{EBE-VISHNU}$ shown as a dark blue band, and EKRT as a purple band. The Initial State T_{RENTo} is shown as a light blue band.

We systematically compared the centrality dependence of the $\text{NSC}(m,n)$ with the event-by-event EKRT+viscous hydrodynamics model [49]. This model provides an integral framework for understanding the complex phenomena involved. In the comprehensive event-by-event EKRT+viscous hydrodynamic calculations [49], the initial energy density profiles are meticulously calculated using a next-to-leading order perturbative-QCD+saturation model [134, 135]. The subsequent space-time evolution is modeled using relativistic dissipative fluid dynamics, employing multiple parameterizations for the temperature dependence of η/s . This ensures a detailed and nuanced representation of the evolving system. This model has demonstrated remarkable accuracy, reliably describing the charged hadron multiplicity and the low p_{T} region of

the charged hadron spectra at RHIC and the LHC. For more details and visual representations, refer to Figs. 11-13 in [49]. Each of the $\eta/s(T)$ parameterizations is particularly adjusted to reproduce the measured v_n from central to mid-peripheral collisions. This adherence to accurate reproduction further enhances the reliability and validity of our model (see Fig. 15 in [49]).

The final state models and data show good agreement for NSC(3,2) and NSC(4,3). Except for NSC(3,2) and NSC(5,4), all other observables exhibit a distinct non-linear hydrodynamic response that overshadows initial state cumulants. All observables exhibit a rising correlation in peripheral collisions, with the exception of NSC(6,3). This suggests that the negative contribution from NSC(3,2) and the increasing correlation towards peripheral collisions result in a decreasing trend of NSC(6,3) in such collisions.

6.3 Asymmetric Cumulants

$$NAC_{a,1}(m,n) = \langle v_m^{2 \cdot a} v_n^{2 \cdot 1} \rangle_c / \langle v_m^2 \rangle^a \langle v_n^2 \rangle^1$$

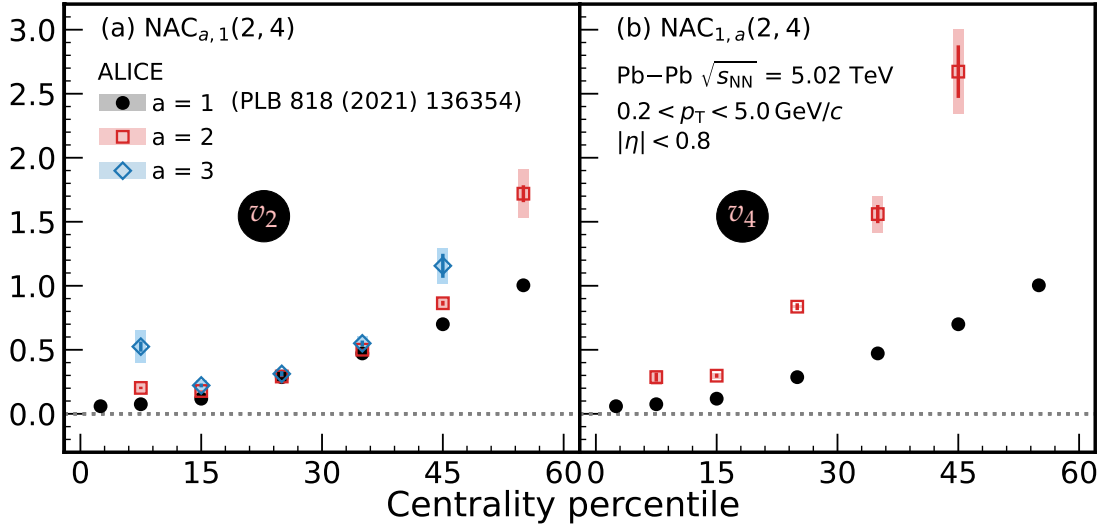


FIGURE 27 Centrality dependence of the different orders $a = 1, \dots, 3$ of $NAC_{a,1}(2,4)$ (left) and $NAC_{1,a}(2,4)$ (right). Reprinted with permission from [23], 2023, American Physical Society.

The first measurements of correlations between the moments of two flow amplitudes [136] in collisions at $\sqrt{s_{NN}} = 5.02$ TeV are presented in [23]. Asymmetric cumulants, where the harmonics under consideration are raised to different moments, are a generalisation of the well-known symmetric cumulants. In Ref. [23], we introduce 34 new observables and discuss their constraining power on QCD matter properties. As illustrated in Fig. 27, the correlations for both v_2 and v_4 depend on the moments and collision centrality. The increase in correlation for higher moments is more pronounced for v_4 . After comparing the results with

state-of-the-art hydrodynamic model calculations, using two different parameterizations from Bayesian optimization, we found discrepancies between data and simulations in many of the observables. This suggests a need for further tuning of the models used in these model calculations.

6.4 Flow signal in small collision systems in LHC

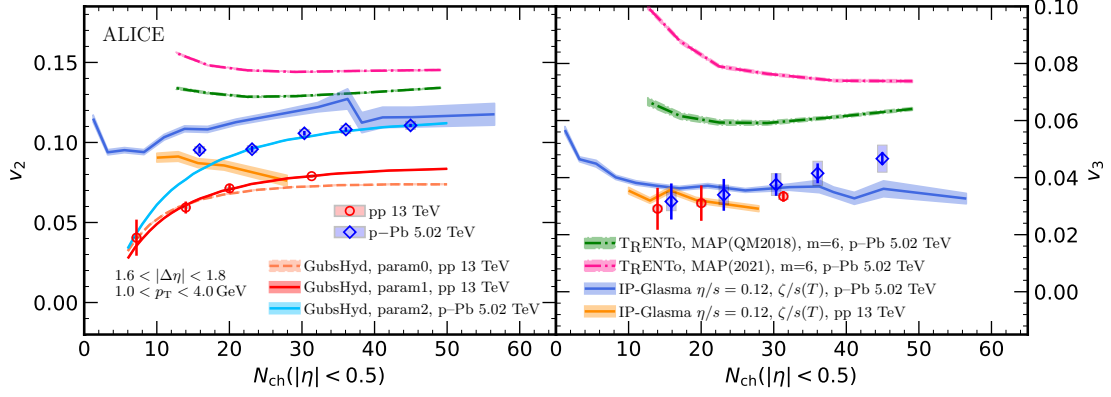


FIGURE 28 The variation of v_2 (on the left) and v_3 (on the right) with multiplicity at mid-rapidity is compared to hydrodynamic calculations. Data points for p–Pb and pp collisions are denoted by blue and red markers, respectively. Hydrodynamic calculations are shown as colored lines, accompanied by bands indicating their statistical uncertainty. Reprinted with permission from [24], 2023, .

This study focuses on both long and short-range correlations between pairs of charged particles in smaller systems, such as pp and p–Pb collisions. The motivation for this analysis is two-folded, on one side it turns out that the jet contribution is not fully removed on the away-side peak in the previous studies [137, 138], hence the new method, so called Low multiplicity template, are thoroughly examined and verified in this paper [24]. On the other hand, this study represents the first attempt to measure the flow signal in the lowest event multiplicity. This technique enables us to eliminate the increased away-side jet fragments in high multiplicity events compared to low-multiplicity events, ensuring that our flow amplitude results are free from jet contributions. For the second part of the motivation, we investigate the lower limit of multiplicity by examining different hydrodynamical models and comparing them to data.

In the final result, the measured v_2 and v_3 from this analysis is compared to three different models; TRenTo+iEBE-VISHNU [22], IP-Glasma+MUSIC+UrQMD hydrodynamic calculations [139], and GubsHyd [140]. It turns out that both TRenTo+iEBE-VISHNU and IP-Glasma+MUSIC+UrQMD are overestimating the data, Trento more than IP-glasma. In terms of TRenTo the multiplicity dependence is opposite to the multiplicity dependence for data for both v_2 and v_3 . For data the trend is that an increase of multiplicity has an increase of the flow magnitude, whereas for Trento the opposite trend is observed. The model that describes the data the best is GubsHyd, which agree for v_2 in both collision systems.

When compared with viscous hydrodynamic models, it is observed that the magnitudes of v_2 and their reliance on multiplicity are not accurately represented

by state-of-art hydrodynamic computations. This is particularly evident in the case of low multiplicity p–Pb and pp collisions that utilize two initial state models. As the importance of the initial state increases with decreasing multiplicity [141, 142], it suggests a need for further refinement and enhancement of the initial state details, guided by experimental measurements.

Direct comparisons with the ATLAS Collaboration’s results [143] aren’t feasible since the multiplicity classes are defined differently and the results have different acceptances. However, an assumption-based comparison is available in the Appendix 2. It’s important to note that correlations between mid-rapidity and forward rapidity multiplicity in small collision systems are not guaranteed. As mentioned in the paper, we evaluated two assumptions of the method within the ALICE acceptance alone, stressing the need to reassess systematic uncertainties when analyzing different kinematic ranges. Their impact might not always be negligible. Future analyses from various collaborations could provide additional insights to clarify the situation.

7 SUMMARY

This thesis presents the results of three separate studies. The first study examines higher-order harmonic symmetric cumulants in PbPb collisions at 5.02 TeV, including v_5 and v_6 . This marks a first in the field. The magnitudes of these observables depend both on the event centralities and the order of the involved harmonics. When measuring the correlations of higher-order harmonics, the interplay between harmonics becomes significantly more noticeable than that of lower-order harmonics. This can be explained by the nonlinear hydrodynamic response. Hence, these measurements are considered highly sensitive observables in the Bayesian analysis mentioned in Section 2.3.1.

The second study quantifies the transport properties of quark-gluon plasma using a Bayesian analysis of LHC Pb-Pb data. It reveals that higher harmonics and higher-order flow fluctuation observables are sensitive to the coefficients of the transport properties. The uncertainty of the extracted transport properties considerably reduces when new collective flow observables from two collision energies are included. However, discrepancies still exist between the model and experimental measurements, indicating a need to enhance our understanding of heavy-ion collision models.

The third study measures the flow signal within the smallest event multiplicity in the small systems such as pp and p-Pb collisions. This research led to the removal of the jet contribution using a new method. This method analyzes correlations of charged particles over both long and short ranges. When compared to viscous hydrodynamic models, the magnitudes of v_2 and their dependence on multiplicity are not adequately described by current hydrodynamic calculations, especially for low multiplicity p-Pb and pp collisions. As the importance of the initial state increases with a decrease in multiplicity, the results suggest that the details of the initial state description need to be improved based on experimental measurements. This improvement could enhance our understanding of the modelling of larger collision systems.

REFERENCES

- [1] John C. Collins and M. J. Perry. “Superdense Matter: Neutrons Or Asymptotically Free Quarks?” In: *Phys. Rev. Lett.* 34 (1975), p. 1353. DOI: 10.1103/PhysRevLett.34.1353 (Cited on page 11).
- [2] N. Cabibbo and G. Parisi. “Exponential Hadronic Spectrum and Quark Liberation”. In: *Phys. Lett. B* 59 (1975), pp. 67–69. DOI: 10.1016/0370-2693(75)90158-6 (Cited on page 11).
- [3] Edward V. Shuryak. “Theory of Hadronic Plasma”. In: *Sov. Phys. JETP* 47 (1978), pp. 212–219 (Cited on page 11).
- [4] John Adams et al. “Experimental and theoretical challenges in the search for the quark gluon plasma: The STAR Collaboration’s critical assessment of the evidence from RHIC collisions”. In: *Nucl. Phys. A* 757 (2005), pp. 102–183. DOI: 10.1016/j.nuclphysa.2005.03.085. arXiv: nucl-ex/0501009 [nucl-ex] (Cited on page 11).
- [5] K. Adcox et al. “Formation of dense partonic matter in relativistic nucleus-nucleus collisions at RHIC: Experimental evaluation by the PHENIX collaboration”. In: *Nucl. Phys. A* 757 (2005), pp. 184–283. DOI: 10.1016/j.nuclphysa.2005.03.086. arXiv: nucl-ex/0410003 [nucl-ex] (Cited on page 11).
- [6] I. Arsene et al. “Quark gluon plasma and color glass condensate at RHIC? The Perspective from the BRAHMS experiment”. In: *Nucl. Phys. A* 757 (2005), pp. 1–27. DOI: 10.1016/j.nuclphysa.2005.02.130. arXiv: nucl-ex/0410020 [nucl-ex] (Cited on page 11).
- [7] B. B. Back et al. “The PHOBOS perspective on discoveries at RHIC”. In: *Nucl. Phys. A* 757 (2005), pp. 28–101. DOI: 10.1016/j.nuclphysa.2005.03.084. arXiv: nucl-ex/0410022 [nucl-ex] (Cited on page 11).
- [8] Jean-Yves Ollitrault. “Anisotropy as a signature of transverse collective flow”. In: *Phys. Rev. D* 46 (1992), pp. 229–245. DOI: 10.1103/PhysRevD.46.229 (Cited on page 11).
- [9] Ulrich W. Heinz and Maurice Jacob. “Evidence for a new state of matter: An Assessment of the results from the CERN lead beam program”. In: (Jan. 2000). arXiv: nucl-th/0002042 (Cited on pages 11, 15).
- [10] Edward Shuryak. “Strongly coupled quark-gluon plasma in heavy ion collisions”. In: *Rev. Mod. Phys.* 89 (2017), p. 035001. DOI: 10.1103/RevModPhys.89.035001. arXiv: 1412.8393 [hep-ph] (Cited on page 11).
- [11] Edward V. Shuryak. “What RHIC experiments and theory tell us about properties of quark-gluon plasma?” In: *Nucl. Phys. A* 750 (2005). Ed. by D. Rischke and G. Levin, pp. 64–83. DOI: 10.1016/j.nuclphysa.2004.10.022. arXiv: hep-ph/0405066 (Cited on page 11).

- [12] Ulrich W. Heinz. “‘RHIC serves the perfect fluid’: Hydrodynamic flow of the QGP”. In: *Workshop on Extreme QCD*. Dec. 2005, pp. 3–12. arXiv: nucl-th/0512051 (Cited on page 11).
- [13] Ulrich Heinz and Raimond Snellings. “Collective flow and viscosity in relativistic heavy-ion collisions”. In: *Ann. Rev. Nucl. Part. Sci.* 63 (2013), pp. 123–151. DOI: 10.1146/annurev-nucl-102212-170540. arXiv: 1301.2826 [nucl-th] (Cited on page 11).
- [14] Betty Abelev et al. “Anisotropic flow of charged hadrons, pions and (anti-)protons measured at high transverse momentum in Pb-Pb collisions at $\sqrt{s_{NN}}=2.76$ TeV”. In: *Phys. Lett. B* 719 (2013), pp. 18–28. DOI: 10.1016/j.physletb.2012.12.066. arXiv: 1205.5761 [nucl-ex] (Cited on page 11).
- [15] Betty Bezverkhny Abelev et al. “Elliptic flow of identified hadrons in Pb–Pb collisions at $\sqrt{s_{NN}} = 2.76$ TeV”. In: *JHEP* 06 (2015), p. 190. DOI: 10.1007/JHEP06(2015)190. arXiv: 1405.4632 [nucl-ex] (Cited on page 11).
- [16] Georges Aad et al. “Measurement of the pseudorapidity and transverse momentum dependence of the elliptic flow of charged particles in lead-lead collisions at $\sqrt{s_{NN}} = 2.76$ TeV with the ATLAS detector”. In: *Phys. Lett. B* 707 (2012), pp. 330–348. DOI: 10.1016/j.physletb.2011.12.056. arXiv: 1108.6018 [hep-ex] (Cited on page 11).
- [17] “The ALICE experiment – A journey through QCD”. In: (Nov. 2022). arXiv: 2211.04384 [nucl-ex] (Cited on pages 11, 33).
- [18] Jonah E. Bernhard, J. Scott Moreland, and Steffen A. Bass. “Bayesian estimation of the specific shear and bulk viscosity of quark–gluon plasma”. In: *Nature Phys.* 15.11 (2019), pp. 1113–1117. DOI: 10.1038/s41567-019-0611-8 (Cited on pages 12, 34).
- [19] Govert Nijss et al. “Transverse Momentum Differential Global Analysis of Heavy-Ion Collisions”. In: *Phys. Rev. Lett.* 126.20 (2021), p. 202301. DOI: 10.1103/PhysRevLett.126.202301. arXiv: 2010.15130 [nucl-th] (Cited on pages 12, 34).
- [20] D. Everett et al. “Multisystem Bayesian constraints on the transport coefficients of QCD matter”. In: *Phys. Rev. C* 103.5 (2021), p. 054904. DOI: 10.1103/PhysRevC.103.054904. arXiv: 2011.01430 [hep-ph] (Cited on pages 12, 34, 51).
- [21] J. E. Parkkila, A. Onnerstad, and D. J. Kim. “Bayesian estimation of the specific shear and bulk viscosity of the quark-gluon plasma with additional flow harmonic observables”. In: (June 2021). arXiv: 2106.05019 [hep-ph] (Cited on pages 12, 30, 32, 34, 40, 69).
- [22] J. E. Parkkila et al. “New constraints for QCD matter from improved Bayesian parameter estimation in heavy-ion collisions at LHC”. In: *Phys. Lett. B* 835 (2022), p. 137485. DOI: 10.1016/j.physletb.2022.137485. arXiv: 2111.08145 [hep-ph] (Cited on pages 12, 34, 74).

- [23] Shreyasi Acharya et al. “Higher-order correlations between different moments of two flow amplitudes in Pb-Pb collisions at $\sqrt{s_{NN}}=5.02$ TeV”. In: *Phys. Rev. C* 108.5 (2023), p. 055203. DOI: 10.1103/PhysRevC.108.055203. arXiv: 2303.13414 [nucl-ex] (Cited on pages 12, 72).
- [24] Shreyasi Acharya et al. “Multiplicity and event-scale dependent flow and jet fragmentation in pp collisions at $\sqrt{s} = 13$ TeV and in p–Pb collisions at $\sqrt{s_{NN}} = 5.02$ TeV”. In: (Aug. 2023). arXiv: 2308.16591 [nucl-ex] (Cited on pages 12, 74, 98).
- [25] Paul Romatschke. “Relativistic Fluid Dynamics Far From Local Equilibrium”. In: *Phys. Rev. Lett.* 120.1 (2018), p. 012301. DOI: 10.1103/PhysRevLett.120.012301. arXiv: 1704.08699 [hep-th] (Cited on page 13).
- [26] Aleks Kurkela et al. “Matching the Nonequilibrium Initial Stage of Heavy Ion Collisions to Hydrodynamics with QCD Kinetic Theory”. In: *Phys. Rev. Lett.* 122.12 (2019), p. 122302. DOI: 10.1103/PhysRevLett.122.122302. arXiv: 1805.01604 [hep-ph] (Cited on page 13).
- [27] Aleks Kurkela et al. “Effective kinetic description of event-by-event pre-equilibrium dynamics in high-energy heavy-ion collisions”. In: *Phys. Rev. C* 99.3 (2019), p. 034910. DOI: 10.1103/PhysRevC.99.034910. arXiv: 1805.00961 [hep-ph] (Cited on page 13).
- [28] Aleks Kurkela and Aleksas Mazeliauskas. “Chemical Equilibration in Hadronic Collisions”. In: *Phys. Rev. Lett.* 122 (2019), p. 142301. DOI: 10.1103/PhysRevLett.122.142301. arXiv: 1811.03040 [hep-ph] (Cited on page 13).
- [29] M. Strickland. “The non-equilibrium attractor for kinetic theory in relaxation time approximation”. In: *JHEP* 12 (2018), p. 128. DOI: 10.1007/JHEP12(2018)128. arXiv: 1809.01200 [nucl-th] (Cited on page 13).
- [30] Syo Kamata et al. “Hydrodynamization and nonequilibrium Green’s functions in kinetic theory”. In: *Phys. Rev. D* 102.5 (2020), p. 056003. DOI: 10.1103/PhysRevD.102.056003. arXiv: 2004.06751 [hep-ph] (Cited on page 13).
- [31] A. K. Chaudhuri. *A short course on Relativistic Heavy Ion Collisions*. IOPP, Sept. 2014. DOI: 10.1088/978-0-750-31060-4. arXiv: 1207.7028 [nucl-th] (Cited on page 14).
- [32] Ulrich W. Heinz and Gregory Kestin. “Jozso’s Legacy: Chemical and Kinetic Freeze-out in Heavy-Ion Collisions”. In: *Eur. Phys. J. ST* 155 (2008), pp. 75–87. DOI: 10.1140/epjst/e2008-00591-4. arXiv: 0709.3366 [nucl-th] (Cited on page 14).
- [33] Enrico Fermi. “High Energy Nuclear Events”. In: *Progress of Theoretical Physics* 5.4 (July 1950), pp. 570–583. DOI: 10.1143/ptp/5.4.570. eprint: <https://academic.oup.com/ptp/article-pdf/5/4/570/5430247/5-4-570.pdf> (Cited on page 15).

- [34] L. D. Landau. “On the multiparticle production in high-energy collisions”. In: *Izv. Akad. Nauk Ser. Fiz.* 17 (1953), pp. 51–64 (Cited on page 15).
- [35] I. M. Khalatnikov. “Some questions of relativistic hydrodynamics”. In: *Zh. Eksp. Teor. Fiz.* 27 (1954), pp. 529–541 (Cited on page 15).
- [36] Charles Gale, Sangyong Jeon, and Bjoern Schenke. “Hydrodynamic Modeling of Heavy-Ion Collisions”. In: *Int. J. Mod. Phys. A* 28 (2013), p. 1340011. DOI: 10.1142/S0217751X13400113. arXiv: 1301.5893 [nucl-th] (Cited on pages 15, 16, 19).
- [37] Derek A. Teaney. “Viscous Hydrodynamics and the Quark Gluon Plasma”. In: (2010). Ed. by Rudolph C. Hwa and Xin-Nian Wang, pp. 207–266. DOI: 10.1142/9789814293297_0004. arXiv: 0905.2433 [nucl-th] (Cited on page 16).
- [38] Laszlo P. Csernai, Joseph. I. Kapusta, and Larry D. McLerran. “On the Strongly-Interacting Low-Viscosity Matter Created in Relativistic Nuclear Collisions”. In: *Phys. Rev. Lett.* 97 (2006), p. 152303. DOI: 10.1103/PhysRevLett.97.152303. arXiv: nucl-th/0604032 (Cited on pages 17, 18).
- [39] Jonah E. Bernhard, J. Scott Moreland, and Steffen A. Bass. “Bayesian estimation of the specific shear and bulk viscosity of quark-gluon plasma”. In: *Nature Physics* (2019). DOI: 10.1038/s41567-019-0611-8 (Cited on pages 17, 18, 30–32, 70).
- [40] Tetsufumi Hirano et al. “Hadronic dissipative effects on elliptic flow in ultrarelativistic heavy-ion collisions”. In: *Phys. Lett. B* 636 (2006), pp. 299–304. DOI: 10.1016/j.physletb.2006.03.060. arXiv: nucl-th/0511046 [nucl-th] (Cited on page 17).
- [41] Paul Romatschke and Ulrike Romatschke. “Viscosity Information from Relativistic Nuclear Collisions: How Perfect is the Fluid Observed at RHIC?” In: *Phys. Rev. Lett.* 99 (2007), p. 172301. DOI: 10.1103/PhysRevLett.99.172301. arXiv: 0706.1522 [nucl-th] (Cited on page 17).
- [42] P. Kovtun, Dan T. Son, and Andrei O. Starinets. “Viscosity in strongly interacting quantum field theories from black hole physics”. In: *Phys. Rev. Lett.* 94 (2005), p. 111601. DOI: 10.1103/PhysRevLett.94.111601. arXiv: hep-th/0405231 [hep-th] (Cited on pages 17, 33).
- [43] Michael L. Miller et al. “Glauber modeling in high energy nuclear collisions”. In: *Ann. Rev. Nucl. Part. Sci.* 57 (2007), pp. 205–243. DOI: 10.1146/annurev.nucl.57.090506.123020. arXiv: nucl-ex/0701025 [nucl-ex] (Cited on pages 20, 22).
- [44] Roger D. Woods and David S. Saxon. “Diffuse Surface Optical Model for Nucleon-Nuclei Scattering”. In: *Phys. Rev.* 95 (2 July 1954), pp. 577–578. DOI: 10.1103/PhysRev.95.577 (Cited on page 20).

- [45] L. C. Chamon et al. “Toward a global description of the nucleus-nucleus interaction”. In: *Phys. Rev. C* 66 (2002), p. 014610. DOI: 10.1103/PhysRevC.66.014610. arXiv: nucl-th/0202015 (Cited on page 22).
- [46] Dmitri Kharzeev, Eugene Levin, and Marzia Nardi. “The Onset of classical QCD dynamics in relativistic heavy ion collisions”. In: *Phys. Rev. C* 71 (2005), p. 054903. DOI: 10.1103/PhysRevC.71.054903. arXiv: hep-ph/0111315 (Cited on page 23).
- [47] Hans-Joachim Drescher et al. “The Eccentricity in heavy-ion collisions from color glass condensate initial conditions”. In: *Phys. Rev. C* 74 (2006), p. 044905. DOI: 10.1103/PhysRevC.74.044905. arXiv: nucl-th/0605012 (Cited on page 23).
- [48] Francois Gelis et al. “The Color Glass Condensate”. In: *Ann. Rev. Nucl. Part. Sci.* 60 (2010), pp. 463–489. DOI: 10.1146/annurev.nucl.010909.083629. arXiv: 1002.0333 [hep-ph] (Cited on page 23).
- [49] H. Niemi, K. J. Eskola, and R. Paatelainen. “Event-by-event fluctuations in a perturbative QCD + saturation + hydrodynamics model: Determining QCD matter shear viscosity in ultrarelativistic heavy-ion collisions”. In: *Phys. Rev. C* 93.2 (2016), p. 024907. DOI: 10.1103/PhysRevC.93.024907. arXiv: 1505.02677 [hep-ph] (Cited on pages 23, 25, 33, 71, 72).
- [50] E. Molnar, H. Niemi, and D. H. Rischke. “Numerical tests of causal relativistic dissipative fluid dynamics”. In: *Eur. Phys. J. C* 65 (2010), pp. 615–635. DOI: 10.1140/epjc/s10052-009-1194-9. arXiv: 0907.2583 [nucl-th] (Cited on page 23).
- [51] J. Scott Moreland, Jonah E. Bernhard, and Steffen A. Bass. “Alternative ansatz to wounded nucleon and binary collision scaling in high-energy nuclear collisions”. In: *Phys. Rev. C* 92.1 (2015), p. 011901. DOI: 10.1103/PhysRevC.92.011901. arXiv: 1412.4708 [nucl-th] (Cited on page 25).
- [52] Jonah E. Bernhard et al. “Applying Bayesian parameter estimation to relativistic heavy-ion collisions: simultaneous characterization of the initial state and quark-gluon plasma medium”. In: *Phys. Rev. C* 94.2 (2016), p. 024907. DOI: 10.1103/PhysRevC.94.024907. arXiv: 1605.03954 [nucl-th] (Cited on page 27).
- [53] Bjoern Schenke, Prithwish Tribedy, and Raju Venugopalan. “Fluctuating Glasma initial conditions and flow in heavy ion collisions”. In: *Phys. Rev. Lett.* 108 (2012), p. 252301. DOI: 10.1103/PhysRevLett.108.252301. arXiv: 1202.6646 [nucl-th] (Cited on pages 27, 28).
- [54] Bjoern Schenke, Prithwish Tribedy, and Raju Venugopalan. “Event-by-event gluon multiplicity, energy density, and eccentricities in ultrarelativistic heavy-ion collisions”. In: *Phys. Rev. C* 86 (2012), p. 034908. DOI: 10.1103/PhysRevC.86.034908. arXiv: 1206.6805 [hep-ph] (Cited on page 29).

- [55] Jia Liu, Chun Shen, and Ulrich Heinz. “Pre-equilibrium evolution effects on heavy-ion collision observables”. In: *Phys. Rev. C* 91.6 (2015). [Erratum: *Phys.Rev.C* 92, 049904 (2015)], p. 064906. DOI: 10.1103/PhysRevC.91.064906. arXiv: 1504.02160 [nucl-th] (Cited on pages 29, 32).
- [56] C. M. Hung and Edward V. Shuryak. “Equation of state, radial flow and freezeout in high-energy heavy ion collisions”. In: *Phys. Rev. C* 57 (1998), pp. 1891–1906. DOI: 10.1103/PhysRevC.57.1891. arXiv: hep-ph/9709264 (Cited on page 30).
- [57] Hannu Holopainen and Pasi Huovinen. “Dynamical Freeze-out in Event-by-Event Hydrodynamics”. In: *J. Phys. Conf. Ser.* 389 (2012). Ed. by Rene Bellwied and Claude A. Pruneau, p. 012018. DOI: 10.1088/1742-6596/389/1/012018. arXiv: 1207.7331 [hep-ph] (Cited on page 30).
- [58] Hannah Petersen et al. “Constraining the initial state granularity with bulk observables in Au+Au collisions at $\sqrt{s_{\text{NN}}} = 200$ GeV”. In: *J. Phys. G* 38 (2011), p. 045102. DOI: 10.1088/0954-3899/38/4/045102. arXiv: 1012.4629 [nucl-th] (Cited on page 30).
- [59] John Novak et al. “Determining Fundamental Properties of Matter Created in Ultrarelativistic Heavy-Ion Collisions”. In: *Phys. Rev. C* 89.3 (2014), p. 034917. DOI: 10.1103/PhysRevC.89.034917. arXiv: 1303.5769 [nucl-th] (Cited on page 30).
- [60] Scott Pratt et al. “Constraining the Eq. of State of Super-Hadronic Matter from Heavy-Ion Collisions”. In: *Phys. Rev. Lett.* 114 (2015), p. 202301. DOI: 10.1103/PhysRevLett.114.202301. arXiv: 1501.04042 [nucl-th] (Cited on page 30).
- [61] Evan Sangaline and Scott Pratt. “Toward a deeper understanding of how experiments constrain the underlying physics of heavy-ion collisions”. In: *Phys. Rev. C* 93.2 (2016), p. 024908. DOI: 10.1103/PhysRevC.93.024908. arXiv: 1508.07017 [nucl-th] (Cited on page 30).
- [62] Jonah E. Bernhard et al. “Quantifying properties of hot and dense QCD matter through systematic model-to-data comparison”. In: *Phys. Rev. C* 91.5 (2015), p. 054910. DOI: 10.1103/PhysRevC.91.054910. arXiv: 1502.00339 [nucl-th] (Cited on pages 30–32).
- [63] Ulrich W. Heinz and Jia Liu. “Pre-equilibrium dynamics and heavy-ion observables”. In: *25th International Conference on Ultra-Relativistic Nucleus-Nucleus Collisions (Quark Matter 2015) Kobe, Japan, September 27-October 3, 2015*. Nucl. Phys. A, in press, 2015. arXiv: 1512.08276 [nucl-th] (Cited on page 30).
- [64] Jussi Auvinen et al. “Temperature dependence of η/s of strongly interacting matter: Effects of the equation of state and the parametric form of $(\eta/s)(T)$ ”. In: *Phys. Rev. C* 102.4 (2020), p. 044911. DOI: 10.1103/PhysRevC.102.044911. arXiv: 2006.12499 [nucl-th] (Cited on page 30).

- [65] Govert Nijs et al. “Bayesian analysis of heavy ion collisions with the heavy ion computational framework Trajectum”. In: *Phys. Rev. C* 103.5 (2021), p. 054909. DOI: 10.1103/PhysRevC.103.054909. arXiv: 2010.15134 [nucl-th] (Cited on page 30).
- [66] Wojciech Broniowski et al. “Free-streaming approximation in early dynamics of relativistic heavy-ion collisions”. In: *Phys. Rev. C* 80 (2009), p. 034902. DOI: 10.1103/PhysRevC.80.034902. arXiv: 0812.3393 [nucl-th] (Cited on page 32).
- [67] Huichao Song and Ulrich W. Heinz. “Causal viscous hydrodynamics in 2+1 dimensions for relativistic heavy-ion collisions”. In: *Phys. Rev. C* 77 (2008), p. 064901. DOI: 10.1103/PhysRevC.77.064901. arXiv: 0712.3715 [nucl-th] (Cited on page 32).
- [68] Huichao Song and Ulrich W. Heinz. “Multiplicity scaling in ideal and viscous hydrodynamics”. In: *Phys. Rev. C* 78 (2008), p. 024902. DOI: 10.1103/PhysRevC.78.024902. arXiv: 0805.1756 [nucl-th] (Cited on page 32).
- [69] S. A. Bass et al. “Microscopic models for ultrarelativistic heavy ion collisions”. In: *Prog. Part. Nucl. Phys.* 41 (1998), pp. 255–369. DOI: 10.1016/S0146-6410(98)00058-1. arXiv: nucl-th/9803035 (Cited on page 32).
- [70] M. Bleicher et al. “Relativistic hadron hadron collisions in the ultrarelativistic quantum molecular dynamics model”. In: *J. Phys. G* 25 (1999), pp. 1859–1896. DOI: 10.1088/0954-3899/25/9/308. arXiv: hep-ph/9909407 (Cited on page 32).
- [71] Peter Brockway Arnold, Caglar Dogan, and Guy D. Moore. “The Bulk Viscosity of High-Temperature QCD”. In: *Phys. Rev. D* 74 (2006), p. 085021. DOI: 10.1103/PhysRevD.74.085021. arXiv: hep-ph/0608012 (Cited on page 33).
- [72] Stefano I. Finazzo et al. “Hydrodynamic transport coefficients for the non-conformal quark-gluon plasma from holography”. In: *JHEP* 02 (2015), p. 051. DOI: 10.1007/JHEP02(2015)051. arXiv: 1412.2968 [hep-ph] (Cited on page 33).
- [73] Jacquelyn Noronha-Hostler et al. “Bulk Viscosity Effects in Event-by-Event Relativistic Hydrodynamics”. In: *Phys. Rev. C* 88.4 (2013), p. 044916. DOI: 10.1103/PhysRevC.88.044916. arXiv: 1305.1981 [nucl-th] (Cited on pages 33, 34).
- [74] Giuliano Giacalone et al. “Hydrodynamic predictions for 5.44 TeV Xe+Xe collisions”. In: *Phys. Rev. C* 97.3 (2018), p. 034904. DOI: 10.1103/PhysRevC.97.034904. arXiv: 1711.08499 [nucl-th] (Cited on page 34).
- [75] S. Voloshin and Y. Zhang. “Flow study in relativistic nuclear collisions by Fourier expansion of Azimuthal particle distributions”. In: *Z. Phys. C* 70 (1996), pp. 665–672. DOI: 10.1007/s002880050141. arXiv: hep-ph/9407282 [hep-ph] (Cited on page 36).

- [76] B. Alver and G. Roland. “Collision geometry fluctuations and triangular flow in heavy-ion collisions”. In: *Phys. Rev. C* 81 (2010). [Erratum: *Phys. Rev. C* 82, 039903(2010)], p. 054905. DOI: 10.1103/PhysRevC.82.039903, 10.1103/PhysRevC.81.054905. arXiv: 1003.0194 [nucl-th] (Cited on page 37).
- [77] Arthur M. Poskanzer and S. A. Voloshin. “Methods for analyzing anisotropic flow in relativistic nuclear collisions”. In: *Phys. Rev. C* 58 (1998), pp. 1671–1678. DOI: 10.1103/PhysRevC.58.1671. arXiv: nucl-ex/9805001 [nucl-ex] (Cited on pages 37, 47).
- [78] Matthew Luzum and Jean-Yves Ollitrault. “Eliminating experimental bias in anisotropic-flow measurements of high-energy nuclear collisions”. In: *Phys. Rev. C* 87.4 (2013), p. 044907. DOI: 10.1103/PhysRevC.87.044907. arXiv: 1209.2323 [nucl-ex] (Cited on pages 37, 47).
- [79] S. Wang et al. “Measurement of collective flow in heavy ion collisions using particle pair correlations”. In: *Phys. Rev. C* 44 (1991), pp. 1091–1095. DOI: 10.1103/PhysRevC.44.1091 (Cited on page 38).
- [80] Roy A. Lacey et al. “Multifragment azimuthal correlation functions: Probes for reaction dynamics in collisions of intermediate energy heavy ions”. In: *Phys. Rev. Lett.* 70 (1993), pp. 1224–1227. DOI: 10.1103/PhysRevLett.70.1224 (Cited on page 38).
- [81] Roy A. Lacey. “Elliptic flow measurements with the PHENIX detector”. In: *Nucl. Phys. A* 698 (2002). Ed. by T. J. Hallman et al., pp. 559–563. DOI: 10.1016/S0375-9474(01)01428-2. arXiv: nucl-ex/0105003 (Cited on page 38).
- [82] Shreyasi Acharya et al. “Higher harmonic non-linear flow modes of charged hadrons in Pb-Pb collisions at $\sqrt{s_{NN}} = 5.02$ TeV”. In: *JHEP* 05 (2020), p. 085. DOI: 10.1007/JHEP05(2020)085. arXiv: 2002.00633 [nucl-ex] (Cited on pages 38, 44–46).
- [83] E. Shuryak. “The sounds of the Little and Big Bangs”. In: *Universe* 3.4 (2017), p. 75. DOI: 10.3390/universe3040075. arXiv: 1710.03776 [hep-ph] (Cited on page 38).
- [84] Shreyasi Acharya et al. “Higher harmonic non-linear flow modes of charged hadrons in Pb-Pb collisions at $\sqrt{s_{NN}} = 5.02$ TeV”. In: *JHEP* 05 (2020), p. 085. DOI: 10.1007/JHEP05(2020)085. arXiv: 2002.00633 [nucl-ex] (Cited on page 39).
- [85] Nicolas Borghini, Phuong Mai Dinh, and Jean-Yves Ollitrault. “Flow analysis from multiparticle azimuthal correlations”. In: *Phys. Rev. C* 64 (2001), p. 054901. DOI: 10.1103/PhysRevC.64.054901. arXiv: nucl-th/0105040 (Cited on pages 39, 40).
- [86] Jaroslav Adam et al. “Correlated event-by-event fluctuations of flow harmonics in Pb-Pb collisions at $\sqrt{s_{NN}} = 2.76$ TeV”. In: *Phys. Rev. Lett.* 117 (2016), p. 182301. DOI: 10.1103/PhysRevLett.117.182301. arXiv: 1604.07663 [nucl-ex] (Cited on pages 40, 41, 46, 64, 66).

- [87] Shreyasi Acharya et al. “Systematic studies of correlations between different order flow harmonics in Pb-Pb collisions at $\sqrt{s_{NN}} = 2.76$ TeV”. In: *Phys. Rev. C* 97.2 (2018), p. 024906. DOI: 10.1103/PhysRevC.97.024906. arXiv: 1709.01127 [nucl-ex] (Cited on pages 40, 46, 64).
- [88] H. Niemi et al. “Event-by-event distributions of azimuthal asymmetries in ultrarelativistic heavy-ion collisions”. In: *Phys. Rev. C* 87.5 (2013), p. 054901. DOI: 10.1103/PhysRevC.87.054901. arXiv: 1212.1008 [nucl-th] (Cited on pages 41, 42).
- [89] Fernando G. Gardim et al. “Mapping the hydrodynamic response to the initial geometry in heavy-ion collisions”. In: *Phys. Rev. C* 85 (2012), p. 024908. DOI: 10.1103/PhysRevC.85.024908. arXiv: 1111.6538 [nucl-th] (Cited on page 41).
- [90] D. Teaney and L. Yan. “Event-plane correlations and hydrodynamic simulations of heavy ion collisions”. In: *Phys. Rev. C* 90.2 (2014), p. 024902. DOI: 10.1103/PhysRevC.90.024902. arXiv: 1312.3689 [nucl-th] (Cited on page 42).
- [91] Li Yan and Jean-Yves Ollitrault. “ v_4, v_5, v_6, v_7 : nonlinear hydrodynamic response versus LHC data”. In: *Phys. Lett. B* 744 (2015), pp. 82–87. DOI: 10.1016/j.physletb.2015.03.040. arXiv: 1502.02502 [nucl-th] (Cited on page 43).
- [92] Derek Teaney and Li Yan. “Non linearities in the harmonic spectrum of heavy ion collisions with ideal and viscous hydrodynamics”. In: *Phys. Rev. C* 86 (2012), p. 044908. DOI: 10.1103/PhysRevC.86.044908. arXiv: 1206.1905 [nucl-th] (Cited on page 43).
- [93] Shreyasi Acharya et al. “Linear and non-linear flow modes in Pb-Pb collisions at $\sqrt{s_{NN}} = 2.76$ TeV”. In: *Phys. Lett. B* 773 (2017), pp. 68–80. DOI: 10.1016/j.physletb.2017.07.060. arXiv: 1705.04377 [nucl-ex] (Cited on page 43).
- [94] Zhi Qiu and Ulrich Heinz. “Hydrodynamic event-plane correlations in Pb+Pb collisions at $\sqrt{s} = 2.76$ ATeV”. In: *Phys. Lett. B* 717 (2012), pp. 261–265. DOI: 10.1016/j.physletb.2012.09.030. arXiv: 1208.1200 [nucl-th] (Cited on page 46).
- [95] Shreyasi Acharya et al. “Measurements of mixed harmonic cumulants in Pb–Pb collisions at $\sqrt{s_{NN}} = 5.02$ TeV”. In: *Phys. Lett. B* 818 (2021), p. 136354. DOI: 10.1016/j.physletb.2021.136354. arXiv: 2102.12180 [nucl-ex] (Cited on pages 46, 66, 71).
- [96] Shreyasi Acharya et al. “Linear and non-linear flow modes in Pb-Pb collisions at $\sqrt{s_{NN}} = 2.76$ TeV”. In: *Phys. Lett. B* 773 (2017), pp. 68–80. DOI: 10.1016/j.physletb.2017.07.060. arXiv: 1705.04377 [nucl-ex] (Cited on page 46).

- [97] Ante Bilandzic et al. “Generic framework for anisotropic flow analyses with multiparticle azimuthal correlations”. In: *Phys. Rev. C* 89.6 (2014), p. 064904. DOI: 10.1103/PhysRevC.89.064904. arXiv: 1312.3572 [nucl-ex] (Cited on pages 47, 48, 64).
- [98] P. Danielewicz and G. Odyniec. “Transverse Momentum Analysis of Collective Motion in Relativistic Nuclear Collisions”. In: *Phys. Lett. B* 157 (1985), pp. 146–150. DOI: 10.1016/0370-2693(85)91535-7 (Cited on page 47).
- [99] Sergei A. Voloshin, Arthur M. Poskanzer, and Raimond Snellings. “Collective phenomena in non-central nuclear collisions”. In: *Landolt-Bornstein* 23 (2010), pp. 293–333. DOI: 10.1007/978-3-642-01539-7_10. arXiv: 0809.2949 [nucl-ex] (Cited on page 49).
- [100] Serguei Chatrchyan et al. “Multiplicity and Transverse Momentum Dependence of Two- and Four-Particle Correlations in pPb and PbPb Collisions”. In: *Phys. Lett. B* 724 (2013), pp. 213–240. DOI: 10.1016/j.physletb.2013.06.028. arXiv: 1305.0609 [nucl-ex] (Cited on page 49).
- [101] Peng Huo et al. “Importance of non-flow in mixed-harmonic multiparticle correlations in small collision systems”. In: *Phys. Lett. B* 777 (2018), pp. 201–206. DOI: 10.1016/j.physletb.2017.12.035. arXiv: 1710.07567 [nucl-ex] (Cited on page 49).
- [102] Esma Mobs. “The CERN accelerator complex. Complexe des accélérateurs du CERN”. In: (July 2016). General Photo (Cited on page 52).
- [103] R. Schmidt et al. “Protection of the CERN Large Hadron Collider”. In: *New J. Phys.* 8 (2006), p. 290. DOI: 10.1088/1367-2630/8/11/290 (Cited on page 53).
- [104] “LHC Machine”. In: *JINST* 3 (2008). Ed. by Lyndon Evans and Philip Bryant, S08001. DOI: 10.1088/1748-0221/3/08/S08001 (Cited on page 53).
- [105] R Perin and J Vlogaert. *Magnets for the Large Hadron Collider*. Tech. rep. Geneva: CERN, Feb. 1994 (Cited on page 54).
- [106] Daniel Boussard. “Schottky noise and beam transfer function diagnostics”. In: (May 1986), 42 p. DOI: 10.5170/CERN-1987-003-V-2.416 (Cited on page 54).
- [107] S Baird. *Accelerators for pedestrians; rev. version*. Tech. rep. Geneva: CERN, Feb. 2007 (Cited on page 54).
- [108] “HL-LHC Preliminary Design Report: Deliverable: D1.5”. In: (Nov. 2014) (Cited on page 54).
- [109] *Collisions, LHC Machine Outreach*. <http://lhc-machine-outreach.web.cern.ch/collisions.htm>. Accessed: 01.03.2024 (Cited on page 55).
- [110] G. Aad et al. “The ATLAS Experiment at the CERN Large Hadron Collider”. In: *JINST* 3 (2008), S08003. DOI: 10.1088/1748-0221/3/08/S08003 (Cited on page 55).

- [111] K. Aamodt et al. “The ALICE experiment at the CERN LHC”. In: *JINST* 3 (2008), S08002. DOI: 10.1088/1748-0221/3/08/S08002 (Cited on pages 55, 56, 62, 63).
- [112] Betty Bezverkhny Abelev et al. “Performance of the ALICE Experiment at the CERN LHC”. In: *Int. J. Mod. Phys. A* 29 (2014), p. 1430044. DOI: 10.1142/S0217751X14300440. arXiv: 1402.4476 [nucl-ex] (Cited on pages 55, 56, 59).
- [113] S. Chatrchyan et al. “The CMS Experiment at the CERN LHC”. In: *JINST* 3 (2008), S08004. DOI: 10.1088/1748-0221/3/08/S08004 (Cited on page 55).
- [114] Jr. Alves A. Augusto et al. “The LHCb Detector at the LHC”. In: *JINST* 3 (2008), S08005. DOI: 10.1088/1748-0221/3/08/S08005 (Cited on page 55).
- [115] Serguei Chatrchyan et al. “Observation of a New Boson at a Mass of 125 GeV with the CMS Experiment at the LHC”. In: *Phys. Lett. B* 716 (2012), pp. 30–61. DOI: 10.1016/j.physletb.2012.08.021. arXiv: 1207.7235 [hep-ex] (Cited on page 55).
- [116] Georges Aad et al. “Observation of a new particle in the search for the Standard Model Higgs boson with the ATLAS detector at the LHC”. In: *Phys. Lett. B* 716 (2012), pp. 1–29. DOI: 10.1016/j.physletb.2012.08.020. arXiv: 1207.7214 [hep-ex] (Cited on page 55).
- [117] R Aaij et al. “First Evidence for the Decay $B_s^0 \rightarrow \mu^+ \mu^-$ ”. In: *Phys. Rev. Lett.* 110.2 (2013), p. 021801. DOI: 10.1103/PhysRevLett.110.021801. arXiv: 1211.2674 [hep-ex] (Cited on page 55).
- [118] Roel Aaij et al. “Measurement of the $B_s^0 \rightarrow \mu^+ \mu^-$ branching fraction and effective lifetime and search for $B^0 \rightarrow \mu^+ \mu^-$ decays”. In: *Phys. Rev. Lett.* 118.19 (2017), p. 191801. DOI: 10.1103/PhysRevLett.118.191801. arXiv: 1703.05747 [hep-ex] (Cited on page 55).
- [119] *ALICE Inner Tracking System (ITS): Technical Design Report*. Technical design report. ALICE. Geneva: CERN, 1999 (Cited on pages 56, 60).
- [120] K Aamodt et al. “Alignment of the ALICE Inner Tracking System with cosmic-ray tracks”. In: *JINST* 5 (2010), P03003. DOI: 10.1088/1748-0221/5/03/P03003. arXiv: 1001.0502 [physics.ins-det] (Cited on pages 56, 60, 63).
- [121] E. Abbas et al. “Performance of the ALICE VZERO system”. In: *JINST* 8 (2013), P10016. DOI: 10.1088/1748-0221/8/10/P10016. arXiv: 1306.3130 [nucl-ex] (Cited on pages 57, 62).
- [122] J. Alme et al. “The ALICE TPC, a large 3-dimensional tracking device with fast readout for ultra-high multiplicity events”. In: *Nucl. Instrum. Meth. A* 622 (2010), pp. 316–367. DOI: 10.1016/j.nima.2010.04.042. arXiv: 1001.1950 [physics.ins-det] (Cited on pages 57, 58, 63).

- [123] Francesca Carnesecchi. “Performance of the ALICE Time-Of-Flight detector at the LHC”. In: *JINST* 14.06 (2019), p. C06023. DOI: 10.1088/1748-0221/14/06/C06023. arXiv: 1806.03825 [physics.ins-det] (Cited on pages 57, 63).
- [124] J. Adolfsson et al. “The upgrade of the ALICE TPC with GEMs and continuous readout”. In: *JINST* 16.03 (2021), P03022. DOI: 10.1088/1748-0221/16/03/P03022. arXiv: 2012.09518 [physics.ins-det] (Cited on page 59).
- [125] Georges Charpak et al. “The Use of Multiwire Proportional Counters to Select and Localize Charged Particles”. In: *Nucl. Instrum. Meth.* 62 (1968), pp. 262–268. DOI: 10.1016/0029-554X(68)90371-6 (Cited on page 59).
- [126] Jasper Parkkila. “Quantifying the transport properties of quark-gluon plasma through measurement of higher harmonic flow and their non-linear response”. Presented 19 Nov 2021. University of Jyväskylä, 2021 (Cited on pages 62, 91).
- [127] Betty Abelev et al. “Centrality determination of Pb-Pb collisions at $\sqrt{s_{NN}} = 2.76$ TeV with ALICE”. In: *Phys. Rev. C* 88.4 (2013), p. 044909. DOI: 10.1103/PhysRevC.88.044909. arXiv: 1301.4361 [nucl-ex] (Cited on page 63).
- [128] “The ALICE definition of primary particles”. In: (June 2017) (Cited on page 64).
- [129] René Brun et al. “GEANT Detector Description and Simulation Tool”. In: (1994). DOI: 10.17181/CERN.MUHF.DMJ1 (Cited on page 64).
- [130] Xin-Nian Wang and Miklos Gyulassy. “HIJING: A Monte Carlo model for multiple jet production in p p, p A and A A collisions”. In: *Phys. Rev. D* 44 (1991), pp. 3501–3516. DOI: 10.1103/PhysRevD.44.3501 (Cited on page 65).
- [131] Miklos Gyulassy and Xin-Nian Wang. “HIJING 1.0: A Monte Carlo program for parton and particle production in high-energy hadronic and nuclear collisions”. In: *Comput. Phys. Commun.* 83 (1994), p. 307. DOI: 10.1016/0010-4655(94)90057-4. arXiv: nucl-th/9502021 [nucl-th] (Cited on page 65).
- [132] Shreyasi Acharya et al. “Systematic studies of correlations between different order flow harmonics in Pb-Pb collisions at $\sqrt{s_{NN}} = 2.76$ TeV”. In: *Phys. Rev. C* 97.2 (2018), p. 024906. DOI: 10.1103/PhysRevC.97.024906. arXiv: 1709.01127 [nucl-ex] (Cited on page 66).
- [133] Roger Barlow. “Systematic errors: Facts and fictions”. In: *Conference on Advanced Statistical Techniques in Particle Physics*. 2002, pp. 134–144. arXiv: hep-ex/0207026 (Cited on page 66).
- [134] R. Paatelainen et al. “Multiplicities and p_T spectra in ultrarelativistic heavy ion collisions from a next-to-leading order improved perturbative QCD + saturation + hydrodynamics model”. In: *Phys. Rev. C* 87.4 (2013), p. 044904. DOI: 10.1103/PhysRevC.87.044904. arXiv: 1211.0461 [hep-ph] (Cited on page 71).

- [135] R. Paatelainen et al. “Fluid dynamics with saturated minijet initial conditions in ultrarelativistic heavy-ion collisions”. In: *Phys. Lett. B* 731 (2014), pp. 126–130. DOI: 10.1016/j.physletb.2014.02.018. arXiv: 1310.3105 [hep-ph] (Cited on page 71).
- [136] Ante Bilandzic et al. “Multivariate cumulants in flow analyses: The next generation”. In: *Phys. Rev. C* 105.2 (2022), p. 024912. DOI: 10.1103/PhysRevC.105.024912. arXiv: 2101.05619 [physics.data-an] (Cited on page 72).
- [137] Shreyasi Acharya et al. “Long- and short-range correlations and their event-scale dependence in high-multiplicity pp collisions at $\sqrt{s} = 13$ TeV”. In: *JHEP* 05 (2021), p. 290. DOI: 10.1007/JHEP05(2021)290. arXiv: 2101.03110 [nucl-ex] (Cited on page 74).
- [138] Shreyasi Acharya et al. “Emergence of long-range angular correlations in low-multiplicity proton-proton collisions”. In: (Nov. 2023). arXiv: 2311.14357 [nucl-ex] (Cited on page 74).
- [139] Bjoern Schenke, Chun Shen, and Prithwish Tribedy. “Running the gamut of high energy nuclear collisions”. In: *Phys. Rev. C* 102.4 (2020), p. 044905. DOI: 10.1103/PhysRevC.102.044905. arXiv: 2005.14682 [nucl-th] (Cited on page 74).
- [140] Seyed Farid Taghavi. “Smallest QCD droplet and multiparticle correlations in p-p collisions”. In: *Phys. Rev. C* 104.5 (2021), p. 054906. DOI: 10.1103/PhysRevC.104.054906. arXiv: 1907.12140 [nucl-th] (Cited on page 74).
- [141] Moritz Greif et al. “Importance of initial and final state effects for azimuthal correlations in p+Pb collisions”. In: *Phys. Rev. D* 96.9 (2017), p. 091504. DOI: 10.1103/PhysRevD.96.091504. arXiv: 1708.02076 [hep-ph] (Cited on page 75).
- [142] J. Scott Moreland, Jonah E. Bernhard, and Steffen A. Bass. “Bayesian calibration of a hybrid nuclear collision model using p-Pb and Pb-Pb data at energies available at the CERN Large Hadron Collider”. In: *Phys. Rev. C* 101.2 (2020), p. 024911. DOI: 10.1103/PhysRevC.101.024911. arXiv: 1808.02106 [nucl-th] (Cited on page 75).
- [143] Morad Aaboud et al. “Measurements of long-range azimuthal anisotropies and associated Fourier coefficients for pp collisions at $\sqrt{s} = 5.02$ and 13 TeV and p+Pb collisions at $\sqrt{s_{NN}} = 5.02$ TeV with the ATLAS detector”. In: *Phys. Rev. C* 96.2 (2017), p. 024908. DOI: 10.1103/PhysRevC.96.024908. arXiv: 1609.06213 [nucl-ex] (Cited on pages 75, 97, 99).
- [144] T. Pierog et al. “EPOS LHC: Test of collective hadronization with data measured at the CERN Large Hadron Collider”. In: *Phys. Rev. C* 92.3 (2015), p. 034906. DOI: 10.1103/PhysRevC.92.034906. arXiv: 1306.0121 [hep-ph] (Cited on page 95).

- [145] Peter Skands, Stefano Carrazza, and Juan Rojo. “Tuning PYTHIA 8.1: the Monash 2013 Tune”. In: *Eur. Phys. J. C* 74.8 (2014), p. 3024. DOI: 10.1140/epjc/s10052-014-3024-y. arXiv: 1404.5630 [hep-ph] (Cited on page 95).

APPENDIX 1 ACCESSING VERY HIGH ORDER FLOW COEFFICIENTS

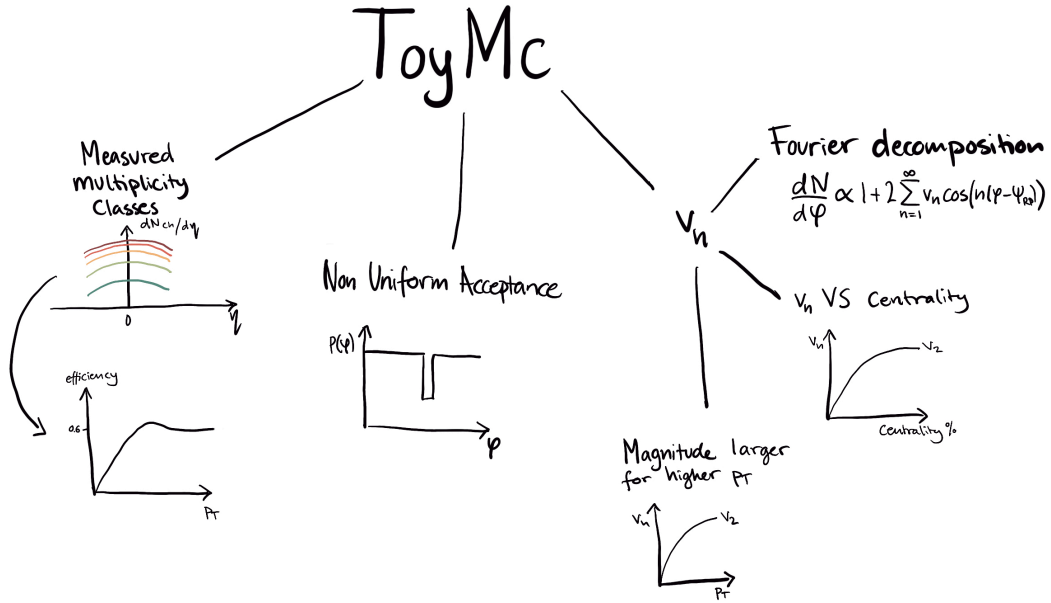


FIGURE 29 A sketch of the three main inputs to the toy Monte-Carlo for investigating the higher order flow coefficients, v_n , $n > 8$.

How far can the harmonic order of flow coefficients be measured in the experiments? Is it possible to measure harmonics beyond $n = 9$? To check for potential experimental bias and to test an extreme case, a toy Monte-Carlo (toy MC) has been made. In this section, the specifics of these toy MC simulations will be outlined.

Figure 29 presents a diagram of what the toy MC accepts as inputs. It requires three main inputs: the v_n information (where the v_n values are taken from measured values up to the seventh harmonic order, with higher order v_n ($n > 7$) extracted using an exponential fit to moderate the value - $v_n \propto \exp(k'n^2)$), the measured multiplicity classes as illustrated in Table 5.2 from Ref. [126], and a non-uniform azimuthal angle to replicate the detector acceptance (NUA). For the NUA, an analytical correction is employed, which for this toy MC takes an extreme case with a large gap in the detector ϕ acceptance (see Fig.30).

In the toy MC calculations, the lower-order flow coefficients ($n < 11$) and higher-order flow coefficients ($n > 10$) showed different behaviors. The results are shown in Fig. 31, where the black squares represent outcomes using measured multiplicity values. The red squares depict an extreme case where we increased the multiplicity by a factor of 1000. We also tested increasing the statistics tenfold for higher multiplicity, represented by the green squares.

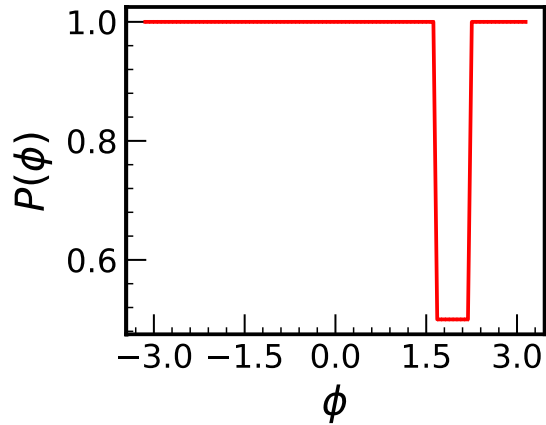


FIGURE 30 The ϕ -modulation imposed on the toy MC particle distribution.

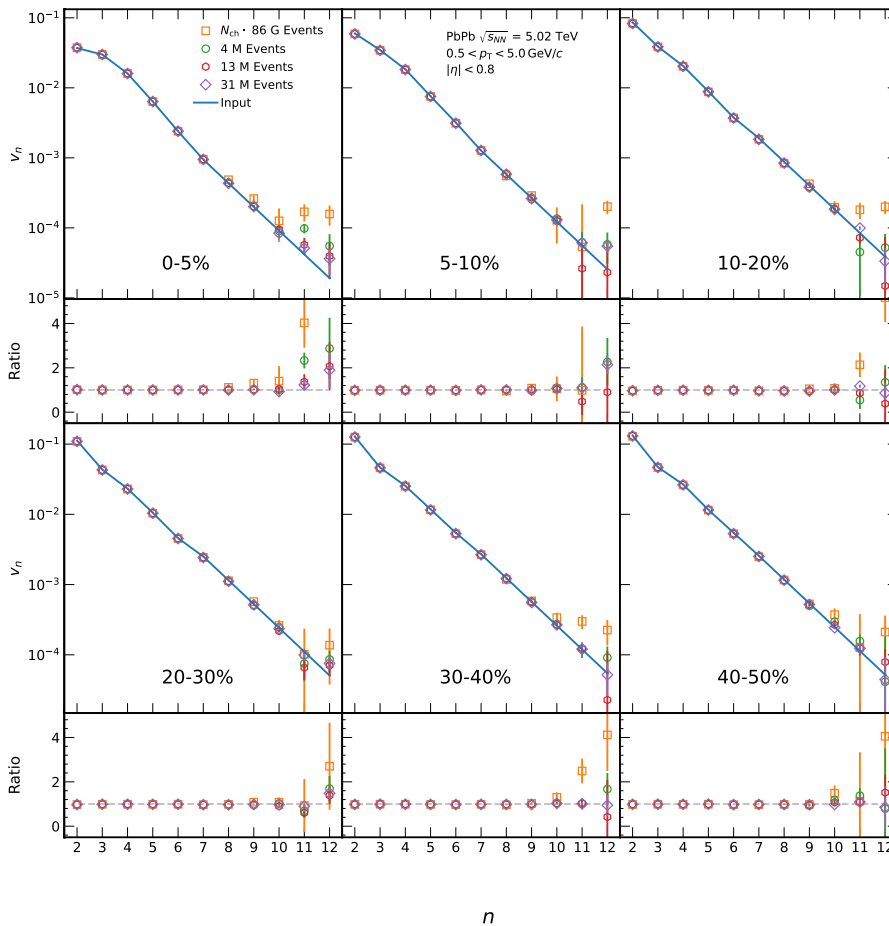


FIGURE 31 Results of the toy MC calculations. Black squares represent outcomes using measured multiplicity values. Red squares depict an extreme case where multiplicity was increased by a factor of 1000. Green squares show results of a test in which the statistics were increased tenfold for higher multiplicity.

Upon data analysis, we observed that the lower-order flow coefficients accurately converged to the input values. However, the higher-order flow coefficients were overestimated compared to the input values within the examined centrality ranges. This discrepancy led us to conduct the extreme case experiments.

In the extreme case, the higher-order flow coefficients aligned well with the input values for larger events. Interestingly, the convergence to the true value slowed down for larger event samples in central collisions, where the flow coefficient was smallest. The relationship between finite event multiplicity and flow coefficients needs further exploration to establish measurement limits.

2 MULTIPLICITY DEPENDENCE IN SMALL SYSTEMS

The reference multiplicity in an experiment provides key information about the energy density, system size, and event activity in a given collision system. However, due to differing definitions of reference multiplicity across various experiments, comparisons can be challenging.

Table 5 defines the reference multiplicity in ALICE and ATLAS experiments. ALICE calculates the reference multiplicity by integrating the from $\eta = -0.5$ to 0.5 for each multiplicity class measured by V0M and V0A in pp and p-Pb collisions, respectively. In contrast, ATLAS calculates the reference multiplicity by counting the number of charged tracks ($N_{\text{ch}}^{\text{reco}}$), uncorrected by tracking efficiency, with $p_{\text{T}} > 0.4 \text{ GeV}/c$ in $|\eta| < 2.5$.

TABLE 5 The definition of the reference multiplicity in ALICE and ATLAS Experiments

	ALICE	ATLAS
pp	V0M multiplicity percentile	$N_{\text{ch}}^{\text{reco}}$ in $ \eta < 2.5$ & $p_{\text{T}} > 0.4$
p-Pb	V0A multiplicity percentile	$N_{\text{ch}}^{\text{reco}}$ in $ \eta < 2.5$ & $p_{\text{T}} > 0.4$

APPENDIX 3 TESTING WITH PYTHIA IN PP COLLISIONS AT $\sqrt{s} = 13$ TEV

The conversion of the ALICE to ATLAS definition of the number of charged particles (N_{ch}) in pp collisions at $\sqrt{s} = 13$ TeV and p-Pb collisions at $\sqrt{s_{\text{NN}}} = 5.02$ TeV, is done using EPOS-LHC [144] since this model describes the data well, but as a test, the conversion was done for pp collisions using PYTHIA8 with the MONASH13 tune [145] and the procedure is described in this section.

The first step is to calculate the multiplicity distributions for the two definitions. The left side of Fig. 32 presents the multiplicity for the ALICE and ATLAS definition. On the right side of Fig. 32, a strong correlation is demonstrated in the plot of ATLAS versus ALICE multiplicity. The centrality percentile classes were determined from the produced N_{ch} distribution using the ALICE definition of multiplicity, as seen in Fig. 33.

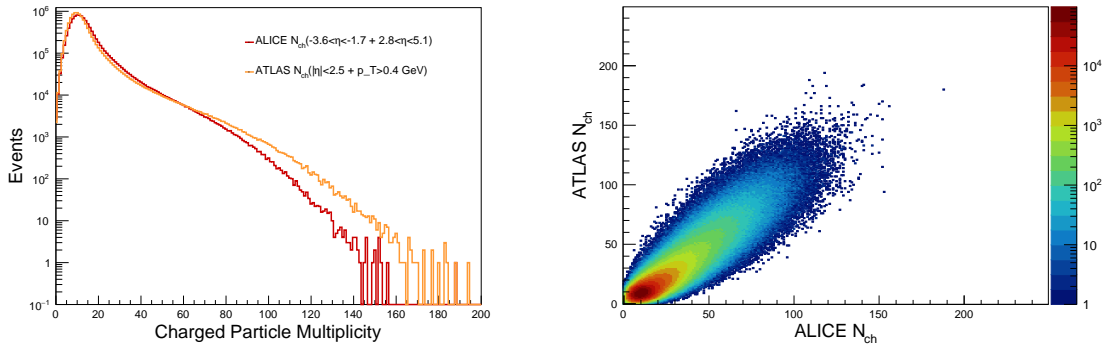


FIGURE 32 **Left:** Number of events as a function of charged particle multiplicity for the ALICE definition in red and ATLAS definition in orange. **Right:** The ATLAS multiplicity is plotted against the ALICE multiplicity in order to see the correlation of the two definitions.

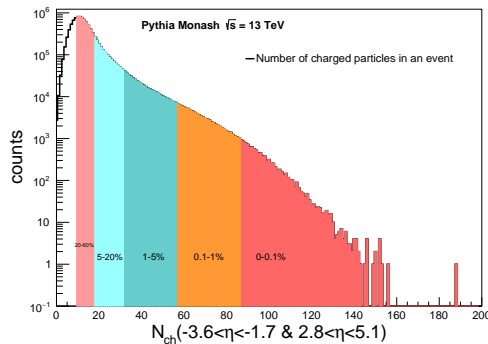


FIGURE 33 Number of counts as a function of number of charged particles using PYTHIA8 Monash13 tune.

The second step is to calculate the pseudorapidity distribution for each definition. In Fig. 34, a comparison is made between the use of a p_{T} -cut and no

p_T -cut, as well as between EPOS and PYTHIA for each centrality class. The left figure shows that the $dN/d\eta$ -yield decreases by a factor of approximately two when a p_T -cut is applied across all centrality classes. Thus, we scale them up for comparison purposes. The shape comparison shows that auto-correlations are not as strong when a p_T -cut is applied. On the right side of Fig. 34, EPOS and PYTHIA both have the same η -acceptance and kinematic cuts. The only difference is that the EPOS distributions are scaled up to match the data reference, while the PYTHIA distributions are not. Therefore, we use a scaling factor, as shown in the figure, to scale them up. When comparing the shape, it's clear that EPOS does not have the same auto-correlations as PYTHIA, but instead has a smoother distribution.

As presented in Fig. 34, the η -distribution appearing on the left side exhibits a noticeable bump when produced using PYTHIA. This bump is indicative of pronounced auto-correlations in PYTHIA, which is largely attributed to the region of partial overlap in the V0C acceptance with ATLAS acceptance, specifically in the range of $-2.5 < \eta < -1.7$. These auto-correlations are not just seen in simulations, but can also be observed in the data. The overlap of the acceptance regions between V0C and ATLAS is likely the cause behind these correlations. To illustrate, V0C operates within the η range of $-3.6 < \eta < -1.7$, while the ATLAS coverage is within $-2.5 < \eta < 2.5$. The overlap in these ranges is a significant factor that contributes to the auto-correlations observed in both the data and the simulations.

The approach we followed for determining the multiplicity involved integrating the histograms for $|\eta| < 0.5$ and $|\eta| < 2.5$ and $p_T > 0.4$. These pseudorapidity histograms are shown in 35, and correspond to the multiplicity definitions of ALICE and ATLAS, respectively.

To understand how much the η acceptance influences the multiplicity, we calculate the ratio of the η acceptance of $|\eta| < 0.5$ over $|\eta| < 2.5$. For p_T , the ratio is based on the definition with $|\eta| < 2.5$ over $|\eta| < 2.5$ with $p_T > 0.4$ GeV/c. We then obtain the conversion factor by calculating the ratio of the multiplicity with the ALICE definition over the multiplicity with the ATLAS definition. These values are summarized in Table 6, where the ratio $\text{ALICE}/\text{ATLAS}_{\text{reco}}$ already takes into account the efficiency correction.

TABLE 6 The correction factors for the respective centrality classes, together with the η acceptance and p_T cut effects.

V0M:	0-0.1%	0.1-1%	1-5%	5-10%	20-60%
η accept. eff.	0.19	0.19	0.19	0.18	0.18
p_T cut eff.	0.56	0.54	0.5	0.45	0.41
ALICE/ATLAS	0.33	0.35	0.37	0.40	0.43
ALICE/ATLAS _{reco}	0.44	0.46	0.49	0.54	0.57

In case of the ATLAS measurement, the charged particle multiplicity was obtained by counting the number of reconstructed particles satisfying $p_T > 0.4$ GeV/c in $|\eta| < 2.5$. The ATLAS results have no efficiency correction (la-

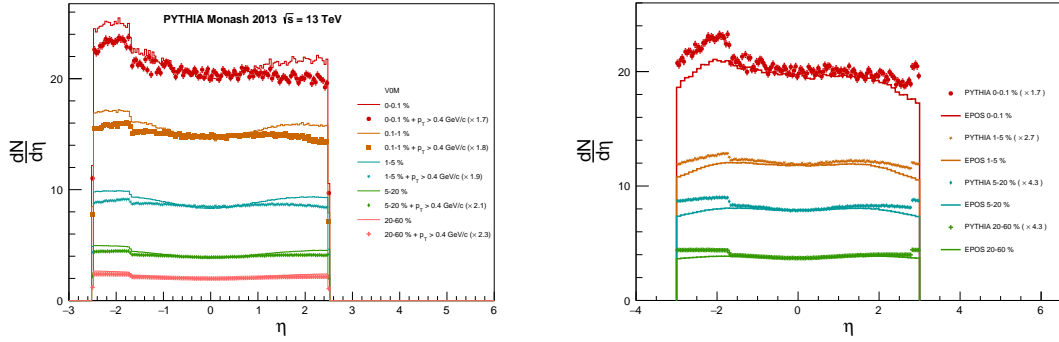


FIGURE 34 **Left:** Comparing η -distributions with and without p_T -cut at 0.4 GeV for all centrality classes. The distributions shown as histograms correspond to no p_T -cut, whereas the ones with markers correspond to with p_T -cut. **Right:** Comparing η -distributions created with different models, PYTHIA8 and EPOS, in η and p_T ranges. PYTHIA8 results are shown with markers, and EPOS results are shown as histograms.

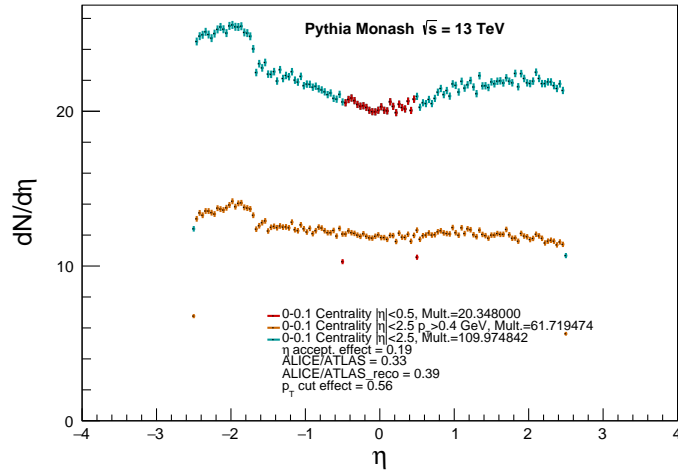


FIGURE 35 The η -distributions for one centrality class (0-0.1%) and for three different definitions of N_{ch} using PYTHIA8 Monash 13 tune. The ALICE definition is shown in red with $|\eta| < 0.5$, in blue η is extended to $|\eta| < 2.5$ which is the η acceptance in ATLAS. The complete ATLAS definition is shown brown with $|\eta| < 2.5$ and $p_T > 0.4$ GeV.

beled as $N_{\text{ch},\text{ATLAS}}^{\text{rec}}$, therefore the result needs to take into account the efficiency reported in Ref. [143] to be compared to our measurements, which are 1.29 ± 0.05 and 1.18 ± 0.05 in p-Pb and pp collisions, respectively.

TABLE 7 Conversion table for p–Pb collisions

Exp.	ALICE	ALICE	ATLAS
Centrality (%)	$N_{\text{ch}}(\eta < 0.5)$	$N_{\text{ch}}(p_{\text{T}} > 0.4, \eta < 0.5)$	$N_{\text{ch,ATLAS}}^{\text{rec}}(p_{\text{T}} > 0.4, \eta < 2.5)$
0–5	44.96	23.66	85.35
5–10	36.05	22.19	83.27
10–20	30.33	17.89	67.26
20–40	23.12	13.24	49.93
40–60	15.89	8.85	33.54
60–100	N/A	3.72	14.25

TABLE 8 Conversion table for pp collisions

Exp.	ALICE	ALICE	ATLAS
Mult. Class (%)	$N_{\text{ch}}(\eta < 0.5)$	$N_{\text{ch}}(p_{\text{T}} > 0.4, \eta < 0.5)$	$N_{\text{ch,ATLAS}}^{\text{rec}}(p_{\text{T}} > 0.4, \eta < 2.5)$
0–0.1	31.33	19.66	84.07 (80.33)
1–5	20.02	11.80	50.10(48.83)
5–20	13.99	7.89	33.70(29.15)
20–60	7.2	3.71	16.11(14.12)
60–100	N/A	1.23	5.23

APPENDIX 3.1 Results

Table 7 and Table 8 contain the original ALICE N_{ch} values. These values have been calculated with great precision and are presented together with the values obtained after the extrapolation in η . Additionally, these tables also present the ALICE to ATLAS conversion values for p–Pb and pp collisions. These values are obtained from using the EPOS model and ALICE measurements. The results derived from the test with pp collisions using the PYTHIA model are presented, within parentheses, in Table 8. This test was performed to compare and contrast the results and to further validate the findings. Upon examining these results, we can see that they exhibit a similarity to the results obtained from the EPOS model. However, these results display slightly lower values than the former method.

Finally, our results compared to ATLAS are shown in Fig. 36, as a function of $N_{\text{ch,ATLAS}}^{\text{rec}}$. Our results in p–Pb collisions agree with those of ATLAS in lower multiplicity and are slightly larger for our highest multiplicity interval. In case of pp collisions, our results agree better with the results by ATLAS for the highest two multiplicity intervals, but are smaller in $N_{\text{ch,ATLAS}}^{\text{rec}} < 40$. It's important to note that there's no certainty in the correlations between mid-rapidity and forward rapidity multiplicity in smaller collision systems. Therefore, the validity of this method is not guaranteed when exploring different kinematic ranges. As stated earlier in the paper [24], two assumptions of the flow extraction method are tested exclusively within the confines of ALICE acceptance. This underscores the need to revisit systematic uncertainties when exploring different kinematic

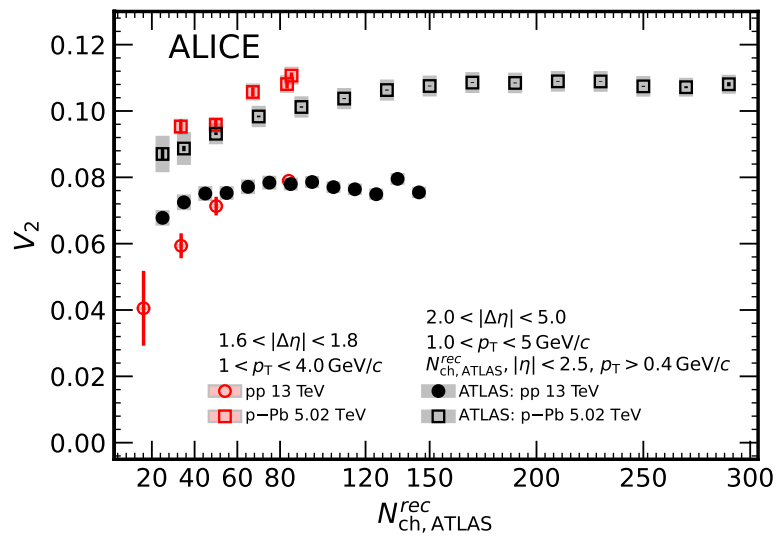


FIGURE 36 A comparison to ATLAS [143] experiment of the v_2 magnitude for two different collision systems, pp and p-Pb, as a function of the ATLAS definition of multiplicity.

ranges, as their impact may not always be negligible. Further analyses from various collaborations could potentially provide more insight into this issue in the future.

ORIGINAL PAPERS

PI




**BAYESIAN ESTIMATION OF THE SPECIFIC SHEAR AND
BULK VISCOSITY OF THE QUARK-GLUON PLASMA WITH
ADDITIONAL FLOW HARMONIC OBSERVABLES**

by

Parkkila, J.E. & Onnerstad, A. & Kim, D.J.

Phys.Rev.C , 104 (2021).

Bayesian estimation of the specific shear and bulk viscosity of the quark-gluon plasma with additional flow harmonic observables

J. E. Parkkila ,* A. Onnerstad , and D. J. Kim 

*University of Jyväskylä, Department of Physics, P.O. Box 35, FI-40014 University of Jyväskylä, Finland
and Helsinki Institute of Physics, P.O. Box 64, FI-00014 University of Helsinki, Finland*



(Received 8 July 2021; accepted 26 October 2021; published 8 November 2021)

The transport properties of the strongly coupled quark-gluon plasma created in ultrarelativistic heavy-ion collisions are extracted by Bayesian parameter estimate methods with the latest collision beam energy data from the CERN Large Hadron Collider. This Bayesian analysis includes sophisticated flow harmonic observables for the first time. We found that the temperature dependence of specific shear viscosity appears weaker than in the previous studies. The results prefer a lower value of specific bulk viscosity and a higher switching temperature to reproduce additional observables. However, the improved statistical uncertainties both on the experimental data and hydrodynamic calculations with additional observables do not help to reduce the final credibility ranges much, indicating a need for improving the dynamical collision model before the hydrodynamic takes place. In addition, the sensitivities of experimental observables to the parameters in hydrodynamic model calculations are quantified. It is found that the analysis benefits most from the symmetric cumulants and nonlinear flow modes, which mostly reflect nonlinear hydrodynamic responses, in constraining the temperature dependence of the specific shear and bulk viscosities in addition to the previously used flow coefficients.

DOI: [10.1103/PhysRevC.104.054904](https://doi.org/10.1103/PhysRevC.104.054904)

I. INTRODUCTION

The primary goal of heavy-ion physics is to investigate and understand the strongly coupled color-deconfined matter, quark-gluon plasma (QGP), which is produced in ultrarelativistic collisions between heavy ions. The QGP is believed to be the predominant form of matter during the first phases of the early universe. This matter behaves like a near-perfect fluid with the smallest specific shear viscosity, the ratio of the shear viscosity to the entropy density (η/s), of any known substance in nature [1].

The most important remaining open questions in the field are the location of the critical point (T_c) in the QCD phase diagram and temperature dependence of specific shear (η) and bulk (ζ) viscosities of the QGP. The flow analysis at the CERN Large Hadron Collider (LHC) has been very successful and provides valuable information to the field [2–6]. For example, the main constraints for the QGP properties using the Bayesian analysis [7] in the theory came from the ALICE measurements [2,8,9] with both low and high beam energy data. Even though the Bayesian analyses [7,10–13] were successful, the current uncertainties from these works

are large because of statistical limitations of the data, limited observables used for the analysis, and computational constraints. In addition to the aforementioned limitations, pinning down the absolute value of η/s at T_c has a few challenges. First, a principle calculation to describe the initial conditions (IC) is still under development. Second, extracting the temperature dependence of $\eta/s(T)$ has been complicated with the existence of the bulk viscosity [14,15]. However, large flow found in small systems like proton-proton (pp) collisions was striking and opened up the importance of gluon fluctuations within protons, and certainly the experimental data would help to improve the understanding of IC both for small and large systems [16]. There are newer observables that give much stronger constraints to the theory [3,4], showing good sensitivities especially to $\eta/s(T)$ and $\zeta/s(T)$. The correlation strength measured in [3,4] was experimentally decomposed into two components of linear and nonlinear flow modes in [5,17] for the first time in the field, which gives a better understanding of our harmonic analysis and its origin with both LHC Run 1 (2009–2013) and Run 2 (2015–2018) data.

In this work, we extend the Bayesian parameter estimation methods employed in [7] with larger statistic LHC Run 2 results [18,19] as well as a few additional observables [5,6] for the first time which require substantial computational power. This work also allows us to quantify the sensitivity of each observable to the hydrodynamic model parameters in a controlled way. In Sec. II, we present a brief overview of Bayesian analysis methods and model setups. The experimental observables are described in Sec. III. Model parameters and calibrations are explained in Sec. IV. The results are presented in Sec. V, after which Sec. VI summarizes our results and findings.

*jasper.parkkila@cern.ch

Published by the American Physical Society under the terms of the Creative Commons Attribution 4.0 International license. Further distribution of this work must maintain attribution to the author(s) and the published article's title, journal citation, and DOI. Funded by SCOAP³.

II. BAYESIAN ANALYSIS

There have been a number of studies that utilized Bayesian methods for heavy ion collisions [20–24]. We employ the recent state-of-the-art development in [7] for our present study. We define a vector of model parameters \mathbf{x} , and a set of experimental data \mathbf{y} that will be compared with model calculations. Bayes's theorem gives the posterior distributions for the model parameters as

$$P(\mathbf{x}|\mathbf{y}) \propto P(\mathbf{y}|\mathbf{x})P(\mathbf{x}). \quad (1)$$

Here $P(\mathbf{y}|\mathbf{x})$ is the likelihood, which quantifies the model agreement with the data. The prior $P(\mathbf{x})$ encapsulates initial knowledge on the parameters.

The model parameters are then extracted from the posterior distributions. We follow the same procedures as [7], where the model is first evaluated at a small $O(10^2)$ number of “design” parameter points. The resulting discrete set of model predictions is then made continuous by the use of a Gaussian process (GP) emulator, which thereby can be used to systematically probe the parameter space with Markov chain Monte Carlo (MCMC) methods.

A. Hydrodynamic model and parameters

The model used in this analysis consists of the T_RENTo model [25] for the initial condition, which is connected with free streaming to a 2 + 1 dimensional causal hydrodynamic model VISH(2 + 1) [26,27]. The evolution continues after particlization via the UrQMD model [28,29]. This hybrid model, denoted T_RENTo + VISH(2 + 1) + UrQMD, has successfully described the previous ALICE measurements [7].

A hydrodynamic modeling relies on the energy and momentum conservation laws of the fluid dynamics. The conservation is expressed in terms of

$$\partial_\mu T^{\mu\nu}(x) = 0, \quad (2)$$

where $T^{\mu\nu}(x)$ is the energy-momentum tensor. In the case of viscous hydrodynamics, the energy-momentum tensor becomes

$$T^{\mu\nu} = \epsilon u^\mu u^\nu - (P + \Pi)\Delta^{\mu\nu} + \pi^{\mu\nu}, \quad (3)$$

where ϵ is the energy density, P is the local pressure given by the equation of state, and $\Delta^{\mu\nu} = g^{\mu\nu} - u^\mu u^\nu$ is a projector onto the transverse four-velocity. The shear and bulk viscosities are encoded into $\pi^{\mu\nu}$ and Π , respectively.

Free parameters of this model include the initial conditions, $\eta/s(T)$ and $\zeta/s(T)$, characterized by a total of 14 model parameters, which together control the prominent features of the model. The parameter set, described in detail in later sections, will enable simultaneous characterization of the initial state and medium response, including any correlations.

Each event consists of a single initial condition given energy density profile and a hydrodynamic simulation followed by multiple samples of the freeze-out hypersurface. The parameter estimation is conducted using 500 parameter design points, sampled evenly from the parameter space using the Latin hypercube scheme [30,31]. At each design point, the model is used to generate around 3×10^5 events with

the corresponding parametrization, with each event surface sampled ten times to produce a total of 3×10^6 events for 0–60% centrality ranges. A large number of events is generated to ensure a better accuracy for high harmonic observables. A GP emulator is then trained to produce predictions for the observables in between the design points, after which the predictions are validated against a validation set. See [7] for details of the emulator. Using the emulator to produce predictions in continuous parameter space, the final posterior distribution is created using MCMC sampling.

B. Calibrating the model parameters

The parameter estimation attempts to calibrate the model parameters for the model to optimally reproduce experimental observables. With Bayesian methods, the optimal parameters are characterized by probability distributions for their true values. As given by Bayes's theorem, the probability for the true parameters \mathbf{x}_* is

$$P(\mathbf{x}_*|X, Y, \mathbf{y}_{\text{exp}}) \propto P(X, Y, \mathbf{y}_{\text{exp}}|\mathbf{x}_*)P(\mathbf{x}_*). \quad (4)$$

The left-hand side is the *posterior*: the probability of \mathbf{x}_* given the design X , computed observables Y , and the experimental data \mathbf{y}_{exp} . On the right-hand side, $P(\mathbf{x}_*)$ is the *prior* probability, encapsulating the initial knowledge of \mathbf{x}_* , and $P(X, Y, \mathbf{y}_{\text{exp}}|\mathbf{x}_*)$ is the likelihood: the probability of observing $(X, Y, \mathbf{y}_{\text{exp}})$ given a proposal \mathbf{x}_* .

The likelihood may be computed using the principal component GP emulators as

$$\begin{aligned} P &= P(X, Y, \mathbf{y}_{\text{exp}}|\mathbf{x}_*) \\ &= P(X, Z, \mathbf{z}_{\text{exp}}|\mathbf{x}_*) \\ &\propto \exp \left\{ -\frac{1}{2}(\mathbf{z}_* - \mathbf{z}_{\text{exp}})^\top \Sigma_z^{-1}(\mathbf{z}_* - \mathbf{z}_{\text{exp}}) \right\}, \end{aligned} \quad (5)$$

where $\mathbf{z}_* = \mathbf{z}_*(\mathbf{x}_*)$ are the principal components predicted by the emulators, \mathbf{z}_{exp} is the principal component transform of the experimental data \mathbf{y}_{exp} , and Σ_z is the covariance (uncertainty) matrix. The covariance matrix encodes all the experimental and model uncertainties [32]. In the principal component space, the covariance matrix can be expressed as

$$\Sigma_z = \Sigma_z^{\text{exp}} + \Sigma_z^{\text{GP}} + (\sigma_m^{\text{sys}})^2 I, \quad (6)$$

where Σ_z^{exp} is the matrix for experimental errors and $\Sigma_z^{\text{GP}} = \text{diag}(\sigma_{z,1}(\mathbf{z}_*)^2, \sigma_{z,2}(\mathbf{z}_*)^2, \dots, \sigma_{z,k}(\mathbf{z}_*)^2)$ is the diagonal GP emulator covariance matrix, representing the model statistical and GP predictive uncertainty. Additionally, σ_m^{sys} is a free parameter ranging from zero to one, with the purpose of including all remaining uncertainties arising from the model imperfections. All model parameters are given a uniform prior. Together with the likelihood (5) and Bayes' theorem (4), the posterior probability can be evaluated at an arbitrary point in the parameter space. To construct the posterior distribution, an MCMC method can be used, which generates random walks through parameter space by accepting or rejecting proposal points based on the posterior probability.

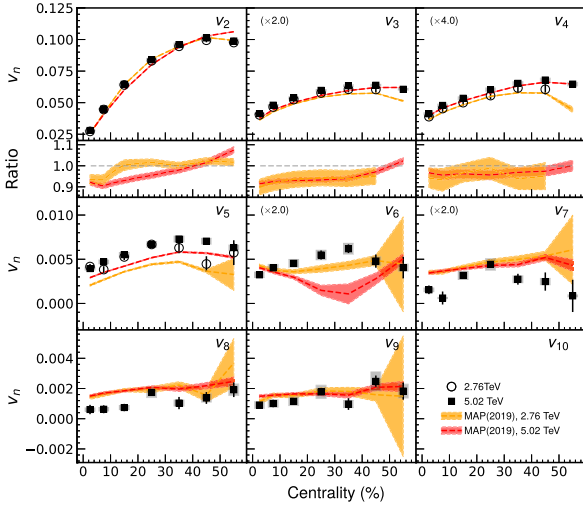


FIG. 1. Model calculations of flow coefficients compared to experimental data at center-of-mass energies of 2.76 and 5.02 TeV. The systematic error for the higher energy data points is shown as a grey band around them. This band is not shown for the lower energy data points since they have combined errors.

III. EXPERIMENTAL OBSERVABLES

In the previous studies, the centrality dependence of identified particle yields dN/dy and mean transverse momenta $\langle p_T \rangle$ for charged pions, kaons, and protons as well as two-particle anisotropic flow coefficients v_n for $n = 2, 3, 4$ were used. The observables are measured by the ALICE Collaboration in Pb-Pb collisions at $\sqrt{s_{NN}} = 2.76$ TeV [2,8,9]. In this work, we mainly focus on the larger statistic higher beam energy collisions at $\sqrt{s_{NN}} = 5.02$ TeV, which give better precision. In addition to the above mentioned observables, we include higher harmonic flow coefficients v_n [5] (up to $n = 9$), the normalized symmetric cumulants NSC(m, n) [6], and the nonlinear flow mode coefficients $\chi_{n,mk}$ [5].

The anisotropic pressure-driven expansion of the QGP, commonly referred to as anisotropic flow, can be characterized by a Fourier decomposition of the azimuthal particle distributions as

$$\frac{dN}{d\phi} \propto 1 + 2 \sum_{n=1}^{\infty} v_n \cos[n(\phi - \psi_n)], \quad (7)$$

where v_n quantifies the magnitude of the n th harmonic flow, and ψ_n its direction. NSC(m, n) quantifies the correlations between event-by-event fluctuations of flow harmonics of different orders, $\text{NSC}(m, n) = (\langle v_m^2 v_n^2 \rangle - \langle v_m^2 \rangle \langle v_n^2 \rangle) / (\langle v_m^2 \rangle \langle v_n^2 \rangle)$ [3,6], and $\chi_{n,mk}$ measures the contribution of lower order harmonic flows to higher order harmonics (i.e., $\chi_{4,22}$ is the nonlinear contribution of v_4 originating from v_2 ; see the details in [5]). These additional observables give better sensitivity to the medium properties and initial conditions, as demonstrated in Refs. [3–6].

As shown in Figs. 1 and 2, a model calculation with the best-fit parametrization given by maximum *a posteriori* (MAP) from the previous Bayesian analysis [7] shows deviations of the measurements for the flow coefficients from

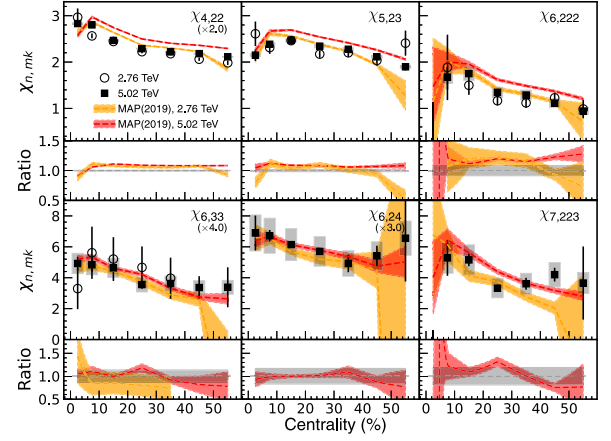


FIG. 2. Model calculations of nonlinear flow mode coefficients compared to experimental data. Most calculations reproduce $\chi_{4,22}$ within the uncertainties of the measurement and calculations. The systematic error for the higher energy data points is shown as a grey band around them. This band is not shown for the lower energy data points since they have combined errors.

$n = 5$ and the nonlinear flow mode coefficients from $\chi_{n,mk}$ ($n = 4$). The black filled and open circles represent the higher ($\sqrt{s_{NN}} = 5.02$ TeV) and lower ($\sqrt{s_{NN}} = 2.76$ TeV) energy data points, respectively, whereas the red and orange bands represent the higher and lower energy model calculations. The v_2 – v_4 values calculated from data were used in model calibration, and, as seen in Fig. 1, the calculations agrees well for v_4 . However, a discrepancy is seen for v_3 with an underestimation of the calculations for the centrality up to $\approx 45\%$ for both energies, and an even larger discrepancy in v_2 for the higher energy calculation, while the lower energy calculation agrees well except for the low centrality of 0–10%. For higher harmonics ($\geq v_5$) the deviation is still visible.

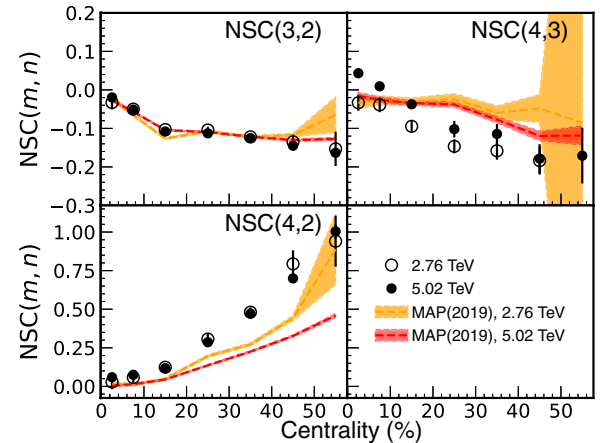


FIG. 3. Model calculations of the normalized symmetric cumulants [NSC(m, n)] compared to experimental data at center-of-mass energies of 2.76 and 5.02 TeV. The systematic error for the higher energy data points is shown as a grey band around them. This band is not shown for the lower energy data points since they have combined errors.

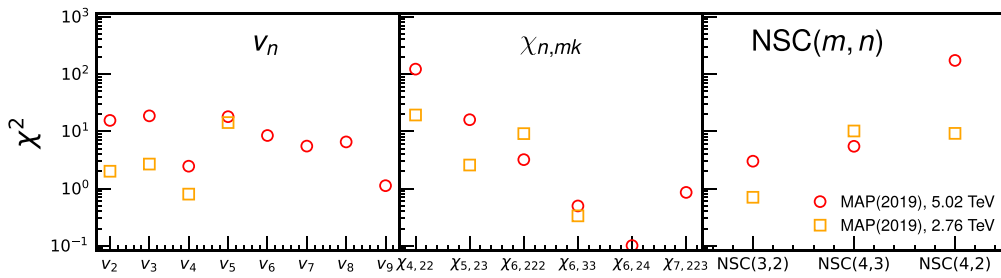


FIG. 4. The χ^2 values calculated between the data and model calculations for both beam energies are shown for v_n , $\chi_{n,mk}$, and $\text{NSC}(m, n)$.

The model calculations for the nonlinear flow mode coefficients in Fig. 2 agree within $\pm 15\%$ for $\chi_{4,22}$ and $+15\%$ for the higher energy model calculation of $\chi_{5,23}$, while the lower energy model calculation goes to -30% in central collisions and even larger than 50% at high centrality ranges. The discrepancies between data and model calculations are significantly larger from $\chi_{6,222}$; however, for $\chi_{6,24}$, most of the higher energy data points agree with the calculations within systematic uncertainties.

Model calculations reproduce the value for $\text{NSC}(3, 2)$ up to the 40–50% centrality class, which is shown in Fig. 3. Both model predictions underestimate the values of $\text{NSC}(4, 2)$ for all centrality classes presented. The model calculations overestimate $\text{NSC}(4, 3)$ for the lower energy data and give similar results for the higher energy. However, the results show clear differences between the two beam energies. The differences get larger toward the central collisions. While it is negative for the lower energy data and the model calculations, the measurement at 5.02 TeV shows the change of the signs in central collisions. Also, the magnitudes are smaller in lower energy collisions, which is attributed to the increasing contribution from the nonlinear hydrodynamic response in v_4 [6].

In order to quantify the agreement of the models with the data, the χ^2 test was performed in the same way as in Eq. (5) in Ref. [4] for the centrality range 5–50%. The results are shown in Fig. 4 for the flow coefficients, non-linear flow mode coefficients, and the normalized symmetric cumulants. A significant difference is observed between the χ^2 values for v_n of higher and lower energies at $n \leq 4$. The χ^2 values for v_5 are larger for both beam energies with similar magnitudes. The higher energy χ^2 value for $\chi_{4,22}$ is significantly larger than the one from the lower energy as shown in Fig. 4. The disagreement is still significant for $\chi_{5,23}$ and $\chi_{6,222}$. For $\text{NSC}(m, n)$, the χ^2 values are larger for higher harmonics at

both beam energies. The χ^2 is especially large for the higher beam energy $\text{NSC}(4, 3)$.

In our calculations of the observables, we used the same methods also used in experimental analysis in Refs. [3–6]. Our centrality classes in this study are chosen to match those used for the experimental data. We define the multiplicity range for each centrality class by simulating events using the MAP parameterization from [7], and sorting the resulting minimum-bias events by charged-particle multiplicity $dN/d\eta$ at midrapidity ($|\eta| < 0.5$). The identified $dN/d\eta$ and $\langle p_T \rangle$ were evaluated by counting and averaging the particle species at midrapidity ($|\eta| < 0.5$). The experimental data are readily corrected and extrapolated to zero p_T [9], and therefore no additional processing is required while preparing the comparison. For the identified $dN/d\eta$, only protons were used in model calibration, as the model did not reproduce the spectra of the other species with any of the parametrizations. Finally, we calculated flow coefficients and other observables for charged particles within the kinematic range of the ALICE detector using the same methods as in the data analyses [5,6]. A summary of all the observables that are included in the Bayesian analysis is given in Table I. The table presents the particle species, kinematic cuts, and centrality classes for each observable.

IV. PARAMETER ESTIMATION USING NEW LHC MEASUREMENTS

The model to be evaluated in this analysis consists of multiple stages, of which a brief overview will be given next. Altogether, the model setup includes the parametric TRENTo initial conditions, free-streaming preequilibrium dynamics, and the VISH(2 + 1) hydrodynamic model for medium evolution. Furthermore, the model performs the hadronization

TABLE I. Experimental data included in Bayesian analysis.

Observable	Particle species	Kinematic cuts	Centrality classes (%)	Ref.
Yields dN/dy	$h^\pm, p\bar{p}$	$ \eta < 0.5$	0–5, 5–10, 10–20, ..., 50–60	[18]
Mean transverse momentum $\langle p_T \rangle$	$\pi^\pm, K^\pm, p\bar{p}$	$ \eta < 0.5$	0–5, 5–10, 10–20, ..., 50–60	[19]
Two-particle flow cumulants $n = 2-8$	h^\pm	$ \eta < 0.8$ $0.2 < p_T < 5.0$ GeV	0–5, 5–10, 10–20, ..., 50–60	[5]
Non-linear flow mode $n = 2-8$	h^\pm	$ \eta < 0.8$ $0.2 < p_T < 5.0$ GeV	0–5, 5–10, 10–20, ..., 50–60	[5]
Symmetric cumulants $n = 2-8$	h^\pm	$ \eta < 0.8$ $0.2 < p_T < 5.0$ GeV	0–5, 5–10, 10–20, ..., 50–60	[6]

TABLE II. Input parameter ranges for the initial condition and hydrodynamic models.

Parameter	Description	Range
Norm	Overall normalization	16.542–25
p	Entropy deposition parameter	0.0042–0.0098
σ_k	Std. dev. of nucleon multiplicity fluctuations	0.5508–1.2852
d_{\min}^3	Minimum volume per nucleon	0.889^3 – 1.524^3
τ_{fs}	Free-streaming time	0.03–1.5
T_c	Temperature of const. $\eta/s(T)$, $T < T_c$	0.135–0.165
$\eta/s(T_c)$	Minimum $\eta/s(T)$	0–0.2
$(\eta/s)_{\text{slope}}$	Slope of $\eta/s(T)$ above T_c	0–4
$(\eta/s)_{\text{crv}}$	Curvature of $\eta/s(T)$ above T_c	–1.3–1
$(\zeta/s)_{\text{peak}}$	Temperature of $\zeta/s(T)$ maximum	0.15–0.2
$(\zeta/s)_{\text{max}}$	Maximum $\zeta/s(T)$	0–0.1
$(\zeta/s)_{\text{width}}$	Width of $\zeta/s(T)$ peak	0–0.1
T_{switch}	Switching/particlization temperature	0.135–0.165

and includes UrQMD hadronic cascade. The model setup used is identical to the one developed and used in [7], except for the number of hypersurface samples taken after evolution. In this work, exactly ten events are sampled from the hypersurface regardless of the cumulative number of particles. The centrality definition is shared for all parametrizations. With close to fixed initial stage parameters, the possible effects of a shared centrality definition should be negligible.

Our main focus will be to investigate the effects of the higher harmonic observables on the temperature dependence of the transport coefficients. The parametrizations of the transport coefficients are [7]

$$(\eta/s)(T) = (\eta/s)(T_c) + (\eta/s)_{\text{slope}}(T - T_c) \left(\frac{T}{T_c} \right)^{(\eta/s)_{\text{crv}}} \quad (8)$$

and

$$(\zeta/s)(T) = \frac{(\zeta/s)_{\text{max}}}{1 + \left(\frac{T - (\zeta/s)_{\text{peak}}}{(\zeta/s)_{\text{width}}} \right)^2} \quad (9)$$

for the ratios of shear viscosity and bulk viscosity over entropy, respectively. Based on previous work, it is known that the lowest value of $\eta/s(T)$ is around the critical temperature T_c , close to the universal minimum $1/(4\pi)$. The temperature dependence of $\eta/s(T)$ is moderate, and increasing with higher values of temperature. Within close proximity of 150 to 500 MeV, the slope of $\eta/s(T)$ is approximately linear. The bulk viscosity over entropy ratio $\zeta/s(T)$ is expected to peak around T_c and to decrease at higher values of temperature.

With this knowledge, we may construct our priors, and assume the initial parameter ranges. The chosen parameter ranges are loosely based on the optimal parameters found in [7]. It was found that in most cases, by taking the optimal parameters in [7] as the center points of the prior range and expanding the range slightly based on a reasonable σ value, those parameters could be further optimized with the additional observables. In this study, we have kept the initial stage parameter ranges narrow around the MAP values found in [7] with the assumption that the additional observables affect mostly the transport coefficients. Very small variation

was allowed to give the parameters space to adjust for minor differences.

The included and varied parameters, of which there are 14 in total, are summarized in Table II. The parametric TRENTo initial conditions comprise an ansatz in terms of five parameters: a normalization factor Norm, entropy deposition parameter p , standard deviation of the nuclear multiplicity fluctuations σ_{fluct} , Gaussian-shaped nucleon width w , and minimum allowed distance between nucleons d_{\min} . The initial conditions are assumed to be already well constrained and presumably not affected by the addition of medium effect

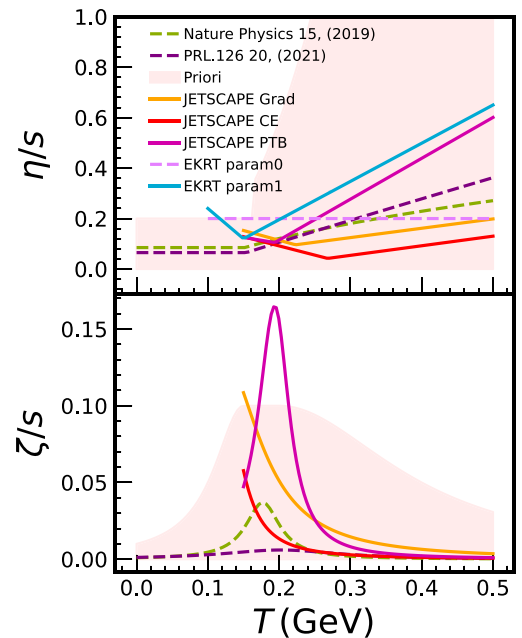


FIG. 5. The specific shear (η/s) and bulk (ζ/s) viscosity ratios as a function of temperature. The region plotted in red visualizes the prior range used in this study. Other curves represent some of the parametrizations found in previous studies: the best-fit $\eta/s(T)$ with EKRT initial conditions [33,34], parametrizations from the JETSCAPE Collaboration with three different particlization distributions [13], and a recent parametrization found in [7].

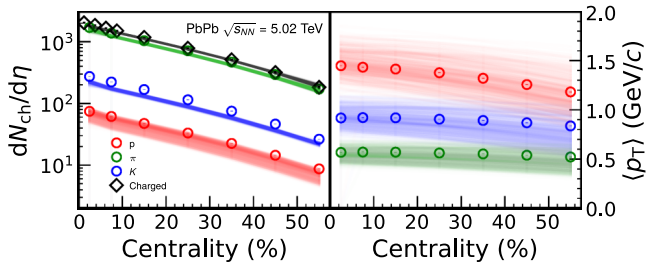


FIG. 6. Charged and identified particle multiplicity and mean transverse momenta $\langle p_T \rangle$ as given by the design parametrizations.

sensitive observables. The range for free-streaming time τ_{fs} characterizing the allotted time for preequilibrium dynamics was kept relatively large.

The rest of the parameters are the components of the transport coefficient parametrizations, and the switching temperature T_{switch} describing the temperature at which the hadronization begins to take place. The initial ranges given for these parameters are more generous, although large deviations in the final parameters compared to the previous study are not expected. The prior range for the transport coefficients is plotted in Fig. 5 among some parametrizations from other related studies [7,13,33,34]. The parametrizations are valid only up to the corresponding limits of the model: 100 MeV in the case of EKRT and 150 MeV for JETSCAPE. We note that the parametrizations EKRT+param0 and EKRT+param1 were not obtained through Bayesian analysis and we do not consider the slightly higher η/s at around $T = 100$ MeV in our prior. Furthermore, we do not consider the large ζ/s reported with the PTB particlization by the JETSCAPE Collaboration [13]. Nevertheless, the ζ/s obtained using the Grad or CE particlization distributions are within our prior, considering the temperature limit $T_{switch} > 150$ MeV.

The model is calibrated to the latest Pb-Pb collision data at $\sqrt{s_{NN}} = 5.02$ TeV from the ALICE Collaboration [5,6,18,19]. Figures 6–9 show the calculations of each observable using the design parametrizations obtained from the prior

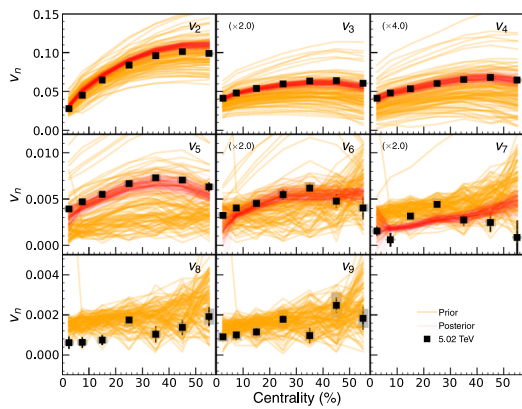


FIG. 7. Flow coefficients v_n as given by the design parametrizations are presented in yellow curves. All harmonics are simultaneously covered by the design parametrizations. The red curves represent a number of curves sampled from the posterior distribution, and are as given by the emulator.

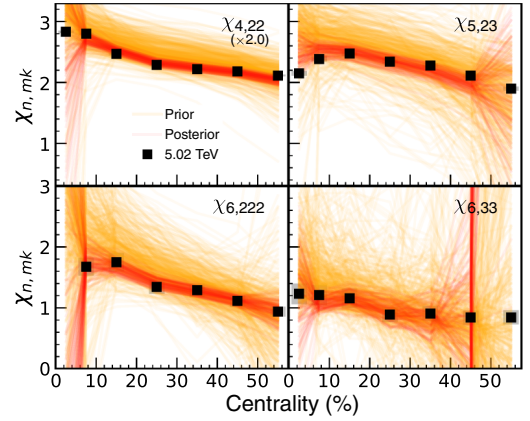


FIG. 8. Design parametrizations for nonlinear flow mode coefficients $\chi_{n,mk}$ (in yellow) and a number of posterior sample curves as given by the emulator (in red).

distribution. The yellow curves represent the calculations corresponding to each design point parametrization, which are used in training the GP emulator, whereas the red curves represent emulator predictions corresponding to random points sampled from the posterior distribution.

V. RESULTS

Figure 10 highlights the posterior and marginal distributions for select components of the transport parameters. The primary components, η/s slope, $\eta/s(T_c)$, $(\zeta/s)_{max}$ in the transport parametrizations, are well constrained. The initial condition parameters are well constrained within the narrow prior range.

Figure 11 presents the estimated temperature dependence of $\eta/s(T)$ and $\zeta/s(T)$ according to the parametrizations from Eqs. (8) and (9), respectively. The shaded region around the curves represents the 90%-credibility region. This region reflects all uncertainties coming from the finite width of the posterior distribution, experimental statistical and systematic uncertainties, statistical uncertainties in model calculations, predictive uncertainty from the GP emulator, and systematic

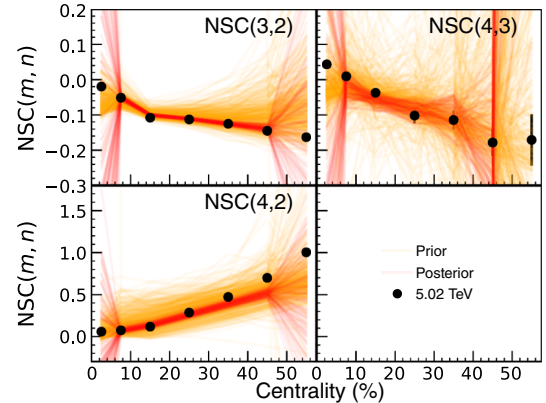


FIG. 9. Design parametrizations for normalized symmetric cumulants (in yellow) and a number of posterior sample curves as given by the emulator (in red).

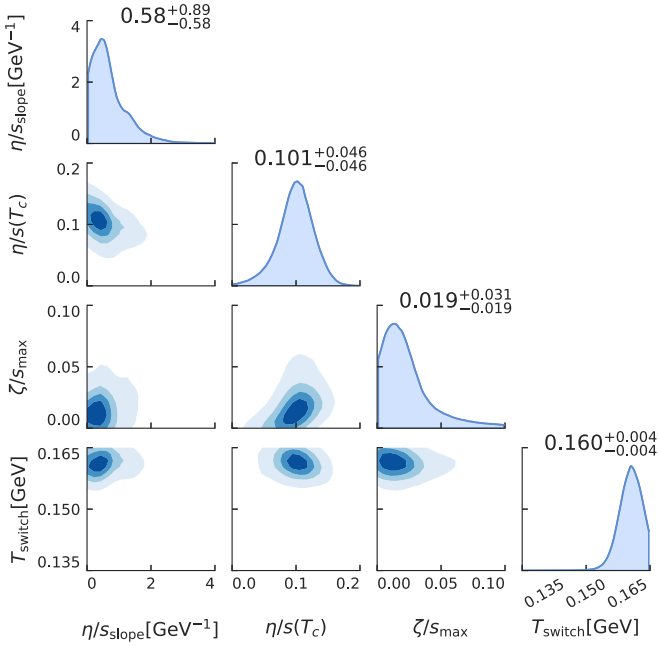


FIG. 10. Dimensionally reduced posterior probability for select transport parameters. The diagonal histograms represent the marginal distributions for the corresponding parameters. The accompanying numbers are the median values, as well as the limits of the 90%-credibility range.

model bias. With high probability, the true curve is located within this region.

Table III presents the best-fit MAP parameters from our analysis. We list here the important findings:

- (1) While the temperature dependence of $\eta/s(T)$ is similar to what was obtained in [7], the curvature of $\eta/s(T)$ is slightly stronger, resulting in lower values at higher temperatures above T_c .
- (2) A notable change is the lower $(\zeta/s(T))_{\max}$ in order to reproduce the additional observables. The obtained $\zeta/s(T)$ is smaller than those found in the previous Bayesian analyses [7,13] where the additional observables were not included. A similar value was reported in Ref. [11]. On average this represents a value an order of magnitude lower compared to the lattice QCD calculation [35] and the parametrizations used

TABLE III. The best-fit MAP parameters.

Initial conditions		Transport	
Parameter	MAP value	Parameter	MAP value
Norm	21.06	$\eta/s(T_c)$	0.104
p	0.0077	$(\eta/s)_{\text{slope}}$	0.425
σ_k	0.881	$(\eta/s)_{\text{crv}}$	0.738
d_{\min}^3	0.975	$(\zeta/s)_{\text{peak}}$	0.170
τ_{fs}	0.901	$(\zeta/s)_{\text{max}}$	0.010
T_c	0.147	$(\zeta/s)_{\text{width}}$	0.057
T_{switch}	0.160		

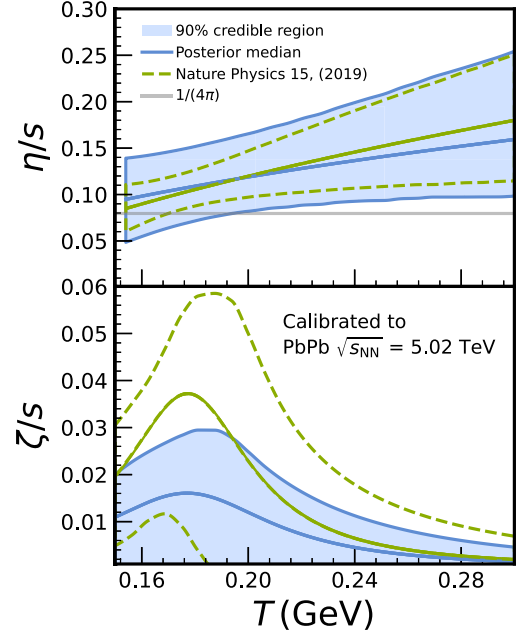


FIG. 11. The 90%-credibility region for the shear (top) and bulk (bottom) viscosity to entropy ratio is given as a blue band. The blue line represents the median of the credible range. The MAP parametrization from [7] as well as the corresponding 90%-credibility range are plotted as green dashed curves.

in [36,37], where the parametrizations were tuned to simultaneously reproduce lower harmonic v_n as well as the charged particle multiplicity and the low- p_T region of the charged hadron spectra.

- (3) The switching temperature on the other hand is higher than the one found in the aforementioned studies, where on average T_{switch} is located around ≈ 0.150 GeV. As discussed in [4,5,17], the additional observables, the nonlinear response modes and the correlations between flow harmonics are sensitive to viscous corrections to the equilibrium distribution at hadronic freeze-out [38–41] and seem to prefer the higher switching temperature.

We performed high-statistics hydrodynamic calculations with the new parametrization. Figures 12 and 13 present the calculations for the flow coefficients v_n and nonlinear flow mode coefficients, respectively. The v_n is reproduced within 10% agreement for $n = 2$ up to $n = 4$. For the fifth harmonic, the calculations underestimate the data. The new parametrization estimates the data better in central and peripheral collisions but deviates significantly in the peripheral region. The magnitude of the successive harmonics from v_6 is not quite captured by the calculations within the statistical uncertainty. Furthermore, with our new parametrization, the predictions for the nonlinear flow mode coefficients have also improved compared to the parametrization from [7], as indicated by the ratio plots. In this case, the lower harmonic nonlinear flow mode coefficients are no longer overestimated, and the magnitude and centrality dependence are correctly captured. We note that the nonlinear flow mode coefficients

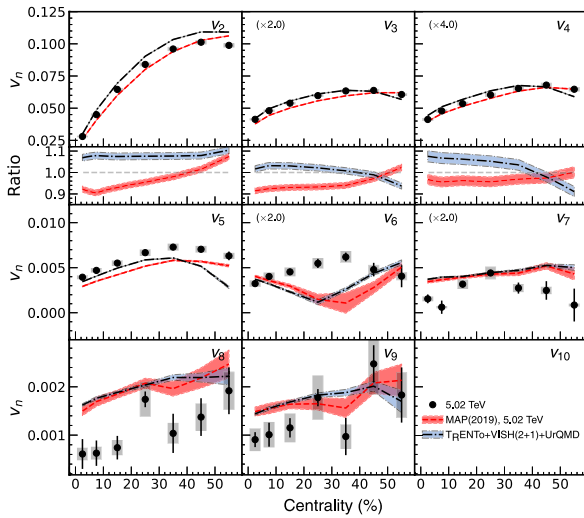


FIG. 12. Flow coefficients from two hydrodynamical calculations are compared to the experimental data [5] at center-of-mass energy 5.02 TeV. The blue band is calculated with the MAP parametrization from this work, whereas the red band uses the parametrization from [7].

have not been included in the model calibration in [7], whereas, coefficients up to $\chi_{6,33}$ and $\chi_{6,222}$ were used in this analysis. Figure 14 presents the calculation of the normalized SC using our obtained parametrization. The performances of the new parametrization and the one from [7] are comparable for NSC(3, 2). For NSC(4, 2) and NSC(4, 3), the centrality dependence is better described by the new parametrization. However, both parametrizations are unable to reproduce the strong centrality dependence of NSC(4, 2), underestimating the most data points in the most peripheral collisions. The multiplicity and the mean- p_T calculations are compared to the results from [7] in Fig. 15. Our parametrization improves the

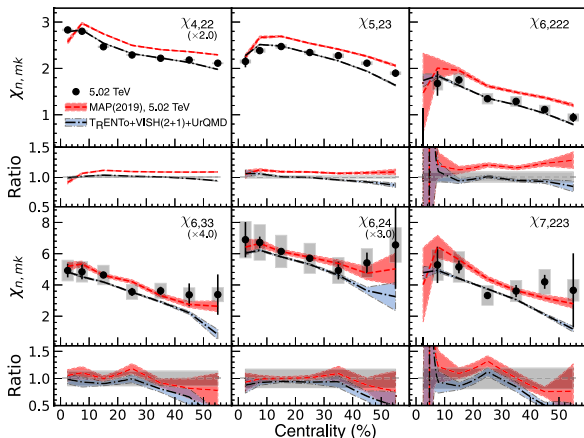


FIG. 13. Nonlinear flow mode coefficients from two hydrodynamical calculations are compared to the experimental data [5] at center-of-mass energy 5.02 TeV. The blue band is calculated with the MAP parametrization from this work, whereas the red band uses the parametrization from [7].

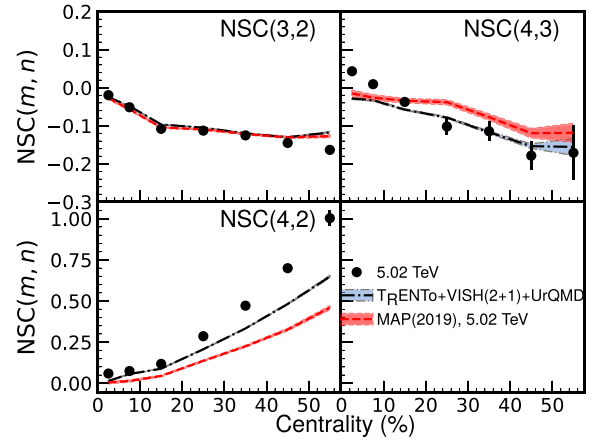


FIG. 14. Normalized symmetric cumulants [NSC(m, n)] from two hydrodynamical calculations are compared to the experimental data [6] at center-of-mass energy 5.02 TeV. The blue band is calculated with the MAP parametrization from this work, whereas the red band uses the parametrization from [7].

estimate of the proton multiplicity and gives the same charged particle multiplicity for 5.02 TeV collisions, while the pion and kaon multiplicities are not in good agreement with the experimental data, as similarly found in [7] for 2.76 TeV calculations. Interestingly, the parametrizations from [7] mainly utilizing 2.76 TeV data give better agreement with pions and kaons in 5.02 TeV collisions than our results while overestimating the proton yields approximately 10%. Agreement of the calculated mean p_T with the experimental data is good for all particle species, as well as with the results from [7] for both beam energies. Refining this analysis by including low beam energy data in the future will help us to understand the beam energy dependence on various observables.

Finally, Fig. 16 shows the χ^2 values with the best-fit MAP parameters extracted from this study for each observable. They are compared to the ones from [7]. The χ^2 values for our new calculation only seem to improve v_3 and v_5 for the v_n observable. For the nonlinear flow mode coefficients the χ^2 values are improved up to $\chi_{6,222}$ with our new parametrization, while the χ^2 values for the higher harmonics are worse than in [7]. For NSC, the χ^2 from the new calculation is worse for

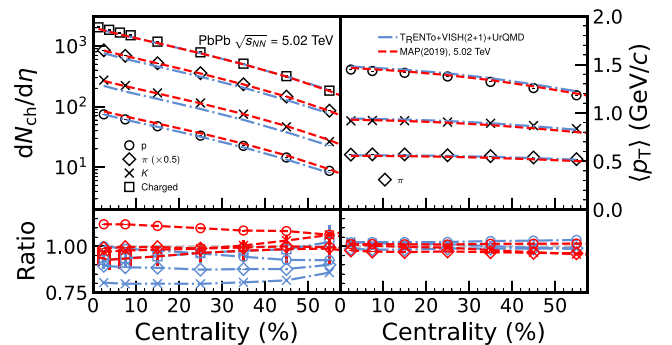


FIG. 15. Charged and identified particle multiplicity and mean p_T from two hydrodynamical calculations are compared to the experimental data at center-of-mass energy 5.02 TeV.

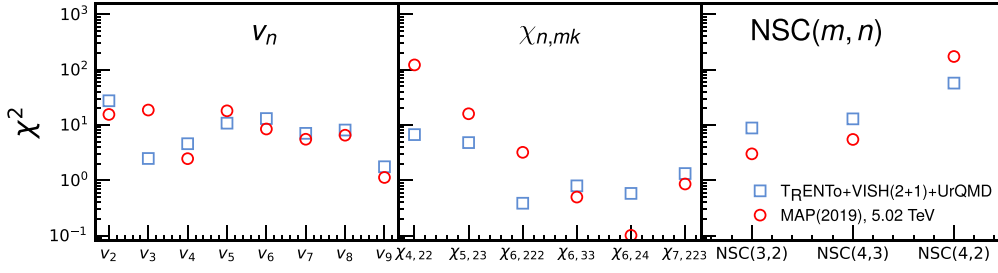


FIG. 16. The χ^2 values with the best-fit MAP parameters extracted from this study are compared to the ones from [7].

NSC(3, 2) and NSC(4, 3), but is improved for NSC(4, 2). We note that the larger statistical error in the calculations using the parametrization of Ref. [7] lowers the corresponding χ^2 values, slightly affecting the direct comparison between the two parametrizations. The sign change of NSC(4, 3) in most central collisions is not reproduced by the models while the beam-energy-dependent magnitudes are better described with new parametrizations. We leave those differences for future research work where the present results should be refined by including experimental data from the lower energy beam data. As a final study in this analysis, we conduct a simple sensitivity analysis of the included observables to the model transport parameters. The sensitivity of each observable is evaluated using the GP emulator by observing the relative difference in the magnitude of the observable between two parameter points in the parameter space. The difference can be formulated as

$$\Delta = \frac{|\hat{O}(\mathbf{x}') - \hat{O}(\mathbf{x})|}{\hat{O}(\mathbf{x})}, \quad (10)$$

where $\hat{O}(\mathbf{x})$ and $\hat{O}(\mathbf{x}')$ represent the values of an observable at parameter points \mathbf{x} and \mathbf{x}' , respectively [13].

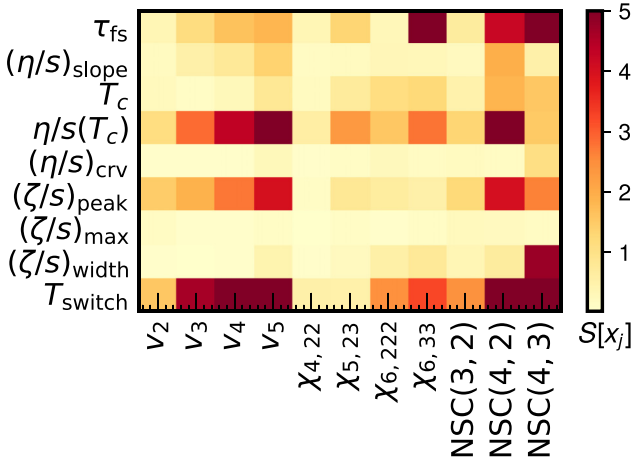


FIG. 17. Sensitivity of the observables to the model parameters visualized as a color map. The sensitivity index is averaged over four centrality classes, from 5% to 40%. Light yellow shades represent a very limited sensitivity or no sensitivity, whereas orange and darker red colors represent moderate or strong sensitivities to the corresponding model parameter, respectively.

In this study, we choose a reference parameter point \mathbf{x} to be the one representing the MAP values obtained in this analysis (see Table III). To probe the sensitivity of a parameter j , another point is defined as $\mathbf{x}' = (x_1, x_2, \dots, (1 + \delta)x_j, \dots, x_p)$, where δ is a small value representing a percentile change in the parameter space. We have used a value $\delta = 0.1$, although larger values were observed to yield similar results.

We then calculate a final sensitivity index for each observable and parameter pair in various centrality classes as

$$S[x_j] = \Delta/\delta. \quad (11)$$

Figure 17 presents the evaluated sensitivity for each observable against the transport parameters. The sensitivity was evaluated over four centrality classes from 5% to 40% and averaged for the final plot. We did not observe large differences in the sensitivity between the individual centrality classes.

For v_n , we can verify a known fact that the sensitivity of the flow coefficients is generally very limited to the temperature dependence of $\eta/s(T)$ [33], although, as expected, the sensitivity to the average $\langle \eta/s \rangle$, in this case, represented by $\eta/s(T_c)$, is very strong, and increasing at higher harmonics. The sensitivity of the v_n to the $(\zeta/s)_{\text{peak}}$ is visible, and also in this case the higher harmonics provide stronger constraints. Based on previous studies, the nonlinear flow mode coefficients $\chi_{n,mk}$ are known to be sensitive to $\eta/s(T)$ at the freeze-out temperature. This is reflected by the observed sensitivity to $\eta/s(T_c)$ as well as T_c . By far, the normalized symmetric

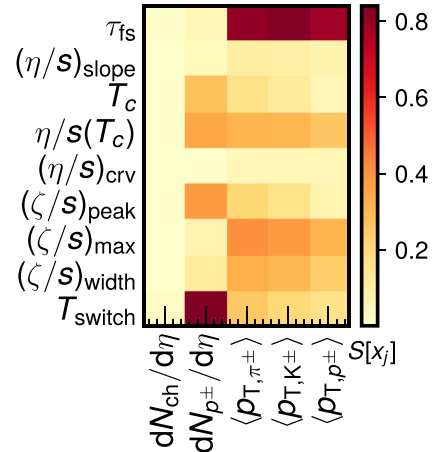


FIG. 18. Sensitivity of the mean multiplicity yields and mean transverse momenta $\langle p_T \rangle$ to the model parameters.

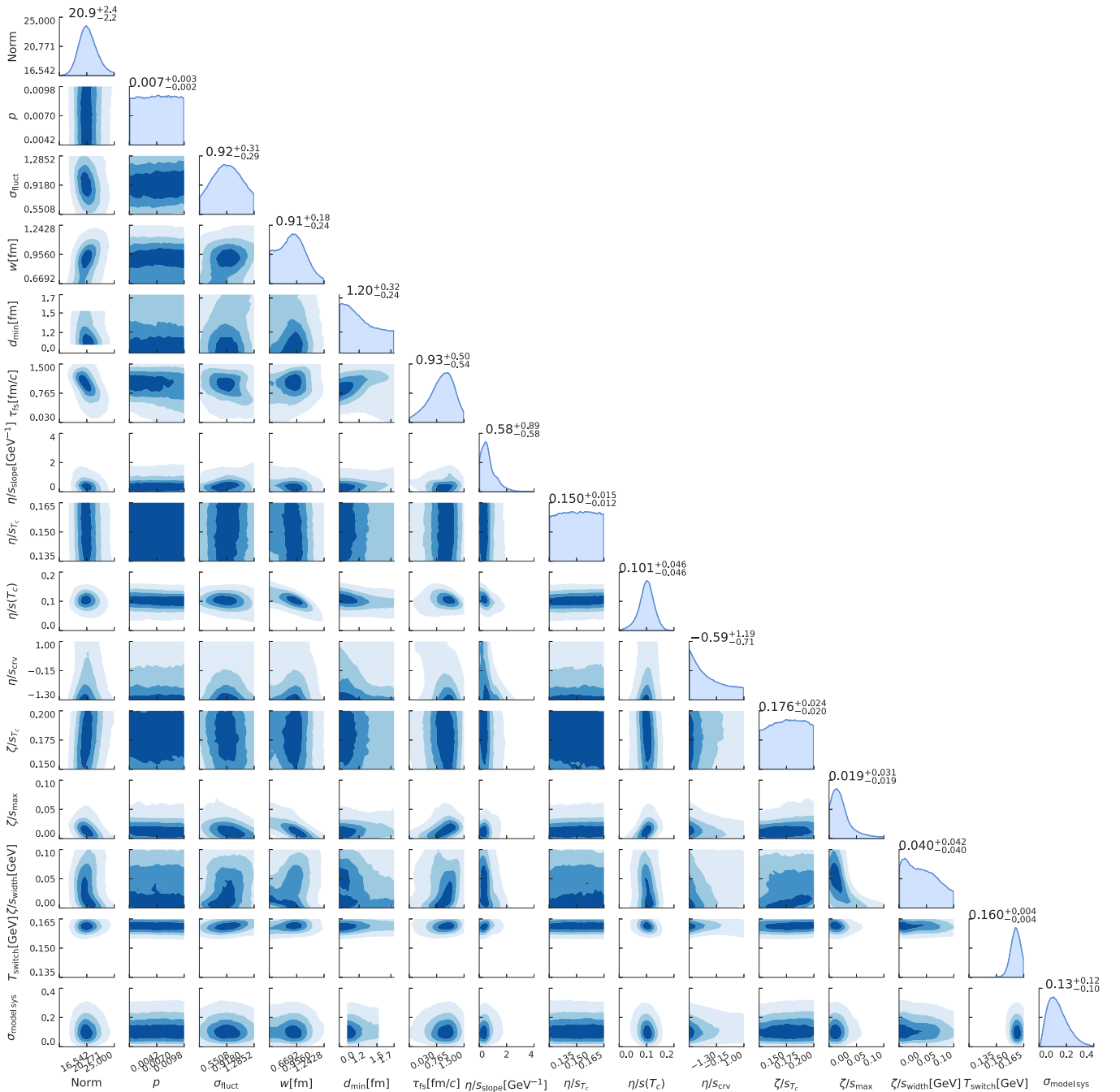


FIG. 19. Dimensionally reduced posterior distribution for all parameters in the analysis. The diagonally placed histograms represent the marginal distributions for each corresponding parameter. For each marginal distribution, a number and a range is given, denoting the median and limits of the 90%-credibility region, respectively.

cumulants provide the strongest constraints to the temperature dependence of $\eta/s(T)$. This is confirmed by higher sensitivity for the other components of $\eta/s(T)$, and not only $\eta/s(T_c)$, which is also higher.

Two other parameters have also been included in this study: the free-streaming time scale τ_{fs} and the switching temperature T_{switch} . On average, the observables are reported to be generally weakly sensitive to τ_{fs} , apart from the symmetric cumulants and $\chi_{6,33}$. Furthermore, most of the observables, such as v_n , $\chi_{6,mk}$ and the NSC(m, n), are seen to be highly

sensitive to the switching temperature T_{switch} . In both cases, the results reported here regarding τ_{fs} and T_{switch} are not compatible with what has been observed in [13].

Figure 18 presents the sensitivity of the multiplicity and the $\langle p_T \rangle$ to the model parametrizations. Most prominently, the switching temperature affects the proton multiplicity. Furthermore, we observe a comparatively large sensitivity of $\langle p_T \rangle$ to the free-streaming timescale τ_{fs} . In the case of the transport parameters, the effect on the observables is relatively small. It is observed that $\langle p_T \rangle$ acts as a subtle

constraint to the parameters describing the specific bulk viscosity. The posterior distribution for all parameters is shown in Fig. 19.

VI. DISCUSSIONS

In summary, we performed a Bayesian analysis with the recently available data from ALICE Collaboration [5,6,18,19] as an extension of the work [7]. We found that the temperature dependence of $\eta/s(T)$ is similar to what was obtained in [7] and that the curvature of $\eta/s(T)$ above T_c is slightly lower at higher temperatures, showing weak temperature dependence of η/s . Notable changes include the lower $(\zeta/s(T))_{\max}$ and the higher switching temperature T_{switch} to reproduce additional observables such as symmetric cumulants and nonlinear flow coefficients. However, the improved statistical uncertainties on both the experimental data and hydrodynamic calculations do not help to reduce the final credibility ranges. It is also noticeable that v_5 is still underestimated as observed in [7]. It is worthwhile to mention that the differences for v_2 , v_3 and NSC(4, 2) still remain about 5–10% for 5.02 TeV. The sign change of NSC(4, 3) in most central collisions is not reproduced by the models while the beam-energy-dependent magnitudes are better described with new parametrizations. We leave those differences for future research work in which the present results should be refined by including the lower energy beam data. The parameter sensitivity analysis for the observables conducted in this study

indicates that observables such as the symmetric cumulants and nonlinear flow modes provide a strong constraining power which, however, is still underutilized in [7] as well as the other Bayesian analyses [10,11,13]. In our study, we confirm that the flow coefficients alongside the symmetric cumulants and nonlinear flow mode can provide some of the strongest constraints for the temperature dependence of $\eta/s(T)$ and T_{switch} . Improving aspects of the collision model, for example by replacing the initial state model with others like EKRT [33,34], IP-Glasma [42], and AMPT [43,44], with incorporation of nucleon substructure [45] in the initial conditions through an improved dynamical collision model before the hydrodynamic takes place [46,47], might help to improve the understanding of the uncertainties of the extracted QGP properties and/or the model building blocks.

ACKNOWLEDGMENTS

We would like to thank Harri Niemi, Kari J. Eskola and Sami Räsänen for fruitful discussions. We thank Jonah E. Bernhard, J. Scott Moreland, and Steffen A. Bass for the use of their viscous relativistic hydrodynamics softwares and their valuable comments on various processes of this work. We acknowledge Victor Gonzalez for his crosscheck for various technical parts of the event generation. We acknowledge CSC-IT Center for Science in Espoo, Finland, for the allocation of the computational resources. This research was completed using ≈ 24 million CPU hours provided by CSC.

-
- [1] P. K. Kovtun, D. T. Son, and A. O. Starinets, Viscosity in Strongly Interacting Quantum Field Theories from Black Hole Physics, *Phys. Rev. Lett.* **94**, 111601 (2005).
 - [2] K. Aamodt *et al.* (ALICE Collaboration), Higher Harmonic Anisotropic Flow Measurements of Charged Particles in Pb-Pb collisions at $\sqrt{s_{NN}} = 2.76$ TeV, *Phys. Rev. Lett.* **107**, 032301 (2011).
 - [3] J. Adam *et al.* (ALICE Collaboration), Correlated Event-by-Event Fluctuations of Flow Harmonics in Pb-Pb Collisions at $\sqrt{s_{NN}} = 2.76$ TeV, *Phys. Rev. Lett.* **117**, 182301 (2016).
 - [4] S. Acharya *et al.* (ALICE Collaboration), Systematic studies of correlations between different order flow harmonics in Pb-Pb collisions at $\sqrt{s_{NN}} = 2.76$ TeV, *Phys. Rev. C* **97**, 024906 (2018).
 - [5] S. Acharya *et al.* (ALICE Collaboration), Higher harmonic non-linear flow modes of charged hadrons in Pb-Pb collisions at $\sqrt{s_{NN}} = 5.02$ TeV, *J. High Energy Phys.* **05** (2020) 085.
 - [6] S. Acharya *et al.* (ALICE Collaboration), Measurements of mixed harmonic cumulants in Pb-Pb collisions at $\sqrt{s_{NN}} = 5.02$ TeV, *Phys. Lett. B* **818**, 136354 (2021).
 - [7] J. E. Bernhard, J. S. Moreland, and S. A. Bass, Bayesian estimation of the specific shear and bulk viscosity of quark-gluon plasma, *Nat. Phys.* **15**, 1113 (2019).
 - [8] K. Aamodt *et al.* (ALICE Collaboration), Centrality Dependence of the Charged-Particle Multiplicity Density at Midrapidity in Pb-Pb Collisions at $\sqrt{s_{NN}} = 2.76$ TeV, *Phys. Rev. Lett.* **106**, 032301 (2011).
 - [9] B. Abelev *et al.* (ALICE Collaboration), Centrality dependence of π , K , p production in Pb-Pb collisions at $\sqrt{s_{NN}} = 2.76$ TeV, *Phys. Rev. C* **88**, 044910 (2013).
 - [10] J. Auvinen, K. J. Eskola, P. Huovinen, H. Niemi, R. Paatelainen, and P. Petreczky, Temperature dependence of η/s of strongly interacting matter: Effects of the equation of state and the parametric form of $(\eta/s)(T)$, *Phys. Rev. C* **102**, 044911 (2020).
 - [11] G. Nijs, W. van der Schee, U. Gürsoy, and R. Snellings, Transverse Momentum Differential Global Analysis of Heavy-Ion Collisions, *Phys. Rev. Lett.* **126**, 202301 (2021).
 - [12] G. Nijs, W. van der Schee, U. Gürsoy, and R. Snellings, Bayesian analysis of heavy ion collisions with the heavy ion computational framework TRAJEUM, *Phys. Rev. C* **103**, 054909 (2021).
 - [13] D. Everett *et al.* (JETSCAPE Collaboration), Multisystem Bayesian constraints on the transport coefficients of QCD matter, *Phys. Rev. C* **103**, 054904 (2021).
 - [14] S. Ryu, J.-F. Paquet, C. Shen, G. Denicol, B. Schenke, S. Jeon, and C. Gale, Effects of bulk viscosity and hadronic rescattering in heavy ion collisions at energies available at the BNL Relativistic Heavy Ion Collider and at the CERN Large Hadron Collider, *Phys. Rev. C* **97**, 034910 (2018).
 - [15] G. S. Denicol, T. Kodama, T. Koide, and P. Mota, Effect of bulk viscosity on elliptic flow near QCD phase transition, *Phys. Rev. C* **80**, 064901 (2009).
 - [16] S. Acharya *et al.* (ALICE Collaboration), Investigations of Anisotropic Flow Using Multiparticle Azimuthal Correlations in pp , p -Pb, Xe-Xe, and Pb-Pb Collisions at the LHC, *Phys. Rev. Lett.* **123**, 142301 (2019).

- [17] S. Acharya *et al.* (ALICE Collaboration), Linear and non-linear flow modes in Pb-Pb collisions at $\sqrt{s_{NN}} = 2.76$ TeV, *Phys. Lett. B* **773**, 68 (2017).
- [18] J. Adam *et al.* (ALICE Collaboration), Centrality dependence of the pseudorapidity density distribution for charged particles in Pb-Pb collisions at $\sqrt{s_{NN}} = 5.02$ TeV, *Phys. Lett. B* **772**, 567 (2017).
- [19] S. Acharya *et al.* (ALICE Collaboration), Production of charged pions, kaons, and (anti-)protons in Pb-Pb and inelastic pp collisions at $\sqrt{s_{NN}} = 5.02$ TeV, *Phys. Rev. C* **101**, 044907 (2020).
- [20] H. Petersen, C. Coleman-Smith, S. A. Bass, and R. Wolpert, Constraining the initial state granularity with bulk observables in Au+Au collisions at $\sqrt{s_{NN}} = 200$ GeV, *J. Phys. G* **38**, 045102 (2011).
- [21] J. Novak, K. Novak, S. Pratt, J. Vredevoogd, C. E. Coleman-Smith, and R. L. Wolpert, Determining fundamental properties of matter created in ultrarelativistic heavy-ion collisions, *Phys. Rev. C* **89**, 034917 (2014).
- [22] S. Pratt, E. Sangaline, P. Sorensen, and H. Wang, Constraining the Equation of State of Superhadronic Matter from Heavy-Ion Collisions, *Phys. Rev. Lett.* **114**, 202301 (2015).
- [23] E. Sangaline and S. Pratt, Toward a deeper understanding of how experiments constrain the underlying physics of heavy-ion collisions, *Phys. Rev. C* **93**, 024908 (2016).
- [24] U. Heinz and J. Liu, Pre-equilibrium dynamics and heavy-ion observables, *Nucl. Phys. A* **956**, 549 (2016).
- [25] J. S. Moreland, J. E. Bernhard, and S. A. Bass, Alternative ansatz to wounded nucleon and binary collision scaling in high-energy nuclear collisions, *Phys. Rev. C* **92**, 011901(R) (2015).
- [26] C. Shen, Z. Qiu, H. Song, J. Bernhard, S. Bass, and U. Heinz, The iEBE-VISHNU code package for relativistic heavy-ion collisions, *Comput. Phys. Commun.* **199**, 61 (2016).
- [27] H. Song and U. W. Heinz, Causal viscous hydrodynamics in 2+1 dimensions for relativistic heavy-ion collisions, *Phys. Rev. C* **77**, 064901 (2008).
- [28] S. A. Bass *et al.*, Microscopic models for ultrarelativistic heavy ion collisions, *Prog. Part. Nucl. Phys.* **41**, 255 (1998).
- [29] M. Bleicher *et al.*, Relativistic hadron hadron collisions in the ultrarelativistic quantum molecular dynamics model, *J. Phys. G* **25**, 1859 (1999).
- [30] B. Tang, Orthogonal array-based latin hypercubes, *J. Am. Stat. Assoc.* **88**, 1392 (1993).
- [31] M. D. Morris and T. J. Mitchell, Exploratory designs for computational experiments, *J. Stat. Plann. Inference* **43**, 381 (1995).
- [32] J. E. Bernhard, Bayesian parameter estimation for relativistic heavy-ion collisions, [arXiv:1804.06469](https://arxiv.org/abs/1804.06469).
- [33] H. Niemi, K. J. Eskola, and R. Paatelainen, Event-by-event fluctuations in a perturbative QCD+saturation+hydrodynamics model: Determining QCD matter shear viscosity in ultrarelativistic heavy-ion collisions, *Phys. Rev. C* **93**, 024907 (2016).
- [34] H. Niemi, K. J. Eskola, R. Paatelainen, and K. Tuominen, Predictions for 5.023 TeV Pb+Pb collisions at the CERN Large Hadron Collider, *Phys. Rev. C* **93**, 014912 (2016).
- [35] A. Nakamura and S. Sakai, Transport Coefficients of Gluon Plasma, *Phys. Rev. Lett.* **94**, 072305 (2005).
- [36] S. McDonald, C. Shen, F. Fillion-Gourdeau, S. Jeon, and C. Gale, Hydrodynamic predictions for Pb+Pb collisions at 5.02 TeV, *Phys. Rev. C* **95**, 064913 (2017).
- [37] W. Zhao, H.-J. Xu, and H. Song, Collective flow in 2.76 and 5.02 A TeV Pb+Pb collisions, *Eur. Phys. J. C* **77**, 645 (2017).
- [38] M. Luzum and J.-Y. Ollitrault, Constraining the viscous freeze-out distribution function with data obtained at the BNL Relativistic Heavy Ion Collider (RHIC), *Phys. Rev. C* **82**, 014906 (2010).
- [39] M. Luzum, C. Gombeaud, and J.-Y. Ollitrault, v_4 in ideal and viscous hydrodynamics simulations of nuclear collisions at the BNL Relativistic Heavy Ion Collider (RHIC) and the CERN Large Hadron Collider (LHC), *Phys. Rev. C* **81**, 054910 (2010).
- [40] D. Teaney and L. Yan, Nonlinearities in the harmonic spectrum of heavy ion collisions with ideal and viscous hydrodynamics, *Phys. Rev. C* **86**, 044908 (2012).
- [41] L. Yan and J.-Y. Ollitrault, v_4, v_5, v_6, v_7 : nonlinear hydrodynamic response versus LHC data, *Phys. Lett. B* **744**, 82 (2015).
- [42] B. Schenke, P. Tribedy, and R. Venugopalan, Fluctuating Glasma Initial Conditions and Flow in Heavy Ion Collisions, *Phys. Rev. Lett.* **108**, 252301 (2012).
- [43] R. S. Bhalerao, A. Jaiswal, and S. Pal, Collective flow in event-by-event partonic transport plus hydrodynamics hybrid approach, *Phys. Rev. C* **92**, 014903 (2015).
- [44] L. Pang, Q. Wang, and X.-N. Wang, Effects of initial flow velocity fluctuation in event-by-event (3+1)D hydrodynamics, *Phys. Rev. C* **86**, 024911 (2012).
- [45] H. Mäntysaari, B. Schenke, C. Shen, and P. Tribedy, Imprints of fluctuating proton shapes on flow in proton-lead collisions at the LHC, *Phys. Lett. B* **772**, 681 (2017).
- [46] W. van der Schee, P. Romatschke, and S. Pratt, Fully Dynamical Simulation of Central Nuclear Collisions, *Phys. Rev. Lett.* **111**, 222302 (2013).
- [47] P. Romatschke and U. Romatschke, *Relativistic Fluid Dynamics In and Out of Equilibrium*, Cambridge Monographs on Mathematical Physics (Cambridge University Press, Cambridge, 2019).

PII

**NEW CONSTRAINTS FOR QCD MATTER FROM IMPROVED
BAYESIAN PARAMETER ESTIMATION IN HEAVY-ION
COLLISIONS AT LHC**

by

Parkkila, J.E. & Onnerstad, A. & Taghavi, S.F & Mordasini, C. & Bilandzic, A. &
Virta, M. & Kim, D.J.

Phys. Lett. B , 835 (2022).



New constraints for QCD matter from improved Bayesian parameter estimation in heavy-ion collisions at LHC



J.E. Parkkila^{a,b,c}, A. Onnerstad^{a,b}, S.F. Taghavi^{d,*}, C. Mordasini^{a,d}, A. Bilandzic^d,
M. Virta^{a,b}, D.J. Kim^{a,b,*}

^a University of Jyväskylä, Department of Physics, P.O. Box 35, FI-40014 University of Jyväskylä, Finland

^b Helsinki Institute of Physics, P.O.Box 64, FI-00014 University of Helsinki, Finland

^c CERN, Experimental Physics Department, Geneva, Switzerland

^d Physik Department, Technische Universität München, Munich, Germany

ARTICLE INFO

Article history:

Received 4 March 2022

Received in revised form 15 September 2022

Accepted 3 October 2022

Available online 6 October 2022

Editor: J.-P. Blaizot

ABSTRACT

The transport properties of quark-gluon plasma created in relativistic heavy-ion collisions are quantified by an improved global Bayesian analysis using the CERN Large Hadron Collider Pb–Pb data at $\sqrt{s_{NN}} = 2.76$ and 5.02 TeV. The results show that the uncertainty of the extracted transport coefficients is significantly reduced by including new sophisticated collective flow observables from two collision energies for the first time. This work reveals the stronger temperature dependence of specific shear viscosity, a lower value of specific bulk viscosity, and a higher hadronization switching temperature than in the previous studies. The sensitivity analysis confirms that the precision measurements of higher-order harmonic flow and their correlations are crucial in extracting accurate values of the transport properties.

© 2022 The Author(s). Published by Elsevier B.V. This is an open access article under the CC BY license (<http://creativecommons.org/licenses/by/4.0/>). Funded by SCOAP³.

1. Introduction

The experiments utilizing ultra-relativistic heavy-ion collisions (HIC) play an important role in understanding many-body Quantum Chromodynamics (QCD). The high center-of-mass energy of heavy-ion collisions at the Relativistic Heavy Ion Collider (RHIC) and Large Hadron Collider (LHC) liberates the confined quarks and gluons inside nuclei to form a medium called quark-gluon plasma (QGP) [1–4]. In the past years, phenomenological multi-stage models (containing initial, pre-equilibrium, QGP, hadron gas stages) have given a solid description of heavy-ion physics. In particular, the QGP stage is successfully explained by causal relativistic hydrodynamics with two first-order transport coefficients, namely the shear and bulk viscosity over entropy density (η/s and ζ/s , respectively). The comparison of model predictions with measurements indicates that the experimental data favor small values for η/s and ζ/s , which implies that the produced QGP in HIC is considered the most perfect fluid observed in nature [5]. The formed QGP is in the strongly coupled regime, in which the applications of the perturbative techniques are limited. On the other hand, the non-perturbative techniques (i.e. gauge/gravity duality and lattice QCD) are restricted to specific scenarios [6–11]. Consequently, accurate

experimental measurements to constrain these quantities are crucial to deepen our understanding of QCD.

To this date, the number of free parameters (including temperature-dependent $\eta/s(T)$ and $\zeta/s(T)$) in a typical multi-stage heavy-ion collision model ranges from 10 to 20. Considering only few of these parameters can be estimated theoretically, they must be extracted from the experimental observations, e.g., particle yields, anisotropy in final particle distribution in momentum space, particle mean transverse momentum, etc. [12–14]. The free parameters usually have a complex relationship with the experimental observables, such that inferring the parameter values from the experimental data is not an easy task. In this respect, a substantial progress has happened in recent years by employing Bayesian analysis. In addition to the seminal works in Refs. [15–18,5] on applying the Bayesian analysis in heavy-ion physics, other studies have been done in which few extra experimental observables are employed to infer the parameters and/or few variations of multi-stage models are considered [19–22].

Among the possible experimental observables, some of them are more sensitive to the properties of the system controlling the details of its collective evolution. For instance, it has been demonstrated that symmetric cumulants (see Ref. [23]) are sensitive to $\eta/s(T)$ [24,25]. These quantities belong to a larger class of experimental observables used to quantify the anisotropic flow, which is one of the most informative experimental probes in heavy-ion physics (see also Refs. [26–34]). In this letter, we start with

* Corresponding authors.

E-mail addresses: s.f.taghavi@tum.de (S.F. Taghavi), dong.jo.kim@jyu.fi (D.J. Kim).

the same multi-stage model as in Ref. [5], but in contrast to the observables used in that work, we employ the new observables that were measured only recently by ALICE experiment in Pb–Pb collisions at two collision energies to increase our sensitivity to hydrodynamic transport coefficients η/s and ζ/s . To this end, we include symmetric cumulants [24,25,35], generalized symmetric cumulants [36], and flow harmonic mode couplings [37] as the input in our Bayesian analysis. The experimental measurements for particle yields and particle mean transverse momentum at $\sqrt{s_{NN}} = 5.02$ TeV [38,39] are added to increase our sensitivity on the collision energy dependence of the model. We employ identical methods in extracting the observables of interest from the output of simulations to the ones which were used in the corresponding experimental measurements, in order to avoid any incompatibilities in comparison. As our main result, we report an improved estimation for $\eta/s(T)$ and $\zeta/s(T)$ as well as the improved sensitivity of the anisotropic flow estimations to the model parameters.

2. Model parameters, experimental observables and Bayesian analysis approach

In the present study, different matter evolution stages are modeled similarly to that in Refs. [5,40]. In the following, we briefly explain the model employed for each stage and highlight their main parameters

Initial state: For the initial state of the Pb–Pb collisions, the $T_{\text{R}}\text{E}\text{N}\text{T}\text{O}$ model is employed [41]. Considering nucleons are distributed inside the Pb nucleus with Woods-Saxon distribution, it is assumed two nucleons have a minimum distance d_{min} . The binary collision of two nucleons from the target and projectile nuclei is determined by using the inelastic nucleon-nucleon cross-section, depending on the beam energy scale [42,43]. The deposited energy of each participant is modeled by a Gaussian distribution with w , the width of the distribution. To find the total participant density, the sum of the distribution of each nucleon is calculated when they are weighted by a random number generated with a gamma distribution with unit mean and standard deviation σ_k . The latter parameter provides a handle to control the final multiplicity fluctuation. The normalization factor N controls the total amount of energy deposited in the collision. After integrating out the longitudinal direction of the participant energy density along the beam axis, the participant's thickness function, $T_{A,B}$, is obtained. The deposited initial energy density in the collision region is eventually modeled via $(T_A^p + T_B^p)^{1/p}$ where p is another free parameter. The values of this parameter in the range $[-1, 1]$ mimic the behavior of different ab initio initial state models, namely IP-Glasma [44,45]. For instance, it turns out that $T_{\text{R}}\text{E}\text{N}\text{T}\text{O}$ with $p \approx 0$ behaves similar to IP-Glasma [17].

Pre-equilibrium: The initial energy density at the initial state level is highly anisotropic locally. Considering the evolution at this stage has no significant dynamics in the transverse direction, the initial energy density is transported via free-streaming until time τ_{fs} . At this time, Landau matching is employed to initiate the energy-momentum tensor for hydrodynamic calculations.

Viscous hydrodynamics: After the pre-equilibrium stage, the energy-momentum tensor is passed to VISH2+1 , a 2+1 viscous relativistic hydrodynamic model [68,69]. The temperature dependence of shear and bulk viscosities over entropy density is parameterized as the following:

$$(\eta/s)(T) = (\eta/s)(T_0) + (\eta/s)_{\text{slope}}(T - T_0) \left(\frac{T}{T_0} \right)^{(\eta/s)_{\text{curve}}}, \quad (1)$$

and

$$(\zeta/s)(T) = \frac{(\zeta/s)_{\text{max}}}{1 + \left(\frac{T - (\zeta/s)_{\text{peak}}}{(\zeta/s)_{\text{width}}} \right)^2}. \quad (2)$$

Hadronic medium evolution: After the collective expansion and cooling down, the partonic degrees of freedom turn into hadrons. We assume that changing from partonic to hadronic description happens at the switching temperature T_{switch} . A hadronization model based on the Cooper-Frye prescription [46,18] models this process. The evolution in the hadron gas continues with the UrQMD model. [47,48].

We have summarized the 15 different parameters of the model in Table 1 with their corresponding prior range, the optimal MAP-value (Maximum A Posteriori), as well as a short description. The only difference of our setup compared to Ref. [5] is that one common centrality definition is shared between all prior parametrizations, unlike in Ref. [5], where the centrality was defined individually for each parametrization by sorting the resulting events into centrality bins. However, our initial condition prior range is narrow, and we do not expect to see large multiplicity variations that would cause bias due to shared centrality definition. Furthermore, for each event, we sample the hypersurface exactly ten times regardless of the cumulative number of particles.

The Bayesian analysis is a powerful tool to obtain the model parameters from the experimental measurements. In the following, we briefly explain its main steps and refer the reader to Ref. [18] for more details. We represent a generic set of the model parameters and output observables by vectors \vec{x} and \vec{y} , respectively. Considering we have poor knowledge about the free parameters initially, our degree of belief on the parameter values is encoded into a uniform *prior* distribution $P(\vec{x})$ in intervals defined in Table 1. According to the Bayes' theorem, the updated degree of belief in the light of experimental data (*posterior* distribution) is given by $P(\vec{x}|\vec{y}) \propto P(\vec{y}|\vec{x})P(\vec{x})$. The probability $P(\vec{y}|\vec{x})$, the likelihood, is obtained by probing the parameter space \vec{x} and comparing it with experimental measurements \vec{y} . Markov Chain Monte Carlo (MCMC) method is employed to probe the parameter phase space to obtain the posterior distribution via Bayes's theorem. Given that heavy-ion models are computationally expensive, instead of using the model directly, the computations are done on 500 parameter design points distributed with Latin hypercube scheme [49,50]. At each designed point, 3×10^6 events are generated for the 5.02 TeV collision energy, and 5×10^6 for the 2.76 TeV, including the ten samples of the hypersurface. The Gaussian process (GP) is used to emulate the model in a continuous parameter phase space. The predictions in between the design points have been validated.

The following measurements from ALICE experiment have been used in Ref. [5]: centrality dependence of charged and identified particles yields dN/dy , mean transverse momentum $\langle p_T \rangle$ [51–55], as well as two-particle anisotropic flow coefficients $v_n\{2\}$ for harmonics $n = 2, 3$, and 4 [14,56]. In the present study, besides the recent measurements for identified particle yields and $\langle p_T \rangle$ at $\sqrt{s_{NN}} = 5.02$ TeV [39,38] that have not been used in the previous study, we employ latest measurements related to the anisotropic flow: two-particle anisotropic flow coefficients $v_n\{2\}$ for $n = 5, \dots, 9$ [56,57,37], normalized symmetric cumulants $\text{NSC}(k, \ell)$ [24,25,35], and flow mode couplings $\chi_{n,mk}$ [58,37]. In a previous study in Ref. [40], only measurements at $\sqrt{s_{NN}} = 5.02$ TeV have been considered, while measurements from both collision energies $\sqrt{s_{NN}} = 2.76$ TeV and 5.02 TeV are implemented into this analysis. In particular, the latest measurements of the generalized normalized symmetric cumulants $\text{NSC}(k, \ell, m)$ at $\sqrt{s_{NN}} = 2.76$ TeV [36] are included.

The methods used for the calculations of the observables are the same as the experimental analysis in Refs. [24,57,37,35]. In order to obtain internally consistent comparison, the centrality

Table 1
Input parameter ranges for the initial condition and hydrodynamic models.

Parameter	Description	Range	MAP
$N(2.76 \text{ TeV})$	Overall normalization (2.76 TeV)	[11.152, 18.960]	14.373
$N(5.02 \text{ TeV})$	Overall normalization (5.02 TeV)	[16.542, 25]	21.044
p	Deposition parameter	[0.0042, 0.0098]	0.0056
w	Nucleon width	[0.67, 1.24]	0.86
σ_k	Std. dev. of nucleon multiplicity fluctuations	[0.5518, 1.2852]	1.0468
d_{min}^3	Minimum volume per nucleon	[0.889 ³ , 1.524 ³]	1.2367 ³
τ_{fs}	Free-streaming time	[0.03, 1.5]	0.71
T_0	Temperature of const. $\eta/s(T)$, $T < T_0$	[0.135, 0.165]	0.141
$\eta/s(T_0)$	Minimum $\eta/s(T)$	[0, 0.2]	0.093
$(\eta/s)_{\text{slope}}$	Slope of $\eta/s(T)$ above T_0	[0, 4]	0.8024
$(\eta/s)_{\text{curve}}$	Curvature of $\eta/s(T)$ above T_0	[-1.3, 1]	0.1568
$(\zeta/s)_{\text{peak}}$	Temperature of $\zeta/s(T)$ maximum	[0.15, 0.2]	0.1889
$(\zeta/s)_{\text{max}}$	Maximum $\zeta/s(T)$	[0, 0.1]	0.01844
$(\zeta/s)_{\text{width}}$	Width of $\zeta/s(T)$ peak	[0, 0.1]	0.04252
T_{switch}	Switching / partitization temperature	[0.135, 0.165]	0.1595

classes for this study were chosen in such a way that they match the centrality classes of the experimental data. The multiplicity range has to be defined for each centrality class. This is done by using the MAP parametrization from [5] to simulate events and select the resulting minimum bias events by charged-particle multiplicity $dN/d\eta$ at midrapidity ($|\eta| < 0.5$). By counting and averaging the particle species at midrapidity, we could evaluate the identified particle multiplicity $dN/d\eta$ and $\langle p_T \rangle$. For the experimental data there is no additional processing required for the preparation of the comparison, since it is already corrected and extrapolated to zero p_T [13]. Our model only reproduces the spectra of protons for the identified $dN/d\eta$, hence they were the only species used for the model calibration. With this information we can calculate the flow coefficients and other observables for charged particles within the acceptance of the ALICE detector, using the same methods as in [37,35].

As it is mentioned before, a uniform prior distribution is considered for the parameters. Since the new observables included in this study should be more sensitive to the transport coefficients, we assume that the parameters of the initial state model are uniformly distributed around the MAP values found in Ref. [5]. A narrow range of variations is allowed for further minor adjustments.

3. Results and discussion

After finding the posterior distribution $P(\vec{x}|\vec{y})$, we extract those values of \vec{x} that maximize the distribution (MAP values). In Fig. 1, the model predictions for observables related to the anisotropic flow are compared with the measurements. As seen from the figure, the overall trend of the data is captured by the model. The observables indicate a different dependence on the collision energy in the simulation than experimental measurements. The difference between two energies is clearly visible in the centrality dependence of v_2 , where the predictions for most central collisions are significantly larger than for peripheral collisions. The experimental measurements for $v_2\{2\}(5.02 \text{ TeV})/v_2\{2\}(2.76 \text{ TeV})$ (black filled markers in the ratio panel) are compatible with unity in a wide range of centrality classes, while the simulation (black curve in the same panel) reaches 25% above unity in some centralities. The ALICE measurement reveals a sign change for NSC(4, 3) at $\sqrt{s_{\text{NN}}} = 5.02 \text{ TeV}$ in central collisions, while there is no sign change in $\sqrt{s_{\text{NN}}} = 2.76 \text{ TeV}$ measurement. We do not observe such a collision energy-dependent behavior in the simulation. One notes that the only collision energy-dependent part of the model is considered to be the overall initial energy density normalization. The simulation also fails to explain data at peripheral collisions for NSC(4, 2). All results considered, the higher energy description is found to be worse for all observables, except for v_5 , $\chi_{6,222}$, and

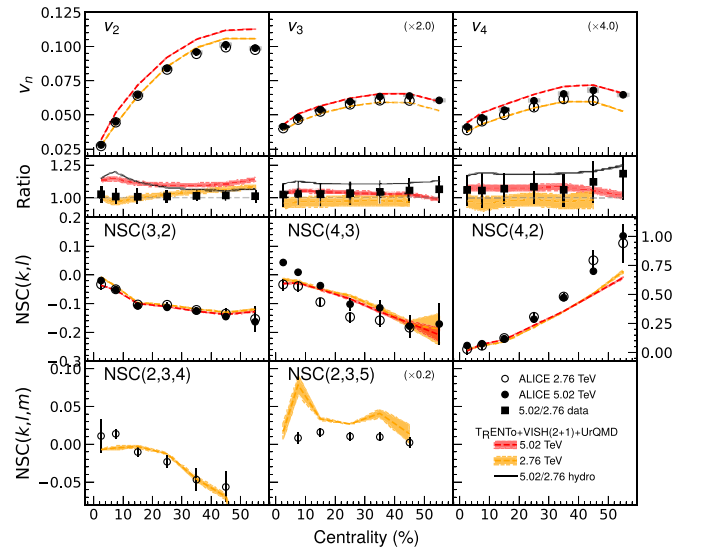


Fig. 1. Flow coefficients v_n and normalized symmetric cumulants (NSC(k, l) and NSC(k, l, m)) from two hydrodynamical calculations using the MAP parametrization are compared to the experimental data [37,35]. The red band corresponds to the calculations at the collision energy of $\sqrt{s_{\text{NN}}} = 5.02 \text{ TeV}$, while the yellow band presents the results at $\sqrt{s_{\text{NN}}} = 2.76 \text{ TeV}$. The corresponding ratio between the data and calculation for the respective collision energies is shown for the v_n . Here, the black markers and black lines are the ratio between the two collision energy results, for data and calculations, respectively.

proton, pion and charged particle multiplicity based on the same χ^2 -test performed in [40].

Switching temperature, T_{switch} , is the temperature at which we switch the description of the medium from relativistic hydrodynamics to a transport model of hadrons. Including the new observables raises the previous estimation for T_{switch} around 5% from 0.152(3) MeV reported in Ref. [5] to 0.159(5) MeV. The lattice QCD study for the QCD phase diagram shows a crossover transition from high temperature QGP phase to low temperature hadronic phase at low baryonic densities [59]. Although the thermodynamic variables vary continuously, they rapidly change in the range $145 \text{ MeV} \leq T_c \leq 163 \text{ MeV}$ [60]. For the hydrodynamic calculations in this study, an equation of state has been employed that consists of lattice QCD calculations of HotQCD collaboration smoothly connected to the hadron resonance gas calculation at lower temperatures (see the details in Ref. [18]). This equation of state is compatible with T_c range [2]. One notes that the switching between the description of the medium from relativistic hydrodynamics to the Boltzmann transport model happens sharply in our model at T_{switch} at which one expects the co-existence of both par-

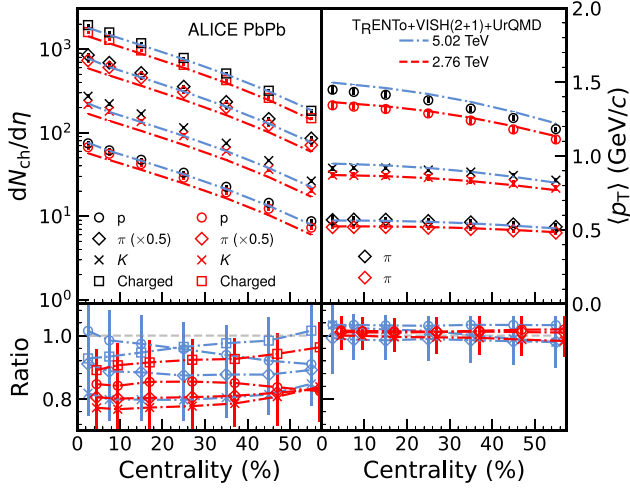


Fig. 2. Charged and identified particle multiplicity and $\langle p_T \rangle$ from two hydrodynamical calculations are compared to the experimental data at center-of-mass energy of 2.76 and 5.02 TeV.

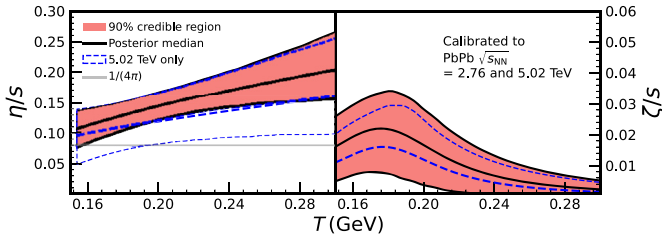


Fig. 3. The 90%-credibility region for the shear (top) and bulk (bottom) viscosity to entropy ratio is given as a red band. The black line represents the median of the credibility range. Our result is compared to the MAP parametrization from [40], for which the calibration was performed using 5.02 TeV data only.

tonic and hadronic degrees of freedom. Considering the different interpretation of T_{switch} and T_c , one however, expects that T_{switch} to be in a reasonable vicinity of T_c . The prior range of T_{switch} in both Ref. [5] and ours study is chosen to be $[0.135, 0.165]$ MeV, which is slightly larger than the T_c range. Both analyses return T_{switch} inside the T_c range up to one sigma credibility.

It has been discussed in Refs. [57,58,37] that the newly added anisotropic flow observables, mode couplings and correlation between harmonics are sensitive to the viscous corrections to the equilibrium distribution at the freeze-out [61–64]. The centrality dependence of charged and identified particle yields and $\langle p_T \rangle$ is shown in Fig. 2. The model predictions with MAP parametrization are shown by red and blue curves for the center-of-mass energies of 2.76 TeV and 5.02 TeV, respectively. As seen from the figure, the simulation does not lead to an accurate prediction for charged and identified particle yields for both energies. For particle yields, the predictions and measurements are in better agreement at the center-of-mass energy 5.02 TeV. Together with what has been observed for $v_2\{2\}$ measurements at central collisions, these discrepancies can be considered as evidence that we need a revision on our understanding about the model collision energy dependence.

In Fig. 3, the temperature dependence of η/s and ζ/s are presented. The result for $\eta/s(T)$ agrees with that reported in Ref. [5]. Compared to the previous analysis with $\sqrt{s_{NN}} = 5.02$ TeV data only [40], an improvement in the uncertainty of $\eta/s(T)$ is observed. Moreover, this parameter shows a stronger temperature dependence than in the previous study, meaning we observe a more substantial departure from the lower bound $1/4\pi$. We also find higher mean values for $\zeta/s(T)$. Including both 2.76 TeV and 5.02 TeV center-of-mass energy data improves the uncertainty of

$\zeta/s(T)$. As it is mentioned earlier, the symmetric cumulants are sensitive to the temperature dependence of η/s . Our new observation in $\zeta/s(T)$ uncertainty improvement indicates that the newly added anisotropic flow observables including normalized symmetric cumulants are sensitive to the temperature dependence of ζ/s as well. In the following, we study the parameter sensitivity more systematically.

To compare the sensitivity of the observables with each other, we follow Refs. [22,65] and define the sensitivity of an observable \hat{O} to the parameter x_j via $S[x_j] = |\hat{O}(\vec{x}') - \hat{O}(\vec{x})|/\delta\hat{O}(\vec{x})$ where $\hat{O}(\vec{x})$ is the value of the observable at the parameter point $\vec{x} = (x_1, \dots, x_p)$. The quantity \vec{x}' is a point in the parameter space with a small difference in a single parameter x_j , $\vec{x}' = (x_1, \dots, (1 + \delta)x_j, \dots, x_p)$. The small quantity δ is chosen to be equal to 0.1. We have found that the larger values for δ lead to similar results. The result is depicted in Fig. 4. As seen from the figure, compared to the other observables, the normalized symmetric cumulants NSC(k, ℓ) and the generalized normalized symmetric cumulants NSC(k, ℓ, m) are very sensitive to the values of transport coefficient parameters. This result is more general and more quantitative evidence of what has been observed in Refs. [24,25] for the sensitivity of SC(k, ℓ) to η/s . Here, we indicate that NSC observables are sensitive to both η/s and ζ/s . An interesting feature that we immediately recognize from Fig. 4 is that by considering the higher harmonics and higher-order cumulants, the shear and bulk viscosity parameters modifications reveal more drastic change on the observables. For temperature-independent η/s , it has been shown that higher harmonics have more sensitivity to η/s modification [66,63]. This study has been generalized to temperature-dependent η/s for v_2 and v_3 by Gardim and Ollitrault [67]. The effect can be understood as follows: the higher harmonics capture finer details of initial state energy density structures. The dissipation effects should wash out the finer structures during hydrodynamic evolution. As a result, small changes in the value of η/s and ζ/s affect the higher harmonic observables more drastically. The high sensitivity of NSCs cannot be merely due to high harmonic flow coefficients, since the mode coupling observables contain the same harmonics but show less sensitivity. We deduce that the genuine correlations between flow amplitudes v_n , captured by NSCs, are particularly sensitive to the transport properties of the medium.

4. Summary

Building on the previous studies, we employed the latest measurements of higher harmonics, higher-order flow fluctuation observables as inputs into a Bayesian analysis. The present study indicated that these observables are sensitive to the transport coefficients and revealed the importance of the precision measurements of these observables to infer the hydrodynamic transport coefficients accurately. Including the latest flow harmonic measurements, we have improved the uncertainty of estimated values for η/s and ζ/s . Despite using the new observables as inputs to extract model parameters, there are remaining discrepancies between model and experimental measurements. For instance, NSC(4,2) model prediction is improved in our new analysis, but it still deviates from measurements at higher centralities. At $\sqrt{s_{NN}} = 5.02$ TeV, the sign change of NSC(4,3) in the lower centralities is not reproduced neither in Ref. [5] nor in our study. Further investigations are needed in this respect. These discrepancies, together with poor model/data compatibility for the energy scale dependence of $v_2\{2\}$ at central collisions and also the particle yields, show the necessity to improve our understanding of the heavy-ion collision models.

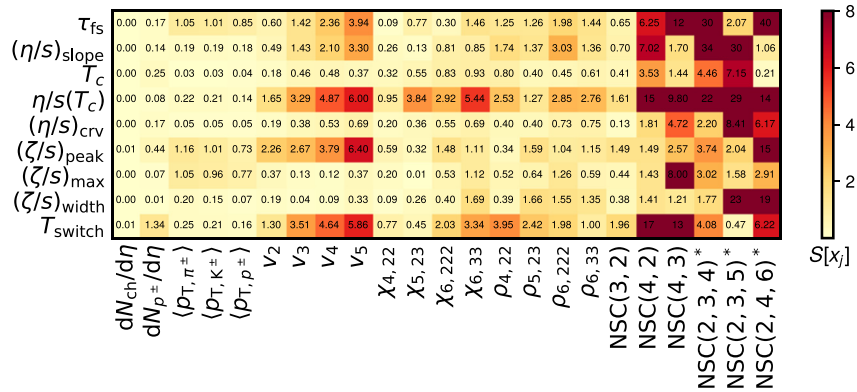


Fig. 4. Sensitivity of the observables to the model parameters visualized as a color map. The asterisk (*) for an observable indicates that the sensitivity was evaluated using 2.76 TeV calculations, whereas the rest are evaluated using 5.02 TeV calculations. The sensitivity index is averaged over four centrality classes, from 5% to 40%, except for NSC(k, l, m), for which only one centrality class 20-30% is used. Light yellow shades represent a very limited sensitivity or no sensitivity, whereas orange and darker red colors represent moderate or strong sensitivities to the corresponding model parameter, respectively.

Declaration of competing interest

The authors declare that they have no known competing financial interests or personal relationships that could have appeared to influence the work reported in this paper.

Data availability

Data will be made available on request.

Acknowledgements

We thank Jonah E. Bernhard, J. Scott Moreland and Steffen A. Bass for the use of their viscous relativistic hydrodynamics software and their valuable comments on various processes of this work. We would like to thank Harri Niemi, Kari J. Eskola and Sami Räsänen for fruitful discussions. We acknowledge Victor Gonzalez for his crosscheck for various technical parts of the event generation. We acknowledge CSC, 2003112 – IT Center for Science in Espoo, Finland, for the allocation of the computational resources. This research was completed using ~ 64 million CPU hours provided by CSC. Three of us (SFT, CM, and AB) have received funding from the European Research Council (ERC) under the European Unions Horizon 2020 research and innovation program (Grant Agreement No. 759257). AO, CM, MV and DJK are supported by the Academy of Finland, the Centre of Excellence in Quark Matter (project 346324).

Appendix A. Further information

This appendix presents extra information about the model predictions with MAP parameterization and posterior distribution of the model parameters.

In the main paper, the model predictions for charged and identified particle yields, $\langle p_T \rangle$, and a few anisotropic flow observables have been compared with the measurements (see Fig. 1 and Fig. 2). Here, we present the comparison between simulation and data for additional anisotropic flow observables. The flow cumulants $v_n\{2\}$ for $n = 5, \dots, 9$, flow mode couplings and symmetry plane correlations for various harmonics are presented in Figs. A.5–A.7, respectively. As seen from the figures, although the overall trends are compatible with the measurement, the model does not accurately explain data for harmonic six and above. We observe more compatibility between simulation and data in mode-coupling observables, even in cases that higher harmonic flow coefficients are involved.

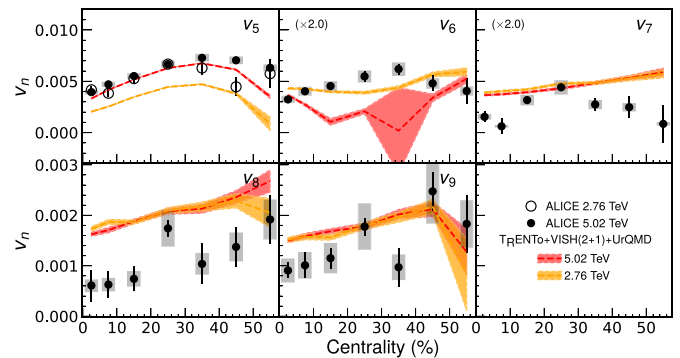


Fig. A.5. Flow coefficients for harmonics 5 to 9. The red and yellow bands present the model prediction for collision energies $\sqrt{s_{NN}} = 5.02$ and 2.76 TeV, respectively. The experimental data are published in Refs. [58,37].

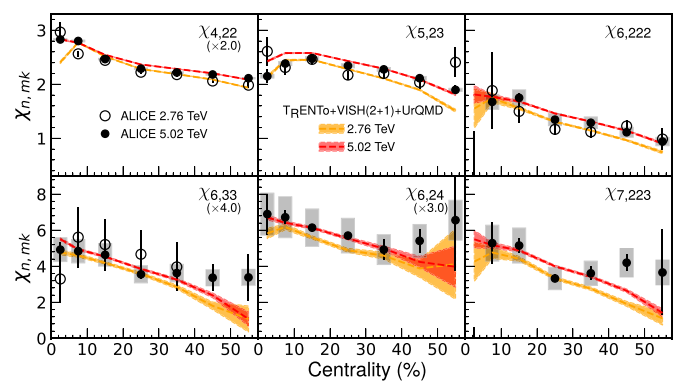


Fig. A.6. Flow mode couplings for six different harmonic combinations. The experimental data are published in Refs. [58,37].

Fig. A.8 presents the same χ^2 -test as in [40] to quantify the agreement of the models with the data for the 0–60% centrality range. In addition to the flow harmonic mode couplings and symmetric cumulants, the generalized symmetric cumulants, particle multiplicity and $\langle p_T \rangle$ were added to the test. These results show that the higher energy description is worse for all observables except for v_5 , $\chi_{6,222}$, and charged particle multiplicities.

The model calculations using the design parametrizations obtained from the prior distribution for each observable at $\sqrt{s_{NN}} = 2.76$ TeV (see Ref. [40] for 5.02 TeV) are shown in Figs. A.9–A.12.

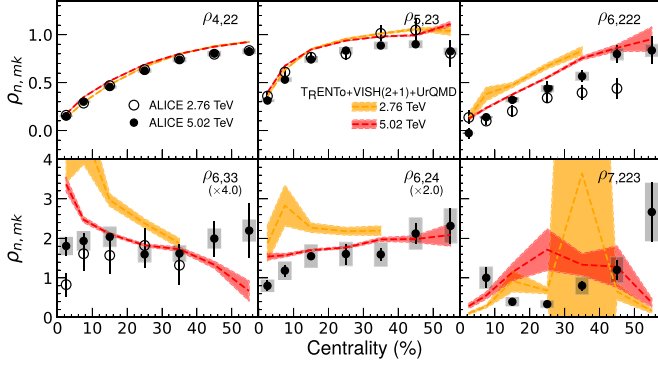


Fig. A.7. Symmetry plane correlations for six different harmonic combinations. The experimental data are published in Refs. [58,37].

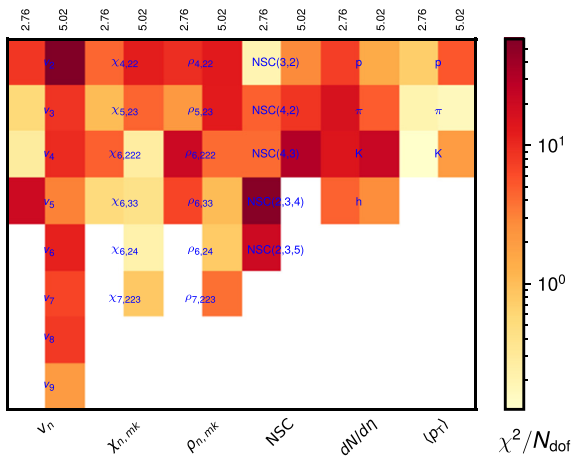


Fig. A.8. The χ^2 -test values calculated between the data and model calculations for both beam energies are shown for all flow harmonic mode couplings, symmetric cumulants, generalized symmetric cumulants, and, charged and identified particle multiplicity and $\langle p_T \rangle$.

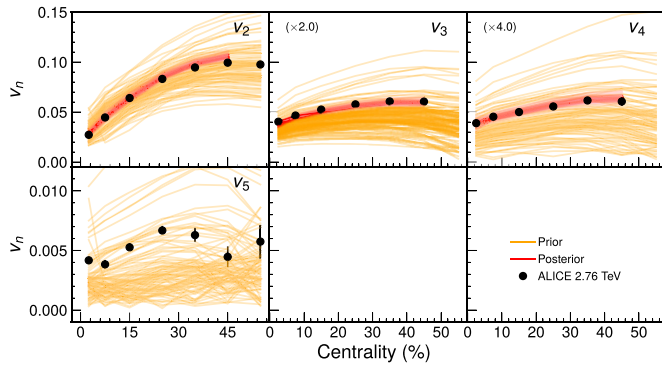


Fig. A.9. Flow coefficients v_n as given by the design parametrizations are presented in yellow curves. All harmonics are simultaneously covered by the design parametrizations. The red curves represent a number of curves sampled from the posterior distribution, and as given by the emulator.

The yellow curves represent the calculations corresponding to each design parametrization point which are used in training the GP emulator. The red curves are from the GP emulator predictions corresponding to random points sampled from the posterior distribution.

The MAP values for the model parameters are presented in Table 1, which are the median of the marginal posterior distribution for a given parameter. For the readers interested in more infor-

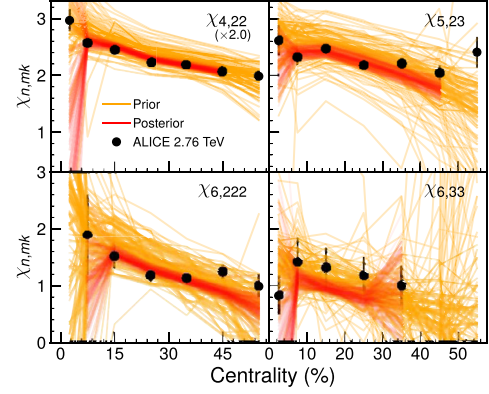


Fig. A.10. Design parametrizations for non-linear flow mode coefficients $\chi_{n,mk}$ (in yellow) and a number of posterior sample curves as given by the emulator (in red).

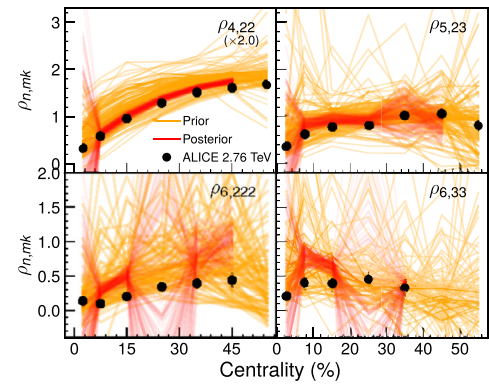


Fig. A.11. Design parametrizations for symmetry plane correlations $\rho_{n,mk}$ (in yellow) and a number of posterior sample curves as given by the emulator (in red).

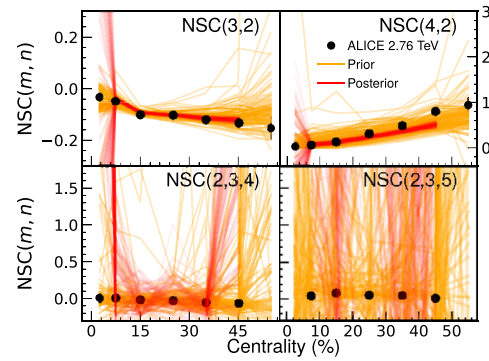


Fig. A.12. Design parametrizations for normalized symmetric cumulants (in yellow) and a number of posterior sample curves as given by the emulator (in red).

mation about the posterior distribution, we present the marginal (diagonal panels) and joint marginal (off-diagonal panels) part of the posterior distribution in Fig. A.13. The results are compatible with previous studies in Refs. [5,40]. However, focusing on parameters related to $\eta/s(T)$ and $\zeta/s(T)$, we find that the parameters are inferred with more accuracy as we expect. For instance, we can see a more sharp peak for parameter $(\zeta/s)_{\text{peak}}$. The marginal distribution of this parameter was more broadened in the previous studies. Moreover, the joint marginal distribution between parameters $(\zeta/s)_{\text{peak}}$ and $(\zeta/s)_{\text{curve}}$ is concentrated in a smaller region of the parameter space.

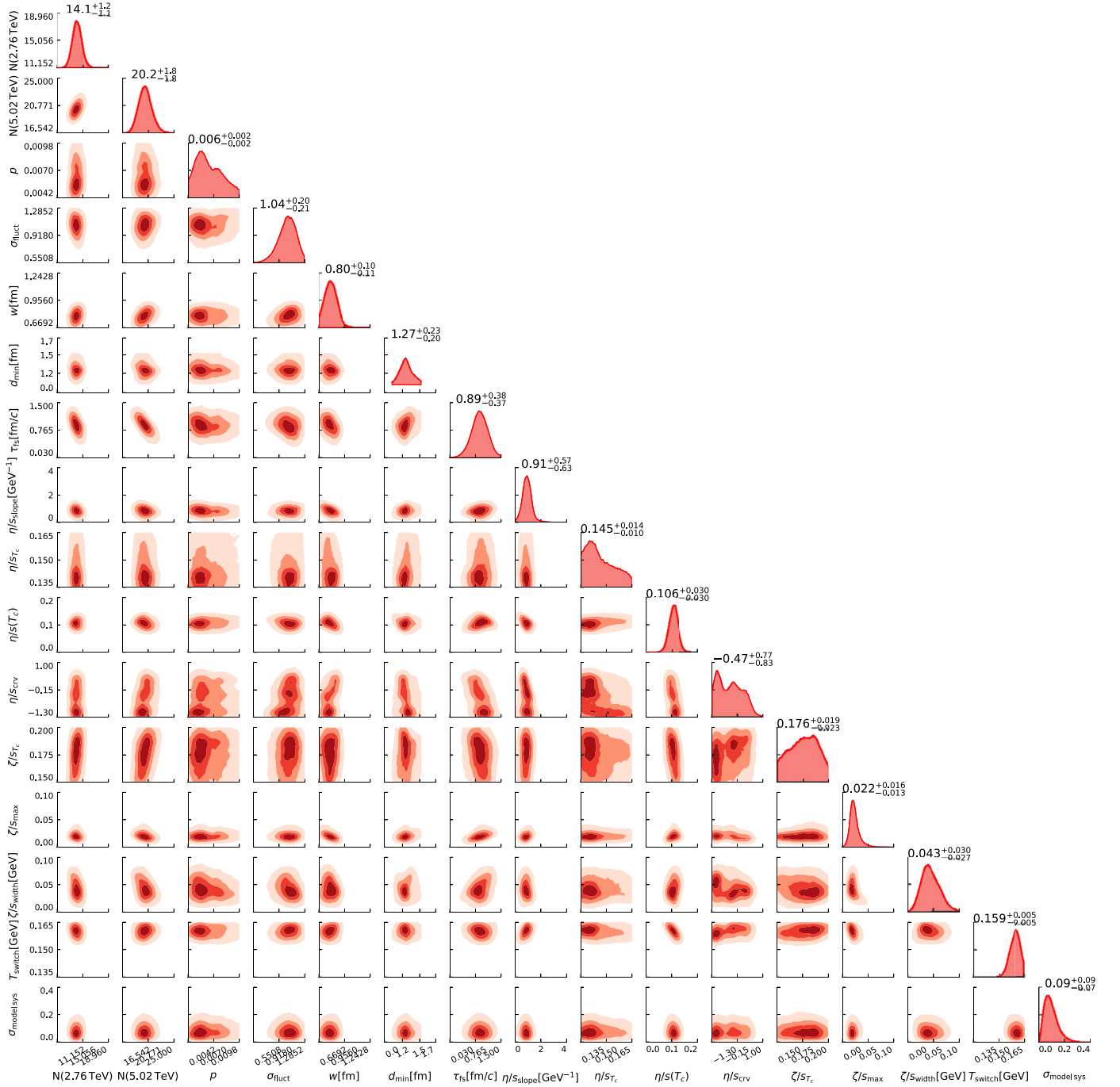


Fig. A.13. Marginal and joint marginal parts of the poster distribution. The numbers denoted on top of marginal distributions are the median together with the range of 90% credibility (in the text, η/s_{T_c} and ζ/s_{T_c} are shown by T_0 and $(\zeta/s)_{\text{peak}}$, respectively).

References

[1] S. Borsanyi, Z. Fodor, C. Hoelbling, S.D. Katz, S. Krieg, K.K. Szabo, Full result for the QCD equation of state with 2+1 flavors, Phys. Lett. B 730 (2014) 99–104, <https://doi.org/10.1016/j.physletb.2014.01.007>, arXiv:1309.5258.

[2] A. Bazavov, et al., Equation of state in (2+1)-flavor QCD, Phys. Rev. D 90 (2014) 094503, <https://doi.org/10.1103/PhysRevD.90.094503>, arXiv:1407.6387.

[3] P. Braun-Munzinger, V. Koch, T. Schäfer, J. Stachel, Properties of hot and dense matter from relativistic heavy ion collisions, Phys. Rep. 621 (2016) 76–126, <https://doi.org/10.1016/j.physrep.2015.12.003>, arXiv:1510.00442.

[4] W. Busza, K. Rajagopal, W. van der Schee, Heavy ion collisions: the big picture, and the big questions, Annu. Rev. Nucl. Part. Sci. 68 (2018) 339–376, <https://doi.org/10.1146/annurev-nucl-101917-020852>, arXiv:1802.04801.

[5] J.E. Bernhard, J.S. Moreland, S.A. Bass, Bayesian estimation of the specific shear and bulk viscosity of quark-gluon plasma, Nat. Phys. (2019), <https://doi.org/10.1038/s41567-019-0611-8>.

[6] P. Kovtun, D.T. Son, A.O. Starinets, Viscosity in strongly interacting quantum field theories from black hole physics, Phys. Rev. Lett. 94 (2005) 111601, <https://doi.org/10.1103/PhysRevLett.94.111601>, arXiv:hep-th/0405231.

[7] A. Bazavov, F. Karsch, S. Mukherjee, P. Petreczky, Hot-dense lattice QCD: USQCD whitepaper 2018, Eur. Phys. J. A 55 (11) (2019) 194, <https://doi.org/10.1140/epja/i2019-12922-0>, arXiv:1904.09951.

[8] H.B. Meyer, A Calculation of the shear viscosity in SU(3) gluodynamics, Phys. Rev. D 76 (2007) 101701, <https://doi.org/10.1103/PhysRevD.76.101701>, arXiv:0704.1801.

[9] N. Astrakhantsev, V. Braguta, A. Kotov, Temperature dependence of shear viscosity of SU(3)-gluodynamics within lattice simulation, J. High Energy

- Phys. J. C 81 (7) (2021) 652, <https://doi.org/10.1140/epjcs/10052-021-09413-0>, arXiv:2005.04742.
- [10] H.B. Meyer, A Calculation of the bulk viscosity in SU(3) gluodynamics, Phys. Rev. Lett. 100 (2008) 162001, <https://doi.org/10.1103/PhysRevLett.100.162001>, arXiv:0710.3717.
- [11] N.Y. Astrakhantsev, V.V. Braguta, A.Y. Kotov, Temperature dependence of the bulk viscosity within lattice simulation of SU(3) gluodynamics, Phys. Rev. D 98 (5) (2018) 054515, <https://doi.org/10.1103/PhysRevD.98.054515>, arXiv:1804.02382.
- [12] K. Aamodt, et al., Centrality dependence of the charged-particle multiplicity density at mid-rapidity in Pb-Pb collisions at $\sqrt{s_{NN}} = 2.76$ TeV, Phys. Rev. Lett. 106 (2011) 032301, <https://doi.org/10.1103/PhysRevLett.106.032301>, arXiv:1012.1657.
- [13] B. Abelev, et al., Centrality dependence of π , K, p production in Pb-Pb collisions at $\sqrt{s_{NN}} = 2.76$ TeV, Phys. Rev. C 88 (2013) 044910, <https://doi.org/10.1103/PhysRevC.88.044910>, arXiv:1303.0737.
- [14] K. Aamodt, et al., Higher harmonic anisotropic flow measurements of charged particles in Pb-Pb collisions at $\sqrt{s_{NN}} = 2.76$ TeV, Phys. Rev. Lett. 107 (2011) 032301, <https://doi.org/10.1103/PhysRevLett.107.032301>, arXiv:1105.3865.
- [15] J.E. Bernhard, P.W. Marcy, C.E. Coleman-Smith, S. Huzurbazar, R.L. Wolpert, S.A. Bass, Quantifying properties of hot and dense QCD matter through systematic model-to-data comparison, Phys. Rev. C 91 (5) (2015) 054910, <https://doi.org/10.1103/PhysRevC.91.054910>, arXiv:1502.00339.
- [16] J.E. Bernhard, J.S. Moreland, S.A. Bass, J. Liu, U. Heinz, Applying Bayesian parameter estimation to relativistic heavy-ion collisions: simultaneous characterization of the initial state and quark-gluon plasma medium, Phys. Rev. C 94 (2016) 024907, <https://doi.org/10.1103/PhysRevC.94.024907>, <https://link.aps.org/doi/10.1103/PhysRevC.94.024907>.
- [17] J.E. Bernhard, J.S. Moreland, S.A. Bass, J. Liu, U. Heinz, Applying Bayesian parameter estimation to relativistic heavy-ion collisions: simultaneous characterization of the initial state and quark-gluon plasma medium, Phys. Rev. C 94 (2) (2016) 024907, <https://doi.org/10.1103/PhysRevC.94.024907>, arXiv:1605.03954.
- [18] J.E. Bernhard, Bayesian parameter estimation for relativistic heavy-ion collisions, Ph.D. thesis, Duke U, 4.2018, arXiv:1804.06469.
- [19] J. Auvinen, K.J. Eskola, P. Huovinen, H. Niemi, R. Paatelainen, P. Petreczky, Temperature dependence of η/s of strongly interacting matter: effects of the equation of state and the parametric form of $(\eta/s)(T)$, Phys. Rev. C 102 (4) (2020) 044911, <https://doi.org/10.1103/PhysRevC.102.044911>, arXiv:2006.12499.
- [20] G. Nijs, W. van der Schee, U. Gürsöy, R. Snellings, A transverse momentum differential global analysis of heavy ion collisions, Phys. Rev. Lett. 126 (20) (2021) 202301, <https://doi.org/10.1103/PhysRevLett.126.202301>, arXiv:2010.15130.
- [21] G. Nijs, W. van der Schee, U. Gürsöy, R. Snellings, Bayesian analysis of heavy ion collisions with the heavy ion computational framework trajectory, Phys. Rev. C 103 (5) (2021) 054909, <https://doi.org/10.1103/PhysRevC.103.054909>, arXiv:2010.15134.
- [22] D. Everett, et al., Multisystem Bayesian constraints on the transport coefficients of QCD matter, Phys. Rev. C 103 (5) (2021) 054904, <https://doi.org/10.1103/PhysRevC.103.054904>, arXiv:2011.01430.
- [23] A. Bilandzic, C.H. Christensen, K. Gulbrandsen, A. Hansen, Y. Zhou, Generic framework for anisotropic flow analyses with multiparticle azimuthal correlations, Phys. Rev. C 89 (6) (2014) 064904, <https://doi.org/10.1103/PhysRevC.89.064904>, arXiv:1312.3572.
- [24] J. Adam, et al., Correlated event-by-event fluctuations of flow harmonics in Pb-Pb collisions at $\sqrt{s_{NN}} = 2.76$ TeV, Phys. Rev. Lett. 117 (2016) 182301, <https://doi.org/10.1103/PhysRevLett.117.182301>, arXiv:1604.07663.
- [25] S. Acharya, et al., Systematic studies of correlations between different order flow harmonics in Pb-Pb collisions at $\sqrt{s_{NN}} = 2.76$ TeV, Phys. Rev. C 97 (2) (2018) 024906, <https://doi.org/10.1103/PhysRevC.97.024906>, arXiv:1709.01127.
- [26] N. Borghini, P.M. Dinh, J.-Y. Ollitrault, A new method for measuring azimuthal distributions in nucleus-nucleus collisions, Phys. Rev. C 63 (2001) 054906, <https://doi.org/10.1103/PhysRevC.63.054906>, arXiv:nucl-th/0007063.
- [27] N. Borghini, P.M. Dinh, J.-Y. Ollitrault, Flow analysis from multiparticle azimuthal correlations, Phys. Rev. C 64 (2001) 054901, <https://doi.org/10.1103/PhysRevC.64.054901>, arXiv:nucl-th/0105040.
- [28] K. Aamodt, et al., Elliptic flow of charged particles in Pb-Pb collisions at 2.76 TeV, Phys. Rev. Lett. 105 (2010) 252302, <https://doi.org/10.1103/PhysRevLett.105.252302>, arXiv:1011.3914.
- [29] J. Jia, Event-shape fluctuations and flow correlations in ultra-relativistic heavy-ion collisions, J. Phys. G 41 (12) (2014) 124003, <https://doi.org/10.1088/0954-3899/41/12/124003>, arXiv:1407.6057.
- [30] P. Di Francesco, M. Guillaud, M. Luzum, J.-Y. Ollitrault, Systematic procedure for analyzing cumulants at any order, Phys. Rev. C 95 (4) (2017) 044911, <https://doi.org/10.1103/PhysRevC.95.044911>, arXiv:1612.05634.
- [31] C. Mordasini, A. Bilandzic, D. Karakoç, S.F. Taghavi, Higher order symmetric cumulants, Phys. Rev. C 102 (2) (2020) 024907, <https://doi.org/10.1103/PhysRevC.102.024907>, arXiv:1901.06968.
- [32] A. Bilandzic, M. Lesch, S.F. Taghavi, New estimator for symmetry plane correlations in anisotropic flow analyses, Phys. Rev. C 102 (2) (2020) 024910, <https://doi.org/10.1103/PhysRevC.102.024910>, arXiv:2004.01066.
- [33] S.F. Taghavi, A Fourier-cumulant analysis for multiharmonic flow fluctuation: by employing a multidimensional generating function approach, Eur. Phys. J. C 81 (7) (2021) 652, <https://doi.org/10.1140/epjcs/10052-021-09413-0>, arXiv:2005.04742.
- [34] A. Bilandzic, M. Lesch, C. Mordasini, S.F. Taghavi, Multivariate cumulants in flow analyses: The Next Generation, arXiv:2101.05619, 1.2021.
- [35] S. Acharya, et al., Measurements of mixed harmonic cumulants in Pb-Pb collisions at $\sqrt{s_{NN}} = 5.02$ TeV, Phys. Lett. B 818 (2021) 136354, <https://doi.org/10.1016/j.physletb.2021.136354>, arXiv:2102.12180.
- [36] S. Acharya, et al., Multiharmonic correlations of different flow amplitudes in Pb-Pb collisions at $\sqrt{s_{NN}} = 2.76$ TeV, Phys. Rev. Lett. 127 (9) (2021) 092302, <https://doi.org/10.1103/PhysRevLett.127.092302>, arXiv:2101.02579.
- [37] S. Acharya, et al., Higher harmonic non-linear flow modes of charged hadrons in Pb-Pb collisions at $\sqrt{s_{NN}} = 5.02$ TeV, J. High Energy Phys. 05 (2020) 085, [https://doi.org/10.1007/JHEP05\(2020\)085](https://doi.org/10.1007/JHEP05(2020)085), arXiv:2002.00633.
- [38] S. Acharya, et al., Production of charged pions, kaons, and (anti-)protons in Pb-Pb and inelastic pp collisions at $\sqrt{s_{NN}} = 5.02$ TeV, Phys. Rev. C 101 (4) (2020) 044907, <https://doi.org/10.1103/PhysRevC.101.044907>, arXiv:1910.07678.
- [39] J. Adam, et al., Centrality dependence of the pseudorapidity density distribution for charged particles in Pb-Pb collisions at $\sqrt{s_{NN}} = 5.02$ TeV, Phys. Lett. B 772 (2017) 567–577, <https://doi.org/10.1016/j.physletb.2017.07.017>, arXiv:1612.08966.
- [40] J.E. Parkkila, A. Onnerstad, D.J. Kim, Bayesian estimation of the specific shear and bulk viscosity of the quark-gluon plasma with additional flow harmonic observables, Phys. Rev. C 104 (2021) 054904, <https://doi.org/10.1103/PhysRevC.104.054904>, arXiv:2106.05019.
- [41] J.S. Moreland, J.E. Bernhard, S.A. Bass, Alternative ansatz to wounded nucleon and binary collision scaling in high-energy nuclear collisions, Phys. Rev. C 92 (1) (2015) 011901, <https://doi.org/10.1103/PhysRevC.92.011901>, arXiv:1412.4708, <http://qcd.phy.duke.edu/trento/>.
- [42] G. Aad, et al., Measurement of the centrality dependence of the charged particle pseudorapidity distribution in lead-lead collisions at $\sqrt{s_{NN}} = 2.76$ TeV with the ATLAS detector, Phys. Lett. B 710 (2012) 363–382, <https://doi.org/10.1016/j.physletb.2012.02.045>, arXiv:1108.6027.
- [43] B. Abelev, et al., Pseudorapidity density of charged particles in p + Pb collisions at $\sqrt{s_{NN}} = 5.02$ TeV, Phys. Rev. Lett. 110 (3) (2013) 032301, <https://doi.org/10.1103/PhysRevLett.110.032301>, arXiv:1210.3615.
- [44] B. Schenke, P. Tribedy, R. Venugopalan, Fluctuating glasma initial conditions and flow in heavy ion collisions, Phys. Rev. Lett. 108 (2012) 252301, <https://doi.org/10.1103/PhysRevLett.108.252301>, arXiv:1202.6646.
- [45] B. Schenke, P. Tribedy, R. Venugopalan, Event-by-event gluon multiplicity, energy density, and eccentricities in ultrarelativistic heavy-ion collisions, Phys. Rev. C 86 (2012) 034908, <https://doi.org/10.1103/PhysRevC.86.034908>, arXiv:1206.6805.
- [46] S. Pratt, G. Torrieri, Coupling relativistic viscous hydrodynamics to Boltzmann descriptions, Phys. Rev. C 82 (2010) 044901, <https://doi.org/10.1103/PhysRevC.82.044901>, arXiv:1003.0413.
- [47] S.A. Bass, et al., Microscopic models for ultrarelativistic heavy ion collisions, Prog. Part. Nucl. Phys. 41 (1998) 255–369, [https://doi.org/10.1016/S0146-6410\(98\)00058-1](https://doi.org/10.1016/S0146-6410(98)00058-1), arXiv:nucl-th/9803035.
- [48] M. Bleicher, et al., Relativistic hadron hadron collisions in the ultrarelativistic quantum molecular dynamics model, J. Phys. G 25 (1999) 1859–1896, <https://doi.org/10.1088/0954-3899/25/9/308>, arXiv:hep-ph/9909407.
- [49] B. Tang, Orthogonal array-based Latin hypercubes, J. Am. Stat. Assoc. 88 (424) (1993) 1392–1397, <http://www.jstor.org/stable/2291282>.
- [50] M.D. Morris, T.J. Mitchell, Exploratory designs for computational experiments, J. Stat. Plan. Inference 43 (3) (1995) 381–402, [https://doi.org/10.1016/0378-3758\(94\)00035-T](https://doi.org/10.1016/0378-3758(94)00035-T), <https://www.sciencedirect.com/science/article/pii/037837589400035T>.
- [51] K. Aamodt, et al., Centrality dependence of the charged-particle multiplicity density at mid-rapidity in Pb-Pb collisions at $\sqrt{s_{NN}} = 2.76$ TeV, Phys. Rev. Lett. 106 (2011) 032301, <https://doi.org/10.1103/PhysRevLett.106.032301>, arXiv:1012.1657.
- [52] B. Abelev, et al., Centrality dependence of π , K, p production in Pb-Pb collisions at $\sqrt{s_{NN}} = 2.76$ TeV, Phys. Rev. C 88 (2013) 044910, <https://doi.org/10.1103/PhysRevC.88.044910>, arXiv:1303.0737.
- [53] J. Adam, et al., Centrality dependence of the charged-particle multiplicity density at midrapidity in Pb-Pb collisions at $\sqrt{s_{NN}} = 5.02$ TeV, Phys. Rev. Lett. 116 (22) (2016) 222302, <https://doi.org/10.1103/PhysRevLett.116.222302>, arXiv:1512.06104.
- [54] J. Adam, et al., Measurement of transverse energy at midrapidity in Pb-Pb collisions at $\sqrt{s_{NN}} = 2.76$ TeV, Phys. Rev. C 94 (3) (2016) 034903, <https://doi.org/10.1103/PhysRevC.94.034903>, arXiv:1603.04775.
- [55] B.B. Abelev, et al., Event-by-event mean p_T fluctuations in pp and Pb-Pb collisions at the LHC, Eur. Phys. J. C 74 (10) (2014) 3077, <https://doi.org/10.1140/epjcs/10052-014-3077-y>, arXiv:1407.5530.
- [56] J. Adam, et al., Anisotropic flow of charged particles in Pb-Pb collisions at $\sqrt{s_{NN}} = 5.02$ TeV, Phys. Rev. Lett. 116 (13) (2016) 132302, <https://doi.org/10.1103/PhysRevLett.116.132302>, arXiv:1602.01119.

- [57] S. Acharya, et al., Systematic studies of correlations between different order flow harmonics in Pb-Pb collisions at $\sqrt{s_{NN}} = 2.76$ TeV, Phys. Rev. C 97 (2) (2018) 024906, <https://doi.org/10.1103/PhysRevC.97.024906>, arXiv:1709.01127.
- [58] S. Acharya, et al., Linear and non-linear flow modes in Pb-Pb collisions at $\sqrt{s_{NN}} = 2.76$ TeV, Phys. Lett. B 773 (2017) 68–80, <https://doi.org/10.1016/j.physletb.2017.07.060>, arXiv:1705.04377.
- [59] C. Bernard, T. Burch, E.B. Gregory, D. Toussaint, C.E. DeTar, J. Osborn, S. Gottlieb, U.M. Heller, R. Sugar, QCD thermodynamics with three flavors of improved staggered quarks, Phys. Rev. D 71 (2005) 034504, <https://doi.org/10.1103/PhysRevD.71.034504>, arXiv:hep-lat/0405029.
- [60] A. Bazavov, et al., The chiral and deconfinement aspects of the QCD transition, Phys. Rev. D 85 (2012) 054503, <https://doi.org/10.1103/PhysRevD.85.054503>, arXiv:1111.1710.
- [61] M. Luzum, J.-Y. Ollitrault, Constraining the viscous freeze-out distribution function with data obtained at the BNL Relativistic Heavy Ion Collider (RHIC), Phys. Rev. C 82 (2010) 014906, <https://doi.org/10.1103/PhysRevC.82.014906>, arXiv:1004.2023.
- [62] M. Luzum, C. Gombeaud, J.-Y. Ollitrault, v_4 in ideal and viscous hydrodynamics simulations of nuclear collisions at the BNL Relativistic Heavy Ion Collider (RHIC) and the CERN Large Hadron Collider (LHC), Phys. Rev. C 81 (2010) 054910, <https://doi.org/10.1103/PhysRevC.81.054910>, arXiv:1004.2024.
- [63] D. Teaney, L. Yan, Non linearities in the harmonic spectrum of heavy ion collisions with ideal and viscous hydrodynamics, Phys. Rev. C 86 (2012) 044908, <https://doi.org/10.1103/PhysRevC.86.044908>, arXiv:1206.1905.
- [64] L. Yan, J.-Y. Ollitrault, v_4, v_5, v_6, v_7 : nonlinear hydrodynamic response versus LHC data, Phys. Lett. B 744 (2015) 82–87, <https://doi.org/10.1016/j.physletb.2015.03.040>, arXiv:1502.02502.
- [65] D. Hamby, Environ. Monit. Assess. 32 (1994) 135.
- [66] B.H. Alver, C. Gombeaud, M. Luzum, J.-Y. Ollitrault, Triangular flow in hydrodynamics and transport theory, Phys. Rev. C 82 (2010) 034913, <https://doi.org/10.1103/PhysRevC.82.034913>, arXiv:1007.5469.
- [67] F.G. Gardim, J.-Y. Ollitrault, Effective shear and bulk viscosities for anisotropic flow, Phys. Rev. C 103 (4) (2021) 044907, <https://doi.org/10.1103/PhysRevC.103.044907>, arXiv:2010.11919.
- [68] C. Shen, Z. Qiu, H. Song, J. Bernhard, S. Bass, U. Heinz, The iEBE-VISHNU code package for relativistic heavy-ion collisions, Comput. Phys. Commun. 199 (2016) 61–85, <https://doi.org/10.1016/j.cpc.2015.08.039>, arXiv:1409.8164, <https://u.osu.edu/vishnu/>.
- [69] H. Song, U.W. Heinz, Causal viscous hydrodynamics in 2+1 dimensions for relativistic heavy-ion collisions, Phys. Rev. C 77 (2008) 064901, <https://doi.org/10.1103/PhysRevC.77.064901>, arXiv:0712.3715.

PIII

**HIGHER-ORDER CORRELATIONS BETWEEN DIFFERENT
MOMENTS OF TWO FLOW AMPLITUDES IN PB-PB
COLLISIONS AT $\sqrt{s_{NN}} = 5.02$ TEV**

by

S. Acharya et al. (ALICE Collaboration)

Phys.Rev.C , 108 (2023).

Higher-order correlations between different moments of two flow amplitudes in Pb-Pb collisions at $\sqrt{s_{NN}} = 5.02$ TeV

S. Acharya *et al.**
(ALICE Collaboration)



(Received 12 April 2023; accepted 11 October 2023; published 14 November 2023)

The correlations between different moments of two flow amplitudes, extracted with the recently developed asymmetric cumulants, are measured in Pb-Pb collisions at $\sqrt{s_{NN}} = 5.02$ TeV recorded by the ALICE detector at the CERN Large Hadron Collider. The magnitudes of the measured observables show a dependence on the different moments as well as on the collision centrality, indicating the presence of nonlinear response in all even moments up to the eighth. Furthermore, the higher-order asymmetric cumulants show different signatures than the symmetric and lower-order asymmetric cumulants. Comparisons with state-of-the-art event generators using two different parametrizations obtained from Bayesian optimization show differences between data and simulations in many of the studied observables, indicating a need for further tuning of the models behind those event generators. These results provide new and independent constraints on the initial conditions and transport properties of the system created in heavy-ion collisions.

DOI: [10.1103/PhysRevC.108.055203](https://doi.org/10.1103/PhysRevC.108.055203)

I. INTRODUCTION

An important ongoing program in high-energy nuclear physics is the exploration of the phase diagram of quantum chromodynamics (QCD) at large values of temperature and/or density. In that regime, quark-gluon plasma (QGP), an extreme state of nuclear matter in which quarks and gluons are deconfined, is formed. Ultrarelativistic heavy-ion collisions at the BNL Relativistic Heavy Ion Collider (RHIC) and the CERN Large Hadron Collider (LHC) recreate the conditions in which the QGP can be produced and, consequently, studied. Properties of the QGP are typically portrayed by specifying its transport properties (e.g., shear or bulk viscosity), or its equation of state. To date, the QGP remains the state of matter with the smallest ratio of shear viscosity to entropy density (η/s) ever discovered. Besides scrutinizing the details of individual states of nuclear matter in the QCD phase diagram, it is equally important to constrain the nature of the transition between different states, i.e., whether it is a smooth crossover, first- or second-order phase transition, etc. Another extensive effort is allocated to the search for the critical point in the QCD phase diagram, whose existence is still not confirmed experimentally. Recent reviews can be found in Refs. [1–4].

In noncentral heavy-ion collisions, the measured correlations in momentum space among detected particles

are dominated by correlations originating from collective anisotropic flow [5]. Since anisotropic flow links the initial-state anisotropies in the collision geometry to the final-state anisotropies in momentum space, its measurements can be used to map out the whole history of the heavy-ion evolution. In particular, anisotropic flow is a sensitive probe of shear viscosity of the QGP, whose collective expansion is successfully described by its hydrodynamic response to the anisotropies in the initial-state geometry. By using a Fourier series decomposition of the azimuthal distribution $f(\varphi)$ of reconstructed particles, anisotropic flow is quantified with flow magnitudes v_n and symmetry planes Ψ_n [6]:

$$f(\varphi) = \frac{1}{2\pi} \left[1 + 2 \sum_{n=1}^{\infty} v_n \cos[n(\varphi - \Psi_n)] \right]. \quad (1)$$

Due to random fluctuations of the impact parameter vector (the vector connecting the centers of the two colliding ions) from one collision to another, this series cannot be obtained directly from the data using the simple relation $v_n e^{in\Psi_n} = \langle e^{in\varphi} \rangle$. Instead, multiparticle azimuthal correlations, which have additional advantages and are not influenced by these fluctuations for suitably chosen harmonics n_i , are utilized as experimental estimators according to the following analytic expression [7]:

$$\langle e^{i(n_1\varphi_1 + \dots + n_k\varphi_k)} \rangle = v_{n_1} \dots v_{n_k} e^{i(n_1\Psi_{n_1} + \dots + n_k\Psi_{n_k})}. \quad (2)$$

In the above equation, angular brackets indicate an average over all distinct sets of k azimuthal angles of the tracks obtained from the same event. Further technical details about multiparticle azimuthal correlations can be found in Refs. [8–11].

With the multiparticle correlation techniques, the correlations between different flow amplitudes v_n or symmetry

*Full author list given at the end of the article.

planes Ψ_n can be used to extract independent information about all stages in the heavy-ion evolution, when compared to the traditional measurements of individual flow amplitudes v_n [12]. Among them, the *symmetric cumulants* (SCs) were designed to study the genuine correlations (or cumulants) between the same lowest-order moments of two different flow amplitudes v_m^2 and v_n^2 . The simplest realization of SC observables in terms of flow amplitudes and the corresponding experimental estimators built from multiparticle azimuthal correlations is given by [11,13,14]

$$\begin{aligned} \text{SC}(m, n) &\equiv \langle v_m^2 v_n^2 \rangle - \langle v_m^2 \rangle \langle v_n^2 \rangle \\ &= \langle \langle e^{i(m\varphi_1 + n\varphi_2 - m\varphi_3 - n\varphi_4)} \rangle \rangle \\ &\quad - \langle \langle e^{im(\varphi_1 - \varphi_2)} \rangle \rangle \langle \langle e^{in(\varphi_1 - \varphi_2)} \rangle \rangle. \end{aligned} \quad (3)$$

In the first line above, $\langle \cdot \rangle$ indicates an average over all events. Meanwhile, $\langle \langle \cdot \rangle \rangle$ in the second line indicates that the averaging is performed in two steps: first over all distinct particle pairs or quadruplets in an event, and then in the second step the all-event averages are obtained from these single-event averages by weighting them with “number of combinations” multiplicity weights $M(M-1)$ and $M(M-1)(M-2)(M-3)$ for two- and four-particle correlations, respectively [10]. Furthermore, defined this way, SC observables are multivariate cumulants of flow amplitudes squared, and therefore they obey all nontrivial mathematical properties of multivariate cumulants for stochastic variables v_n^2 by definition [15]. The azimuthal correlators are then used only via Eq. (2) to estimate each individual term in the cumulant expansion [16], i.e., the cumulant expansion is not performed directly on the azimuthal angles.

The particular importance of SCs in flow studies is that they bring new information on QGP properties, as shown in Ref. [13]. From experimental measurements of various combinations of $\text{SC}(m, n)$ and their comparison to theoretical predictions, it was concluded that SCs are sensitive to the temperature dependence of η/s . On the other hand, the analyses of single flow amplitudes can only probe the average value $\langle \eta/s(T) \rangle$ [13,14,17]. Motivated by this access to new information on the system properties, studies were conducted to generalize the SCs from two to any number of harmonics using the cumulant formalism [18]. The resulting three-harmonic SCs were recently measured by the ALICE Collaboration in Pb-Pb collisions recorded in 2010 [19] and 2015 [17].

In parallel to the measurements of new flow observables, techniques like Bayesian optimization, where the model parameters are systematically varied to find the best fit to all selected experimental measurements, were applied. In recent years, multiple Bayesian studies were conducted to constrain the QGP transport properties and details of the initial conditions in Pb-Pb collisions [12,20–27]. While much information on Pb-Pb collisions was obtained through Bayesian analyses, the uncertainties on the extracted parameters are still quite large. As demonstrated in recent studies [12,27], this problem can partially be solved by increasing the scope of the input experimental data, either from various beam-energy ranges or from additional independent observables sensitive to the

initial conditions and system properties. In recent publications [12,27], dedicated sensitivity studies were also performed on sophisticated higher-harmonic observables for the first time, and it was concluded that the higher-order flow observables exhibit the highest sensitivity to the QGP transport properties.

The success of the SC observables in providing crucial input to Bayesian analyses has prompted a natural quest towards further generalizing the SCs to a new and independent set of multiharmonic observables involving different moments of the flow amplitudes without any influence from the symmetry planes. Among examples of such estimators are the *asymmetric cumulants* (ACs) [16]. As they probe the genuine correlations between different moments of the flow amplitudes, they can, by definition, extract new information (about event-by-event flow fluctuations, nonlinear response, etc.) which is inaccessible to the SCs themselves.

The structure of this article is as follows. Section II reviews the theoretical definitions of ACs and the corresponding experimental estimators. The technical details of the data analysis are introduced in Sec. III. In Sec. IV, the first experimental measurements of the ACs and their comparisons with state-of-the-art model predictions are presented. The article is summarized in Sec. V, while additional support material can be found in the Appendix.

II. DEFINITIONS AND SCOPE

This article presents the experimental measurements of the AC observables in their simplest realization, which involves only two flow amplitudes, evaluated for three different pairs of harmonics chosen to be the same as the ones studied in Ref. [12]. For a given pair of different harmonics (m, n) , measuring the genuine correlations between v_m^{2a} and v_n^{2b} with AC observables (where a and b are non-equal positive integers) leads to independent information, due to the uniqueness of each multivariate cumulant. Therefore, this analysis focuses on the new $\text{AC}_{a,b}(m, n)$ flow observables $\text{AC}_{2,1}(m, n)$, $\text{AC}_{3,1}(m, n)$, and $\text{AC}_{4,1}(m, n)$, to study correlations of the second, third, and fourth moments of v_m^2 with the first moment of v_n^2 . Two remarks have to be made: the lowest-order AC, $\text{AC}_{1,1}(m, n)$, corresponds to the well-known $\text{SC}(m, n)$ [Eq. (3)], showing that ACs are a natural generalization of SCs. Furthermore, AC observables are invariant under a simultaneous permutation of the indices and the harmonics, e.g., $\text{AC}_{a,b}(m, n) = \text{AC}_{b,a}(n, m)$. These properties will be exploited in Sec. IV to discuss the comparisons between $\text{AC}_{a,b}(m, n)$ and $\text{AC}_{a,b}(n, m)$.

The expressions for the ACs in terms of flow amplitudes are derived in Ref. [16] and are recalled as

$$\text{AC}_{2,1}(m, n) \equiv \langle v_m^4 v_n^2 \rangle - \langle v_m^4 \rangle \langle v_n^2 \rangle - 2 \langle v_m^2 v_n^2 \rangle \langle v_m^2 \rangle + 2 \langle v_m^2 \rangle^2 \langle v_n^2 \rangle, \quad (4)$$

$$\begin{aligned} \text{AC}_{3,1}(m, n) &\equiv \langle v_m^6 v_n^2 \rangle - \langle v_m^6 \rangle \langle v_n^2 \rangle - 3 \langle v_m^2 v_n^2 \rangle \langle v_m^4 \rangle - 3 \langle v_m^4 v_n^2 \rangle \langle v_m^2 \rangle \\ &\quad + 6 \langle v_m^4 \rangle \langle v_m^2 \rangle \langle v_n^2 \rangle + 6 \langle v_m^2 v_n^2 \rangle \langle v_m^2 \rangle^2 - 6 \langle v_m^2 \rangle^3 \langle v_n^2 \rangle, \end{aligned} \quad (5)$$

$$\begin{aligned}
AC_{4,1}(m, n) \equiv & \langle v_m^8 v_n^2 \rangle - \langle v_m^8 \rangle \langle v_n^2 \rangle - 4 \langle v_m^2 v_n^2 \rangle \langle v_m^6 \rangle \\
& - 6 \langle v_m^4 v_n^2 \rangle \langle v_m^4 \rangle + 6 \langle v_m^4 \rangle \langle v_n^2 \rangle - 4 \langle v_m^6 v_n^2 \rangle \langle v_m^2 \rangle \\
& + 8 \langle v_m^6 \rangle \langle v_m^2 \rangle \langle v_n^2 \rangle + 24 \langle v_m^2 v_n^2 \rangle \langle v_m^4 \rangle \langle v_m^2 \rangle \\
& + 12 \langle v_m^4 v_n^2 \rangle \langle v_m^2 \rangle^2 - 36 \langle v_m^4 \rangle \langle v_m^2 \rangle^2 \langle v_n^2 \rangle \\
& - 24 \langle v_m^2 v_n^2 \rangle \langle v_m^2 \rangle^3 + 24 \langle v_m^2 \rangle^4 \langle v_n^2 \rangle. \quad (6)
\end{aligned}$$

Due to their cumulant nature, much information can already be extracted from the SCs and ACs themselves. One example is the sign of the measured observables. In Ref. [13], it was shown how the event-by-event flow fluctuation patterns and the signatures of SC observables are related. This idea was also applied in the interpretation of the three-harmonic SC presented in Ref. [19]. For ACs, however, the defining equations are more involved and the direct physical interpretation of their signature, positive or negative, is not straightforward, even in the simplest case of $AC_{2,1}$. Another example is the observation of zero magnitude, indicating either an absence of genuine correlations between all involved variables or a trivial consequence of underlying symmetries. In the case of cumulants, however, this has to be interpreted carefully because in the absence of underlying symmetries either all the cumulants at given order are identically zero, or none of them are identically zero [15]. Therefore, the nonvanishing results for SC(2, 4), obtained previously in Refs. [13,14], imply that all of $AC_{a,b}(2, 4)$ must be nonvanishing as well, and the fact that some of them are consistent with zero would indicate only the limited sensitivity in the available datasets. In addition, a multivariate cumulant is nonvanishing if and only if all variables in its definition are correlated to each other [15].

As was done for the SCs, the ACs can also be normalized to remove the sensitivity of the observable to the strength of the individual harmonics and extract only the contribution of the genuine correlations between the various moments of v_m^2 and v_n^2 . This is done according to the standard procedure from Refs. [16,28], using

$$NAC_{a,1}(m, n) \equiv \frac{AC_{a,1}(m, n)}{\langle v_m^2 \rangle^a \langle v_n^2 \rangle}, \quad a = 2, \dots, 4. \quad (7)$$

Equations (4) to (6) cannot be used experimentally, as only the azimuthal angles of the final-state particles can be measured. Reliable experimental estimators for the various ACs were presented in Appendix C 2 of Ref. [16]. As an example, the expression corresponding to Eq. (4) is

$$\begin{aligned}
AC_{2,1}(m, n) = & \langle \langle e^{i(m\varphi_1 + m\varphi_2 + n\varphi_3 - m\varphi_4 - m\varphi_5 - n\varphi_6)} \rangle \rangle \\
& - \langle \langle e^{im(\varphi_1 + \varphi_2 - \varphi_3 - \varphi_4)} \rangle \rangle \langle \langle e^{in(\varphi_1 - \varphi_2)} \rangle \rangle \\
& - 2 \langle \langle e^{i(m\varphi_1 + n\varphi_2 - m\varphi_3 - n\varphi_4)} \rangle \rangle \langle \langle e^{im(\varphi_1 - \varphi_2)} \rangle \rangle \\
& + 2 \langle \langle e^{im(\varphi_1 - \varphi_2)} \rangle \rangle^2 \langle \langle e^{in(\varphi_1 - \varphi_2)} \rangle \rangle. \quad (8)
\end{aligned}$$

Each of the azimuthal correlators in the above expression is isotropic (i.e., invariant under the transformation $\varphi \rightarrow \varphi + \alpha$ where α is an arbitrary angle), which ensures that ACs are not affected by random event-by-event fluctuations of the impact parameter vector. In addition, in each azimuthal correlator, each harmonic appears an equal number of times with positive

and negative signs, which ensures that any dependence on symmetry planes is canceled out exactly [see Eq. (2)].

III. DATA ANALYSIS

The analysis is performed with data from Pb-Pb collisions at the center-of-mass energy per nucleon pair $\sqrt{s_{NN}} = 5.02$ TeV recorded by the ALICE detector in 2015 during the LHC Run 2 period.

A detailed description of the ALICE detector and its sub-detectors can be found in Refs. [29,30]. The time projection chamber (TPC) [31] was used to reconstruct the charged-particle tracks and measure their momenta. Two scintillator arrays, V0A and V0C [29,32], were used for triggering and the determination of the centrality of the collisions [33]. The TPC, V0A, and V0C cover the full azimuthal range within the pseudorapidity ranges $|\eta| < 0.9$, $2.8 < \eta < 5.1$, and $-3.7 < \eta < -1.7$, respectively.

The detector closest to the beam pipe is the inner tracking system (ITS) [34,35], which, besides the TPC, is also used for track reconstruction. It covers the full range in azimuthal angle and consists of six silicon layers, with three different detector technologies. The two innermost layers, the silicon pixel detectors (SPD), have a high spatial granularity making them ideal for reconstructing both primary and secondary vertices.

Minimum bias (MB) events are triggered by a coincident signal in both the V0A and V0C. The selected MB Pb-Pb events all have a reconstructed primary vertex within ± 8.0 cm from the nominal interaction point along the beam direction. Background events like beam-gas collisions and pileup were removed using the correlation between the information from the V0 detector and the SPD, as well as the correlation between the number of reconstructed tracks and the information from the ITS and TPC. A further reduction of the pileup events was obtained using the correlation between the information provided by the SPD and by the time-of-flight detector [36]. Furthermore, the data taken with each of the two possible directions of the magnetic field in the central barrel are both considered for the analysis. Finally, an additional event criterion is applied after the track selection to reject all remaining events with less than ten reconstructed tracks. This requirement is motivated by the calculation of the multiparticle azimuthal correlators themselves, and their corresponding event-by-event multiplicity weights. For a k -particle correlator, at least k tracks are needed to have a valid expression for the correlator and corresponding multiplicity weight. This criterion is set to ten tracks, as this is the minimum number of tracks needed to calculate the largest correlator in this analysis, $AC_{4,1}(m, n)$ (see Appendix C in Ref. [16] for the full estimator). After all event selections are applied, approximately 5×10^7 events in the centrality range of 5% to 60% are used in the analysis. Furthermore, this range is divided into the following centrality classes: the two central classes 5–10% and 10–20% and the four semicentral classes 20–30%, 30–40%, 40–50%, and 50–60%.

Tracks are reconstructed using the combined information given by the ITS and the TPC. These tracks are selected to be within $|\eta| < 0.8$ and $0.2 < p_T < 5$ GeV/ c , where p_T is the

transverse momentum. The low p_T cutoff is implemented for reducing biases due to a smaller reconstruction efficiency at very low transverse momentum, while the high p_T cutoff is chosen for suppressing the contribution to the anisotropies in the measured azimuthal correlations from jets. In order to avoid contributions from secondary particles, each track is required to have a distance of closest approach (DCA) to the primary vertex of less than 2 cm in the longitudinal direction and less than $0.0105 + 0.0350/p_T^{1.1}$ cm in the transverse direction, meaning a value ranging from 0.016 cm at $p_T = 5.0$ GeV/c to 0.22 cm at $p_T = 0.2$ GeV/c. Additionally, each track is required to have a minimum of 70 TPC space points out of the maximum of 159, and a χ^2 value per space point from the track fit to be within the range of 0.1 to 2.5. The tracks are required to have a minimum of two hits in the ITS. Requirements were also added to reject tracks with a kink topology (i.e., tracks that appear to change direction due to multiple scatterings and/or weak decays).

Corrections for both nonuniform reconstruction efficiency (NUE) as a function of transverse momentum and nonuniform acceptance (NUA) as a function of azimuthal angle are applied in the same way as in Refs. [11,19,37]. For the NUE corrections, a HIJING (Heavy-Ion Jet Interaction Generator) [38] simulation with a GEANT3 [39] detector model is used to correct for the effects of track reconstruction efficiency and contamination from secondary particles by constructing a p_T -dependent track weighting correction. The NUA corrections are obtained in a data-driven manner, based on the method presented in Ref. [11]. Finally, the nonflow contribution from the two-particle correlations appearing in the denominator of the NAC is suppressed with the use of a pseudorapidity gap $|\Delta\eta| > 1$. As the ACs themselves were shown to be robust against nonflow [16], no gap is used in their computation.

Obtaining the statistical uncertainty through standard error propagation is impractical due to both nontrivial functional dependence and many covariance terms. Therefore, in this analysis, the statistical uncertainties were determined using the standard subsampling procedure (see Appendix F in Ref. [16]).

The systematic uncertainties are estimated by independent variations of each selection criterion. The significance of each variation is determined according to the Barlow test [40]. For each variation, the results for $AC_{a,b}(m, n)$ are compared with the ones obtained with the default selection, taking into account the correlations between their statistical uncertainties. If the deviation is larger than one σ , where σ is the uncertainty on the difference, the variation is deemed significant according to the Barlow test and is included into the quadratic sum to get the total systematic uncertainties. Each selection criterion variation is described below and the trend of their relative deviations with respect to the default values observed in semicentral collisions (collisions in the centrality range 20–60%) is reported in parentheses. Due to the small size of the signal, the variations measured in central events (centrality up to 20%) and for higher-order observables can fluctuate more significantly than the ones indicated here.

The effects of the centrality determination are estimated by changing the default V0 estimator to the SPD (20%). The quality of the event selection is further tested by varying

the longitudinal position of the primary vertex from ± 8 cm to ± 6 cm (10%), and by applying a tighter pileup rejection factor (4%). Furthermore, the impact of the two configurations of the magnetic field polarity in the solenoid magnet of ALICE is investigated by performing the same analysis on the data sets taken for each orientation separately (5%). The minimum number of space points in the TPC required for the track reconstruction is increased from 70 to 80 (2%), and the quality of the reconstruction fit per TPC cluster is reduced from $0.1 < \chi^2 < 2.5$ to $0.1 < \chi^2 < 2.3$ (4%). The longitudinal DCA is also tightened from 2 cm to 1 cm. It has to be noticed that this systematic variation mainly affects the higher-order combinations (3–60%). Finally, a change of the default tracking requirements to the so-called hybrid tracks, which are TPC-ITS tracks with looser DCA requirements in the transverse plane and along the beam axis, leads to an effect on all studied observables (0–30%).

IV. RESULTS AND DISCUSSION

The results obtained in this analysis are first presented together, in order to gain insights on the strength of the different multiharmonic correlations and their dependence on centrality and cumulant order. Then, specific comparisons between the data and the model predictions are presented for a few selected ACs and NACs.

The centrality dependence of the thirty-four different $AC_{a,b}(m, n)$ and $NAC_{a,b}(m, n)$ is shown in Fig. 1. However, due to their large uncertainties, $NAC_{4,1}(m, n)$ and $NAC_{1,4}(m, n)$ are not presented here. As the results for $AC_{a,b}(2, 3)$ and $AC_{a,b}(2, 4)$ [Figs. 1(a) and 1(c), respectively] present similar behaviors, albeit with different signs, they are here discussed together. In the following lines, the notation (m, n) thus stands for both pairs of harmonics (2,3) and (2,4). A dependence of the magnitude of the genuine correlations on the cumulant order is observed. The results for $SC(m, n) \equiv AC_{1,1}(m, n)$ present the largest signals, followed by $AC_{2,1}(m, n)$, while $AC_{3,1}(m, n)$ and $AC_{4,1}(m, n)$ are several orders of magnitude smaller. This decreasing effect is more pronounced for the mirror combinations $AC_{b,a}(m, n)$ when compared to their respective counterparts. The splitting between the results for $AC_{a,b}(m, n)$ and its mirror $AC_{b,a}(m, n)$ is also present for $NAC_{a,b}(2, 3)$ and $NAC_{a,b}(2, 4)$ [Fig. 1(b) and 1(d), respectively]. While the results for $NAC_{2,1}(2, 3)$ and $NAC_{3,1}(2, 3)$ demonstrate a trend similar as $NSC(2, 3)$, albeit with smaller magnitudes, the ones for $NAC_{2,1}(2, 4)$ and $NAC_{3,1}(2, 4)$ are in good agreement with $NSC(2, 4)$ and deviate only in more peripheral collisions. In both panels, the mirror combinations (open markers) show an increase of the magnitude with the cumulant order. Finally, Figs. 1(e) and 1(f) present the centrality dependence of the different orders of $AC_{a,b}(3, 4)$ and $NAC_{a,b}(3, 4)$, respectively. The results for $AC_{a,b}(3, 4)$ present the same ordering of the magnitudes with the order of the AC itself, as observed in the two other pairs of harmonics. However, no splitting between $AC_{a,1}(3, 4)$ and $AC_{1,a}(3, 4)$ can be seen at any order $a = 1, \dots, 4$ within uncertainties.

The measurements are compared with results from simulated events generated with the state-of-the-art chain of

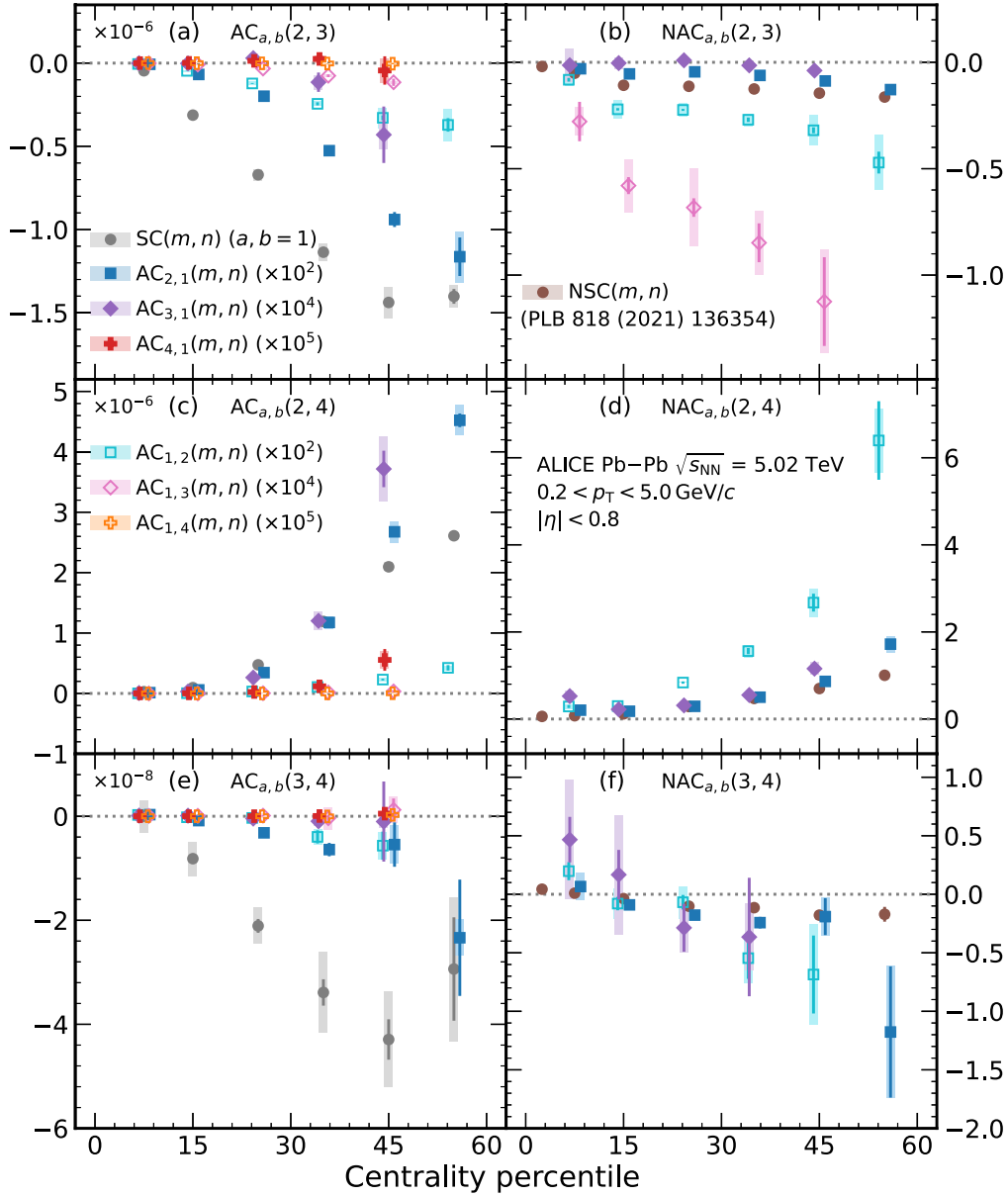


FIG. 1. Centrality dependence of the different orders of $AC_{a,b}(m,n)$ (left) and $NAC_{a,b}(m,n)$ (right) for four pairs of indices (a,b) and three pairs of harmonics (m,n) in Pb-Pb collisions at $\sqrt{s_{NN}} = 5.02$ TeV. The mirror combinations of $AC_{a,b}(m,n)$ (closed markers), i.e., $AC_{b,a}(m,n)$, are indicated with open markers and similar color scheme. The statistical (systematic) uncertainties are shown with lines (boxes). The data points are shifted horizontally for visibility.

models $T_{R}ENTo + VISH(2+1) + UrQMD$ [41–44], which will be referred to here as $T_{R}ENTo + iEBE-VISHNU$. This model chain consists of the $T_{R}ENTo$ model [45] for the initial conditions, which are connected by free streaming to a 2 + 1-dimensional hydrodynamical model $VISH(2+1)$ [41]. The description of the heavy-ion evolution after the collision is continued after partlization with a hadronic cascade ($UrQMD$) model [43,44]. The initial conditions, the specific shear viscosity $\eta/s(T)$, the specific bulk viscosity $\zeta/s(T)$, and other free parameters of this hybrid model, for instance, the Gaussian nucleon width and the minimum inter-nucleon distance, are obtained from a global Bayesian analysis. The data-to-model comparisons are performed with two sets of best-fit parametrizations given by maximum a

posteriori (MAP) from two independent Bayesian analysis groups. As the values for these two sets of best-fit parameters agree within their respective uncertainties from the Bayesian analysis, this work allows the observation of the deviations between the two parametrizations in the predictions of observables that were not used in the Bayesian optimization. The extraction of the Duke 2019 parametrization [22] used a series of ALICE measurements (two-particle correlations, charged-particle multiplicities, etc.) as inputs into the Bayesian analysis. However, most of the used data are from Pb-Pb collisions at $\sqrt{s_{NN}} = 2.76$ TeV and only a subset of available flow observables were used. The Jyväskylä 2022 parametrization [12] utilized for the first time higher-order flow observables and data from Pb-Pb collisions at both

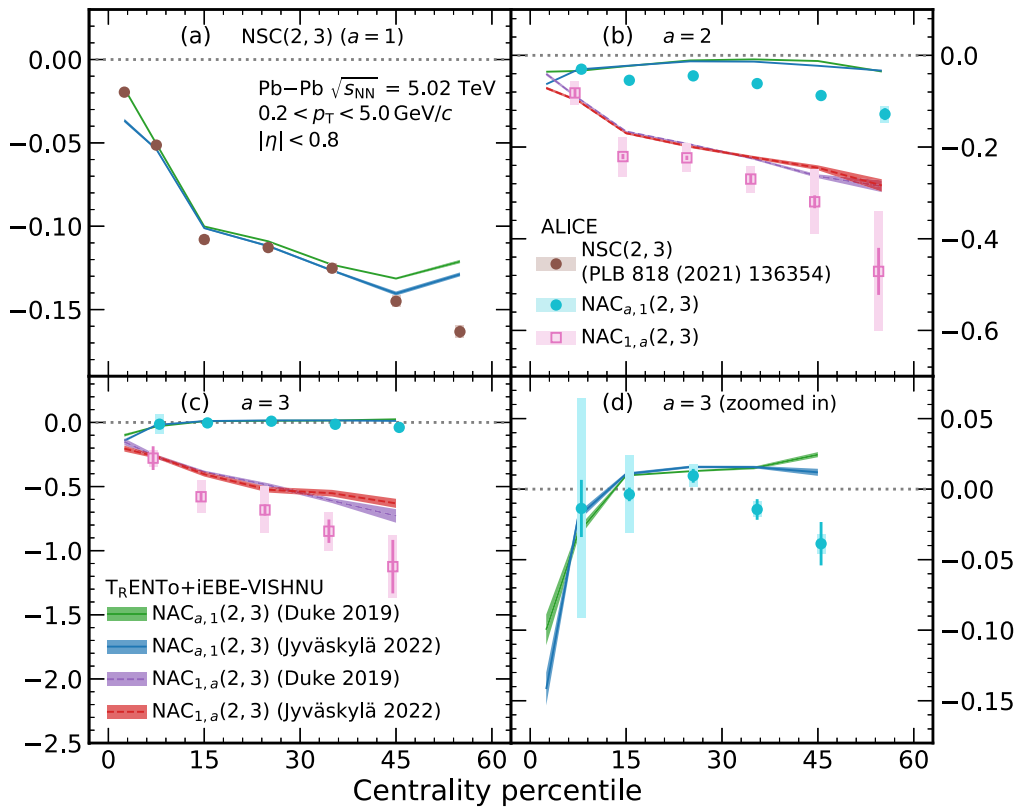


FIG. 2. Centrality dependence of the different orders $a = 1, \dots, 3$ of $NAC_{a,1}(2, 3)$ (cyan closed circles) and $NAC_{1,a}(2, 3)$ (pink open squares) compared with the theoretical predictions from $T_{R}ENTo + iEBE-VISHNU$ for the Duke 2019 [22] and Jyväskylä 2022 [12] parametrizations. Panel (d) shows a close-up of the results of $NAC_{3,1}(2, 3)$. The statistical uncertainties in the calculations are indicated by the thicknesses of the colored bands. The data points for $NSC(2, 3)$ are taken from Ref. [17].

$\sqrt{s_{NN}} = 2.76$ TeV and $\sqrt{s_{NN}} = 5.02$ TeV. New observables, such as SC [13, 14, 17, 19] and flow harmonic mode couplings [37], recently measured by the ALICE Collaboration, are more sensitive to the hydrodynamic transport coefficients η/s and ζ/s . This resulted in a reduction of the uncertainties of the extracted transport coefficients [12]. In these hydrodynamical model calculations, all the kinematic selections, such as p_T and η ranges, are matched with the ones reported in this article. In addition, the observables are extracted from the simulations using the same experimental analysis techniques.

Figure 2 shows the comparisons of the experimental data for $NAC_{a,b}(2, 3)$ with the predictions from hydrodynamic simulation using the Duke 2019 and Jyväskylä 2022 parametrizations. As discussed above for the data, the same splitting between $NAC_{a,1}(2, 3)$ and $NAC_{1,a}(2, 3)$ ($a = 2, 3$) can be observed in both model calculations. The negative sign is visible both for $NSC(2, 3)$ [Fig. 2(a)] and for some AC observables in the same pair of flow harmonics. The notable exception here is $NAC_{3,1}(2, 3)$, which is close to zero for the data and predicted to be positive in semicentral collisions by both model parametrizations [see Fig. 2(d) for a close-up of the results]. Furthermore, no major difference can be seen between the predictions from Duke 2019 and Jyväskylä 2022 for any of the observables in Fig. 2. As the linear response $v_n = k_n \epsilon_n$ ($n = 2, 3$), where k_n are the linear response coefficients and ϵ_n the eccentricities in the initial state, dominates in central collisions, the genuine correlations between v_2 and

v_3 are expected to be sensitive only to the initial conditions in this regime. Therefore, a possible explanation of the similar predictions is the use of $T_{R}ENTo$ for both parametrizations. Future studies would thus benefit from the comparison between different initial state models. It also has to be noted that both calculations reproduce the experimental data only qualitatively, and thus the use of such new measurements as input in future Bayesian studies would allow further constraints on the descriptions of the early stages of heavy-ion collisions.

The comparison of the results for $AC_{a,b}(2, 4)$ with the calculations from both model parametrizations is shown in Fig. 3. Overall, the behavior of the experimental data is better reproduced by the Jyväskylä 2022 parametrization, quantitatively for SC and qualitatively for the higher orders. The model predictions are also closer to the experimental values for $AC_{1,a}(2, 4)$ than for $AC_{a,1}(2, 4)$, for $a = 2, 3, 4$. The observable $AC_{a,1}(2, 4)$ presents the same positive sign as $SC(2, 4)$. This is the case as well for $AC_{1,2}(2, 4)$ and $AC_{1,3}(2, 4)$ in semicentral collisions [see Fig. 3(e) for a close-up of the latter observable]. However, both experimental and theoretical results for $AC_{1,4}(2, 4)$ are in agreement with zero within uncertainties up to centralities of 30% for the data and 45% for the model [Fig. 3(f)]. Because of previous nonvanishing results for $SC(2, 4)$, this indicates that the used sample of Run 2 data is not sufficient to extract nonvanishing values for these particular AC observables. Past studies have shown the existence of a nonlinear response between the fourth-order flow

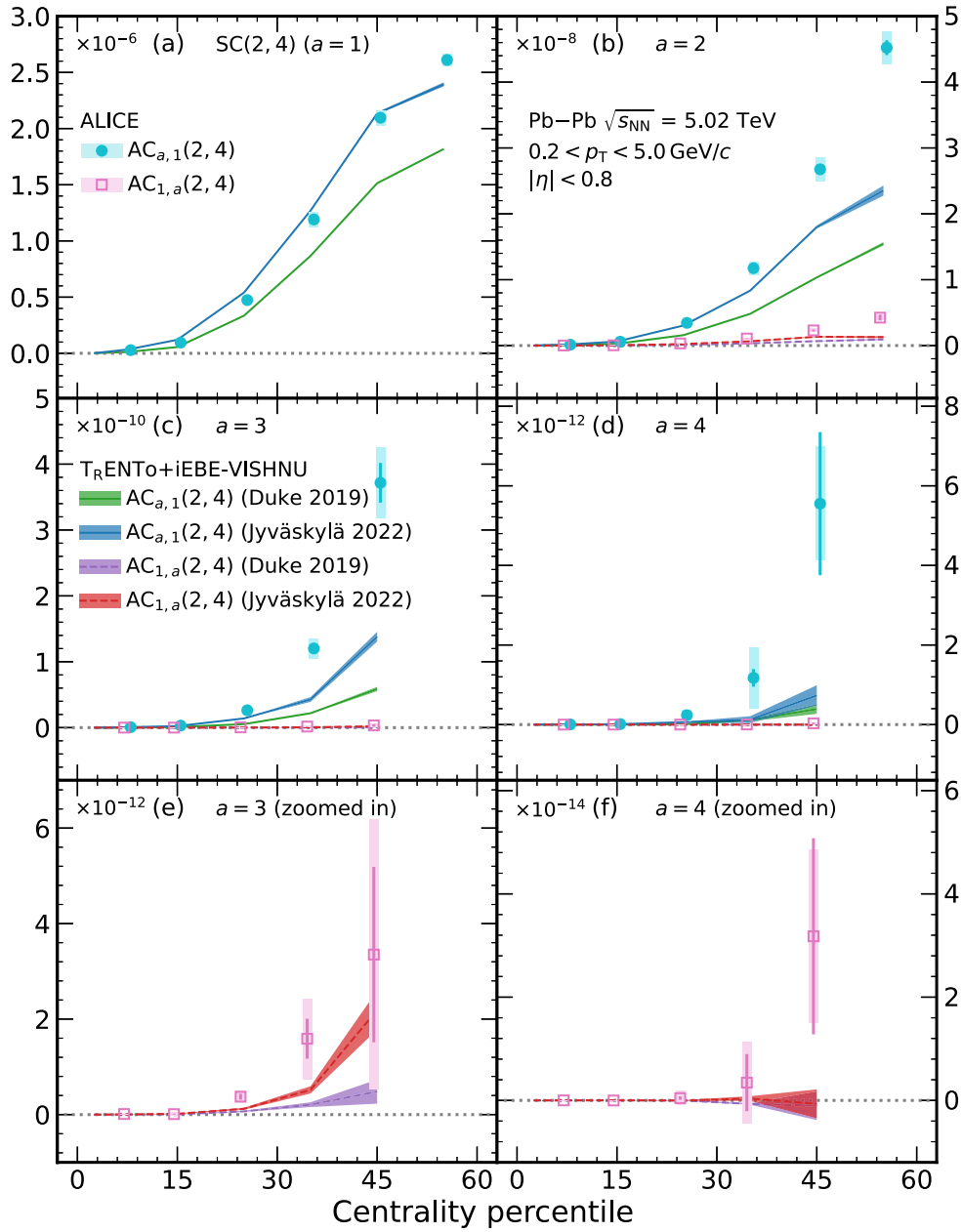


FIG. 3. Centrality dependence of the different orders $a = 1, \dots, 4$ of $AC_{a,1}(2, 4)$ (cyan closed circles) and $AC_{1,a}(2, 4)$ (pink open squares) compared with the theoretical predictions from $T_R ENT o + iEBE-VISHNU$ for the Duke 2019 [22] and Jyväskylä 2022 [12] parametrizations. Panels (e) and (f) show a close-up of the results of $AC_{1,3}(2, 4)$ and $AC_{1,4}(2, 4)$, respectively. The statistical uncertainties in the calculations are indicated by the thicknesses of the colored bands.

amplitude v_4 and the initial-state ellipticity term ϵ_2^2 , which is dominant in noncentral collisions [46,47]. Furthermore, higher-order harmonics are more sensitive to small variations of η/s and ζ/s than the lower-order coefficients [47–49]. This latter point was further discussed in recent Bayesian estimations [12], where higher-order cumulants of flow amplitudes exhibit better sensitivity to QGP properties when compared to the traditional lower-order flow observables, generalizing the findings from Refs. [13,14,49]. The remaining tensions between data and predictions observed in the current analysis for $AC_{1,a}(2, 4)$ are thus a sign that the measurements of the genuine correlations between v_2^2 and v_4^{2a} can bring additional

input on the higher-order terms of the nonlinear response of v_4 . Comparisons between the initial and final state predictions for these observables would be one of the crucial steps in that direction, as any discrepancies between those would shed more light on the hydrodynamic description of v_4 in the models.

The experimental results for $NAC_{a,b}(3, 4)$ are compared with the theoretical calculations from the two model parametrizations, as shown in Fig. 4. Similarly to the results for the data, the predictions for $NAC_{2,1}(3, 4)$ and $NAC_{1,2}(3, 4)$ are in good agreement with each other within uncertainties [Fig. 4(b)], for both the Duke 2019 and

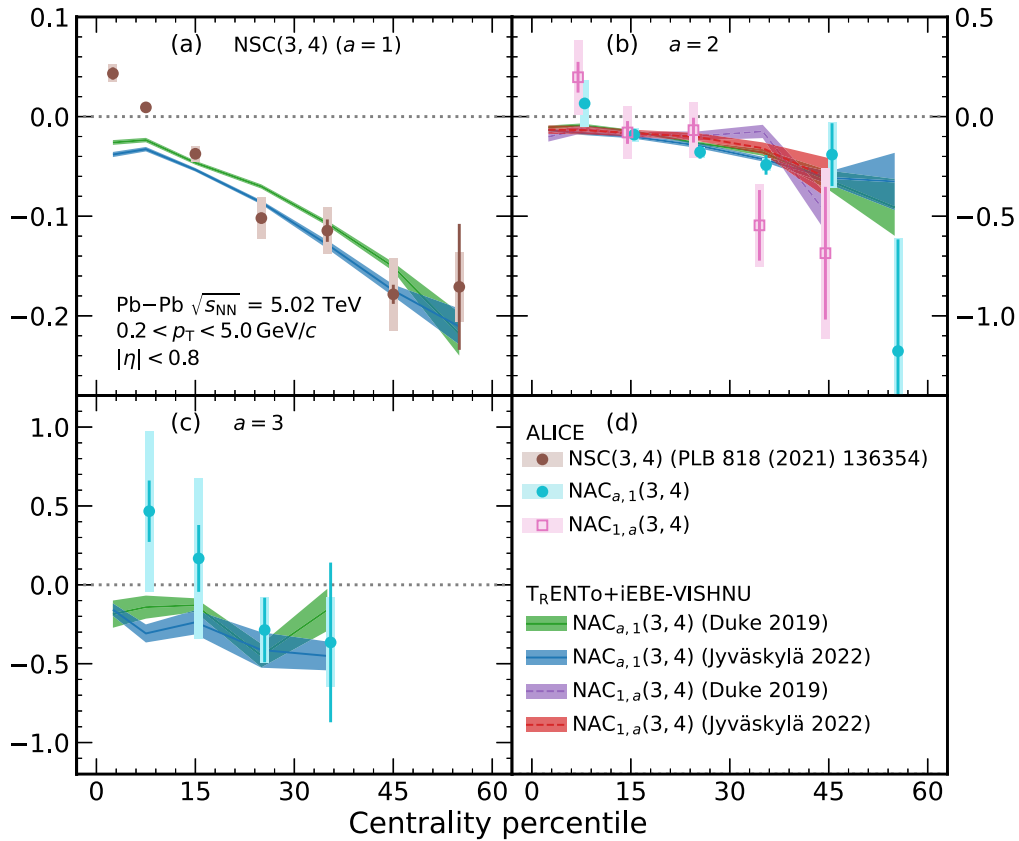


FIG. 4. Centrality dependence of the different orders $a = 1, \dots, 3$ of $NAC_{a,1}(3, 4)$ (cyan closed circles) and $NAC_{1,a}(3, 4)$ (pink open squares) compared with the theoretical predictions from $T_{\text{R}}\text{ENTo} + i\text{EBE-VISHNU}$ for the Duke 2019 [22] and Jyväskylä 2022 [12] parametrizations. The statistical uncertainties in the calculations are indicated by the thicknesses of the colored bands. The data points for $NSC(3, 4)$ are taken from Ref. [17].

Jyväskylä 2022 parametrizations. Additionally, previous studies [46] have shown that the measurements of v_4 can be explained by a contribution from ϵ_2^2 and none from ϵ_3 . The observed agreement may then originate from the interplay between the different stages of the evolution of the heavy-ion collisions. For instance, an agreement between the initial-state predictions for $NAC_{2,1}(3, 4)$ and $NAC_{1,2}(3, 4)$ could indicate an absence of nonlinear response between the higher orders of ϵ_3 and v_4 . Similarly, different initial-state predictions could mean that the hydrodynamic evolution differently impacts the correlations between the higher moments of ϵ_3 with v_4 and the ones between ϵ_3 and the higher moments of v_4 . However, these non-linear hydrodynamic effects would be such that the two observables converge onto each other in the final state. Future studies of both the initial and final state, for instance, comparisons of the AC results from this study with initial-state predictions, would help in understanding the origin of the different behaviors—splitting or no splitting—observed in the various combinations of NAC. Furthermore, it is noted that there is good agreement between the predictions obtained from the Duke 2019 and Jyväskylä 2022 parametrizations, and that they both capture quantitatively the experimental data for centralities higher than 15%. However, none of the parametrizations capture the sign change between central and semicentral events observed in the experimen-

tal data. In Ref. [17], this effect was already observed for $NSC(3, 4)$, where the sign change could be reproduced by models using AMPT initial conditions but not by the ones using $T_{\text{R}}\text{ENTo}$. It is therefore expected that future precision measurements of $NAC_{a,b}(3, 4)$ and their use as input data in Bayesian studies would help in tuning the different details of system evolution as a function of the collision centrality in the models.

Figure 5 summarizes the trends and ordering obtained for $NAC_{a,b}(2, 3)$ and $NAC_{a,b}(2, 4)$.

The main findings of this study on ACs and NACs are summarized here as follows:

- (1) The magnitude of the NAC observables varies with different moments as well as with the collision centrality, indicating that nonlinear responses are also reflected in higher moments.
- (2) While the $NAC_{2,1}(2, 3)$ observable shows a negative decreasing magnitude toward peripheral collisions, the higher-moment correlations, $NAC_{3,1}(2, 3)$, are close to zero except in the most central collisions. The model calculations show a similar trend, but underestimate the data.
- (3) Interestingly, the $AC_{3,1}(2, 4)$ observable is much stronger than $AC_{1,3}(2, 4)$ in peripheral collisions. The

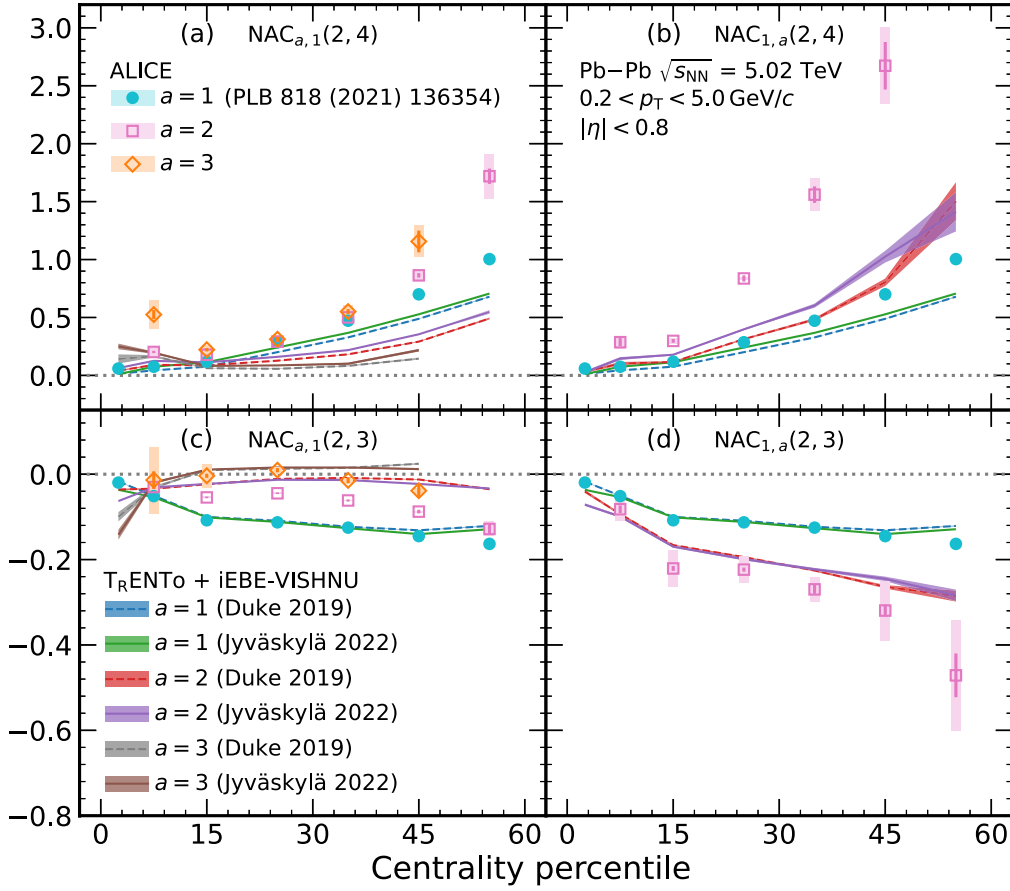


FIG. 5. Centrality dependence of the different orders $a = 1, \dots, 3$ of $NAC_{a,1}(m, n)$ and $NAC_{1,a}(m, n)$ compared with the theoretical predictions from $T_{R}ENTo + iEBE-VISHNU$ for the Duke 2019 [22] and Jyväskylä 2022 [12] parametrizations. The last point of $NAC_{1,2}(2, 4)$ and the results for $NAC_{1,3}(2, 3)$ are not shown for visibility purposes. The statistical uncertainties in the calculations are indicated by the thicknesses of the colored bands. The data points for $a = 1$ are taken from Ref. [17].

$AC_{1,3}(2, 4)$ observable is close to zero, while the $AC_{1,4}(2, 4)$ is compatible with zero within uncertainties. As nonzero measurements for $SC(2, 4)$ [13] indicate that v_2^2 and v_4^2 are positively correlated, this does not mean that the higher-order fluctuations of v_2^2 and v_4^2 are uncorrelated, but that the used data sample is not enough to extract their nonvanishing values.

- (4) $NAC_{a,1}(2, n)$ shows an inverted dependence on the moments when compared to $NAC_{1,a}(2, n)$ for $n = 3, 4$. No splitting is observed for $NAC_{a,1}(3, 4)$ and $NAC_{1,a}(3, 4)$.

The agreement between model and data for each cumulant order is now quantified with the χ^2 test (χ^2/N_{dof}), performed as in Ref. [14]:

$$\chi^2/N_{\text{dof}} = \frac{1}{N_{\text{dof}}} \sum_{i=1}^{N_{\text{dof}}} \frac{(y_i - f_i)^2}{\sigma_i^2}, \quad (9)$$

where y_i (f_i) is a measurement (model) value in a centrality bin i . The systematic and statistical uncertainties from the data are combined in quadrature $\sigma_i^2 = \sigma_{i,\text{stat}}^2 + \sigma_{i,\text{sys}}^2 + \sigma_{f_i,\text{stat}}^2$, to-

gether with the statistical errors of the model calculations. The quantity N_{dof} corresponds to the number of bins in the centrality range used in χ^2 calculations. The results are shown in Fig. 6 for both model parametrizations indicated on the upper x axis. A grey box indicates that the experimental data have large uncertainties, which may influence the interpretation of the obtained χ^2 value. For instance, an agreement between these large uncertainties of the data and the predictions could bias the χ^2 test, leading to an artificially small value. Such bias would then be resolved with a larger data sample. As they were not measured in the current analysis, $NAC_{1,3}(2, 4)$ and $NAC_{1,3}(3, 4)$ are shown with a white filling. A better agreement between the data and a model parametrization is represented by lower χ^2 values. In Fig. 6, it is observed that the model description is better for higher-order harmonics such as all $AC_{a,b}(3, 4)$, and higher-order moments such as $AC_{4,1}(m, n)$, as well as most of $NAC_{2,1}(m, n)$ and $NAC_{3,1}(m, n)$. Generally, the Jyväskylä 2022 parametrization describes the data better than the Duke 2019 parametrization. This result is expected as a larger set of data and higher-order observables are included in Jyväskylä 2022. However, Duke 2019 still provides better predictions than the newer parametrization in the case of $SC(2, 3)$, $AC_{3,1}(2, 3)$ and

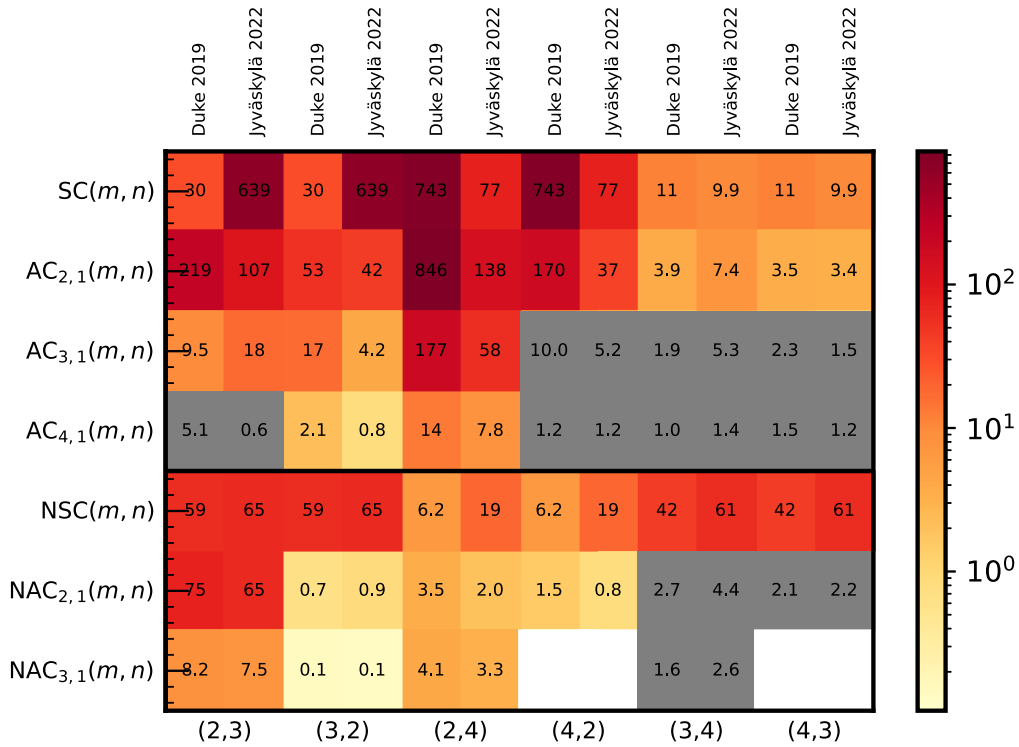


FIG. 6. Values for χ^2 test calculated between the data and two different model calculations for all ACs and NACs and all pairs of harmonics presented in this paper. The observables with large uncertainties are indicated with a grey filling, while an absence of observable (see Fig. 1) is shown with a white filling.

NSC(m, n) for all three pairs of harmonics. It is also known that Jyväskylä 2022 has a deviation in its prediction of v_2 at $\sqrt{s_{NN}} = 5.02$ TeV [12], which may explain the differences observed in the descriptions of ACs involving v_2 but not of the NACs. Ultimately, the χ^2 test indicates that the independent AC observables are needed as input for future Bayesian analyses in order to reduce the uncertainty on the initial conditions and/or on the hydrodynamic transport coefficients such as $\eta/s(T)$ and $\zeta/s(T)$.

V. SUMMARY

In conclusion, the first measurements of the correlations between different moments of two flow amplitudes in Pb-Pb collisions at $\sqrt{s_{NN}} = 5.02$ TeV, using asymmetric cumulants, are shown. This work is a generalization of the previous measurements obtained with symmetric cumulants, proven to have an increased sensitivity to the initial conditions and medium properties. Due to the cumulant uniqueness, each AC has access to new and independent information unreachable by measuring the SC only. Therefore, this article provides new measurements and resulting additional constraints for 34 new observables. A dependence of the magnitude of the correlations on the moments and the centrality of the collision is observed, showing an influence of the non-linear response between the higher-moments as well. Furthermore, it has been seen that an increasing (decreasing) dependence with the moments for a given pair (m, n) in NAC _{$a,1$} (m, n) generally leads to the decreasing (increasing) dependence for the mirror com-

bination NAC _{$1,a$} (m, n). The comparison of the experimental results with the predictions from two different parametrizations of the T_RENTo + iEBE-VISHNU model chain obtained with Bayesian analyses shows a need for further improvements of the initial conditions and nonlinear response. Due to the high sensitivity of these measurements to the model parameters [12,27], the results can improve the current understanding of the detailed nucleon structure in nuclei [50,51], the nuclear skin effect [52], and the preequilibrium phase [53–58]. Incorporating these details into the models used by the Duke and Jyväskylä groups will lead to a better quantitative understanding of the properties of QCD matter.

ACKNOWLEDGMENTS

The ALICE Collaboration would like to thank all its engineers and technicians for their invaluable contributions to the construction of the experiment and the CERN accelerator teams for the outstanding performance of the LHC complex. The ALICE Collaboration gratefully acknowledges the resources and support provided by all Grid centres and the Worldwide LHC Computing Grid (WLCG) collaboration. The ALICE Collaboration acknowledges the following funding agencies for their support in building and running the ALICE detector: A. I. Alikhanyan National Science Laboratory (Yerevan Physics Institute) Foundation (ANSL), State Committee of Science and World Federation of Scientists (WFS), Armenia; Austrian Academy of Sciences, Austrian Science Fund (FWF) (M 2467-N36) and Nationalstiftung für Forschung,

Technologie und Entwicklung, Austria; Ministry of Communications and High Technologies, National Nuclear Research Center, Azerbaijan; Conselho Nacional de Desenvolvimento Científico e Tecnológico (CNPq), Financiadora de Estudos e Projetos (Finep), Fundação de Amparo à Pesquisa do Estado de São Paulo (FAPESP), and Universidade Federal do Rio Grande do Sul (UFRGS), Brazil; Bulgarian Ministry of Education and Science, within the National Roadmap for Research Infrastructures 2020–2027 (object CERN), Bulgaria; Ministry of Education of China (MOEC), Ministry of Science & Technology of China (MSTC), and National Natural Science Foundation of China (NSFC), China; Ministry of Science and Education and Croatian Science Foundation, Croatia; Centro de Aplicaciones Tecnológicas y Desarrollo Nuclear (CEADEN), Cubaenergía, Cuba; Ministry of Education, Youth and Sports of the Czech Republic, Czech Republic; The Danish Council for Independent Research–Natural Sciences, the VILLUM FONDEN, and Danish National Research Foundation (DNRF), Denmark; Helsinki Institute of Physics (HIP), Finland; Commissariat à l’Energie Atomique (CEA) and Institut National de Physique Nucléaire et de Physique des Particules (IN2P3) and Centre National de la Recherche Scientifique (CNRS), France; Bundesministerium für Bildung und Forschung (BMBF) and GSI Helmholtzzentrum für Schwerionenforschung GmbH, Germany; General Secretariat for Research and Technology, Ministry of Education, Research and Religions, Greece; National Research, Development and Innovation Office, Hungary; Department of Atomic Energy Government of India (DAE), Department of Science and Technology, Government of India (DST), University Grants Commission, Government of India (UGC), and Council of Scientific and Industrial Research (CSIR), India; National Research and Innovation Agency–BRIN, Indonesia; Istituto Nazionale di Fisica Nucleare (INFN), Italy; Japanese Ministry of Education, Culture, Sports, Science and Technology (MEXT) and Japan Society for the Promotion of Science (JSPS) KAKENHI, Japan; Consejo Nacional de Ciencia (CONACYT) y Tecnología, through Fondo de Cooperación Internacional en Ciencia y Tecnología (FONCICYT) and Dirección General de Asuntos del Personal Académico (DGAPA), Mexico; Nederlandse Organisatie voor Wetenschappelijk Onderzoek (NWO), Netherlands; The Research Council of Norway, Norway; Commission on Science and Technology for Sustainable Development in the South (COMSATS), Pakistan; Pontificia Universidad Católica del Perú, Peru; Ministry of Education and Science, National Science Centre, and WUT ID-UB, Poland; Korea Institute of Science and Technology Information and National Research Foundation of Korea (NRF), Republic of Korea; Ministry of Education and Scientific Research, Institute of Atomic Physics, Ministry of Research and Innovation, and Institute of Atomic Physics and University Politehnica of Bucharest, Romania; Ministry of Education, Science, Research and Sport of the Slovak Republic, Slovakia; National Research Foundation of South Africa, South Africa; Swedish Research Council (VR) and Knut & Alice Wallenberg Foundation (KAW), Sweden; European Organization for Nuclear Research, Switzerland; Suranaree University of Technology (SUT), National Science and Technology Development

Agency (NSTDA), Thailand Science Research and Innovation (TSRI), and National Science, Research and Innovation Fund (NSRF), Thailand; Turkish Energy, Nuclear and Mineral Research Agency (TENMAK), Turkey; National Academy of Sciences of Ukraine, Ukraine; Science and Technology Facilities Council (STFC), United Kingdom; National Science Foundation of the United States of America (NSF) and United States Department of Energy, Office of Nuclear Physics (DOE NP), United States of America. In addition, individual groups or members have received support from European Research Council, Strong 2020-Horizon 2020 (Grants No. 950692 and No. 824093), European Union; Academy of Finland (Center of Excellence in Quark Matter) (Grants No. 346327 and No. 346328), Finland; and Programa de Apoyos para la Superación del Personal Académico, UNAM, Mexico.

APPENDIX: ADDITIONAL OBSERVABLES

The comparisons of the model predictions to the experimental data for $NAC_{a,b}(2, 3)$, $AC_{a,b}(2, 4)$, and $NAC_{a,b}(3, 4)$ are presented in the main part of this article. In this Appendix, the comparisons for the other observables of this analysis are discussed. The complete list of combinations can be found in Figs. 1 and 6.

The predictions from Duke 2019 and Jyväskylä 2022 parametrizations and the experimental data for $AC_{a,b}(2, 3)$ and $NAC_{a,b}(2, 4)$ are presented in Figs. 7 and 8, respectively. The same splitting with the cumulant order as observed in Fig. 3 for $NAC_{a,b}(2, 3)$ and $AC_{a,b}(2, 4)$ can be seen here. In both cases, $NAC_{a,1}(2, 4)$ show increasingly larger magnitudes than $NAC_{a,1}(4, 2)$, while the opposite stands true for the unnormalized AC. The observables $AC_{a,b}(2, 3)$ and $AC_{a,b}(2, 4)$ (Figs. 7 and 3) show similar agreements between predictions and data. The Jyväskylä 2022 parametrization has overall a better agreement with the data than the Duke 2019 one, and the higher-order ACs are overall better reproduced than $SC(m, n)$ and $AC_{2,1}(m, n)$. It can be noted, however, that while the Jyväskylä 2022 parametrization reproduces quantitatively $SC(2, 4)$, whereas the Duke 2019 one does not, the opposite behavior is observed for $SC(2, 3)$. On the other hand, no big difference in the predictions of $NAC_{a,1}(2, 4)$ and $NAC_{a,1}(4, 2)$ between the Duke 2019 and Jyväskylä 2022 parametrizations can be observed. Possible effects, such as the ones at the origin of the 10% discrepancy in the description of v_2 at 5.02 TeV by the Jyväskylä 2022 parametrization [12], could be at play in $SC(2, 3)$ and cancel out in $NSC(2, 3)$.

In the case of $NAC_{a,b}(2, 4)$ (Fig. 8), a slightly better agreement with the data from Jyväskylä 2022 over Duke 2019 parametrizations can be observed. As stated above, the non-linear response between v_4 and ϵ_2^2 makes $AC_{a,b}(2, 4)$, and thus $NAC_{a,b}(2, 4)$, especially sensitive to the hydrodynamical description of the collision.

The predictions for $AC_{a,b}(3, 4)$ are shown in Fig. 9. As was already discussed for $NAC_{a,b}(3, 4)$ (Fig. 4), the measurements for $AC_{a,1}(3, 4)$ and $AC_{a,1}(4, 3)$ are in agreement within uncertainties for both the data and the calculations. Furthermore, the predictions from the Jyväskylä 2022 and Duke 2019 parametrizations are both in overall good agreement with the experimental data.

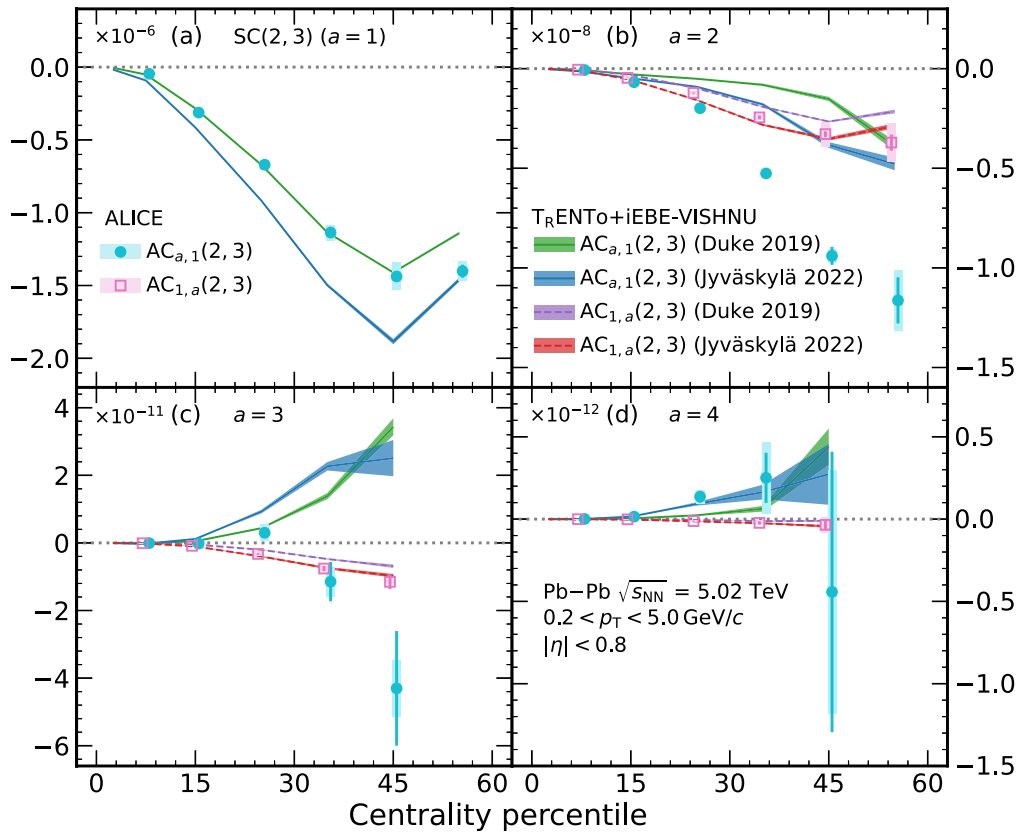


FIG. 7. Centrality dependence of the different orders $a = 1, \dots, 4$ of $AC_{a,1}(2, 3)$ (cyan closed circles) and $AC_{1,a}(2, 3)$ (pink open squares) compared with the theoretical predictions from $T_{\text{R}}\text{ENTo} + i\text{EBE-VISHNU}$ for the Duke 2019 [22] and Jyväskylä 2022 [12] parametrizations. The statistical uncertainties in the calculations are indicated by the thicknesses of the colored bands.

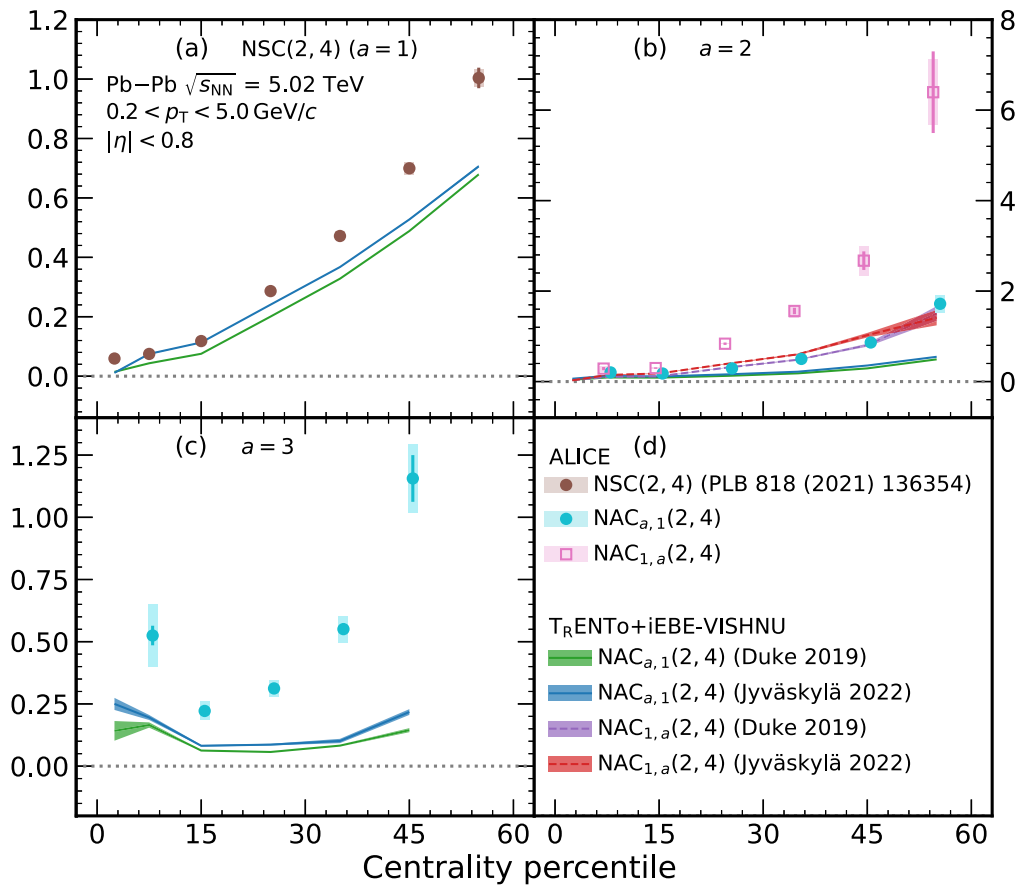


FIG. 8. Centrality dependence of the different orders $a = 1, \dots, 3$ of $NAC_{a,1}(2, 4)$ (cyan closed circles) and $NAC_{1,a}(2, 4)$ (pink open squares) compared with the theoretical predictions from T_RENTo + iEBE-VISHNU for the Duke 2019 [22] and Jyvaskylä 2022 [12] parametrizations. The statistical uncertainties in the calculations are indicated by the thicknesses of the colored bands. The data points for NSC(2, 4) are taken from Ref. [17].

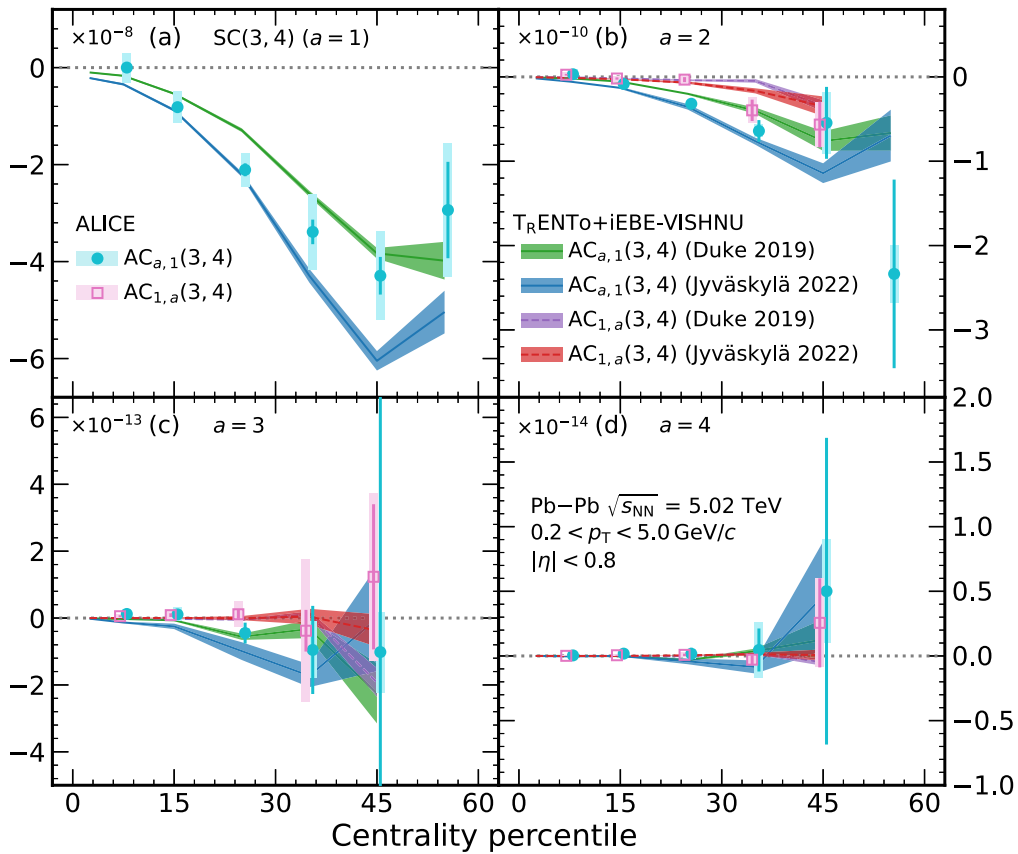


FIG. 9. Centrality dependence of the different orders $a = 1, \dots, 4$ of $AC_{a,1}(3, 4)$ (cyan closed circles) and $AC_{1,a}(3, 4)$ (pink open squares) compared with the theoretical predictions from $T_R ENT o + iEBE-VISHNU$ for the Duke 2019 [22] and Jyvaskylä 2022 [12] parametrizations. The statistical uncertainties in the calculations are indicated by the thicknesses of the colored bands.

- [1] U. Heinz and R. Snellings, Collective flow and viscosity in relativistic heavy-ion collisions, *Annu. Rev. Nucl. Part. Sci.* **63**, 123 (2013).
- [2] P. Braun-Munzinger, V. Koch, T. Schäfer, and J. Stachel, Properties of hot and dense matter from relativistic heavy ion collisions, *Phys. Rep.* **621**, 76 (2016).
- [3] W. Busza, K. Rajagopal, and W. van der Schee, Heavy ion collisions: The big picture, and the big questions, *Annu. Rev. Nucl. Part. Sci.* **68**, 339 (2018).
- [4] ALICE Collaboration, The ALICE experiment – A journey through QCD, [arXiv:2211.04384](https://arxiv.org/abs/2211.04384) [nucl-ex].
- [5] J.-Y. Ollitrault, Anisotropy as a signature of transverse collective flow, *Phys. Rev. D* **46**, 229 (1992).
- [6] S. Voloshin and Y. Zhang, Flow study in relativistic nuclear collisions by Fourier expansion of azimuthal particle distributions, *Z. Phys. C* **70**, 665 (1996).
- [7] R. S. Bhalerao, M. Luzum, and J.-Y. Ollitrault, Determining initial-state fluctuations from flow measurements in heavy-ion collisions, *Phys. Rev. C* **84**, 034910 (2011).
- [8] N. Borghini, P. M. Dinh, and J.-Y. Ollitrault, New method for measuring azimuthal distributions in nucleus-nucleus collisions, *Phys. Rev. C* **63**, 054906 (2001).
- [9] N. Borghini, P. M. Dinh, and J.-Y. Ollitrault, Flow analysis from multiparticle azimuthal correlations, *Phys. Rev. C* **64**, 054901 (2001).
- [10] A. Bilandzic, R. Snellings, and S. Voloshin, Flow analysis with cumulants: Direct calculations, *Phys. Rev. C* **83**, 044913 (2011).
- [11] A. Bilandzic, C. H. Christensen, K. Gulbrandsen, A. Hansen, and Y. Zhou, Generic framework for anisotropic flow analyses with multiparticle azimuthal correlations, *Phys. Rev. C* **89**, 064904 (2014).
- [12] J. E. Parkkila, A. Onnerstad, S. F. Taghavi, C. Mordasini, A. Bilandzic, M. Virta, and D. J. Kim, New constraints for QCD matter from improved Bayesian parameter estimation in heavy-ion collisions at LHC, *Phys. Lett. B* **835**, 137485 (2022).
- [13] J. Adam *et al.* (ALICE Collaboration), Correlated event-by-event fluctuations of flow harmonics in Pb-Pb collisions at $\sqrt{s_{NN}} = 2.76$ TeV, *Phys. Rev. Lett.* **117**, 182301 (2016).
- [14] S. Acharya *et al.* (ALICE Collaboration), Systematic studies of correlations between different order flow harmonics in Pb-Pb collisions at $\sqrt{s_{NN}} = 2.76$ TeV, *Phys. Rev. C* **97**, 024906 (2018).
- [15] R. Kubo, Generalized cumulant expansion method, *J. Phys. Soc. Jpn.* **17**, 1100 (1962).
- [16] A. Bilandzic, M. Lesch, C. Mordasini, and S. F. Taghavi, Multivariate cumulants in flow analyses: The next generation, *Phys. Rev. C* **105**, 024912 (2022).
- [17] S. Acharya *et al.* (ALICE Collaboration), Measurements of mixed harmonic cumulants in Pb-Pb collisions

- at $\sqrt{s_{NN}} = 5.02$ TeV, *Phys. Lett. B* **818**, 136354 (2021).
- [18] C. Mordasini, A. Bilandzic, D. Karakoç, and S. F. Taghavi, Higher order symmetric cumulants, *Phys. Rev. C* **102**, 024907 (2020).
- [19] S. Acharya *et al.* (ALICE Collaboration), Multiharmonic correlations of different flow amplitudes in Pb-Pb collisions at $\sqrt{s_{NN}} = 2.76$ TeV, *Phys. Rev. Lett.* **127**, 092302 (2021).
- [20] J. E. Bernhard, P. W. Marcy, C. E. Coleman-Smith, S. Huzurbazar, R. L. Wolpert, and S. A. Bass, Quantifying properties of hot and dense QCD matter through systematic model-to-data comparison, *Phys. Rev. C* **91**, 054910 (2015).
- [21] J. E. Bernhard, J. S. Moreland, S. A. Bass, J. Liu, and U. Heinz, Applying Bayesian parameter estimation to relativistic heavy-ion collisions: Simultaneous characterization of the initial state and quark-gluon plasma medium, *Phys. Rev. C* **94**, 024907 (2016).
- [22] J. E. Bernhard, J. S. Moreland, and S. A. Bass, Bayesian estimation of the specific shear and bulk viscosity of quark-gluon plasma, *Nat. Phys.* **15**, 1113 (2019).
- [23] J. Auvinen, K. J. Eskola, P. Huovinen, H. Niemi, R. Paatelainen, and P. Petreczky, Temperature dependence of η/s of strongly interacting matter: Effects of the equation of state and the parametric form of $(\eta/s)(T)$, *Phys. Rev. C* **102**, 044911 (2020).
- [24] G. Nijs, W. van der Schee, U. Gürsoy, and R. Snellings, A transverse momentum differential global analysis of heavy ion collisions, *Phys. Rev. Lett.* **126**, 202301 (2021).
- [25] G. Nijs, W. van der Schee, U. Gürsoy, and R. Snellings, Bayesian analysis of heavy ion collisions with the heavy ion computational framework TRAJECTUM, *Phys. Rev. C* **103**, 054909 (2021).
- [26] D. Everett *et al.* (JETSCAPE Collaboration), Multisystem Bayesian constraints on the transport coefficients of QCD matter, *Phys. Rev. C* **103**, 054904 (2021).
- [27] J. E. Parkkila, A. Onnerstad, and D. J. Kim, Bayesian estimation of the specific shear and bulk viscosity of the quark-gluon plasma with additional flow harmonic observables, *Phys. Rev. C* **104**, 054904 (2021).
- [28] S. F. Taghavi, A Fourier-cumulant analysis for multiharmonic flow fluctuation: by employing a multidimensional generating function approach, *Eur. Phys. J. C* **81**, 652 (2021).
- [29] K. Aamodt *et al.* (ALICE Collaboration), The ALICE experiment at the CERN LHC, *J. Instrum.* **3**, S08002 (2008).
- [30] B. B. Abelev *et al.* (ALICE Collaboration), Performance of the ALICE Experiment at the CERN LHC, *Int. J. Mod. Phys. A* **29**, 1430044 (2014).
- [31] J. Alme *et al.*, The ALICE TPC, a large 3-dimensional tracking device with fast readout for ultra-high multiplicity events, *Nucl. Instrum. Methods Phys. Res., Sect. A* **622**, 316 (2010).
- [32] E. Abbas *et al.* (ALICE Collaboration), Performance of the ALICE VZERO system, *J. Instrum.* **8**, P10016 (2013).
- [33] J. Adam *et al.* (ALICE Collaboration), Centrality dependence of the charged-particle multiplicity density at midrapidity in Pb-Pb collisions at $\sqrt{s_{NN}} = 5.02$ TeV, *Phys. Rev. Lett.* **116**, 222302 (2016).
- [34] G. Dellacasa *et al.* (ALICE Collaboration), ALICE Inner Tracking System (ITS): Technical Design Report, CERN report, Geneva, 1999 (unpublished), <http://cds.cern.ch/record/391175>.
- [35] K. Aamodt *et al.* (ALICE Collaboration), Alignment of the ALICE Inner Tracking System with cosmic-ray tracks, *J. Instrum.* **5**, P03003 (2010).
- [36] F. Carnesecchi *et al.* (ALICE Collaboration), Performance of the ALICE Time-Of-Flight detector at the LHC, *J. Instrum.* **14**, C06023 (2019).
- [37] S. Acharya *et al.* (ALICE Collaboration), Higher harmonic non-linear flow modes of charged hadrons in Pb-Pb collisions at $\sqrt{s_{NN}} = 5.02$ TeV, *J. High Energy Phys.* **05** (2020) 085.
- [38] M. Gyulassy and X.-N. Wang, HIJING 1.0: A Monte Carlo program for parton and particle production in high-energy hadronic and nuclear collisions, *Comput. Phys. Commun.* **83**, 307 (1994).
- [39] R. Brun, F. Bruyant, F. Carminati, S. Giani, M. Maire, A. McPherson, G. Patrick, and L. Urban, GEANT Detector Description and Simulation Tool, CERN-W5013, CERN-W-5013, W5013, W-5013 (1994).
- [40] R. Barlow, Systematic errors: Facts and fictions, in *Conference on Advanced Statistical Techniques in Particle Physics* (University of Durham, Durham, UK, 2002), pp. 134–144.
- [41] C. Shen, Z. Qiu, H. Song, J. Bernhard, S. Bass, and U. Heinz, The iEBE-VISHNU code package for relativistic heavy-ion collisions, *Comput. Phys. Commun.* **199**, 61 (2016).
- [42] H. Song and U. W. Heinz, Causal viscous hydrodynamics in 2+1 dimensions for relativistic heavy-ion collisions, *Phys. Rev. C* **77**, 064901 (2008).
- [43] S. A. Bass *et al.*, Microscopic models for ultrarelativistic heavy ion collisions, *Prog. Part. Nucl. Phys.* **41**, 255 (1998).
- [44] M. Bleicher *et al.*, Relativistic hadron hadron collisions in the ultrarelativistic quantum molecular dynamics model, *J. Phys. G* **25**, 1859 (1999).
- [45] J. S. Moreland, J. E. Bernhard, and S. A. Bass, Alternative ansatz to wounded nucleon and binary collision scaling in high-energy nuclear collisions, *Phys. Rev. C* **92**, 011901(R) (2015).
- [46] F. G. Gardim, F. Grassi, M. Luzum, and J.-Y. Ollitrault, Mapping the hydrodynamic response to the initial geometry in heavy-ion collisions, *Phys. Rev. C* **85**, 024908 (2012).
- [47] D. Teaney and L. Yan, Non linearities in the harmonic spectrum of heavy ion collisions with ideal and viscous hydrodynamics, *Phys. Rev. C* **86**, 044908 (2012).
- [48] B. H. Alver, C. Gombeaud, M. Luzum, and J.-Y. Ollitrault, Triangular flow in hydrodynamics and transport theory, *Phys. Rev. C* **82**, 034913 (2010).
- [49] H. Niemi, G. S. Denicol, H. Holopainen, and P. Huovinen, Event-by-event distributions of azimuthal asymmetries in ultrarelativistic heavy-ion collisions, *Phys. Rev. C* **87**, 054901 (2013).
- [50] H. Mäntysaari and B. Schenke, Evidence of strong proton shape fluctuations from incoherent diffraction, *Phys. Rev. Lett.* **117**, 052301 (2016).
- [51] H. Mäntysaari, B. Schenke, C. Shen, and W. Zhao, Bayesian inference of the fluctuating proton shape, *Phys. Lett. B* **833**, 137348 (2022).
- [52] G. Giacalone, G. Nijs, and W. van der Schee, Determination of the neutron skin of ^{208}Pb from ultrarelativistic nuclear collisions, [arXiv:2305.00015](https://arxiv.org/abs/2305.00015) [nucl-th].
- [53] P. Romatschke, Relativistic fluid dynamics far from local equilibrium, *Phys. Rev. Lett.* **120**, 012301 (2018).
- [54] A. Kurkela, A. Mazeliauskas, J.-F. Paquet, S. Schlichting, and D. Teaney, Matching the nonequilibrium initial stage of heavy ion collisions to hydrodynamics with QCD kinetic theory, *Phys. Rev. Lett.* **122**, 122302 (2019).

- [55] A. Kurkela, A. Mazeliauskas, J.-F. Paquet, S. Schlichting, and D. Teaney, Effective kinetic description of event-by-event pre-equilibrium dynamics in high-energy heavy-ion collisions, *Phys. Rev. C* **99**, 034910 (2019).
- [56] A. Kurkela and A. Mazeliauskas, Chemical equilibration in hadronic collisions, *Phys. Rev. Lett.* **122**, 142301 (2019).
- [57] M. Strickland, The non-equilibrium attractor for kinetic theory in relaxation time approximation, *J. High Energy Phys.* **12** (2018) 128.
- [58] S. Kamata, M. Martinez, P. Plaschke, S. Ochsensfeld, and S. Schlichting, Hydrodynamization and nonequilibrium Green's functions in kinetic theory, *Phys. Rev. D* **102**, 056003 (2020).

- S. Acharya¹²⁵, D. Adamová⁸⁶, A. Adler⁶⁹, G. Aglieri Rinella³², M. Agnello²⁹, N. Agrawal⁵⁰, Z. Ahammed¹³², S. Ahmad¹⁵, S. U. Ahn⁷⁰, I. Ahuja³⁷, A. Akindinov¹⁴⁰, M. Al-Turany⁹⁷, D. Aleksandrov¹⁴⁰, B. Alessandro⁵⁵, H. M. Alfanda⁶, R. Alfaro Molina⁶⁶, B. Ali¹⁵, A. Alici²⁵, N. Alizadehvandchali¹¹⁴, A. Alkin³², J. Alme²⁰, G. Alocco⁵¹, T. Alt⁶³, I. Altsybeev¹⁴⁰, M. N. Anaam⁶, C. Andrei⁴⁵, A. Andronic¹³⁵, V. Anguelov⁹⁴, F. Antinori⁵³, P. Antonioli⁵⁰, N. Apadula⁷⁴, L. Aphecetche¹⁰³, H. Appelshäuser⁶³, C. Arata⁷³, S. Arcelli²⁵, M. Aresti⁵¹, R. Arnaldi⁵⁵, J. G. M. C. A. Arneiro¹¹⁰, I. C. Arsene¹⁹, M. Arslanok¹³⁷, A. Augustinus³², R. Averbeck⁹⁷, M. D. Azmi¹⁵, A. Badalà⁵², J. Bae¹⁰⁴, Y. W. Baek⁴⁰, X. Bai¹¹⁸, R. Bailhache⁶³, Y. Bailung⁴⁷, A. Balbino²⁹, A. Baldisseri¹²⁸, B. Balis², D. Banerjee⁴, Z. Banoo⁹¹, R. Barbera²⁶, F. Barile⁶³, L. Barioglio⁹⁵, M. Barlou⁷⁸, G. G. Barnaföldi¹³⁶, L. S. Barnby⁸⁵, V. Barret¹²⁵, L. Barreto¹¹⁰, C. Bartels¹¹⁷, K. Barth³², E. Bartsch⁶³, N. Bastid¹²⁵, S. Basu⁷⁵, G. Batigne¹⁰³, D. Battistini⁹⁵, B. Batyunya¹⁴¹, D. Bauri⁴⁶, J. L. Bazo Alba¹⁰¹, I. G. Bearden⁸³, C. Beattie¹³⁷, P. Becht⁹⁷, D. Behera⁴⁷, I. Belikov¹²⁷, A. D. C. Bell Hechavarria¹³⁵, F. Bellini²⁵, R. Bellwied¹¹⁴, S. Belokurova¹⁴⁰, G. Bencedi¹³⁶, S. Beole²⁴, A. Bercuci⁴⁵, Y. Berdnikov¹⁴⁰, A. Berdnikova⁹⁴, L. Bergmann⁹⁴, M. G. Besoiu⁶², L. Betev³², P. P. Bhaduri¹³², A. Bhasin⁹¹, M. A. Bhat⁴, B. Bhattacharjee⁴¹, L. Bianchi²⁴, N. Bianchi⁴⁸, J. Bielčák³⁵, J. Bielčková⁸⁶, J. Biernat¹⁰⁷, A. P. Bigot¹²⁷, A. Bilandzic⁹⁵, G. Biro¹³⁶, S. Biswas⁴, N. Bize¹⁰³, J. T. Blair¹⁰⁸, D. Blau¹⁴⁰, M. B. Blidaru⁹⁷, N. Bluhme³⁸, C. Blume⁶³, G. Boca^{21,54}, F. Bock⁸⁷, T. Bodova²⁰, A. Bogdanov¹⁴⁰, S. Boi²², J. Bok⁵⁷, L. Boldizsár¹³⁶, M. Bombara³⁷, P. M. Bond³², G. Bonomi^{131,54}, H. Borel¹²⁸, A. Borissov¹⁴⁰, A. G. Borquez Carcamo⁹⁴, H. Bossi¹³⁷, E. Botta²⁴, Y. E. M. Bouziani⁶³, L. Bratrud⁶³, P. Braun-Munzinger⁹⁷, M. Bregant¹¹⁰, M. Broz³⁵, G. E. Bruno^{96,31}, M. D. Buckland²³, D. Budnikov¹⁴⁰, H. Buesching⁶³, S. Bufalino²⁹, P. Buhler¹⁰², Z. Buthelezi^{67,121}, A. Bylinkin²⁰, S. A. Bysiak¹⁰⁷, M. Cai⁶, H. Caines¹³⁷, A. Caliva²⁸, E. Calvo Villar¹⁰¹, J. M. M. Camacho¹⁰⁹, P. Camerini²³, F. D. M. Canedo¹¹⁰, M. Carabas¹²⁴, A. A. Carballo³², F. Carnesecchi³², R. Caron¹²⁶, L. A. D. Carvalho¹¹⁰, J. Castillo Castellanos¹²⁸, F. Catalano^{32,24}, C. Ceballos Sanchez¹⁴¹, I. Chakaberia⁷⁴, P. Chakraborty⁴⁶, S. Chandra¹³², S. Chapeland³², M. Chartier¹¹⁷, S. Chattopadhyay¹³², S. Chattopadhyay⁹⁹, T. G. Chavez⁴⁴, T. Cheng^{97,6}, C. Cheshkov¹²⁶, B. Cheynis¹²⁶, V. Chibante Barroso³², D. D. Chinellato¹¹¹, E. S. Chizzali^{95,a}, J. Cho⁵⁷, S. Cho⁵⁷, P. Chochula³², P. Christakoglou⁸⁴, C. H. Christensen⁸³, P. Christiansen⁷⁵, T. Chujo¹²³, M. Ciaccio²⁹, C. Cicalo⁵¹, F. Cindolo⁵⁰, M. R. Ciupek⁹⁷, G. Clai^{50,b}, F. Colamaria⁴⁹, J. S. Colburn¹⁰⁰, D. Colella^{96,31}, M. Colocci²⁵, G. Conesa Balbastre⁷³, Z. Conesa del Valle⁷², G. Contin²³, J. G. Contreras³⁵, M. L. Coquet¹²⁸, T. M. Cormier^{87,c}, P. Cortese^{130,55}, M. R. Cosentino¹¹², F. Costa³², S. Costanza^{21,54}, C. Cot⁷², J. Crkovská⁹⁴, P. Crochet¹²⁵, R. Cruz-Torres⁷⁴, P. Cui⁶, A. Dainese⁵³, M. C. Danisch⁹⁴, A. Danu⁶², P. Das⁸⁰, P. Das⁴, S. Das⁴, A. R. Dash¹³⁵, S. Dash⁴⁶, A. De Caro²⁸, G. de Cataldo⁴⁹, J. de Cuveland³⁸, A. De Falco²², D. De Gruttola²⁸, N. De Marco⁵⁵, C. De Martin²³, S. De Pasquale²⁸, R. Deb¹³¹, S. Deb⁴⁷, K. R. Deja¹³³, R. Del Grande⁹⁵, L. Dello Stritto²⁸, W. Deng⁶, P. Dhankeher¹⁸, D. Di Bari³¹, A. Di Mauro³², B. Diab¹²⁸, R. A. Diaz^{141,7}, T. Dietel¹¹³, Y. Ding⁶, R. Divià³², D. U. Dixit¹⁸, Ø. Djuvsland²⁰, U. Dmitrieva¹⁴⁰, A. Dobrin⁶², B. Dönigus⁶³, J. M. Dubinski¹³³, A. Dubla⁹⁷, S. Dudi⁹⁰, P. Dupieux¹²⁵, M. Durkac¹⁰⁶, N. Dzalaiova¹², T. M. Eder¹³⁵, R. J. Ehlers⁷⁴, F. Eisenhut⁶³, D. Elia⁴⁹, B. Erazmus¹⁰³, F. Ercolessi²⁵, F. Erhardt⁸⁹, M. R. Erstad²⁰, B. Espagnon⁷², G. Eulisse³², D. Evans¹⁰⁰, S. Evdokimov¹⁴⁰, L. Fabbietti⁹⁵, M. Faggin²⁷, J. Favre⁷³, F. Fan⁶, W. Fan⁷⁴, A. Fantoni⁴⁸, M. Fasel⁸⁷, P. Fecchio²⁹, A. Feliciello⁵⁵, G. Feofilov¹⁴⁰, A. Fernández Téllez⁴⁴, L. Ferrandi¹¹⁰, M. B. Ferrer³², A. Ferrero¹²⁸, C. Ferrero⁵⁵, A. Ferretti²⁴, V. J. G. Feuillard⁹⁴, V. Filova³⁵, D. Finogeev¹⁴⁰, F. M. Fionda⁵¹, F. Flor¹¹⁴, A. N. Flores¹⁰⁸, S. Foertsch⁶⁷, I. Fokin⁹⁴, S. Fokin¹⁴⁰, E. Fragiaco⁵⁶, E. Frajna¹³⁶, U. Fuchs³², N. Funicello²⁸, C. Furget⁷³, A. Furs¹⁴⁰, T. Fusayasu⁹⁸, J. J. Gaardhøje⁸³, M. Gagliardi²⁴, A. M. Gago¹⁰¹, C. D. Galvan¹⁰⁹, D. R. Gangadharan¹¹⁴, P. Ganoti⁷⁸, C. Garabatos⁹⁷, J. R. A. Garcia⁴⁴, E. Garcia-Solis⁹, C. Gargiulo³², A. Garibli⁸¹, K. Garner¹³⁵, P. Gasik⁹⁷, A. Gautam¹¹⁶, M. B. Gay Ducati⁶⁵, M. Germain¹⁰³, A. Ghimouz¹²³, C. Ghosh¹³², M. Giacalone^{50,25}, P. Giubellino^{97,55}, P. Giubilato²⁷, A. M. C. Glaenger¹²⁸, P. Glässel⁹⁴, E. Glimos¹²⁰, D. J. Q. Goh⁷⁶, V. Gonzalez¹³⁴, S. Gorbunov³⁸, M. Gorgon², K. Goswami⁴⁷, S. Gotovac³³, V. Grabski⁶⁶, L. K. Graczykowski¹³³, E. Grecka⁸⁶, A. Grelli⁵⁸, C. Grigoras³², V. Grigoriev¹⁴⁰, S. Grigoryan^{141,1}, F. Grosa³², J. F. Grosse-Oetringhaus³², R. Grosso⁹⁷, D. Grund³⁵, G. G. Guardiano¹¹¹, R. Guernane⁷³, M. Guilbaud¹⁰³, K. Gulbrandsen⁸³, T. Gundem⁶³, T. Gunji¹²², W. Guo⁶, A. Gupta⁹¹, R. Gupta⁹¹, R. Gupta⁴⁷

- S. P. Guzman ⁴⁴, K. Gwizdziel ¹³³, L. Gyulai ¹³⁶, M. K. Habib ⁹⁷, C. Hadjidakis ⁷², F. U. Haider ⁹¹, H. Hamagaki ⁷⁶, A. Hamdi ⁷⁴, M. Hamid ⁶, Y. Han ¹³⁸, B. G. Hanley ¹³⁴, R. Hannigan ¹⁰⁸, J. Hansen ⁷⁵, M. R. Haque ¹³³, J. W. Harris ¹³⁷, A. Harton ⁹, H. Hassan ⁸⁷, D. Hatzifotiadou ⁵⁰, P. Hauer ⁴², L. B. Havener ¹³⁷, S. T. Heckel ⁹⁵, E. Hellbär ⁹⁷, H. Helstrup ³⁴, M. Hemmer ⁶³, T. Herman ³⁵, G. Herrera Corral ⁸, F. Herrmann ¹³⁵, S. Herrmann ¹²⁶, K. F. Hetland ³⁴, B. Heybeck ⁶³, H. Hillemanns ³², B. Hippolyte ¹²⁷, F. W. Hoffmann ⁶⁹, B. Hofman ⁵⁸, B. Hohlweger ⁸⁴, G. H. Hong ¹³⁸, M. Horst ⁹⁵, A. Horzyk ², Y. Hou ⁶, P. Hristov ³², C. Hughes ¹²⁰, P. Huhn ⁶³, L. M. Huhta ¹¹⁵, T. J. Humanic ⁸⁸, A. Hutson ¹¹⁴, D. Hutter ³⁸, R. Ilkaev ¹⁴⁰, H. Ilyas ¹³, M. Inaba ¹²³, G. M. Innocenti ³², M. Ippolitov ¹⁴⁰, A. Isakov ⁸⁶, T. Isidori ¹¹⁶, M. S. Islam ⁹⁹, M. Ivanov ¹², M. Ivanov ⁹⁷, V. Ivanov ¹⁴⁰, K. E. Iversen ⁷⁵, M. Jablonski ², B. Jacak ⁷⁴, N. Jacazio ²⁵, P. M. Jacobs ⁷⁴, S. Jadlovská ¹⁰⁶, J. Jadlovsky ¹⁰⁶, S. Jaelani ⁸², C. Jahnke ¹¹¹, M. J. Jakubowska ¹³³, M. A. Janik ¹³³, T. Janson ⁶⁹, M. Jercic ⁸⁹, S. Ji ¹⁶, S. Jia ¹⁰, A. A. P. Jimenez ⁶⁴, F. Jonas ⁸⁷, J. M. Jowett ^{32,97}, J. Jung ⁶³, M. Jung ⁶³, A. Junique ³², A. Jusko ¹⁰⁰, M. J. Kabus ^{32,133}, J. Kaewjai ¹⁰⁵, P. Kalinak ⁵⁹, A. S. Kalteyer ⁹⁷, A. Kalweit ³², V. Kaplin ¹⁴⁰, A. Karasu Uysal ⁷¹, D. Karatovic ⁸⁹, O. Karavichev ¹⁴⁰, T. Karavicheva ¹⁴⁰, P. Karczmarczyk ¹³³, E. Karpechev ¹⁴⁰, U. Keschull ⁶⁹, R. Keidel ¹³⁹, D. L. D. Keijdener ⁵⁸, M. Keil ³², B. Ketzer ⁴², S. S. Khade ⁴⁷, A. M. Khan ^{118,6}, S. Khan ¹⁵, A. Khanzadeev ¹⁴⁰, Y. Kharlov ¹⁴⁰, A. Khatun ¹¹⁶, A. Khuntia ¹⁰⁷, M. B. Kidson ¹¹³, B. Kileng ³⁴, B. Kim ¹⁰⁴, C. Kim ¹⁶, D. J. Kim ¹¹⁵, E. J. Kim ⁶⁸, J. Kim ¹³⁸, J. S. Kim ⁴⁰, J. Kim ⁵⁷, J. Kim ⁶⁸, M. Kim ¹⁸, S. Kim ¹⁷, T. Kim ¹³⁸, K. Kimura ⁹², S. Kirsch ⁶³, I. Kisel ³⁸, S. Kiselev ¹⁴⁰, A. Kisiel ¹³³, J. P. Kitowski ², J. L. Klay ⁵, J. Klein ³², S. Klein ⁷⁴, C. Klein-Bösing ¹³⁵, M. Kleiner ⁶³, T. Klemenz ⁹⁵, A. Kluge ³², A. G. Knospe ¹¹⁴, C. Kobdaj ¹⁰⁵, T. Kollegger ⁹⁷, A. Kondratyev ¹⁴¹, N. Kondratyeva ¹⁴⁰, E. Kondratyuk ¹⁴⁰, J. König ⁶³, S. A. Königstorfer ⁹⁵, P. J. Konopka ³², G. Kornakov ¹³³, S. D. Koryciak ², A. Kotliarov ⁸⁶, V. Kovalenko ¹⁴⁰, M. Kowalski ¹⁰⁷, V. Kozuharov ³⁶, I. Králik ⁵⁹, A. Kravčáková ³⁷, L. Krcal ^{32,38}, M. Krivda ^{100,59}, F. Krizek ⁸⁶, K. Krizkova Gajdosova ³², M. Kroesen ⁹⁴, M. Krüger ⁶³, D. M. Krupova ³⁵, E. Kryshen ¹⁴⁰, V. Kučera ⁵⁷, C. Kuhn ¹²⁷, P. G. Kuijper ⁸⁴, T. Kumaoka ¹²³, D. Kumar ¹³², L. Kumar ⁹⁰, N. Kumar ⁹⁰, S. Kumar ³¹, S. Kundu ³², P. Kurashvili ⁷⁹, A. Kurepin ¹⁴⁰, A. B. Kurepin ¹⁴⁰, A. Kuryakin ¹⁴⁰, S. Kushpil ⁸⁶, J. Kvapil ¹⁰⁰, M. J. Kwon ⁵⁷, Y. Kwon ¹³⁸, S. L. La Pointe ³⁸, P. La Rocca ²⁶, A. Lakrathok ¹⁰⁵, M. Lamanna ³², R. Langoy ¹¹⁹, P. Larionov ³², E. Laudi ³², L. Lautner ^{32,95}, R. Lavicka ¹⁰², R. Lea ^{131,54}, H. Lee ¹⁰⁴, I. Legrand ⁴⁵, G. Legras ¹³⁵, J. Lehrbach ³⁸, T. M. Lelek ², R. C. Lemmon ⁸⁵, I. León Monzón ¹⁰⁹, M. M. Lesch ⁹⁵, E. D. Lesser ¹⁸, P. Lévai ¹³⁶, X. Li ¹⁰, X. L. Li ⁶, J. Lien ¹¹⁹, R. Lietava ¹⁰⁰, I. Likmeta ¹¹⁴, B. Lim ²⁴, S. H. Lim ¹⁶, V. Lindenstruth ³⁸, A. Lindner ⁴⁵, C. Lippmann ⁹⁷, A. Liu ¹⁸, D. H. Liu ⁶, J. Liu ¹¹⁷, G. S. S. Liveraro ¹¹¹, I. M. Lofnes ²⁰, C. Loizides ⁸⁷, S. Lokos ¹⁰⁷, J. Lomker ⁵⁸, P. Loncar ³³, J. A. Lopez ⁹⁴, X. Lopez ¹²⁵, E. López Torres ⁷, P. Lu ^{97,118}, J. R. Luhder ¹³⁵, M. Lunardon ²⁷, G. Luparello ⁵⁶, Y. G. Ma ³⁹, M. Mager ³², A. Maire ¹²⁷, M. V. Makariev ³⁶, M. Malaev ¹⁴⁰, G. Malfattore ²⁵, N. M. Malik ⁹¹, Q. W. Malik ¹⁹, S. K. Malik ⁹¹, L. Malinina ^{141,d}, D. Mallick ⁸⁰, N. Mallick ⁴⁷, G. Mandaglio ^{30,52}, S. K. Mandal ⁷⁹, V. Manko ¹⁴⁰, F. Manso ¹²⁵, V. Manzari ⁴⁹, Y. Mao ⁶, R. W. Marcjan ², G. V. Margagliotti ²³, A. Margotti ⁵⁰, A. Marín ⁹⁷, C. Markert ¹⁰⁸, P. Martinengo ³², M. I. Martínez ⁴⁴, G. Martínez García ¹⁰³, M. P. P. Martins ¹¹⁰, S. Masciocchi ⁹⁷, M. Maserà ²⁴, A. Masoni ⁵¹, L. Massacrier ⁷², A. Mastroserio ^{129,49}, O. Matonoha ⁷⁵, S. Mattiazzi ²⁷, P. F. T. Matuoka ¹¹⁰, A. Matyja ¹⁰⁷, C. Mayer ¹⁰⁷, A. L. Mazuecos ³², F. Mazzaschi ²⁴, M. Mazzilli ³², J. E. Mdhluli ¹²¹, A. F. Mechler ⁶³, Y. Melikyan ^{43,140}, A. Menchaca-Rocha ⁶⁶, E. Meninno ^{102,28}, A. S. Menon ¹¹⁴, M. Meres ¹², S. Mhlanga ^{113,67}, Y. Miake ¹²³, L. Micheletti ³², L. C. Migliorin ¹²⁶, D. L. Mihaylov ⁹⁵, K. Mikhaylov ^{141,140}, A. N. Mishra ¹³⁶, D. Miśkowiec ⁹⁷, A. Modak ⁴, A. P. Mohanty ⁵⁸, B. Mohanty ⁸⁰, M. Mohisin Khan ^{15,e}, M. A. Molander ⁴³, Z. Moravcova ⁸³, C. Mordasini ⁹⁵, D. A. Moreira De Godoy ¹³⁵, I. Morozov ¹⁴⁰, A. Morsch ³², T. Mrnjavac ³², V. Muccifora ⁴⁸, S. Muhuri ¹³², J. D. Mulligan ⁷⁴, A. Mulliri ²², M. G. Munhoz ¹¹⁰, R. H. Munzer ⁶³, H. Murakami ¹²², S. Murray ¹¹³, L. Musa ³², J. Musinsky ⁵⁹, J. W. Myrcha ¹³³, B. Naik ¹²¹, A. I. Nambrath ¹⁸, B. K. Nandi ⁴⁶, R. Nania ⁵⁰, E. Nappi ⁴⁹, A. F. Nassirpour ^{17,75}, A. Nath ⁹⁴, C. Nattrass ¹²⁰, M. N. Naydenov ³⁶, A. Neagu ¹⁹, A. Negru ¹²⁴, L. Nellen ⁶⁴, G. Neskovic ³⁸, B. S. Nielsen ⁸³, E. G. Nielsen ⁸³, S. Nikolaev ¹⁴⁰, S. Nikulin ¹⁴⁰, V. Nikulin ¹⁴⁰, F. Noferini ⁵⁰, S. Noh ¹¹, P. Nomokonov ¹⁴¹, J. Norman ¹¹⁷, N. Novitzky ¹²³, P. Nowakowski ¹³³, A. Nyanin ¹⁴⁰, J. Nystrand ²⁰, M. Ogino ⁷⁶, A. Ohlson ⁷⁵, V. A. Okorokov ¹⁴⁰, J. Oleniacz ¹³³, A. C. Oliveira Da Silva ¹²⁰, M. H. Oliver ¹³⁷, A. Onnerstad ¹¹⁵, C. Oppedisano ⁵⁵, A. Ortiz Velasquez ⁶⁴, J. Otwinowski ¹⁰⁷, M. Oya ⁹², K. Oyama ⁷⁶, Y. Pachmayer ⁹⁴, S. Padhan ⁴⁶, D. Pagano ^{131,54}, G. Paic ⁶⁴, A. Palasciano ⁴⁹, S. Panebianco ¹²⁸, H. Park ¹²³, H. Park ¹⁰⁴, J. Park ⁵⁷, J. E. Parkkila ³², R. N. Patra ⁹¹, B. Paul ²², H. Pei ⁶, T. Peitzmann ⁵⁸, X. Peng ⁶, M. Pennisi ²⁴, D. Peresunko ¹⁴⁰, G. M. Perez ⁷, S. Perrin ¹²⁸, Y. Pestov ¹⁴⁰, V. Petrovic ¹⁴⁰, M. Petrovici ⁴⁵, R. P. Pezzi ^{103,65}, S. Piano ⁵⁶, M. Pikna ¹², P. Pillot ¹⁰³, O. Pinazza ^{50,32}, L. Pinsky ¹¹⁴, C. Pinto ⁹⁵, S. Pisano ⁴⁸, M. Płoskoń ⁷⁴, M. Planinic ⁸⁹, F. Pliquett ⁶³, M. G. Poghosyan ⁸⁷, B. Polichtchouk ¹⁴⁰, S. Politano ²⁹, N. Poljak ⁸⁹, A. Pop ⁴⁵, S. Porteboeuf-Houssais ¹²⁵, V. Pozdniakov ¹⁴¹, I. Y. Pozos ⁴⁴, K. K. Pradhan ⁴⁷, S. K. Prasad ⁴, S. Prasad ⁴⁷, R. Preghenella ⁵⁰, F. Prino ⁵⁵, C. A. Pruneau ¹³⁴, I. Pshenichnov ¹⁴⁰, M. Puccio ³², S. Pucillo ²⁴, Z. Pugelova ¹⁰⁶, S. Qiu ⁸⁴, L. Quaglia ²⁴, R. E. Quishpe ¹¹⁴, S. Ragoni ¹⁴, A. Rakotozafindrabe ¹²⁸, L. Ramello ^{130,55}, F. Rami ¹²⁷, S. A. R. Ramirez ⁴⁴, T. A. Rancien ⁷³, M. Rasa ²⁶, S. S. Räsänen ⁴³, R. Rath ⁵⁰, M. P. Rauch ²⁰, I. Ravasenga ⁸⁴, K. F. Read ^{87,120}, C. Reckziegel ¹¹², A. R. Redelbach ³⁸, K. Redlich ^{79,f}, C. A. Reetz ⁹⁷, A. Rehman ²⁰, F. Reidt ³², H. A. Reme-Ness ³⁴, Z. Rescakova ³⁷, K. Reygers ⁹⁴

A. Riabov¹⁴⁰, V. Riabov¹⁴⁰, R. Ricci²⁸, M. Richter¹⁹, A. A. Riedel⁹⁵, W. Riegler³², C. Ristea⁶², M. V. Rodriguez³², M. Rodríguez Cahuantzi⁴⁴, K. Røed¹⁹, R. Rogalev¹⁴⁰, E. Rogochaya¹⁴¹, T. S. Rogoschinski⁶³, D. Rohr³², D. Röhrich²⁰, P. F. Rojas⁴⁴, S. Rojas Torres³⁵, P. S. Rokita¹³³, G. Romanenko¹⁴¹, F. Ronchetti⁴⁸, A. Rosano^{30,52}, E. D. Rosas⁶⁴, K. Roslon¹³³, A. Rossi⁵³, A. Roy⁴⁷, S. Roy⁴⁶, N. Rubini²⁵, O. V. Rueda¹¹⁴, D. Ruggiano¹³³, R. Rui²³, P. G. Russek², R. Russo⁸⁴, A. Rustamov⁸¹, E. Ryabinkin¹⁴⁰, Y. Ryabov¹⁴⁰, A. Rybicki¹⁰⁷, H. Rytönen¹¹⁵, J. Ryu¹⁶, W. Rzeska¹³³, O. A. M. Saarimaki⁴³, R. Sadek¹⁰³, S. Sadhu³¹, S. Sadovskiy¹⁴⁰, J. Saetre²⁰, K. Šafařík³⁵, P. Saha⁴¹, S. K. Saha⁴, S. Saha⁸⁰, B. Sahoo⁴⁶, B. Sahoo⁴⁷, R. Sahoo⁴⁷, S. Sahoo⁶⁰, D. Sahu⁴⁷, P. K. Sahu⁶⁰, J. Saini¹³², K. Sajdakova³⁷, S. Sakai¹²³, M. P. Salvan⁹⁷, S. Sambyal⁹¹, I. Sanna^{32,95}, T. B. Saramela¹¹⁰, D. Sarkar¹³⁴, N. Sarkar¹³², P. Sarma⁴¹, V. Sarritzu²², V. M. Sarti⁹⁵, M. H. P. Sas¹³⁷, J. Schambach⁸⁷, H. S. Scheid⁶³, C. Schiaua⁴⁵, R. Schicker⁹⁴, A. Schmah⁹⁴, C. Schmidt⁹⁷, H. R. Schmidt⁹³, M. O. Schmidt³², M. Schmidt⁹³, N. V. Schmidt⁸⁷, A. R. Schmier¹²⁰, R. Schotter¹²⁷, A. Schröter³⁸, J. Schukraft³², K. Schwarz⁹⁷, K. Schweda⁹⁷, G. Scioli²⁵, E. Scomparin⁵⁵, J. E. Seger¹⁴, Y. Sekiguchi¹²², D. Sekihata¹²², I. Selyuzhenkov⁹⁷, S. Senyukov¹²⁷, J. J. Seo⁵⁷, D. Serebryakov¹⁴⁰, L. Šerkšnytė⁹⁵, A. Sevcenco⁶², T. J. Shaba⁶⁷, A. Shabetai¹⁰³, R. Shahoyan³², A. Shangaraev¹⁴⁰, A. Sharma⁹⁰, B. Sharma⁹¹, D. Sharma⁴⁶, H. Sharma^{53,107}, M. Sharma⁹¹, S. Sharma⁷⁶, S. Sharma⁹¹, U. Sharma⁹¹, A. Shatat⁷², O. Sheibani¹¹⁴, K. Shigaki⁹², M. Shimomura⁷⁷, J. Shin¹¹, S. Shirinkin¹⁴⁰, Q. Shou³⁹, Y. Sibirak¹⁴⁰, S. Siddhanta⁵¹, T. Siemiarzuk⁷⁹, T. F. Silva¹¹⁰, D. Silvermyr⁷⁵, T. Simantathammakul¹⁰⁵, R. Simeonov³⁶, B. Singh⁹¹, B. Singh⁹⁵, K. Singh⁴⁷, R. Singh⁸⁰, R. Singh⁹¹, R. Singh⁴⁷, S. Singh¹⁵, V. K. Singh¹³², V. Singhal¹³², T. Sinha⁹⁹, B. Sitar¹², M. Sitta^{130,55}, T. B. Skaali¹⁹, G. Skorodumovs⁹⁴, M. Slupecki⁴³, N. Smirnov¹³⁷, R. J. M. Snellings⁵⁸, E. H. Solheim¹⁹, J. Song¹¹⁴, A. Songmoolnak¹⁰⁵, C. Sonnabend^{32,97}, F. Soramel²⁷, A. B. Soto-hernandez⁸⁸, R. Spijkers⁸⁴, I. Sputowska¹⁰⁷, J. Staa⁷⁵, J. Stachel⁹⁴, I. Stan⁶², P. J. Steffanic¹²⁰, S. F. Stiefelmaier⁹⁴, D. Stocco¹⁰³, I. Storehaug¹⁹, P. Stratmann¹³⁵, S. Strazzi²⁵, C. P. Stylianidis⁸⁴, A. A. P. Suaide¹¹⁰, C. Suire⁷², M. Sukhanov¹⁴⁰, M. Suljic³², R. Sultanov¹⁴⁰, V. Sumberia⁹¹, S. Sumowidagdo⁸², S. Swain⁶⁰, I. Szarka¹², M. Szymkowski¹³³, S. F. Taghavi⁹⁵, G. Taillepied⁹⁷, J. Takahashi¹¹¹, G. J. Tambave⁸⁰, S. Tang⁶, Z. Tang¹¹⁸, J. D. Tapia Takaki¹¹⁶, N. Tapus¹²⁴, L. A. Tarasovicova¹³⁵, M. G. Tarzila⁴⁵, G. F. Tassielli³¹, A. Tauro³², G. Tejada Muñoz⁴⁴, A. Telesca³², L. Terlizzi²⁴, C. Terrevoli¹¹⁴, S. Thakur⁴, D. Thomas¹⁰⁸, A. Tikhonov¹⁴⁰, A. R. Timmins¹¹⁴, M. Tkacik¹⁰⁶, T. Tkacik¹⁰⁶, A. Toia⁶³, R. Tokumoto⁹², N. Topilskaya¹⁴⁰, M. Toppi⁴⁸, T. Tork⁷², A. G. Torres Ramos³¹, A. Trifiró^{30,52}, A. S. Triolo^{32,30,52}, S. Tripathy⁵⁰, T. Tripathy⁴⁶, S. Trogolo³², V. Trubnikov³, W. H. Trzaska¹¹⁵, T. P. Trzcinski¹³³, A. Tumkin¹⁴⁰, R. Turrisi⁵³, T. S. Tveter¹⁹, K. Ullaland²⁰, B. Ulukutlu⁹⁵, A. Uras¹²⁶, M. Urioni^{54,131}, G. L. Usai²², M. Vala³⁷, N. Valle²¹, L. V. R. van Doremalen⁵⁸, M. van Leeuwen⁸⁴, C. A. van Veen⁹⁴, R. J. G. van Weelden⁸⁴, P. Vande Vyvre³², D. Varga¹³⁶, Z. Varga¹³⁶, M. Vasileiou⁷⁸, A. Vasiliev¹⁴⁰, O. Vázquez Doce⁴⁸, V. Vechemin¹⁴⁰, E. Vercellin²⁴, S. Vergara Limón⁴⁴, L. Vermunt⁹⁷, R. Vértesi¹³⁶, M. Verweij⁵⁸, L. Vickovic³³, Z. Vilakazi¹²¹, O. Villalobos Baillie¹⁰⁰, A. Villani²³, G. Vino⁴⁹, A. Vinogradov¹⁴⁰, T. Virgili²⁸, M. M. O. Virta¹¹⁵, V. Vislavicius⁷⁵, A. Vodopyanov¹⁴¹, B. Volkel³², M. A. Völkl⁹⁴, K. Voloshin¹⁴⁰, S. A. Voloshin¹³⁴, G. Volpe³¹, B. von Haller³², I. Vorobyev⁹⁵, N. Vozniuk¹⁴⁰, J. Vrláková³⁷, J. Wan³⁹, C. Wang³⁹, D. Wang³⁹, Y. Wang³⁹, A. Wegrzynek³², F. T. Weighofer³⁸, S. C. Wenzel³², J. P. Wessels¹³⁵, S. L. Weyhmler¹³⁷, J. Wiechula⁶³, J. Wikne¹⁹, G. Wilk⁷⁹, J. Wilkinson⁹⁷, G. A. Willems¹³⁵, B. Windelband⁹⁴, M. Winn¹²⁸, J. R. Wright¹⁰⁸, W. Wu³⁹, Y. Wu¹¹⁸, R. Xu⁶, A. Yadav⁴², A. K. Yadav¹³², S. Yalcin⁷¹, Y. Yamaguchi⁹², S. Yang²⁰, S. Yano⁹², Z. Yin⁶, I.-K. Yoo¹⁶, J. H. Yoon⁵⁷, H. Yu¹¹, S. Yuan²⁰, A. Yuncu⁹⁴, V. Zaccolo²³, C. Zampolli³², F. Zanone⁹⁴, N. Zardoshti³², A. Zarochentsev¹⁴⁰, P. Závada⁶¹, N. Zaviyalov¹⁴⁰, M. Zhalov¹⁴⁰, B. Zhang⁶, L. Zhang³⁹, S. Zhang³⁹, X. Zhang⁶, Y. Zhang¹¹⁸, Z. Zhang⁶, M. Zhao¹⁰, V. Zhrebchevskii¹⁴⁰, Y. Zhi¹⁰, D. Zhou⁶, Y. Zhou⁸³, J. Zhu^{97,6}, Y. Zhu⁶, S. C. Zugravel⁵⁵ and N. Zurlo^{131,54}

(ALICE Collaboration)

¹A.I. Alikhanyan National Science Laboratory (Yerevan Physics Institute) Foundation, Yerevan, Armenia²AGH University of Science and Technology, Cracow, Poland³Bogolyubov Institute for Theoretical Physics, National Academy of Sciences of Ukraine, Kiev, Ukraine⁴Department of Physics and Centre for Astroparticle Physics and Space Science (CAPSS), Bose Institute, Kolkata, India⁵California Polytechnic State University, San Luis Obispo, California, USA⁶Central China Normal University, Wuhan, China⁷Centro de Aplicaciones Tecnológicas y Desarrollo Nuclear (CEADEN), Havana, Cuba⁸Centro de Investigación y de Estudios Avanzados (CINVESTAV), Mexico City and Mérida, Mexico⁹Chicago State University, Chicago, Illinois, USA¹⁰China Institute of Atomic Energy, Beijing, China¹¹Chungbuk National University, Cheongju, Republic of Korea¹²Faculty of Mathematics, Physics and Informatics, Comenius University Bratislava, Bratislava, Slovak Republic¹³COMSATS University Islamabad, Islamabad, Pakistan

- ¹⁴Creighton University, Omaha, Nebraska, USA
- ¹⁵Department of Physics, Aligarh Muslim University, Aligarh, India
- ¹⁶Department of Physics, Pusan National University, Pusan, Republic of Korea
- ¹⁷Department of Physics, Sejong University, Seoul, Republic of Korea
- ¹⁸Department of Physics, University of California, Berkeley, California, USA
- ¹⁹Department of Physics, University of Oslo, Oslo, Norway
- ²⁰Department of Physics and Technology, University of Bergen, Bergen, Norway
- ²¹Dipartimento di Fisica, Università di Pavia, Pavia, Italy
- ²²Dipartimento di Fisica dell'Università and Sezione INFN, Cagliari, Italy
- ²³Dipartimento di Fisica dell'Università and Sezione INFN, Trieste, Italy
- ²⁴Dipartimento di Fisica dell'Università and Sezione INFN, Turin, Italy
- ²⁵Dipartimento di Fisica e Astronomia dell'Università and Sezione INFN, Bologna, Italy
- ²⁶Dipartimento di Fisica e Astronomia dell'Università and Sezione INFN, Catania, Italy
- ²⁷Dipartimento di Fisica e Astronomia dell'Università and Sezione INFN, Padova, Italy
- ²⁸Dipartimento di Fisica "E.R. Caianiello" dell'Università and Gruppo Collegato INFN, Salerno, Italy
- ²⁹Dipartimento DISAT del Politecnico and Sezione INFN, Turin, Italy
- ³⁰Dipartimento di Scienze MIFT, Università di Messina, Messina, Italy
- ³¹Dipartimento Interateneo di Fisica "M. Merlin" and Sezione INFN, Bari, Italy
- ³²European Organization for Nuclear Research (CERN), Geneva, Switzerland
- ³³Faculty of Electrical Engineering, Mechanical Engineering and Naval Architecture, University of Split, Split, Croatia
- ³⁴Faculty of Engineering and Science, Western Norway University of Applied Sciences, Bergen, Norway
- ³⁵Faculty of Nuclear Sciences and Physical Engineering, Czech Technical University in Prague, Prague, Czech Republic
- ³⁶Faculty of Physics, Sofia University, Sofia, Bulgaria
- ³⁷Faculty of Science, P.J. Šafárik University, Košice, Slovak Republic
- ³⁸Frankfurt Institute for Advanced Studies, Johann Wolfgang Goethe-Universität Frankfurt, Frankfurt, Germany
- ³⁹Fudan University, Shanghai, China
- ⁴⁰Gangneung-Wonju National University, Gangneung, Republic of Korea
- ⁴¹Department of Physics, Gauhati University, Guwahati, India
- ⁴²Helmholtz-Institut für Strahlen- und Kernphysik, Rheinische Friedrich-Wilhelms-Universität Bonn, Bonn, Germany
- ⁴³Helsinki Institute of Physics (HIP), Helsinki, Finland
- ⁴⁴High Energy Physics Group, Universidad Autónoma de Puebla, Puebla, Mexico
- ⁴⁵Horia Hulubei National Institute of Physics and Nuclear Engineering, Bucharest, Romania
- ⁴⁶Indian Institute of Technology Bombay (IIT), Mumbai, India
- ⁴⁷Indian Institute of Technology Indore, Indore, India
- ⁴⁸INFN, Laboratori Nazionali di Frascati, Frascati, Italy
- ⁴⁹INFN, Sezione di Bari, Bari, Italy
- ⁵⁰INFN, Sezione di Bologna, Bologna, Italy
- ⁵¹INFN, Sezione di Cagliari, Cagliari, Italy
- ⁵²INFN, Sezione di Catania, Catania, Italy
- ⁵³INFN, Sezione di Padova, Padova, Italy
- ⁵⁴INFN, Sezione di Pavia, Pavia, Italy
- ⁵⁵INFN, Sezione di Torino, Turin, Italy
- ⁵⁶INFN, Sezione di Trieste, Trieste, Italy
- ⁵⁷Inha University, Incheon, Republic of Korea
- ⁵⁸Institute for Gravitational and Subatomic Physics (GRASP), Utrecht University/Nikhef, Utrecht, Netherlands
- ⁵⁹Institute of Experimental Physics, Slovak Academy of Sciences, Košice, Slovak Republic
- ⁶⁰Institute of Physics, Homi Bhabha National Institute, Bhubaneswar, India
- ⁶¹Institute of Physics of the Czech Academy of Sciences, Prague, Czech Republic
- ⁶²Institute of Space Science (ISS), Bucharest, Romania
- ⁶³Institut für Kernphysik, Johann Wolfgang Goethe-Universität Frankfurt, Frankfurt, Germany
- ⁶⁴Instituto de Ciencias Nucleares, Universidad Nacional Autónoma de México, Mexico City, Mexico
- ⁶⁵Instituto de Física, Universidade Federal do Rio Grande do Sul (UFRGS), Porto Alegre, Brazil
- ⁶⁶Instituto de Física, Universidad Nacional Autónoma de México, Mexico City, Mexico
- ⁶⁷iThemba LABS, National Research Foundation, Somerset West, South Africa
- ⁶⁸Jeonbuk National University, Jeonju, Republic of Korea
- ⁶⁹Fachbereich Informatik und Mathematik, Johann-Wolfgang-Goethe Universität Frankfurt Institut für Informatik, Frankfurt, Germany
- ⁷⁰Korea Institute of Science and Technology Information, Daejeon, Republic of Korea
- ⁷¹KTO Karatay University, Konya, Turkey
- ⁷²Laboratoire de Physique des 2 Infinis, Irène Joliot-Curie, Orsay, France

- ⁷³Laboratoire de Physique Subatomique et de Cosmologie, Université Grenoble-Alpes, CNRS-IN2P3, Grenoble, France
- ⁷⁴Lawrence Berkeley National Laboratory, Berkeley, California, USA
- ⁷⁵Division of Particle Physics, Department of Physics, Lund University, Lund, Sweden
- ⁷⁶Nagasaki Institute of Applied Science, Nagasaki, Japan
- ⁷⁷Nara Women's University (NWU), Nara, Japan
- ⁷⁸Department of Physics, School of Science, National and Kapodistrian University of Athens, Athens, Greece
- ⁷⁹National Centre for Nuclear Research, Warsaw, Poland
- ⁸⁰National Institute of Science Education and Research, Homi Bhabha National Institute, Jatni, India
- ⁸¹National Nuclear Research Center, Baku, Azerbaijan
- ⁸²National Research and Innovation Agency - BRIN, Jakarta, Indonesia
- ⁸³Niels Bohr Institute, University of Copenhagen, Copenhagen, Denmark
- ⁸⁴Nikhef, National Institute for Subatomic Physics, Amsterdam, Netherlands
- ⁸⁵Nuclear Physics Group, STFC Daresbury Laboratory, Daresbury, United Kingdom
- ⁸⁶Nuclear Physics Institute of the Czech Academy of Sciences, Husinec-Řež, Czech Republic
- ⁸⁷Oak Ridge National Laboratory, Oak Ridge, Tennessee, USA
- ⁸⁸Ohio State University, Columbus, Ohio, USA
- ⁸⁹Physics Department, Faculty of science, University of Zagreb, Zagreb, Croatia
- ⁹⁰Physics Department, Panjab University, Chandigarh, India
- ⁹¹Physics Department, University of Jammu, Jammu, India
- ⁹²Physics Program and International Institute for Sustainability with Knotted Chiral Meta Matter (SKCM2), Hiroshima University, Hiroshima, Japan
- ⁹³Physikalisches Institut, Eberhard-Karls-Universität Tübingen, Tübingen, Germany
- ⁹⁴Physikalisches Institut, Ruprecht-Karls-Universität Heidelberg, Heidelberg, Germany
- ⁹⁵Physik Department, Technische Universität München, Munich, Germany
- ⁹⁶Politecnico di Bari and Sezione INFN, Bari, Italy
- ⁹⁷Research Division and ExtreMe Matter Institute EMMI, GSI Helmholtzzentrum für Schwerionenforschung GmbH, Darmstadt, Germany
- ⁹⁸Saga University, Saga, Japan
- ⁹⁹Saha Institute of Nuclear Physics, Homi Bhabha National Institute, Kolkata, India
- ¹⁰⁰School of Physics and Astronomy, University of Birmingham, Birmingham, United Kingdom
- ¹⁰¹Sección Física, Departamento de Ciencias, Pontificia Universidad Católica del Perú, Lima, Peru
- ¹⁰²Stefan Meyer Institut für Subatomare Physik (SMI), Vienna, Austria
- ¹⁰³SUBATECH, IMT Atlantique, Nantes Université, CNRS-IN2P3, Nantes, France
- ¹⁰⁴Sungkyunkwan University, Suwon City, Republic of Korea
- ¹⁰⁵Suranaree University of Technology, Nakhon Ratchasima, Thailand
- ¹⁰⁶Technical University of Košice, Košice, Slovak Republic
- ¹⁰⁷The Henryk Niewodniczanski Institute of Nuclear Physics, Polish Academy of Sciences, Cracow, Poland
- ¹⁰⁸The University of Texas at Austin, Austin, Texas, USA
- ¹⁰⁹Universidad Autónoma de Sinaloa, Culiacán, Mexico
- ¹¹⁰Universidade de São Paulo (USP), São Paulo, Brazil
- ¹¹¹Universidade Estadual de Campinas (UNICAMP), Campinas, Brazil
- ¹¹²Universidade Federal do ABC, Santo Andre, Brazil
- ¹¹³University of Cape Town, Cape Town, South Africa
- ¹¹⁴University of Houston, Houston, Texas, USA
- ¹¹⁵University of Jyväskylä, Jyväskylä, Finland
- ¹¹⁶University of Kansas, Lawrence, Kansas, USA
- ¹¹⁷University of Liverpool, Liverpool, United Kingdom
- ¹¹⁸University of Science and Technology of China, Hefei, China
- ¹¹⁹University of South-Eastern Norway, Kongsberg, Norway
- ¹²⁰University of Tennessee, Knoxville, Tennessee, USA
- ¹²¹University of the Witwatersrand, Johannesburg, South Africa
- ¹²²University of Tokyo, Tokyo, Japan
- ¹²³University of Tsukuba, Tsukuba, Japan
- ¹²⁴University Politehnica of Bucharest, Bucharest, Romania
- ¹²⁵Université Clermont Auvergne, CNRS/IN2P3, LPC, Clermont-Ferrand, France
- ¹²⁶Institut de Physique des 2 Infinis de Lyon, Université de Lyon, CNRS/IN2P3, Lyon, France
- ¹²⁷Université de Strasbourg, CNRS, IPHC UMR 7178, F-67000 Strasbourg, France, Strasbourg, France
- ¹²⁸Département de Physique Nucléaire (DPhN), Université Paris-Saclay Centre d'Etudes de Saclay (CEA), IRFU, Saclay, France
- ¹²⁹Università degli Studi di Foggia, Foggia, Italy
- ¹³⁰Università del Piemonte Orientale, Vercelli, Italy

¹³¹*Università di Brescia, Brescia, Italy*

¹³²*Variable Energy Cyclotron Centre, Homi Bhabha National Institute, Kolkata, India*

¹³³*Warsaw University of Technology, Warsaw, Poland*

¹³⁴*Wayne State University, Detroit, Michigan, USA*

¹³⁵*Institut für Kernphysik, Westfälische Wilhelms-Universität Münster, Münster, Germany*

¹³⁶*Wigner Research Centre for Physics, Budapest, Hungary*

¹³⁷*Yale University, New Haven, Connecticut, USA*

¹³⁸*Yonsei University, Seoul, Republic of Korea*

¹³⁹*Zentrum für Technologie und Transfer (ZTT), Worms, Germany*

¹⁴⁰*Affiliated with an institute covered by a cooperation agreement with CERN*

¹⁴¹*Affiliated with an international laboratory covered by a cooperation agreement with CERN*

^aAlso at: Max-Planck-Institut für Physik, Munich, Germany.

^bAlso at: Italian National Agency for New Technologies, Energy and Sustainable Economic Development (ENEA), Bologna, Italy.

^cDeceased.

^dAlso at: An institution covered by a cooperation agreement with CERN.

^eAlso at: Department of Applied Physics, Aligarh Muslim University, Aligarh, India.

^fAlso at: Institute of Theoretical Physics, University of Wrocław, Poland.

PIV

**MULTIPLICITY AND EVENT-SCALE DEPENDENT FLOW AND
JET FRAGMENTATION IN PP COLLISIONS AT $\sqrt{s} = 13$ TEV
AND IN P-PB COLLISIONS AT $\sqrt{s_{NN}} = 5.02$ TEV**

by

S. Acharya et al. (ALICE Collaboration)

arXiv:2308.165911, accepted by PLB, final proof here , 0 (2024).

Multiplicity and event-scale dependent flow and jet fragmentation in pp collisions at $\sqrt{s} = 13$ TeV and in p–Pb collisions at $\sqrt{s_{NN}} = 5.02$ TeV

The ALICE collaboration

E-mail: alice-publications@cern.ch

ABSTRACT: Long- and short-range correlations for pairs of charged particles are studied via two-particle angular correlations in pp collisions at $\sqrt{s} = 13$ TeV and p–Pb collisions at $\sqrt{s_{NN}} = 5.02$ TeV. The correlation functions are measured as a function of relative azimuthal angle $\Delta\varphi$ and pseudorapidity separation $\Delta\eta$ for pairs of primary charged particles within the pseudorapidity interval $|\eta| < 0.9$ and the transverse-momentum interval $1 < p_T < 4$ GeV/c. Flow coefficients are extracted for the long-range correlations ($1.6 < |\Delta\eta| < 1.8$) in various high-multiplicity event classes using the low-multiplicity template fit method. The method is used to subtract the enhanced yield of away-side jet fragments in high-multiplicity events. These results show decreasing flow signals toward lower multiplicity events. Furthermore, the flow coefficients for events with hard probes, such as jets or leading particles, do not exhibit any significant changes compared to those obtained from high-multiplicity events without any specific event selection criteria. The results are compared with hydrodynamic-model calculations, and it is found that a better understanding of the initial conditions is necessary to describe the results, particularly for low-multiplicity events.

KEYWORDS: Collective Flow, Hadron-Hadron Scattering, Jets

ARXIV EPRINT: [2308.16591](https://arxiv.org/abs/2308.16591)

Contents

1	Introduction	1
2	Experimental setup and data samples	3
3	Analysis procedure	4
3.1	Two-particle angular correlations	4
3.2	Extraction of flow coefficients	5
4	Systematic uncertainties	10
5	Results	12
5.1	Transverse-momentum and multiplicity dependence of anisotropic flow	12
5.2	Event-scale dependence of the flow coefficients	13
5.3	Comparisons with models	14
6	Conclusions	16
	The ALICE collaboration	27

1 Introduction

High-energy nucleus-nucleus (AA) collisions exhibit strong collectivity, which has been observed through anisotropy in the momentum distribution of emitted final-state particles at RHIC [1–4] and the LHC [5–8]. This momentum anisotropy is developed by the pressure-driven expansion of the strongly interacting quark-gluon plasma (QGP), which emerges from the initial spatial anisotropy in such collisions. The collective nature of the momentum anisotropy is mostly deduced via particle correlations which span over a wide range of pseudorapidity. The collective motion of the emitted particles, which reflects the collectivity of the initial medium, is generally quantified using a Fourier expansion, characterizing the so-called “anisotropic flow” [9]. In recent years, long-range correlations have been also observed in smaller collision systems such as high-multiplicity proton-proton (pp) [10–16], proton-nucleus (pA) [17–20], and in collisions of light nuclei [21, 22]. These observations raise the question to what extent do small-system collisions and heavy-ion collisions share the underlying mechanism, which is responsible for the observed long-range correlations. A crucial evidence of a strongly interacting medium in small-system collisions would be the presence of jet quenching [23, 24]. However, this phenomenon has not yet been observed in either high-multiplicity pp or p–Pb collisions [25–29], possibly due to the current experimental uncertainties being too large to observe it in such small-system collisions.

Current approaches to model heavy-ion collisions divide the evolution of the out-of-equilibrium, strongly-coupled, quantum-chromodynamic medium into multiple stages, and each stage is described by an effective theory. To this date, the combination of color-glass

condensate effective field theory (CGC-EFT) [30, 31], causal hydrodynamics [32–40], and a hadronic cascade model [41–43] leads to the most successful description of a wide range of observables in heavy-ion collisions, e.g., particle spectra, centrality dependence of average particle transverse momenta, and multi-particle correlations [44–51]. By employing global Bayesian analyses, parameters of the multi-stage model, including those quantifying the transport properties of the QGP, can be constrained using measured data [52–55]. Despite the studies describing both heavy AA and pA collisions in a single framework [56], the origin of the flow-like correlations is still under debate. It is unclear whether the flow-like behavior originates from the early stages of the collision in the realm of applicability of CGC-EFT [57, 58] or whether it develops during the collective evolution, where causal hydrodynamics is applicable [59, 60]. Both scenarios may be responsible for the observed correlations in the final state [59]. Although collective models are successful in describing available two-particle correlation data from small-system collisions, they predict the opposite sign for four-particle azimuthal cumulants compared to experiment [12, 14, 61]. On the other hand, a semi-analytical toy model based on the Gubser hydrodynamic solution [62, 63] can explain the two- and four-particle correlations in pp collisions [64]. In particular, this model has explained the relationship between the sign of the four-particle cumulants and fluctuations in the initial state [64].

Besides the models based on the causal hydrodynamic framework, there are other attempts to explain the observed flow-like signals in small-system collisions using alternative descriptions. For instance, a study based on the A Multi-Phase Transport model (AMPT) [65] leads to satisfactory agreement with the experimental data [66]. The applicability of fluid-dynamical simulations and partonic cascade models in small-system collisions was explored in ref. [67]. In a kinetic-theory framework with isotropization-time approximation, it is possible to explain the long-range correlations by fluid-like (hydrodynamic) excitation for Pb–Pb collisions and particle-like (or non-hydrodynamic) excitation for pp or p–Pb collisions [68–70]. Another potential description for the collectivity in small-system collisions is provided by PYTHIA 8, in which interacting strings repel one another in a transverse direction by a mechanism dubbed as “string shoving” [71, 72]. The repulsion of the strings causes microscopic transverse pressure, giving rise to long-range correlations of particles. The string shoving approach in PYTHIA 8 successfully reproduces the near-side ridge yield observed in measurements by ALICE [73] and CMS [12]. A systematic mapping of correlation effects across collision systems of various sizes is currently underway on the theoretical side, for example, see ref. [74]. A quantitative description of the full set of experimental data has not been achieved yet. A summary of various explanations for the observed correlations in small-system collisions is given in refs. [75–77].

Measurements of anisotropic flow in small-system collisions are strongly affected by non-flow effects, predominantly originating from correlations among the constituents of jet fragmentation processes. In case of two-particle correlations, the non-flow contribution is usually suppressed by requiring a large $\Delta\eta$ gap between the two particles. This separation in pseudorapidity is also widely used in cumulant methods [13, 78]. However, this $\Delta\eta$ -gap method removes the non-flow contribution only on the near side ($\Delta\varphi \sim 0$) and not on the away side ($\Delta\varphi \sim \pi$). Later, a low-multiplicity template fit method was proposed to remove

non-flow contributions on the away-side [10, 19, 79]. This method takes into account that the yield of jet fragments increases with increasing particle multiplicity [80–82]. By using the template fit method, the yield of away-side jet fragments can be subtracted, provided that the distribution that quantifies the shape of jet fragments is independent of the multiplicity class and therefore can be described by the low-multiplicity template.

As an extension of the studies of the near-side long-range ridge and jet-fragmentation yields in pp collisions at the center-of-mass energy $\sqrt{s} = 13$ TeV [73] and in p–Pb collisions at the center-of-mass energy per nucleon pair $\sqrt{s_{NN}} = 5.02$ TeV [17, 83], this article studies the interplay of jet production and collective effects, i.e., short- and long-range correlations simultaneously in these systems. The article also reports flow coefficients extracted for collisions tagged with different event-scale selections. The event-scale selection requires a minimum transverse momentum of the leading particle or the reconstructed jet at midrapidity, which is expected to bias the impact parameter of pp collisions to be smaller on average [84–86]. At the same time, the transverse momentum of the leading particle or the reconstructed jet provides a measure of the four-momentum transfer (Q^2) in the hard-parton scattering [87–89]. The transverse-momentum threshold implies a higher Q^2 for the collision. Such events with a large Q^2 may, on average, have a lower impact parameter than pp events without any requirement on Q^2 [85].

This article is organized as follows. First, the experimental setup and analysis method are described in section 2 and section 3, respectively. Section 4 discusses the systematic uncertainties. The results and their comparison with model calculations are presented and discussed in section 5. Finally, the results are summarized in section 6.

2 Experimental setup and data samples

The analysis is based on pp and p–Pb data collected during the LHC Run 2 period. The pp collisions had a center-of-mass energy $\sqrt{s} = 13$ TeV, and they were recorded from 2016 to 2018. The p–Pb collisions had a center-of-mass energy per nucleon-nucleon pair $\sqrt{s_{NN}} = 5.02$ TeV, and they were collected in 2016. It is worth noting that in p–Pb collisions there is a shift in the center-of-mass rapidity of $\Delta y = 0.465$ in the direction of the proton beam due to the asymmetric collision system.

A comprehensive description of the ALICE detector and its performance can be found in refs. [8, 90, 91]. The analysis utilizes the V0 detector [92], the Inner Tracking System (ITS) [93, 94], and the Time Projection Chamber (TPC) [95].

The V0 detector consists of two stations on both sides of the interaction point, V0A and V0C, each comprising 32 plastic scintillator tiles, covering the full azimuthal angle within the pseudorapidity intervals $2.8 < \eta < 5.1$ and $-3.7 < \eta < -1.7$, respectively. The ITS is a silicon tracker with six layers of silicon sensors. The two innermost layers of the ITS are called the Silicon Pixel Detector (SPD) [96]. In addition to the two SPD layers, the middle two layers are the Silicon Drift Detector, and the outermost layers are the Silicon Strip Detector. The TPC is a gas-filled cylindrical tracking detector providing up to 159 reconstruction points for charged tracks traversing the full radial extent of the detector.

The V0 provides a minimum bias (MB) trigger in both pp and p–Pb collisions and an additional high-multiplicity trigger in pp collisions. The MB trigger is obtained by a time

coincidence of V0A and V0C signals. Amplitudes of V0A and V0C signals are proportional to charged-particle multiplicity, and their sum is denoted as V0M. The high-multiplicity trigger in pp collisions requires the V0M signal to exceed five times the mean value measured in MB collisions, selecting the 0.1% of MB events with the largest V0M multiplicity. The centrality in p–Pb collisions is determined using the V0A detector, which is located in the Pb-going direction [25]. The analyzed data samples of MB and high-multiplicity pp events at $\sqrt{s} = 13$ TeV correspond to integrated luminosities (\mathcal{L}_{int}) of about 19 nb^{-1} and 11 pb^{-1} , respectively [97]. In p–Pb collisions at $\sqrt{s_{\text{NN}}} = 5.02$ TeV, the corresponding integrated luminosity is $\mathcal{L}_{\text{int}} \sim 0.3 \text{ nb}^{-1}$.

Positions of primary vertices are reconstructed from signals measured by the SPD. The reconstructed primary vertices are required to be within 8 cm of the nominal interaction point along the beam direction. Pileup events are identified as events with multiple reconstructed primary vertices. These events are rejected if the distance between any of the vertices to the main primary vertex is greater than 0.8 cm. The probability of pileup events is estimated to range from 10^{-3} to 10^{-2} for MB and high-multiplicity events in pp collisions [98]. The pileup probability is estimated to be negligible in p–Pb collisions [29].

Charged-particle tracks are reconstructed using the combined information from the ITS and TPC. For charged particles emitted from a vertex located within $|z_{\text{vtx}}| < 8$ cm along the beam direction, the ITS and TPC provide a pseudorapidity coverage of $|\eta| < 1.4$ and 0.9, respectively. Both detectors have full coverage in azimuth. They are placed in a uniform magnetic field of 0.5 T that is oriented along the beam direction.

The charged-particle selection criteria are optimized to ensure a uniform efficiency over the midrapidity range $|\eta| < 0.9$ to mitigate the effects of small areas where some ITS layers are inactive in both collision systems. The selected sample of tracks consists of two classes. Tracks in the first class must have at least one hit in the SPD. Tracks of the second class do not have any hits in the SPD, but their origin is constrained to the primary vertex [17]. Charged-particle tracks are reconstructed down to a transverse momentum (p_{T}) of $0.15 \text{ GeV}/c$ with an efficiency of approximately 65% [99]. The efficiency increases to 80% for particles with $p_{\text{T}} > 1 \text{ GeV}/c$. The p_{T} resolution is approximately 1% for primary charged particles [100] with $p_{\text{T}} < 1 \text{ GeV}/c$, and it linearly increases to 6% at $p_{\text{T}} \sim 50 \text{ GeV}/c$ in pp collisions and 10% in p–Pb collisions [101].

3 Analysis procedure

3.1 Two-particle angular correlations

Two-particle angular correlations are measured as a function of the relative azimuthal angle ($\Delta\varphi$) and the relative pseudorapidity ($\Delta\eta$) between a trigger and associated particles

$$\frac{1}{N_{\text{trig}}} \frac{d^2 N_{\text{pair}}}{d\Delta\eta d\Delta\varphi} = B(0,0) \frac{S(\Delta\eta, \Delta\varphi)}{B(\Delta\eta, \Delta\varphi)} \Big|_{p_{\text{T, trig}}, p_{\text{T, assoc}}}, \quad (3.1)$$

where $p_{\text{T, trig}}$ and $p_{\text{T, assoc}}$ denote the transverse momentum of the trigger and associated particles, respectively. While the transverse momentum range for associated particles is fixed to $1 < p_{\text{T, assoc}} < 4 \text{ GeV}/c$ for trigger particles, several transverse momentum ranges are

considered. The lower limit of $p_{T,\text{trig}}$ and $p_{T,\text{assoc}}$ ($> 1 \text{ GeV}/c$) is chosen in order to avoid jet-like contributions from lower p_T particles which extend into the larger $\Delta\eta$ range because of the limited η acceptance [73]. The numbers of trigger particles and trigger-associated particle pairs are denoted as N_{trig} and N_{pair} , respectively. The average number of pairs in the same event, denoted by $S(\Delta\eta, \Delta\varphi)$, is given by $\frac{1}{N_{\text{trig}}} \frac{d^2 N_{\text{same}}}{d\Delta\eta d\Delta\varphi}$. The $B(\Delta\eta, \Delta\varphi)$ represents the number of pairs in mixed events and is normalized with its value at the point where $\Delta\eta = 0$ and $\Delta\varphi = 0$, denoted as $B(0, 0)$. To correct for acceptance effects, $S(\Delta\eta, \Delta\varphi)$ is divided by $B(\Delta\eta, \Delta\varphi)/B(0, 0)$. The particles are weighted by the inverse of the tracking efficiency, which is obtained in the same way as in ref. [73]. In that study, the tracking efficiency and the secondary contamination (fake rate) were calculated using a detector simulation with the PYTHIA 8 event generator and the GEANT3 transport code [102]. To account for differences in particle composition between real data and PYTHIA, the tracking efficiency is determined from the above mentioned PYTHIA-based simulation with reweighted primary particle-species composition. The weights reflect realistic abundances of different particle species, which were extracted by a data-driven method [101, 103]. Events to be mixed are required to have primary vertices within the same 2 cm wide z_{vtx} interval. The correlation functions are averaged over the vertex intervals, resulting in the final per-trigger yield [104, 105].

The fully corrected correlation functions from pp and p-Pb collisions are shown in figure 1. The z -axis is scaled in order to exhibit the ridge structures at large $\Delta\eta$ regions. As a result, the jet peaks are sheared off in all figures. The flow modulation structure is clearly observed to emerge in the high-multiplicity collisions for both systems, while it is not seen in the low-multiplicity collisions. The away-side regions are populated mostly by back-to-back jet correlations.

The per-trigger yield is determined by integrating the correlation function at large $\Delta\eta$ ($1.6 < |\Delta\eta| < 1.8$) to remove non-flow contributions from near-side jet fragments. The per-trigger yield as a function of $\Delta\varphi$ is expressed as

$$Y(\Delta\varphi) = \frac{1}{N_{\text{trig}}} \frac{dN_{\text{pair}}}{d\Delta\varphi} = \int_{1.6 < |\Delta\eta| < 1.8} \left[\frac{1}{N_{\text{trig}}} \frac{d^2 N_{\text{pair}}}{d\Delta\eta d\Delta\varphi} \right] \frac{1}{\delta_{\Delta\eta}} d\Delta\eta, \quad (3.2)$$

where the factor $\delta_{\Delta\eta} = 0.4$ normalizes the obtained per-trigger yield per unit of pseudorapidity. The per-trigger yields are extracted for the considered $p_{T,\text{trig}}$ and $p_{T,\text{assoc}}$ intervals in several multiplicity classes: 0–0.1%, 1–5%, 5–20%, 20–60%, and 60–100% in pp collisions, and 0–5%, 5–10%, 10–20%, 20–40%, 40–60%, and 60–100% in p-Pb collisions. The conversion of the measured forward event multiplicities to the charge-particle multiplicities N_{ch} at midrapidity ($|\eta| < 0.5$) used in section 5 is based on ref. [98].

3.2 Extraction of flow coefficients

As discussed in refs. [10, 19], the correlation function in a given multiplicity interval is fitted with

$$Y_{\text{HM}}(\Delta\varphi) = G (1 + 2v_{2,2} \cos(2\Delta\varphi) + 2v_{3,3} \cos(3\Delta\varphi)) + F Y_{\text{LM}}(\Delta\varphi), \quad (3.3)$$

where $Y_{\text{LM}}(\Delta\varphi)$ is the measured per-trigger yield from low-multiplicity events. The normalization factor for the first three Fourier terms, which parameterize the long-range, flow-like

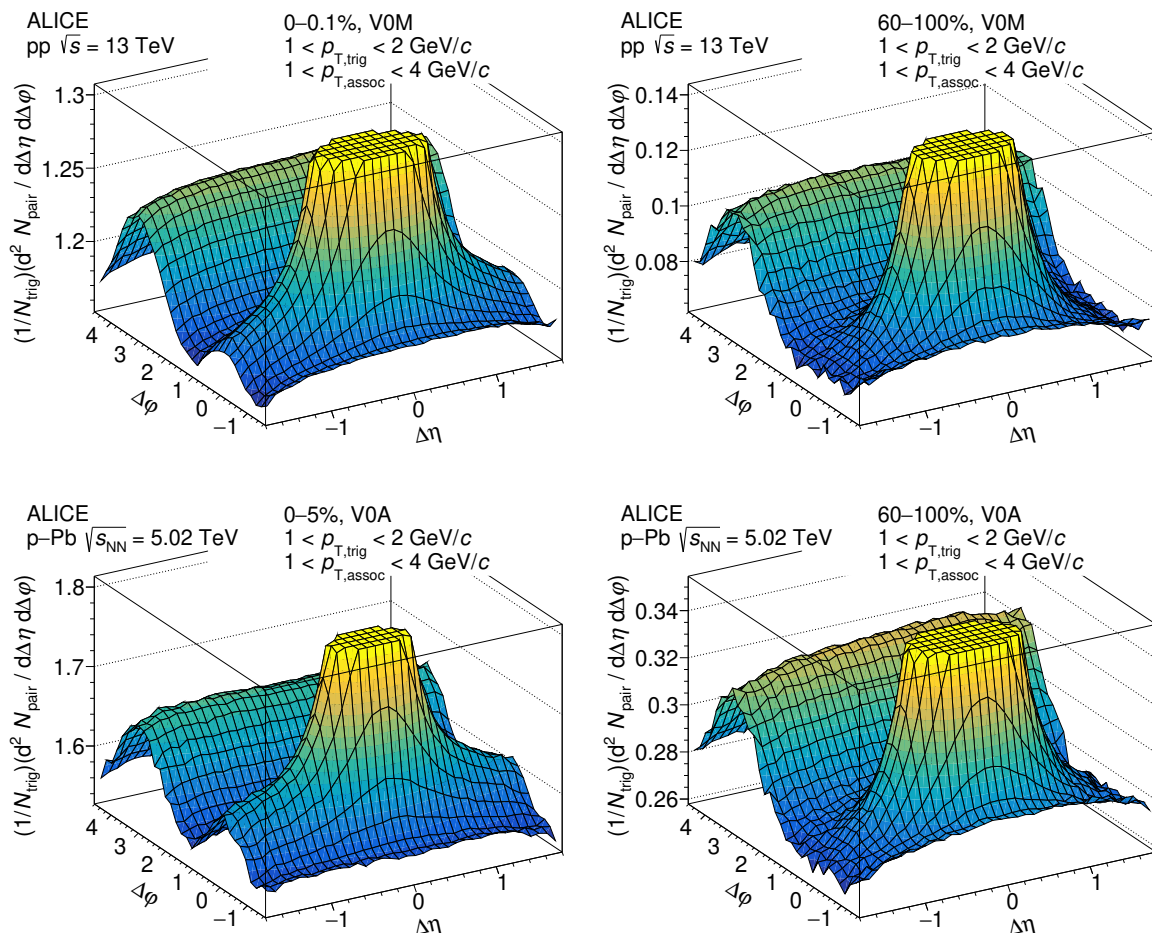


Figure 1. Two-dimensional correlation functions are presented for high-multiplicity (0–0.1% or 0–5%, on the left) and low-multiplicity (60–100%, on the right) events in $\sqrt{s} = 13$ TeV pp collisions in the top panels. The corresponding distributions for $\sqrt{s_{NN}} = 5.02$ TeV p–Pb collisions are shown in the bottom panels. All correlation functions are shown for $1 < p_{T,\text{trig}} < 2$ GeV/c and $1 < p_{T,\text{assoc}} < 4$ GeV/c, respectively.

correlation, is denoted as G . The scale factor F compensates for the increased yield of away-side-jet hadrons in the analyzed multiplicity class relative to the low-multiplicity template that corresponds to the 60–100% class [81, 82]. The fit determines the scale factor F , pedestal G , and $v_{n,n}$ and is performed in various high-multiplicity classes as well as in different $p_{T,\text{trig}}$ intervals. This method assumes that Y_{LM} does not contain a near-side-peak structure that would originate from jet fragmentation or a near-side ridge. Furthermore it is assumed that the shape of the away-side-peak structure remains the same when changing the multiplicity class. The first assumption is ensured using the selected low-multiplicity template which does not have a strong near-side-peak structure compared to the studied higher-multiplicity classes. The second assumption, which involves the modification of jet shapes, was tested by projecting the near-side jet peaks onto $\Delta\eta$. This modification of the jet shape is considered as one of the sources of systematic uncertainty and will be discussed in section 4.

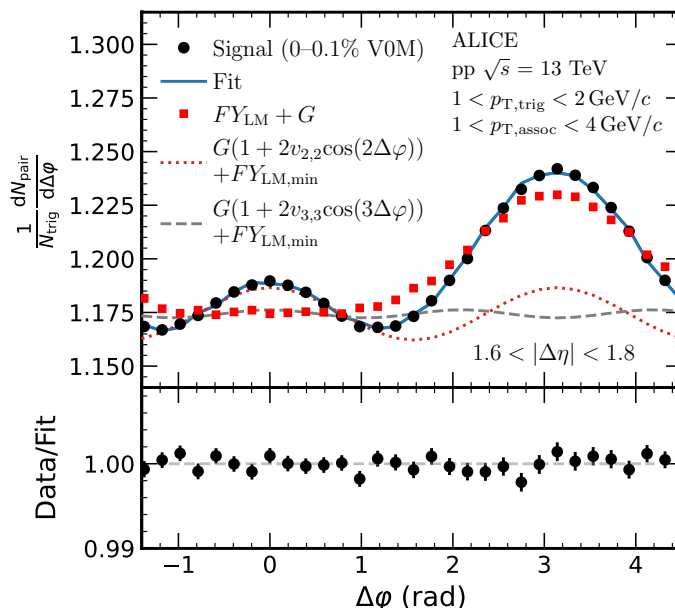


Figure 2. Per-trigger yield in $1.6 < |\Delta\eta| < 1.8$ extracted from 0–0.1% and 60–100% multiplicity percentile events in $\sqrt{s} = 13$ TeV pp collisions. The data are fitted with the template fit method described by eq. 3.3. The black markers show the signal for the 0–0.1% multiplicity percentile. The red squares correspond to the low-multiplicity signal. The red and gray curves correspond to the extracted $v_{2,2}$ and $v_{3,3}$ signals, respectively. To improve visibility, the baselines of flow signals are shifted by $FY_{LM,min}$, which represents the minimum yield of $FY_{LM}(\Delta\phi)$. The signal-to-fit ratio is shown in the bottom panel. The χ^2 divided by the number of degrees of freedom is 0.894.

Figure 2 shows the template fit results for the 0–0.1% multiplicity interval in pp collisions at $\sqrt{s} = 13$ TeV. Values of the extracted scale factor F in different multiplicity intervals and systems are summarized in table 1. In pp collisions, the value of F is observed to increase slightly as the event multiplicity increases. The F value, which is measured for the highest-multiplicity bin, is approximately 25% larger than the value found for the 20–60% bin. A similar dependence on multiplicity is observed for p–Pb collisions, although the dependence on the multiplicity interval is weaker. In the first three columns of table 1, representing collisions with higher multiplicities, there is an increase in the F value, while as shown by the subsequent columns, there is a decrease for lower multiplicity collisions. When comparing the F values from pp and p–Pb collisions, which have similar centrality, the value of F in p–Pb collisions is found to be smaller and closer to unity. This suggests that the jet fragmentation yield on the away-side increases with multiplicity, and that this feature is more pronounced in pp collisions. The difference between the two systems is likely to be explained by the true-geometry-driven centrality in p–Pb collisions, as opposed to the jet-dominated bias in pp collisions. The previous analyses published by ALICE in refs. [17, 83] assumed that the jet contribution remains constant as a function of multiplicity (i.e. F was assumed to be 1). However, this assumption may lead to an underestimation of non-flow contamination in the measurements of anisotropic flow.

V0M (pp)	0–0.1%	1–5%	5–20%	20–60%		
F	1.504±0.017	1.414±0.030	1.360±0.019	1.208±0.015		
V0A (p–Pb)	0–5%	5–10%	10–20%	0–20%	20–40%	40–60%
F	1.135±0.026	1.140±0.026	1.152±0.021	1.145±0.017	1.092±0.015	1.083±0.015

Table 1. The scale factor F for various multiplicity intervals in pp collisions (top) and p–Pb collisions (bottom), with $1 < p_{T,\text{trig}} < 2 \text{ GeV}/c$ and $1 < p_{T,\text{assoc}} < 4 \text{ GeV}/c$. The table reports statistical uncertainties only. Average systematic uncertainty of F is about 3.8% for both collision systems and multiplicity intervals.

In the following, the near and away-side jet fragmentation yields are calculated to verify the template fit method by comparing the jet fragmentation yields to the PYTHIA model. The away-side jet fragmentation yields in the PYTHIA model are obtained using the standard $\Delta\varphi$ analysis [106], while in the data, the away-side jet fragmentation yields are extracted using the template fit method because of the flow modulations in the data. The comparison between the data and the PYTHIA model provides a validation of the template fit method.

Equivalently to eq. (3.2), measured data are used to obtain the near-side $\Delta\eta$ correlations with

$$Y(\Delta\eta) = \frac{1}{N_{\text{trig}}} \frac{dN_{\text{pair}}}{d\Delta\eta} = \int_{|\Delta\varphi| < 1.3} \left[\frac{1}{N_{\text{trig}}} \frac{d^2 N_{\text{pair}}}{d\Delta\eta d\Delta\varphi} \right] \frac{1}{\delta_{\Delta\varphi}} d\Delta\varphi - D_{\text{ZYAM}}, \quad (3.4)$$

where $\delta_{\Delta\varphi} = 2.6$ and D_{ZYAM} defines the baseline of the ZYAM background subtraction [107]. The baseline is obtained by finding the minimum of the distribution defined by the integral in eq. (3.4). As flow has a weak η dependence [7, 108, 109], the jet-fragmentation yield can be calculated after the ZYAM background subtraction [107]. The near-side jet-like yields were extracted by integrating the $Y(\Delta\eta)$

$$Y_{\text{frag}}^{\text{near}} = \int_{|\Delta\eta| < 1.3} \left(\frac{1}{N_{\text{trig}}} \frac{dN_{\text{pair}}}{d\Delta\eta} \right) d\Delta\eta. \quad (3.5)$$

The away-side jet-like yield in data is calculated by integrating the low-multiplicity template over $\pi/2 < \Delta\varphi < 3/2\pi$ and scaling it by the parameter F from eq. (3.3), $Y_{\text{frag}}^{\text{away, HM}} = Y_{\text{frag}}^{\text{away, LM}} \times F$. The $Y_{\text{frag}}^{\text{away, LM}}$ is directly obtained by integrating the away-side low-multiplicity $\Delta\varphi$ correlation function in the low-multiplicity sample over $\pi/2 < \Delta\varphi < 3\pi/2$. As PYTHIA does not include any flow contributions in its model, Y^{away} can be directly measured from the $\Delta\varphi$ correlation functions.

Figure 3 presents the $Y_{\text{frag}}^{\text{near}}$ and $Y_{\text{frag}}^{\text{away}}$, for both ALICE data and PYTHIA 8 Tune 4C [110], as a function of the V0M multiplicity intervals in pp collisions at $\sqrt{s} = 13 \text{ TeV}$. The transverse momentum range for trigger particles is $1 < p_{T,\text{trig}} < 2 \text{ GeV}/c$ and for associated particles $1 < p_{T,\text{assoc}} < 4 \text{ GeV}/c$. The near- to away-side ratio for ALICE and PYTHIA data is shown in the bottom panel. While PYTHIA overestimates both near-side and away-side yields measured by ALICE, the corresponding ratio is consistent with the ALICE data in the all considered V0M multiplicity intervals. The value of this ratio can be explained by the pair acceptance effect caused by the limited ALICE η acceptance [106]. The observed agreement

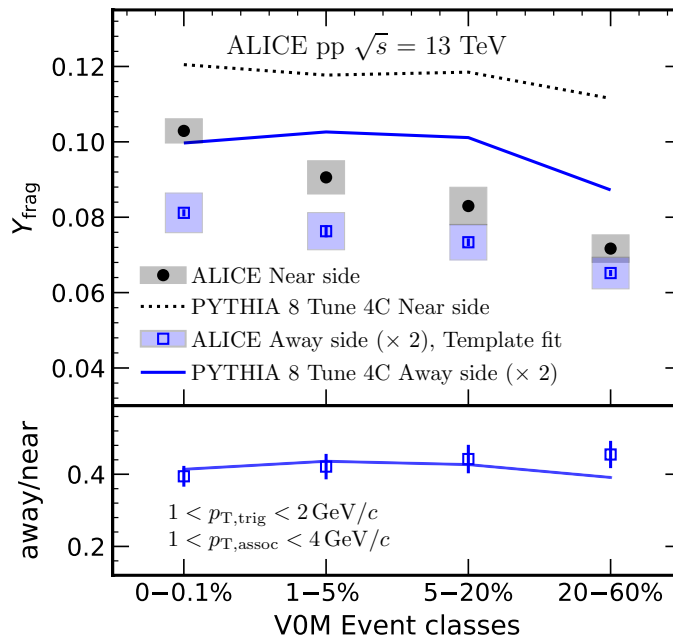


Figure 3. The Y_{frag} for the near- and away-side as a function of multiplicity percentiles with both ALICE and PYTHIA data. Systematic uncertainties are represented by the boxes. The bottom panel presents ratios of the yields. Here the reported uncertainty is obtained by adding statistical error and systematic uncertainty in quadrature. For PYTHIA, the statistical uncertainty is smaller than the thickness of the lines.

implies that the enhanced jet fragmentation yields in the away-side in high-multiplicity events with respect to low-multiplicity events [81, 82] are taken into account by the low-multiplicity template method. In summary, the difference between the near-side and away-side jet fragmentation yields in PYTHIA is solely caused by the jet acceptance effects which affect the two-particle correlation functions. The corresponding ratio in data, where the away-side jet fragmentation yields are measured with the low-multiplicity template, agrees well with PYTHIA as well as with the expectation in ref. [106].

The flow coefficients, v_n , of the trigger particles, can be extracted from the template fit with the use of the observed factorization of $v_{n,n}$ coefficients to single harmonics [10, 19] by using

$$v_n(p_{T,\text{trig}}) = v_{n,n}(p_{T,\text{trig}}, p_{T,\text{assoc}}) / \sqrt{v_{n,n}(p_{T,\text{assoc}}, p_{T,\text{assoc}})}, \quad (3.6)$$

where $v_{n,n}(p_{T,\text{assoc}}, p_{T,\text{assoc}})$ denote $v_{n,n}$ coefficients extracted using trigger and associated particles with p_T in the range 1–4 GeV/c. In the following sections, unless explicitly stated otherwise, v_n will refer to $v_n(p_{T,\text{trig}})$. Different event scale selections were investigated by selecting events that include a hard jet or a high- p_T leading particle at midrapidity (i.e., the particle with the highest reconstructed p_T inside the acceptance region in an event). This event scale was set by requiring a minimum p_T of the leading track ($p_{T,\text{LP}}$) or the reconstructed jet ($p_{T,\text{jet}}^{\text{ch}}$) at midrapidity [73]. The leading particle track was required to be within $|\eta| < 0.9$ and $0 < \varphi < 2\pi$, and the jets were reconstructed with the anti- k_T

Sources	Systematic uncertainty (%)						
	Y^{near}	$Y^{\text{away,LM}}$	F	v_2		v_3	
	pp	pp	pp	pp	p-Pb	pp	p-Pb
Primary vertex	$\pm 0.2\text{--}0.5$	± 0.1	$\pm 1.0\text{--}2.5$	$\pm 0.2\text{--}1.8$	± 0.8	± 1.4	± 3.9
Pileup rejection	$\pm 0.1\text{--}0.5$	± 0.2	$\pm 0.4\text{--}1.5$	negl.	± 0.6	negl.	± 1.4
Tracking	$\pm 1.0\text{--}3.0$	± 2.0	$\pm 0.6\text{--}2.4$	$\pm 0.2\text{--}3.0$	negl.	$\pm 5.0\text{--}6.9$	negl.
Event mixing	$\pm 0.2\text{--}0.7$	$\pm 0.2\text{--}0.5$	$\pm 0.0\text{--}3.3$	$\pm 0.3\text{--}4.6$	± 0.8	$\pm 2.8\text{--}3.1$	± 0.8
Low-mult. definition	N.A.	$\pm 0.5\text{--}3.5$	$\pm 0.7\text{--}6.0$	negl.	± 1.9	negl.	± 9.2
ITS-TPC matching	$\pm 2.0\text{--}3.0$	$\pm 2.0\text{--}3.0$	N.A.	N.A.	N.A.	N.A.	N.A.
Efficiency correction	$\pm 1.0\text{--}4.4$	$\pm 1.0\text{--}4.4$	N.A.	N.A.	N.A.	N.A.	N.A.
$\Delta\eta$ gap range	N.A.	N.A.	$\pm 0.1\text{--}3.2$	$\pm 1.0\text{--}5.0$	± 0.4	negl.	negl.
Jet shape modification	N.A.	N.A.	N.A.	± 1.0	± 1.0	± 3.0	± 8.0
Total (in quadrature)	$\pm 2.5\text{--}6.1$	$\pm 5.0\text{--}5.5$	$\pm 1.8\text{--}7.1$	$\pm 1.3\text{--}5.8$	± 2.5	$\pm 6.8\text{--}8.0$	± 12.8

Table 2. The relative systematic uncertainties of Y^{near} , $Y^{\text{away,LM}}$, F , v_2 , and v_3 . The quantities Y^{near} , $Y^{\text{away,LM}}$, F are only measured in pp collisions, whereas v_2 and v_3 are measured in both pp and p-Pb collisions. The quoted ranges correspond to minimum and maximum uncertainties. Those uncertainties that are considered to be negligible are marked “negl.”. The systematic variations which are not relevant for the measurement are denoted as “N.A.”.

algorithm [111, 112], with $R = 0.4$ using charged particles only. Jet constituents were combined using the boost-invariant p_T recombination scheme. The jets are selected in the full azimuth ($0 < \varphi < 2\pi$) and their pseudorapidity is constrained to $|\eta_{\text{jet}}| < 0.4$. The p_T of jets $p_{T,\text{jet}}^{\text{ch}}$ is corrected for the underlying event density that is measured using the k_T algorithm with $R = 0.2$ following the procedure described in ref. [113].

4 Systematic uncertainties

Systematic uncertainties are estimated by varying the analysis selection criteria and corrections. Independent systematic checks are performed and the differences between results obtained from each variation and the default selection are considered as the systematic uncertainty for each source [114]. The total systematic uncertainty is obtained by adding the contributions from different sources in quadrature. A summary of all systematic uncertainties is provided in table 2.

The uncertainty attributed to the chosen primary vertex range is estimated by varying the selected range from $|z_{\text{vtx}}| < 8$ cm to $|z_{\text{vtx}}| < 6$ cm. The variation of the range allows testing detector acceptance effects on the measurement.

Another source of systematic uncertainty is related to pileup rejection. The rejection of pileup events is adjusted by modifying the number of track contributors required for the reconstruction of pileup event vertices, changing it from the default value of 3 to 5.

The systematic uncertainty due to the choice of track-selection criteria is estimated by employing alternative track-selection criteria, which single out so-called “global track”, which are described in ref. [115]. A global track is required to have two hits in the ITS (at least one

in the SPD) and at least 70 clusters in the TPC. Due to inefficiencies in certain parts of the SPD, the azimuthal distribution of global tracks is not uniform. This can be corrected by using corresponding mixed events and accounting for the corresponding tracking efficiency.

An additional systematic uncertainty from the event-mixing is estimated by varying the interval of the primary vertex range, where events are mixed. The default size of the primary vertex bins of mixed events is decreased from 2 cm to 1 cm.

The systematic uncertainty associated with the low-multiplicity definition is estimated by changing the range of the low-V0M-multiplicity interval. There is no universal definition for the low-multiplicity interval. The default range for the low-multiplicity interval in the present article is 60–100%, and it is changed to 70–100% to estimate the related systematic uncertainty. Note that for the measurement of Y^{near} , the low-multiplicity-interval definition is irrelevant.

The systematic uncertainty resulting from matching a track reconstructed by the TPC and the corresponding signal in the ITS is estimated by evaluating the fraction of mismatches in real data using simulations. Primary tracks have a higher matching efficiency than secondary tracks produced far from the interaction point or in interactions with detector material. To address the effect of different fractions of primary and secondary tracks in data and simulations on the matching efficiency, particle abundances in the simulation are reweighted to reflect real data. This resulted in modified matching efficiency.

The systematic uncertainty arising from the efficiency correction is estimated by performing a closure test, where two correlation functions are compared. The first correlation function is constructed using true information from the Monte Carlo samples described in section 2. This provides a baseline for the expected correlation function. The second correlation function is constructed using reconstructed tracks corrected for tracking efficiency. By comparing the two correlation functions, it is possible to estimate the magnitude of the uncertainty introduced by the correction.

Due to the limited η acceptance of the TPC, non-flow contributions, mainly originating from fragmentation of jets, affect the flow measurement. As the shape of short-range correlations, mostly attributed to jets, is getting broader with decreasing p_T , the systematic uncertainty from η acceptance significantly depends on p_T . To estimate the related uncertainty, the long range $\Delta\varphi$ correlations are measured for an extended $\Delta\eta$ gap, the default size of $\Delta\eta$ gap 1.6 is increased to 1.7.

Finally, it is worth considering the possible impact of the multiplicity dependence of the jet-shape modifications discussed in section 3. This is studied by examining the shape modification of the jet-peak distribution in the near-side region as a function of $\Delta\eta$ and multiplicity. The observed change in the width is used to estimate the possible effect on the long-range, per-trigger-yield distribution as a function of $\Delta\varphi$. The effect on v_2 is found to be less than 1% in pp and p–Pb collisions for the kinematic ranges analyzed. The effect on v_3 is found to be less than 8% in p–Pb collisions. These values are included in the total systematic uncertainty. However, it is important to note that other analyses with different kinematic ranges should also perform a similar check to assess the systematic uncertainty associated with this effect. It is possible that this effect may not always be as small as in our analysis.

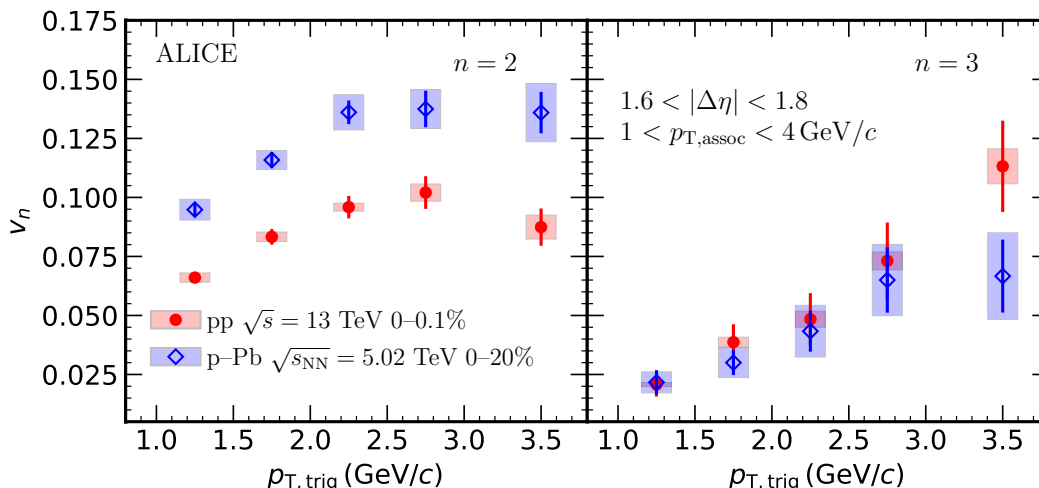


Figure 4. The magnitude of v_2 (left) and v_3 (right) as a function of p_T for the 0–0.1% multiplicity interval in pp collisions at $\sqrt{s} = 13$ TeV and 0–20% in p–Pb collisions at $\sqrt{s_{NN}} = 5.02$ TeV. The boxes around the data points represent the estimated systematic uncertainty and the error bars correspond to statistical errors.

5 Results

5.1 Transverse-momentum and multiplicity dependence of anisotropic flow

Figure 4 illustrates the extracted values of v_2 and v_3 as a function of $p_{T, \text{trig}}$ as obtained from eq. (3.3). The results correspond to the high-multiplicity pp collisions at $\sqrt{s} = 13$ TeV and p–Pb collisions at $\sqrt{s_{NN}} = 5.02$ TeV. Both sets of results demonstrate an increasing trend in the magnitudes of v_n with rising $p_{T, \text{trig}}$. The v_2 data points reach a maximum between 2.5 and 3.0 GeV/c, similarly to what has been observed in Pb–Pb collisions [5, 116]. The magnitudes of v_2 in p–Pb collisions are higher than those in pp collisions, which might be related to the larger p–Pb system size together with a likely longer lifetime of the hypothetically created medium. However, the magnitudes of v_3 are similar in both systems, indicating that v_3 is less sensitive to the size of the systems. These results are comparable to those obtained by ATLAS in different multiplicity classes, where the same method was used to extract the flow coefficients [19]. Even though the $\Delta\eta$ and $p_{T, \text{assoc}}$ ranges used by ATLAS are wider, $2.0 < |\Delta\eta| < 5.0$ and $0.5 < p_{T, \text{assoc}} < 5$ GeV/c, respectively, the results are consistent within uncertainties.

Figure 5 presents the magnitudes of v_2 and v_3 , as a function of charged-particle multiplicity at midrapidity for both pp collisions at $\sqrt{s} = 13$ TeV and p–Pb collisions at $\sqrt{s_{NN}} = 5.02$ TeV. As in figure 4, the $\Delta\eta$ gap is $1.6 < |\Delta\eta| < 1.8$ and v_2 is measured in $1 < p_T < 4$ GeV/c for both collision systems. Additionally, the corresponding results for pp collisions at $\sqrt{s} = 13$ TeV with $1 < p_T < 2$ GeV/c are presented. First, it is observed that the magnitude of v_n increases with increasing multiplicity for both collision systems and p_T -ranges. Second, v_2 in p–Pb is higher than in pp collisions in the measured multiplicity range. These two observations are compatible with previous results from refs. [10, 11, 19]. There is no significant difference between the two collision systems when considering the v_3 dependence on multiplicity as shown on the right-

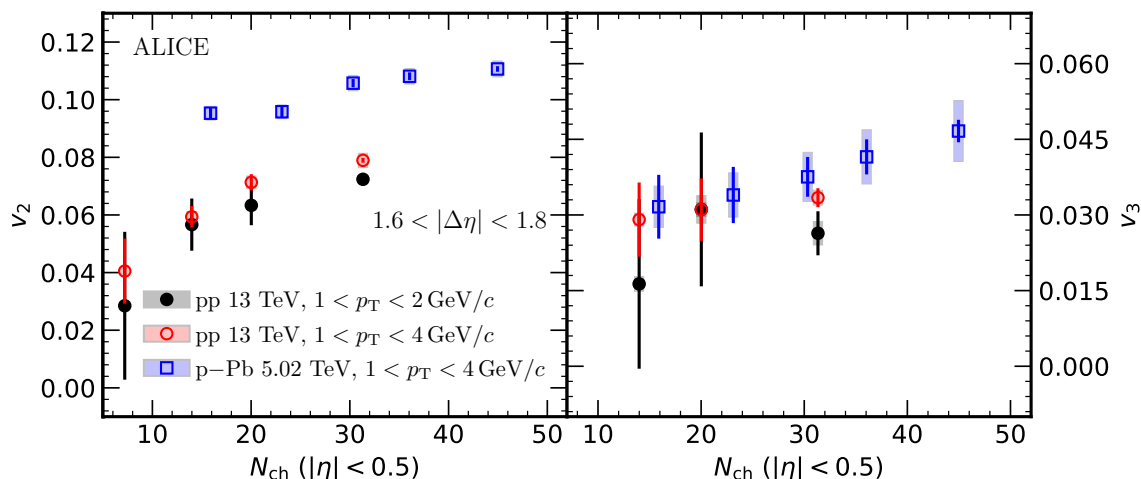


Figure 5. The magnitudes of v_2 (left panel) and v_3 (right panel) for two different collision systems, pp and p–Pb as a function of charged-particle multiplicity at midrapidity. For pp collisions, two different p_T intervals are shown, $1.0 < p_T < 2.0$ GeV/ c and $1.0 < p_T < 4.0$ GeV/ c . The boxes around the data points represent the estimated systematic uncertainties and the error bars corresponds to statistical errors.

hand-side panel of figure 5. The v_3 measurements exhibit a comparable subtle dependence on multiplicity, with higher values observed in collisions with greater particle multiplicities. For the two different p_T intervals presented for the pp collisions, the v_2 in $1.0 < p_T < 4.0$ GeV/ c shows a hint of larger magnitude than the v_2 in $1.0 < p_T < 2.0$ GeV/ c . The difference in magnitude is significant only in the highest multiplicity point. This agrees with what is observed in figure 4, where the v_2 magnitude has its largest value in $2.5 < p_T < 3.0$ GeV/ c . It is found that for the considered p_T selections, the observed multiplicity dependencies differ only marginally. It is worth noting that the results presented from pp and p–Pb collisions were obtained from two different beam energies. In ref. [19], it was found that the magnitudes of v_2 and v_3 in pp collisions between 13 and 5.02 TeV show no significant variation with center-of-mass energy.

5.2 Event-scale dependence of the flow coefficients

Figure 6 presents the extracted magnitude of v_2 and v_3 as a function of the minimum p_T of the leading particle ($p_{T,\min}^{\text{LP}}$) and that of the jet ($p_{T,\min}^{\text{jet}}$) as introduced in section 1. The results are presented for the 0–0.1% multiplicity class of pp collisions at $\sqrt{s} = 13$ TeV and for the two different p_T -ranges. To reduce the impact of the detector edge effects on the jet measurements, the jet axes are required to have a pseudorapidity $|\eta_{\text{jet}}| < 0.4$, following a similar selection as in refs. [117–119]. The v_2 and v_3 values for both p_T ranges do not show any dependence on event-scale selection within the uncertainties. This finding is consistent with the results of the ridge yields [73] and v_2 measurements with a tagged Z boson from the ATLAS collaboration [120]. These results suggest that the presence of a hard-scattering process does not significantly change the long-range correlation involving soft particles. However, the presented measurements are only limited to the low p_T^{jet} . Future measurements

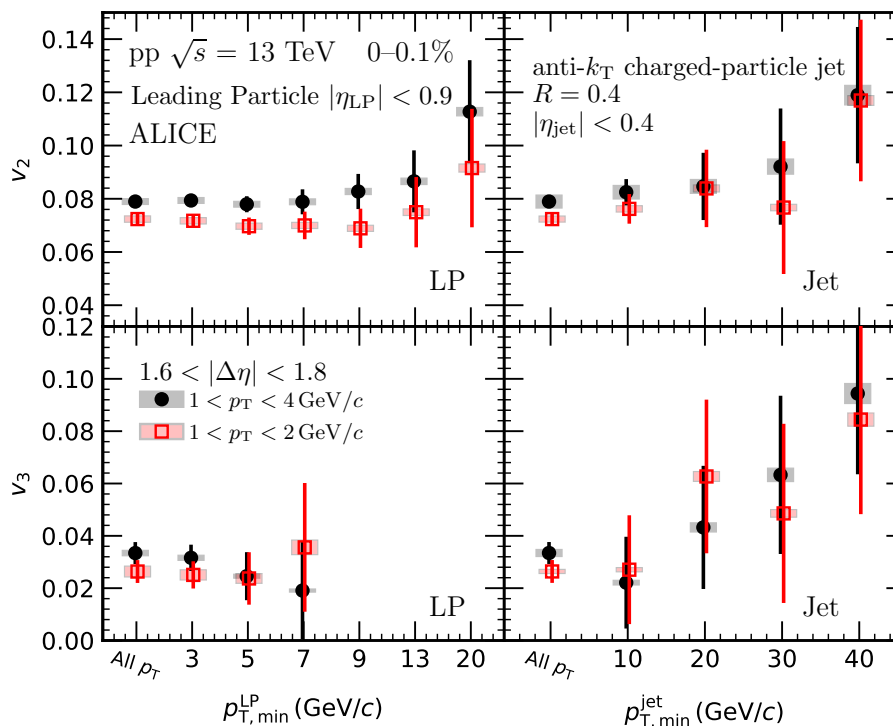


Figure 6. The magnitudes of v_2 (top) and v_3 (bottom) as a function of $p_{T,\min}^{\text{LP}}$ (left) and $p_{T,\min}^{\text{jet}}$ (right) for the high-multiplicity in pp collisions at $\sqrt{s} = 13$ TeV. The measured p_T intervals are $1 < p_T < 2$ GeV/c (in red) and $1 < p_T < 4$ GeV/c (in black). The statistical errors and systematic uncertainties are shown as vertical bars and boxes, respectively.

with multi-jet events at midrapidity with higher Q^2 reach can shed more light on the expected impact parameter dependence [84–86].

5.3 Comparisons with models

In this section, the results are compared to various model calculations. The results from p–Pb collisions are compared with hydrodynamic calculations using the parameterization from an improved global Bayesian analysis. The analysis involves new sophisticated collective flow observables as obtained from two different beam energies in Pb–Pb collisions [55], constraining the initial conditions and transport properties of the QGP. This hydrodynamic model, T_{RENT}o+iEBE-VISHNU, consists of the T_{RENT}o model [121] to simulate the initial condition, which is connected with a free streaming to a 2+1 dimensional causal hydrodynamic model VISH2+1 [122]. The evolution is continued after hadronization with a hadronic cascade model (UrQMD) [41, 42]. A model calculation is performed using the best-fit parameterization for transport coefficients selected based on maximum a posteriori (MAP) for Pb–Pb collisions at $\sqrt{s_{\text{NN}}} = 5.02$ TeV. Two different MAP values are used for the calculations. They are based on ref. [55] and ref. [52] and in figure 7 they are labeled MAP(2021) and MAP(QM2018), respectively. The parameterization for the initial conditions, which include a sub-nucleon structure with six constituent partons per nucleon ($m = 6$), is taken from a model calibration with additional p–Pb data [56]. All kinematic selections, such as the transverse momentum

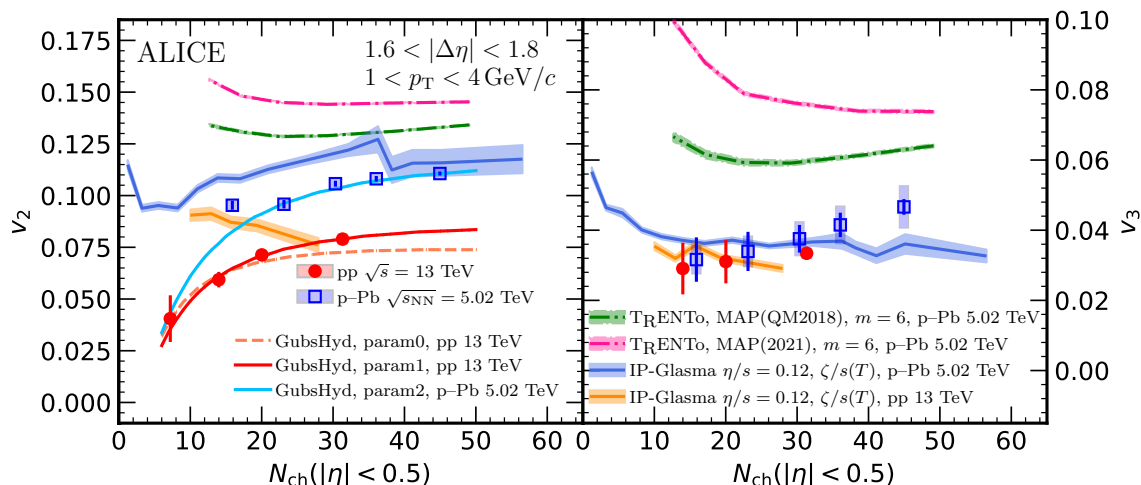


Figure 7. The measured and calculated evolution of v_2 (left) and v_3 (right) in pp and p–Pb collisions as a function of charged-particle multiplicity at midrapidity. The blue and red markers represent the measured p–Pb and pp data, respectively. The calculations provided by hydrodynamical models [52, 55, 64, 74] are presented with colored lines. The corresponding bands mark their statistical uncertainty. For GubsHyd calculations, the statistical uncertainty is smaller than the line thickness.

and pseudorapidity intervals, are matched to the data reported in this article. The flow coefficients in the hydrodynamic calculation are extracted with the two-particle cumulant method, as the TRenTo+iEBE-VISHNU does not contain any non-flow.

Figure 7 shows that TRenTo+iEBE-VISHNU overestimates both v_2 and v_3 . In the studied range, the v_2 and v_3 data increase with multiplicity. However, TRenTo+iEBE-VISHNU predicts the opposite trend, which is similar to what is found in large collision systems [47]. The large discrepancies in the prediction might be alleviated by inclusion of the newly measured p–Pb constraints in a future Bayesian parameter estimation as well as by improvements of the initial condition model for small-system collisions.

The results are also compared with IP-Glasma+MUSIC+UrQMD hydrodynamic calculations [74]. This model uses IP-Glasma initial conditions [30] including sub-nucleonic fluctuations with three hot spots per nucleon. The hydrodynamic evolution is performed by MUSIC [36] and coupled with UrQMD [41, 42], which performs hadronic cascade. The model calculations are performed assuming constant $\eta/s = 0.12$ and a temperature dependent $\zeta/s(T)$ [123]. This model describes well the multiplicity dependence of v_2 in p–Pb collisions and the magnitude at the highest multiplicity within the statistical uncertainties of the model but overestimates the data for the lower multiplicity classes. As for pp collisions, the calculations clearly miss both the observed magnitude except for $N_{ch} > 25$ as well as the trend of the multiplicity dependence. The model shows that v_2 decreases with increasing multiplicity, while the experimental result shows the opposite. For v_3 , the model accurately describes the magnitudes and multiplicity dependence across the measured multiplicity ranges. The magnitudes of v_3 are slightly smaller in pp collisions than in p–Pb collisions according to the calculations, which agrees with the data within the uncertainties. The level of agreement between data and the IP Glasma model calculations is found to be similar to the results reported in ref. [13].

Finally, the results are compared with the GubsHyd model, a semi-analytical model based on the analytical Gubser solution to hydrodynamic equations [62, 63], known as Gubser flow. In Gubser flow, the initial state of conformal matter is linearly perturbed by an initial elliptic shape. The model is employed to shed light on the possible sources of the observed discrepancy between more realistic models mentioned above and the measurements in pp collisions [64]. Instead of modeling the initial entropy density in this model, as it is typically done in T_RENTo or IP-Glasma, the initial state fluctuation is modeled directly. It assumes that proton ellipticity ϵ_2 and RMS radius r_{rms} fluctuate independently. These fluctuations are described by Gaussian probability distributions, which have widths σ_ϵ and σ_r , respectively. The multiplicity dependence of the $v_2\{2\}$ of two-particle correlation functions depends on σ_r and $\chi\sigma_\epsilon$, where the coefficient χ encapsulates a correction for idealizations used in GubsHyd, including the absence of dissipation effects. The values of σ_r and $\chi\sigma_\epsilon$ were obtained by comparing the model with data. Since no non-flow effect is considered in the calculation, $v_2\{2\}$ is comparable with the flow measurements in the present study. The calculations for two sets of parameters are compared to data in figure 7. The “param0” parameterization is based on the prediction proposed in ref. [64] that $\chi\sigma_\epsilon = 0.097$ and $\sigma_r = 0.4$ fm. The other parameterizations “param1” and “param2” employ different $\chi\sigma_\epsilon$ and σ_r values. The model captures the multiplicity dependence of v_2 well.

In summary, the measured v_2 value decrease with decreasing multiplicity in both pp and p–Pb collisions. This trend is also predicted by GubsHyd model calculations (refs. [64] and [124]). Interestingly, the opposite trend is observed for the IP-GLASMA+MUSIC+UrQMD hydrodynamic calculations of v_2 , where the value decreases with increasing charged-particle multiplicity [74]. Approaching a lower bound for the size of a hydrodynamized system as predicted in ref. [64], the decreasing trend of v_2 , obtained by lowering the charged-particle multiplicity, changes and turns out to raise again after the observed minimum. However, this change in multiplicity dependence of v_2 at low multiplicities is still challenging to test with the current experimental uncertainties. For v_3 , the IP-Glasma+MUSIC+UrQMD hydrodynamic calculations [74] are the only ones that accurately describe its magnitude and multiplicity dependence across the measured ranges. The calculations predict that the magnitudes of v_3 are slightly smaller in pp collisions than in p–Pb collisions, within the measured multiplicity ranges. The discrepancies between the predictions and the data can be further studied by including these measurements in a future Bayesian parameter estimation, as well as by improving the initial-condition model for the small-system collisions.

6 Conclusions

Long-range angular correlations for pairs of charged particles are studied in pp collisions at $\sqrt{s} = 13$ TeV and p–Pb collisions at $\sqrt{s_{\text{NN}}} = 5.02$ TeV. Flow coefficients are extracted from long-range correlations ($1.6 < |\Delta\eta| < 1.8$) for a broad range of charged-particle-multiplicity classes using the template method, which allows one to subtract the enhanced away-side jet fragmentation yields in high-multiplicity events with respect to low-multiplicity events. The method that was used to measure the flow coefficients within the considered kinematic ranges has been verified to be stable. The systematic uncertainties on v_2 and v_3 measurements, which reflect the possible differences in the away-side jet peak shapes in high- and low-multiplicity

events, were found to be 1% and 3–8%, respectively. However, it is important that these systematic uncertainties are reevaluated, when analyzing different kinematic ranges, as the effect may not always be negligible. The measured p_T dependence of v_2 and v_3 is consistent with the measurements by ATLAS and shows that both v_2 and v_3 increase with p_T and reach their maximum at $2.5 < p_T < 3.0$ GeV/ c . The measurement of v_2 as a function of charged-particle multiplicity in $|\eta| < 0.5$ shows a weak multiplicity dependence both for pp and p–Pb collisions and tends to decrease toward lower multiplicities. The pp data suggests that the v_2 signal may disappear when the measurement is pursued further below $N_{\text{ch}} = 10$.

The comparisons to viscous hydrodynamic models show that the magnitudes of v_2 and their multiplicity dependence are not described by state-of-the-art hydrodynamic calculations, which simulated initial conditions with two initial state models, especially for low-multiplicity p–Pb and pp collisions. As initial state effects tend to be more important at low multiplicity [56, 59], these results may help to constrain the modeling of the initial state. Furthermore, the events including hard probes such as jets or high- p_T leading particles do not show any changes both in v_2 and v_3 within the uncertainties, which implies that the long-range correlation of soft particles is not significantly modified by the presence of the hard-scattering process. Even though it would be interesting to compare these results to the EPOS LHC [125] and PYTHIA8 String Shoving models [71, 72] as done in ref. [17] for the ridge yields, it is not possible to reliably extract the flow coefficients because these models exhibit a near-side ridge structure in low-multiplicity events, thus making the use of the low-multiplicity template ill defined [126].

Acknowledgments

The ALICE Collaboration would like to thank all its engineers and technicians for their invaluable contributions to the construction of the experiment and the CERN accelerator teams for the outstanding performance of the LHC complex. The ALICE Collaboration gratefully acknowledges the resources and support provided by all Grid centres and the Worldwide LHC Computing Grid (WLCG) collaboration. The ALICE Collaboration acknowledges the following funding agencies for their support in building and running the ALICE detector: A. I. Alikhanyan National Science Laboratory (Yerevan Physics Institute) Foundation (ANSL), State Committee of Science and World Federation of Scientists (WFS), Armenia; Austrian Academy of Sciences, Austrian Science Fund (FWF): [M 2467-N36] and Nationalstiftung für Forschung, Technologie und Entwicklung, Austria; Ministry of Communications and High Technologies, National Nuclear Research Center, Azerbaijan; Conselho Nacional de Desenvolvimento Científico e Tecnológico (CNPq), Financiadora de Estudos e Projetos (Finep), Fundação de Amparo à Pesquisa do Estado de São Paulo (FAPESP) and Universidade Federal do Rio Grande do Sul (UFRGS), Brazil; Bulgarian Ministry of Education and Science, within the National Roadmap for Research Infrastructures 2020-2027 (object CERN), Bulgaria; Ministry of Education of China (MOEC), Ministry of Science & Technology of China (MSTC) and National Natural Science Foundation of China (NSFC), China; Ministry of Science and Education and Croatian Science Foundation, Croatia; Centro de Aplicaciones Tecnológicas y Desarrollo Nuclear (CEADEN), Cubaenergía, Cuba; Ministry of Education, Youth and Sports of the Czech Republic, Czech Republic; The Danish Council for Independent Research | Natural Sciences, the VILLUM FONDEN and Danish National Research Foundation (DNRF),

Denmark; Helsinki Institute of Physics (HIP), Finland; Commissariat à l’Energie Atomique (CEA) and Institut National de Physique Nucléaire et de Physique des Particules (IN2P3) and Centre National de la Recherche Scientifique (CNRS), France; Bundesministerium für Bildung und Forschung (BMBF) and GSI Helmholtzzentrum für Schwerionenforschung GmbH, Germany; General Secretariat for Research and Technology, Ministry of Education, Research and Religions, Greece; National Research, Development and Innovation Office, Hungary; Department of Atomic Energy Government of India (DAE), Department of Science and Technology, Government of India (DST), University Grants Commission, Government of India (UGC) and Council of Scientific and Industrial Research (CSIR), India; National Research and Innovation Agency - BRIN, Indonesia; Istituto Nazionale di Fisica Nucleare (INFN), Italy; Japanese Ministry of Education, Culture, Sports, Science and Technology (MEXT) and Japan Society for the Promotion of Science (JSPS) KAKENHI, Japan; Consejo Nacional de Ciencia (CONACYT) y Tecnología, through Fondo de Cooperación Internacional en Ciencia y Tecnología (FONCICYT) and Dirección General de Asuntos del Personal Académico (DGAPA), Mexico; Nederlandse Organisatie voor Wetenschappelijk Onderzoek (NWO), Netherlands; The Research Council of Norway, Norway; Commission on Science and Technology for Sustainable Development in the South (COMSATS), Pakistan; Pontificia Universidad Católica del Perú, Peru; Ministry of Education and Science, National Science Centre and WUT ID-UB, Poland; Korea Institute of Science and Technology Information and National Research Foundation of Korea (NRF), Republic of Korea; Ministry of Education and Scientific Research, Institute of Atomic Physics, Ministry of Research and Innovation and Institute of Atomic Physics and University Politehnica of Bucharest, Romania; Ministry of Education, Science, Research and Sport of the Slovak Republic, Slovakia; National Research Foundation of South Africa, South Africa; Swedish Research Council (VR) and Knut & Alice Wallenberg Foundation (KAW), Sweden; European Organization for Nuclear Research, Switzerland; Suranaree University of Technology (SUT), National Science and Technology Development Agency (NSTDA) and National Science, Research and Innovation Fund (NSRF via PMU-B B05F650021), Thailand; Turkish Energy, Nuclear and Mineral Research Agency (TENMAK), Turkey; National Academy of Sciences of Ukraine, Ukraine; Science and Technology Facilities Council (STFC), United Kingdom; National Science Foundation of the United States of America (NSF) and United States Department of Energy, Office of Nuclear Physics (DOE NP), United States of America. In addition, individual groups or members have received support from: European Research Council, Strong 2020 - Horizon 2020 (grant nos. 950692, 824093), European Union; Academy of Finland (Center of Excellence in Quark Matter) (grant nos. 346327, 346328), Finland.

Open Access. This article is distributed under the terms of the Creative Commons Attribution License ([CC-BY4.0](https://creativecommons.org/licenses/by/4.0/)), which permits any use, distribution and reproduction in any medium, provided the original author(s) and source are credited.

References

- [1] STAR collaboration, *Experimental and theoretical challenges in the search for the quark gluon plasma: The STAR Collaboration's critical assessment of the evidence from RHIC collisions*, *Nucl. Phys. A* **757** (2005) 102 [[nucl-ex/0501009](#)] [[INSPIRE](#)].
- [2] PHENIX collaboration, *Formation of dense partonic matter in relativistic nucleus-nucleus collisions at RHIC: Experimental evaluation by the PHENIX collaboration*, *Nucl. Phys. A* **757** (2005) 184 [[nucl-ex/0410003](#)] [[INSPIRE](#)].
- [3] BRAHMS collaboration, *Quark gluon plasma and color glass condensate at RHIC? The Perspective from the BRAHMS experiment*, *Nucl. Phys. A* **757** (2005) 1 [[nucl-ex/0410020](#)] [[INSPIRE](#)].
- [4] PHOBOS collaboration, *The PHOBOS perspective on discoveries at RHIC*, *Nucl. Phys. A* **757** (2005) 28 [[nucl-ex/0410022](#)] [[INSPIRE](#)].
- [5] ALICE collaboration, *Anisotropic flow of charged hadrons, pions and (anti-)protons measured at high transverse momentum in Pb-Pb collisions at $\sqrt{s_{NN}}=2.76$ TeV*, *Phys. Lett. B* **719** (2013) 18 [[arXiv:1205.5761](#)] [[INSPIRE](#)].
- [6] ALICE collaboration, *Elliptic flow of identified hadrons in Pb-Pb collisions at $\sqrt{s_{NN}} = 2.76$ TeV*, *JHEP* **06** (2015) 190 [[arXiv:1405.4632](#)] [[INSPIRE](#)].
- [7] ATLAS collaboration, *Measurement of the pseudorapidity and transverse momentum dependence of the elliptic flow of charged particles in lead-lead collisions at $\sqrt{s_{NN}} = 2.76$ TeV with the ATLAS detector*, *Phys. Lett. B* **707** (2012) 330 [[arXiv:1108.6018](#)] [[INSPIRE](#)].
- [8] ALICE collaboration, *The ALICE experiment — A journey through QCD*, [arXiv:2211.04384](#) [[INSPIRE](#)].
- [9] J.-Y. Ollitrault, *Anisotropy as a signature of transverse collective flow*, *Phys. Rev. D* **46** (1992) 229 [[INSPIRE](#)].
- [10] ATLAS collaboration, *Observation of Long-Range Elliptic Azimuthal Anisotropies in $\sqrt{s} = 13$ and 2.76 TeV pp Collisions with the ATLAS Detector*, *Phys. Rev. Lett.* **116** (2016) 172301 [[arXiv:1509.04776](#)] [[INSPIRE](#)].
- [11] CMS collaboration, *Measurement of long-range near-side two-particle angular correlations in pp collisions at $\sqrt{s} = 13$ TeV*, *Phys. Rev. Lett.* **116** (2016) 172302 [[arXiv:1510.03068](#)] [[INSPIRE](#)].
- [12] CMS collaboration, *Evidence for collectivity in pp collisions at the LHC*, *Phys. Lett. B* **765** (2017) 193 [[arXiv:1606.06198](#)] [[INSPIRE](#)].
- [13] ALICE collaboration, *Investigations of Anisotropic Flow Using Multiparticle Azimuthal Correlations in pp, p-Pb, Xe-Xe, and Pb-Pb Collisions at the LHC*, *Phys. Rev. Lett.* **123** (2019) 142301 [[arXiv:1903.01790](#)] [[INSPIRE](#)].
- [14] ATLAS collaboration, *Measurement of long-range multiparticle azimuthal correlations with the subevent cumulant method in pp and p + Pb collisions with the ATLAS detector at the CERN Large Hadron Collider*, *Phys. Rev. C* **97** (2018) 024904 [[arXiv:1708.03559](#)] [[INSPIRE](#)].
- [15] CMS collaboration, *Observation of Long-Range Near-Side Angular Correlations in Proton-Proton Collisions at the LHC*, *JHEP* **09** (2010) 091 [[arXiv:1009.4122](#)] [[INSPIRE](#)].
- [16] LHCb collaboration, *Measurements of long-range near-side angular correlations in $\sqrt{s_{NN}} = 5$ TeV proton-lead collisions in the forward region*, *Phys. Lett. B* **762** (2016) 473 [[arXiv:1512.00439](#)] [[INSPIRE](#)].

- [17] ALICE collaboration, *Long-range angular correlations on the near and away side in p-Pb collisions at $\sqrt{s_{NN}} = 5.02$ TeV*, *Phys. Lett. B* **719** (2013) 29 [[arXiv:1212.2001](#)] [[INSPIRE](#)].
- [18] ATLAS collaboration, *Measurement of long-range pseudorapidity correlations and azimuthal harmonics in $\sqrt{s_{NN}} = 5.02$ TeV proton-lead collisions with the ATLAS detector*, *Phys. Rev. C* **90** (2014) 044906 [[arXiv:1409.1792](#)] [[INSPIRE](#)].
- [19] ATLAS collaboration, *Measurements of long-range azimuthal anisotropies and associated Fourier coefficients for pp collisions at $\sqrt{s} = 5.02$ and 13 TeV and p+Pb collisions at $\sqrt{s_{NN}} = 5.02$ TeV with the ATLAS detector*, *Phys. Rev. C* **96** (2017) 024908 [[arXiv:1609.06213](#)] [[INSPIRE](#)].
- [20] CMS collaboration, *Pseudorapidity dependence of long-range two-particle correlations in pPb collisions at $\sqrt{s_{NN}} = 5.02$ TeV*, *Phys. Rev. C* **96** (2017) 014915 [[arXiv:1604.05347](#)] [[INSPIRE](#)].
- [21] PHENIX collaboration, *Creation of quark-gluon plasma droplets with three distinct geometries*, *Nature Phys.* **15** (2019) 214 [[arXiv:1805.02973](#)] [[INSPIRE](#)].
- [22] PHENIX collaboration, *Measurements of Multiparticle Correlations in d + Au Collisions at 200, 62.4, 39, and 19.6 GeV and p + Au Collisions at 200 GeV and Implications for Collective Behavior*, *Phys. Rev. Lett.* **120** (2018) 062302 [[arXiv:1707.06108](#)] [[INSPIRE](#)].
- [23] M. Gyulassy and M. Plumer, *Jet Quenching in Dense Matter*, *Phys. Lett. B* **243** (1990) 432 [[INSPIRE](#)].
- [24] X.-N. Wang and M. Gyulassy, *Gluon shadowing and jet quenching in A + A collisions at $\sqrt{s} = 200$ -GeV*, *Phys. Rev. Lett.* **68** (1992) 1480 [[INSPIRE](#)].
- [25] ALICE collaboration, *Centrality dependence of particle production in p-Pb collisions at $\sqrt{s_{NN}} = 5.02$ TeV*, *Phys. Rev. C* **91** (2015) 064905 [[arXiv:1412.6828](#)] [[INSPIRE](#)].
- [26] CMS collaboration, *Charged-particle nuclear modification factors in PbPb and pPb collisions at $\sqrt{s_{NN}} = 5.02$ TeV*, *JHEP* **04** (2017) 039 [[arXiv:1611.01664](#)] [[INSPIRE](#)].
- [27] ALICE collaboration, *Centrality dependence of charged jet production in p-Pb collisions at $\sqrt{s_{NN}} = 5.02$ TeV*, *Eur. Phys. J. C* **76** (2016) 271 [[arXiv:1603.03402](#)] [[INSPIRE](#)].
- [28] ALICE collaboration, *Multiplicity dependence of charged pion, kaon, and (anti)proton production at large transverse momentum in p-Pb collisions at $\sqrt{s_{NN}} = 5.02$ TeV*, *Phys. Lett. B* **760** (2016) 720 [[arXiv:1601.03658](#)] [[INSPIRE](#)].
- [29] ALICE collaboration, *Constraints on jet quenching in p-Pb collisions at $\sqrt{s_{NN}} = 5.02$ TeV measured by the event-activity dependence of semi-inclusive hadron-jet distributions*, *Phys. Lett. B* **783** (2018) 95 [[arXiv:1712.05603](#)] [[INSPIRE](#)].
- [30] B. Schenke, P. Tribedy and R. Venugopalan, *Fluctuating Glasma initial conditions and flow in heavy ion collisions*, *Phys. Rev. Lett.* **108** (2012) 252301 [[arXiv:1202.6646](#)] [[INSPIRE](#)].
- [31] B. Schenke, P. Tribedy and R. Venugopalan, *Event-by-event gluon multiplicity, energy density, and eccentricities in ultrarelativistic heavy-ion collisions*, *Phys. Rev. C* **86** (2012) 034908 [[arXiv:1206.6805](#)] [[INSPIRE](#)].
- [32] P.F. Kolb and U.W. Heinz, *Hydrodynamic description of ultrarelativistic heavy ion collisions*, [nucl-th/0305084](#) [[INSPIRE](#)].
- [33] H. Song and U.W. Heinz, *Causal viscous hydrodynamics in 2+1 dimensions for relativistic heavy-ion collisions*, *Phys. Rev. C* **77** (2008) 064901 [[arXiv:0712.3715](#)] [[INSPIRE](#)].
- [34] K. Dusling and D. Teaney, *Simulating elliptic flow with viscous hydrodynamics*, *Phys. Rev. C* **77** (2008) 034905 [[arXiv:0710.5932](#)] [[INSPIRE](#)].

- [35] H. Holopainen, H. Niemi and K.J. Eskola, *Event-by-event hydrodynamics and elliptic flow from fluctuating initial state*, *Phys. Rev. C* **83** (2011) 034901 [[arXiv:1007.0368](#)] [[INSPIRE](#)].
- [36] B. Schenke, S. Jeon and C. Gale, *Elliptic and triangular flow in event-by-event (3+1)D viscous hydrodynamics*, *Phys. Rev. Lett.* **106** (2011) 042301 [[arXiv:1009.3244](#)] [[INSPIRE](#)].
- [37] P. Romatschke and U. Romatschke, *Viscosity Information from Relativistic Nuclear Collisions: How Perfect is the Fluid Observed at RHIC?*, *Phys. Rev. Lett.* **99** (2007) 172301 [[arXiv:0706.1522](#)] [[INSPIRE](#)].
- [38] H. Niemi, K.J. Eskola and R. Paatelainen, *Event-by-event fluctuations in a perturbative QCD + saturation + hydrodynamics model: Determining QCD matter shear viscosity in ultrarelativistic heavy-ion collisions*, *Phys. Rev. C* **93** (2016) 024907 [[arXiv:1505.02677](#)] [[INSPIRE](#)].
- [39] S. Jeon and U. Heinz, *Introduction to Hydrodynamics*, *Int. J. Mod. Phys. E* **24** (2015) 1530010 [[arXiv:1503.03931](#)] [[INSPIRE](#)].
- [40] P. Romatschke and U. Romatschke, *Relativistic Fluid Dynamics In and Out of Equilibrium*, Cambridge University Press (2019) [[DOI:10.1017/9781108651998](#)] [[INSPIRE](#)].
- [41] S.A. Bass et al., *Microscopic models for ultrarelativistic heavy ion collisions*, *Prog. Part. Nucl. Phys.* **41** (1998) 255 [[nucl-th/9803035](#)] [[INSPIRE](#)].
- [42] M. Bleicher et al., *Relativistic hadron hadron collisions in the ultrarelativistic quantum molecular dynamics model*, *J. Phys. G* **25** (1999) 1859 [[hep-ph/9909407](#)] [[INSPIRE](#)].
- [43] SMASH collaboration, *Particle production and equilibrium properties within a new hadron transport approach for heavy-ion collisions*, *Phys. Rev. C* **94** (2016) 054905 [[arXiv:1606.06642](#)] [[INSPIRE](#)].
- [44] ALICE collaboration, *Correlated event-by-event fluctuations of flow harmonics in Pb-Pb collisions at $\sqrt{s_{NN}} = 2.76$ TeV*, *Phys. Rev. Lett.* **117** (2016) 182301 [[arXiv:1604.07663](#)] [[INSPIRE](#)].
- [45] ALICE collaboration, *Systematic studies of correlations between different order flow harmonics in Pb-Pb collisions at $\sqrt{s_{NN}} = 2.76$ TeV*, *Phys. Rev. C* **97** (2018) 024906 [[arXiv:1709.01127](#)] [[INSPIRE](#)].
- [46] ALICE collaboration, *Linear and non-linear flow modes in Pb-Pb collisions at $\sqrt{s_{NN}} = 2.76$ TeV*, *Phys. Lett. B* **773** (2017) 68 [[arXiv:1705.04377](#)] [[INSPIRE](#)].
- [47] ALICE collaboration, *Higher harmonic non-linear flow modes of charged hadrons in Pb-Pb collisions at $\sqrt{s_{NN}} = 5.02$ TeV*, *JHEP* **05** (2020) 085 [[arXiv:2002.00633](#)] [[INSPIRE](#)].
- [48] ALICE collaboration, *Multiharmonic Correlations of Different Flow Amplitudes in Pb-Pb Collisions at $\sqrt{s_{NN}} = 2.76$ TeV*, *Phys. Rev. Lett.* **127** (2021) 092302 [[arXiv:2101.02579](#)] [[INSPIRE](#)].
- [49] ALICE collaboration, *Measurements of mixed harmonic cumulants in Pb-Pb collisions at $\sqrt{s_{NN}} = 5.02$ TeV*, *Phys. Lett. B* **818** (2021) 136354 [[arXiv:2102.12180](#)] [[INSPIRE](#)].
- [50] ALICE collaboration, *Centrality dependence of π , K, p production in Pb-Pb collisions at $\sqrt{s_{NN}} = 2.76$ TeV*, *Phys. Rev. C* **88** (2013) 044910 [[arXiv:1303.0737](#)] [[INSPIRE](#)].
- [51] ALICE collaboration, *Higher harmonic anisotropic flow measurements of charged particles in Pb-Pb collisions at $\sqrt{s_{NN}} = 2.76$ TeV*, *Phys. Rev. Lett.* **107** (2011) 032301 [[arXiv:1105.3865](#)] [[INSPIRE](#)].

- [52] J.E. Bernhard et al., *Applying Bayesian parameter estimation to relativistic heavy-ion collisions: simultaneous characterization of the initial state and quark-gluon plasma medium*, *Phys. Rev. C* **94** (2016) 024907 [[arXiv:1605.03954](#)] [[INSPIRE](#)].
- [53] J.E. Bernhard, J.S. Moreland and S.A. Bass, *Bayesian estimation of the specific shear and bulk viscosity of quark-gluon plasma*, *Nature Phys.* **15** (2019) 1113 [[INSPIRE](#)].
- [54] J.E. Parkkila, A. Onnerstad and D.J. Kim, *Bayesian estimation of the specific shear and bulk viscosity of the quark-gluon plasma with additional flow harmonic observables*, *Phys. Rev. C* **104** (2021) 054904 [[arXiv:2106.05019](#)] [[INSPIRE](#)].
- [55] J.E. Parkkila et al., *New constraints for QCD matter from improved Bayesian parameter estimation in heavy-ion collisions at LHC*, *Phys. Lett. B* **835** (2022) 137485 [[arXiv:2111.08145](#)] [[INSPIRE](#)].
- [56] J.S. Moreland, J.E. Bernhard and S.A. Bass, *Bayesian calibration of a hybrid nuclear collision model using p-Pb and Pb-Pb data at energies available at the CERN Large Hadron Collider*, *Phys. Rev. C* **101** (2020) 024911 [[arXiv:1808.02106](#)] [[INSPIRE](#)].
- [57] K. Dusling and R. Venugopalan, *Evidence for BFKL and saturation dynamics from dihadron spectra at the LHC*, *Phys. Rev. D* **87** (2013) 051502 [[arXiv:1210.3890](#)] [[INSPIRE](#)].
- [58] A. Bzdak, B. Schenke, P. Tribedy and R. Venugopalan, *Initial state geometry and the role of hydrodynamics in proton-proton, proton-nucleus and deuteron-nucleus collisions*, *Phys. Rev. C* **87** (2013) 064906 [[arXiv:1304.3403](#)] [[INSPIRE](#)].
- [59] M. Greif et al., *Importance of initial and final state effects for azimuthal correlations in p+Pb collisions*, *Phys. Rev. D* **96** (2017) 091504 [[arXiv:1708.02076](#)] [[INSPIRE](#)].
- [60] H. Mäntysaari, B. Schenke, C. Shen and P. Tribedy, *Imprints of fluctuating proton shapes on flow in proton-lead collisions at the LHC*, *Phys. Lett. B* **772** (2017) 681 [[arXiv:1705.03177](#)] [[INSPIRE](#)].
- [61] W. Zhao et al., *Hydrodynamic collectivity in proton-proton collisions at 13 TeV*, *Phys. Lett. B* **780** (2018) 495 [[arXiv:1801.00271](#)] [[INSPIRE](#)].
- [62] S.S. Gubser, *Symmetry constraints on generalizations of Bjorken flow*, *Phys. Rev. D* **82** (2010) 085027 [[arXiv:1006.0006](#)] [[INSPIRE](#)].
- [63] S.S. Gubser and A. Yarom, *Conformal hydrodynamics in Minkowski and de Sitter spacetimes*, *Nucl. Phys. B* **846** (2011) 469 [[arXiv:1012.1314](#)] [[INSPIRE](#)].
- [64] S.F. Taghavi, *Smallest QCD droplet and multiparticle correlations in p-p collisions*, *Phys. Rev. C* **104** (2021) 054906 [[arXiv:1907.12140](#)] [[INSPIRE](#)].
- [65] Z.-W. Lin et al., *A Multi-phase transport model for relativistic heavy ion collisions*, *Phys. Rev. C* **72** (2005) 064901 [[nucl-th/0411110](#)] [[INSPIRE](#)].
- [66] J.D. Orjuela Koop, A. Adare, D. McGlinchey and J.L. Nagle, *Azimuthal anisotropy relative to the participant plane from a multiphase transport model in central p + Au , d + Au , and $^3\text{He} + \text{Au}$ collisions at $\sqrt{s_{NN}} = 200 \text{ GeV}$* , *Phys. Rev. C* **92** (2015) 054903 [[arXiv:1501.06880](#)] [[INSPIRE](#)].
- [67] K. Gallmeister, H. Niemi, C. Greiner and D.H. Rischke, *Exploring the applicability of dissipative fluid dynamics to small systems by comparison to the Boltzmann equation*, *Phys. Rev. C* **98** (2018) 024912 [[arXiv:1804.09512](#)] [[INSPIRE](#)].
- [68] A. Kurkela, U.A. Wiedemann and B. Wu, *Flow in AA and pA as an interplay of fluid-like and non-fluid like excitations*, *Eur. Phys. J. C* **79** (2019) 965 [[arXiv:1905.05139](#)] [[INSPIRE](#)].

- [69] A. Kurkela, S.F. Taghavi, U.A. Wiedemann and B. Wu, *Hydrodynamization in systems with detailed transverse profiles*, *Phys. Lett. B* **811** (2020) 135901 [[arXiv:2007.06851](#)] [[INSPIRE](#)].
- [70] V.E. Ambrus, S. Schlichting and C. Werthmann, *Development of transverse flow at small and large opacities in conformal kinetic theory*, *Phys. Rev. D* **105** (2022) 014031 [[arXiv:2109.03290](#)] [[INSPIRE](#)].
- [71] C. Bierlich, G. Gustafson and L. Lönnblad, *Collectivity without plasma in hadronic collisions*, *Phys. Lett. B* **779** (2018) 58 [[arXiv:1710.09725](#)] [[INSPIRE](#)].
- [72] C. Bierlich, *Soft modifications to jet fragmentation in high energy proton–proton collisions*, *Phys. Lett. B* **795** (2019) 194 [[arXiv:1901.07447](#)] [[INSPIRE](#)].
- [73] ALICE collaboration, *Long- and short-range correlations and their event-scale dependence in high-multiplicity pp collisions at $\sqrt{s} = 13$ TeV*, *JHEP* **05** (2021) 290 [[arXiv:2101.03110](#)] [[INSPIRE](#)].
- [74] B. Schenke, C. Shen and P. Tribedy, *Running the gamut of high energy nuclear collisions*, *Phys. Rev. C* **102** (2020) 044905 [[arXiv:2005.14682](#)] [[INSPIRE](#)].
- [75] M. Strickland, *Small system studies: A theory overview*, *Nucl. Phys. A* **982** (2019) 92 [[arXiv:1807.07191](#)] [[INSPIRE](#)].
- [76] C. Loizides, *Experimental overview on small collision systems at the LHC*, *Nucl. Phys. A* **956** (2016) 200 [[arXiv:1602.09138](#)] [[INSPIRE](#)].
- [77] J.L. Nagle and W.A. Zajc, *Small System Collectivity in Relativistic Hadronic and Nuclear Collisions*, *Ann. Rev. Nucl. Part. Sci.* **68** (2018) 211 [[arXiv:1801.03477](#)] [[INSPIRE](#)].
- [78] A. Bilandzic, R. Snellings and S. Voloshin, *Flow analysis with cumulants: Direct calculations*, *Phys. Rev. C* **83** (2011) 044913 [[arXiv:1010.0233](#)] [[INSPIRE](#)].
- [79] ATLAS collaboration, *Correlated long-range mixed-harmonic fluctuations measured in pp, p+Pb and low-multiplicity Pb+Pb collisions with the ATLAS detector*, *Phys. Lett. B* **789** (2019) 444 [[arXiv:1807.02012](#)] [[INSPIRE](#)].
- [80] CMS collaboration, *Jet and Underlying Event Properties as a Function of Charged-Particle Multiplicity in Proton–Proton Collisions at $\sqrt{s} = 7$ TeV*, *Eur. Phys. J. C* **73** (2013) 2674 [[arXiv:1310.4554](#)] [[INSPIRE](#)].
- [81] ALICE collaboration, *Multiplicity dependence of two-particle azimuthal correlations in pp collisions at the LHC*, *JHEP* **09** (2013) 049 [[arXiv:1307.1249](#)] [[INSPIRE](#)].
- [82] ALICE collaboration, *Multiplicity dependence of jet-like two-particle correlation structures in p–Pb collisions at $\sqrt{s_{NN}} = 5.02$ TeV*, *Phys. Lett. B* **741** (2015) 38 [[arXiv:1406.5463](#)] [[INSPIRE](#)].
- [83] ALICE collaboration, *Long-range angular correlations of π , K and p in p–Pb collisions at $\sqrt{s_{NN}} = 5.02$ TeV*, *Phys. Lett. B* **726** (2013) 164 [[arXiv:1307.3237](#)] [[INSPIRE](#)].
- [84] T. Sjostrand and M. van Zijl, *Multiple Parton-parton Interactions in an Impact Parameter Picture*, *Phys. Lett. B* **188** (1987) 149 [[INSPIRE](#)].
- [85] L. Frankfurt, M. Strikman and C. Weiss, *Dijet production as a centrality trigger for pp collisions at CERN LHC*, *Phys. Rev. D* **69** (2004) 114010 [[hep-ph/0311231](#)] [[INSPIRE](#)].
- [86] L. Frankfurt, M. Strikman and C. Weiss, *Transverse nucleon structure and diagnostics of hard parton-parton processes at LHC*, *Phys. Rev. D* **83** (2011) 054012 [[arXiv:1009.2559](#)] [[INSPIRE](#)].
- [87] CMS collaboration, *Measurement of the Underlying Event Activity in pp Collisions at $\sqrt{s} = 0.9$ and 7 TeV with the Novel Jet-Area/Median Approach*, *JHEP* **08** (2012) 130 [[arXiv:1207.2392](#)] [[INSPIRE](#)].

- [88] CMS collaboration, *Measurement of the Underlying Event Activity at the LHC with $\sqrt{s} = 7$ TeV and Comparison with $\sqrt{s} = 0.9$ TeV*, *JHEP* **09** (2011) 109 [[arXiv:1107.0330](#)] [[INSPIRE](#)].
- [89] ALICE collaboration, *Underlying-event properties in pp and p-Pb collisions at $\sqrt{s_{NN}} = 5.02$ TeV*, *JHEP* **06** (2023) 023 [[arXiv:2204.10389](#)] [[INSPIRE](#)].
- [90] ALICE collaboration, *The ALICE experiment at the CERN LHC*, 2008 *JINST* **3** S08002 [[INSPIRE](#)].
- [91] ALICE collaboration, *Performance of the ALICE Experiment at the CERN LHC*, *Int. J. Mod. Phys. A* **29** (2014) 1430044 [[arXiv:1402.4476](#)] [[INSPIRE](#)].
- [92] ALICE collaboration, *Performance of the ALICE VZERO system*, 2013 *JINST* **8** P10016 [[arXiv:1306.3130](#)] [[INSPIRE](#)].
- [93] ALICE collaboration, *Alignment of the ALICE Inner Tracking System with cosmic-ray tracks*, 2010 *JINST* **5** P03003 [[arXiv:1001.0502](#)] [[INSPIRE](#)].
- [94] ALICE collaboration, *Technical Design Report for the Upgrade of the ALICE Inner Tracking System*, *J. Phys. G* **41** (2014) 087002 [[INSPIRE](#)].
- [95] J. Alme et al., *The ALICE TPC, a large 3-dimensional tracking device with fast readout for ultra-high multiplicity events*, *Nucl. Instrum. Meth. A* **622** (2010) 316 [[arXiv:1001.1950](#)] [[INSPIRE](#)].
- [96] R. Santoro et al., *The ALICE Silicon Pixel Detector: Readiness for the first proton beam*, 2009 *JINST* **4** P03023 [[INSPIRE](#)].
- [97] ALICE collaboration, *ALICE luminosity determination for pp collisions at $\sqrt{s} = 13$ TeV*, *ALICE-PUBLIC-2016-002* (2016).
- [98] ALICE collaboration, *Pseudorapidity distributions of charged particles as a function of mid- and forward rapidity multiplicities in pp collisions at $\sqrt{s} = 5.02, 7$ and 13 TeV*, *Eur. Phys. J. C* **81** (2021) 630 [[arXiv:2009.09434](#)] [[INSPIRE](#)].
- [99] M. Ivanov, I. Belikov, P. Hristov and K. Safarik, *Track reconstruction in high density environment*, *Nucl. Instrum. Meth. A* **566** (2006) 70 [[INSPIRE](#)].
- [100] ALICE collaboration, *The ALICE definition of primary particles*, *ALICE-PUBLIC-2017-005* (2017).
- [101] ALICE collaboration, *Transverse momentum spectra and nuclear modification factors of charged particles in pp, p-Pb and Pb-Pb collisions at the LHC*, *JHEP* **11** (2018) 013 [[arXiv:1802.09145](#)] [[INSPIRE](#)].
- [102] R. Brun et al., *GEANT Detector Description and Simulation Tool*, CERN-W5013 (1994) [[DOI:10.17181/CERN.MUHF.DMJ1](#)] [[INSPIRE](#)].
- [103] ALICE collaboration, *Transverse momentum spectra and nuclear modification factors of charged particles in Xe-Xe collisions at $\sqrt{s_{NN}} = 5.44$ TeV*, *Phys. Lett. B* **788** (2019) 166 [[arXiv:1805.04399](#)] [[INSPIRE](#)].
- [104] G.I. Kopylov, *Like particle correlations as a tool to study the multiple production mechanism*, *Phys. Lett. B* **50** (1974) 472 [[INSPIRE](#)].
- [105] ALICE collaboration, *Anomalous evolution of the near-side jet peak shape in Pb-Pb collisions at $\sqrt{s_{NN}} = 2.76$ TeV*, *Phys. Rev. Lett.* **119** (2017) 102301 [[arXiv:1609.06643](#)] [[INSPIRE](#)].
- [106] PHENIX collaboration, *Jet properties from dihadron correlations in p^+p collisions at $\sqrt{s} = 200$ -GeV*, *Phys. Rev. D* **74** (2006) 072002 [[hep-ex/0605039](#)] [[INSPIRE](#)].

- [107] N.N. Ajitanand et al., *Decomposition of harmonic and jet contributions to particle-pair correlations at ultra-relativistic energies*, *Phys. Rev. C* **72** (2005) 011902 [[nucl-ex/0501025](#)] [[INSPIRE](#)].
- [108] PHENIX collaboration, *Pseudorapidity Dependence of Particle Production and Elliptic Flow in Asymmetric Nuclear Collisions of p+Al, p+Au, d+Au, and $^3\text{He}+\text{Au}$ at $\sqrt{s_{NN}} = 200$ GeV*, *Phys. Rev. Lett.* **121** (2018) 222301 [[arXiv:1807.11928](#)] [[INSPIRE](#)].
- [109] ALICE collaboration, *Pseudorapidity dependence of the anisotropic flow of charged particles in Pb-Pb collisions at $\sqrt{s_{NN}} = 2.76$ TeV*, *Phys. Lett. B* **762** (2016) 376 [[arXiv:1605.02035](#)] [[INSPIRE](#)].
- [110] P. Skands, S. Carrazza and J. Rojo, *Tuning PYTHIA 8.1: the Monash 2013 Tune*, *Eur. Phys. J. C* **74** (2014) 3024 [[arXiv:1404.5630](#)] [[INSPIRE](#)].
- [111] M. Cacciari, G.P. Salam and G. Soyez, *The anti- k_t jet clustering algorithm*, *JHEP* **04** (2008) 063 [[arXiv:0802.1189](#)] [[INSPIRE](#)].
- [112] M. Cacciari, G.P. Salam and G. Soyez, *FastJet User Manual*, *Eur. Phys. J. C* **72** (2012) 1896 [[arXiv:1111.6097](#)] [[INSPIRE](#)].
- [113] ALICE collaboration, *Charged jet cross section and fragmentation in proton-proton collisions at $\sqrt{s} = 7$ TeV*, *Phys. Rev. D* **99** (2019) 012016 [[arXiv:1809.03232](#)] [[INSPIRE](#)].
- [114] R. Barlow, *Systematic errors: Facts and fictions*, in the proceedings of the *Conference on Advanced Statistical Techniques in Particle Physics*, Durham, U.K., March 18–22 (2002) [[hep-ex/0207026](#)] [[INSPIRE](#)].
- [115] ALICE collaboration, *Production of $K^*(892)^0$ and $\phi(1020)$ in pp and Pb-Pb collisions at $\sqrt{s_{NN}} = 5.02$ TeV*, *Phys. Rev. C* **106** (2022) 034907 [[arXiv:2106.13113](#)] [[INSPIRE](#)].
- [116] ALICE collaboration, *Anisotropic flow of identified particles in Pb-Pb collisions at $\sqrt{s_{NN}} = 5.02$ TeV*, *JHEP* **09** (2018) 006 [[arXiv:1805.04390](#)] [[INSPIRE](#)].
- [117] CDF collaboration, *Charged Jet Evolution and the Underlying Event in $p\bar{p}$ Collisions at 1.8 TeV*, *Phys. Rev. D* **65** (2002) 092002 [[INSPIRE](#)].
- [118] ATLAS collaboration, *Measurement of the inclusive jet cross-section in proton-proton collisions at $\sqrt{s} = 7$ TeV using 4.5fb^{-1} of data with the ATLAS detector*, *JHEP* **02** (2015) 153 [*Erratum ibid.* **09** (2015) 141] [[arXiv:1410.8857](#)] [[INSPIRE](#)].
- [119] CMS collaboration, *Measurement of the inclusive jet cross section in pp collisions at $\sqrt{s} = 2.76$ TeV*, *Eur. Phys. J. C* **76** (2016) 265 [[arXiv:1512.06212](#)] [[INSPIRE](#)].
- [120] ATLAS collaboration, *Measurement of long-range two-particle azimuthal correlations in Z-boson tagged pp collisions at $\sqrt{s}=8$ and 13 TeV*, *Eur. Phys. J. C* **80** (2020) 64 [[arXiv:1906.08290](#)] [[INSPIRE](#)].
- [121] J.S. Moreland, J.E. Bernhard and S.A. Bass, *Alternative ansatz to wounded nucleon and binary collision scaling in high-energy nuclear collisions*, *Phys. Rev. C* **92** (2015) 011901 [[arXiv:1412.4708](#)] [[INSPIRE](#)].
- [122] C. Shen et al., *The iEBE-VISHNU code package for relativistic heavy-ion collisions*, *Comput. Phys. Commun.* **199** (2016) 61 [[arXiv:1409.8164](#)] [[INSPIRE](#)].
- [123] J.-B. Rose, J.M. Torres-Rincon and H. Elfner, *Inclusive and effective bulk viscosities in the hadron gas*, *J. Phys. G* **48** (2020) 015005 [[arXiv:2005.03647](#)] [[INSPIRE](#)].

- [124] R.D. Weller and P. Romatschke, *One fluid to rule them all: viscous hydrodynamic description of event-by-event central $p+p$, $p+Pb$ and $Pb+Pb$ collisions at $\sqrt{s} = 5.02$ TeV*, *Phys. Lett. B* **774** (2017) 351 [[arXiv:1701.07145](#)] [[INSPIRE](#)].
- [125] T. Pierog et al., *EPOS LHC: Test of collective hadronization with data measured at the CERN Large Hadron Collider*, *Phys. Rev. C* **92** (2015) 034906 [[arXiv:1306.0121](#)] [[INSPIRE](#)].
- [126] S. Ji et al., *Toward unbiased flow measurements in pp collisions at the CERN Large Hadron Collider*, *Phys. Rev. C* **108** (2023) 034909 [[arXiv:2303.05806](#)] [[INSPIRE](#)].

The ALICE collaboration

S. Acharya [ID](#)¹²⁸, D. Adamová [ID](#)⁸⁷, G. Aglieri Rinella [ID](#)³³, M. Agnello [ID](#)³⁰, N. Agrawal [ID](#)⁵², Z. Ahammed [ID](#)¹³⁶, S. Ahmad [ID](#)¹⁶, S.U. Ahn [ID](#)⁷², I. Ahuja [ID](#)³⁸, A. Akindinov [ID](#)¹⁴², M. Al-Turany [ID](#)⁹⁸, D. Aleksandrov [ID](#)¹⁴², B. Alessandro [ID](#)⁵⁷, H.M. Alfanda [ID](#)⁶, R. Alfaro Molina [ID](#)⁶⁸, B. Ali [ID](#)¹⁶, A. Alici [ID](#)²⁶, N. Alizadehvandchali [ID](#)¹¹⁷, A. Alkin [ID](#)³³, J. Alme [ID](#)²¹, G. Alocco [ID](#)⁵³, T. Alt [ID](#)⁶⁵, A.R. Altamura [ID](#)⁵¹, I. Altsybeev [ID](#)⁹⁶, J.R. Alvarado [ID](#)⁴⁵, M.N. Anaam [ID](#)⁶, C. Andrei [ID](#)⁴⁶, N. Andreou [ID](#)¹¹⁶, A. Andronic [ID](#)¹²⁷, V. Anguelov [ID](#)⁹⁵, F. Antinori [ID](#)⁵⁵, P. Antonioli [ID](#)⁵², N. Apadula [ID](#)⁷⁵, L. Aphecetche [ID](#)¹⁰⁴, H. Appelshäuser [ID](#)⁶⁵, C. Arata [ID](#)⁷⁴, S. Arcelli [ID](#)²⁶, M. Aresti [ID](#)²³, R. Arnaldi [ID](#)⁵⁷, J.G.M.C.A. Arneiro [ID](#)¹¹¹, I.C. Arsene [ID](#)²⁰, M. Arslandok [ID](#)¹³⁹, A. Augustinus [ID](#)³³, R. Averbeck [ID](#)⁹⁸, M.D. Azmi [ID](#)¹⁶, H. Baba¹²⁵, A. Badalà [ID](#)⁵⁴, J. Bae [ID](#)¹⁰⁵, Y.W. Baek [ID](#)⁴¹, X. Bai [ID](#)¹²¹, R. Bailhache [ID](#)⁶⁵, Y. Bailung [ID](#)⁴⁹, A. Balbino [ID](#)³⁰, A. Baldisseri [ID](#)¹³¹, B. Balis [ID](#)², D. Banerjee [ID](#)⁴, Z. Banoo [ID](#)⁹², R. Barbera [ID](#)²⁷, F. Barile [ID](#)³², L. Barioglio [ID](#)⁹⁶, M. Barlou⁷⁹, B. Barman⁴², G.G. Barnaföldi [ID](#)⁴⁷, L.S. Barnby [ID](#)⁸⁶, V. Barret [ID](#)¹²⁸, L. Barreto [ID](#)¹¹¹, C. Bartels [ID](#)¹²⁰, K. Barth [ID](#)³³, E. Bartsch [ID](#)⁶⁵, N. Bastid [ID](#)¹²⁸, S. Basu [ID](#)⁷⁶, G. Batigne [ID](#)¹⁰⁴, D. Battistini [ID](#)⁹⁶, B. Batyunya [ID](#)¹⁴³, D. Bauri⁴⁸, J.L. Bazo Alba [ID](#)¹⁰², I.G. Bearden [ID](#)⁸⁴, C. Beattie [ID](#)¹³⁹, P. Becht [ID](#)⁹⁸, D. Behera [ID](#)⁴⁹, I. Belikov [ID](#)¹³⁰, A.D.C. Bell Hechavarría [ID](#)¹²⁷, F. Bellini [ID](#)²⁶, R. Bellwied [ID](#)¹¹⁷, S. Belokurova [ID](#)¹⁴², Y.A.V. Beltran [ID](#)⁴⁵, G. Bencedi [ID](#)⁴⁷, S. Beole [ID](#)²⁵, Y. Berdnikov [ID](#)¹⁴², A. Berdnikova [ID](#)⁹⁵, L. Bergmann [ID](#)⁹⁵, M.G. Besoiu [ID](#)⁶⁴, L. Betev [ID](#)³³, P.P. Bhaduri [ID](#)¹³⁶, A. Bhasin [ID](#)⁹², M.A. Bhat [ID](#)⁴, B. Bhattacharjee [ID](#)⁴², L. Bianchi [ID](#)²⁵, N. Bianchi [ID](#)⁵⁰, J. Bielčák [ID](#)³⁶, J. Bielčíková [ID](#)⁸⁷, J. Biernat [ID](#)¹⁰⁸, A.P. Bigot [ID](#)¹³⁰, A. Bilandzic [ID](#)⁹⁶, G. Biro [ID](#)⁴⁷, S. Biswas [ID](#)⁴, N. Bize [ID](#)¹⁰⁴, J.T. Blair [ID](#)¹⁰⁹, D. Blau [ID](#)¹⁴², M.B. Blidaru [ID](#)⁹⁸, N. Bluhme³⁹, C. Blume [ID](#)⁶⁵, G. Boca [ID](#)^{22,56}, F. Bock [ID](#)⁸⁸, T. Bodova [ID](#)²¹, A. Bogdanov¹⁴², S. Boi [ID](#)²³, J. Bok [ID](#)⁵⁹, L. Boldizsár [ID](#)⁴⁷, M. Bombara [ID](#)³⁸, P.M. Bond [ID](#)³³, G. Bonomi [ID](#)^{135,56}, H. Borel [ID](#)¹³¹, A. Borissov [ID](#)¹⁴², A.G. Borquez Carcamo [ID](#)⁹⁵, H. Bossi [ID](#)¹³⁹, E. Botta [ID](#)²⁵, Y.E.M. Bouziani [ID](#)⁶⁵, L. Bratrud [ID](#)⁶⁵, P. Braun-Munzinger [ID](#)⁹⁸, M. Bregant [ID](#)¹¹¹, M. Broz [ID](#)³⁶, G.E. Bruno [ID](#)^{97,32}, M.D. Buckland [ID](#)²⁴, D. Budnikov [ID](#)¹⁴², H. Buesching [ID](#)⁶⁵, S. Bufalino [ID](#)³⁰, P. Buhler [ID](#)¹⁰³, N. Burmasov [ID](#)¹⁴², Z. Buthelezi [ID](#)^{69,124}, A. Bylinkin [ID](#)²¹, S.A. Bysiak¹⁰⁸, M. Cai [ID](#)⁶, H. Caines [ID](#)¹³⁹, A. Caliva [ID](#)²⁹, E. Calvo Villar [ID](#)¹⁰², J.M.M. Camacho [ID](#)¹¹⁰, P. Camerini [ID](#)²⁴, F.D.M. Canedo [ID](#)¹¹¹, S.L. Cantway [ID](#)¹³⁹, M. Carabas [ID](#)¹¹⁴, A.A. Carballo [ID](#)³³, F. Carnesecchi [ID](#)³³, R. Caron [ID](#)¹²⁹, L.A.D. Carvalho [ID](#)¹¹¹, J. Castillo Castellanos [ID](#)¹³¹, F. Catalano [ID](#)^{33,25}, C. Ceballos Sanchez [ID](#)¹⁴³, I. Chakaberia [ID](#)⁷⁵, P. Chakraborty [ID](#)⁴⁸, S. Chandra [ID](#)¹³⁶, S. Chapeland [ID](#)³³, M. Chartier [ID](#)¹²⁰, S. Chattopadhyay [ID](#)¹³⁶, S. Chattopadhyay [ID](#)¹⁰⁰, T. Cheng [ID](#)^{98,6}, C. Cheshkov [ID](#)¹²⁹, B. Cheynis [ID](#)¹²⁹, V. Chibante Barroso [ID](#)³³, D.D. Chinellato [ID](#)¹¹², E.S. Chizzali [ID](#)^{11,96}, J. Cho [ID](#)⁵⁹, S. Cho [ID](#)⁵⁹, P. Chochula [ID](#)³³, D. Choudhury⁴², P. Christakoglou [ID](#)⁸⁵, C.H. Christensen [ID](#)⁸⁴, P. Christiansen [ID](#)⁷⁶, T. Chujo [ID](#)¹²⁶, M. Ciaccio [ID](#)³⁰, C. Cicalo [ID](#)⁵³, F. Cindolo [ID](#)⁵², M.R. Ciupek⁹⁸, G. Clai^{III,52}, F. Colamaria [ID](#)⁵¹, J.S. Colburn¹⁰¹, D. Colella [ID](#)^{97,32}, M. Colocci [ID](#)²⁶, M. Concas [ID](#)^{IV,33}, G. Conesa Balbastre [ID](#)⁷⁴, Z. Conesa del Valle [ID](#)¹³², G. Contin [ID](#)²⁴, J.G. Contreras [ID](#)³⁶, M.L. Coquet [ID](#)¹³¹, P. Cortese [ID](#)^{134,57}, M.R. Cosentino [ID](#)¹¹³, F. Costa [ID](#)³³, S. Costanza [ID](#)^{22,56}, C. Cot [ID](#)¹³², J. Crkovská [ID](#)⁹⁵, P. Crochet [ID](#)¹²⁸, R. Cruz-Torres [ID](#)⁷⁵, P. Cui [ID](#)⁶, A. Dainese [ID](#)⁵⁵, M.C. Danisch [ID](#)⁹⁵, A. Danu [ID](#)⁶⁴, P. Das [ID](#)⁸¹, P. Das [ID](#)⁴, S. Das [ID](#)⁴, A.R. Dash [ID](#)¹²⁷, S. Dash [ID](#)⁴⁸, A. De Caro [ID](#)²⁹, G. de Cataldo [ID](#)⁵¹, J. de Cuveland³⁹,

A. De Falco [ID](#)²³, D. De Gruttola [ID](#)²⁹, N. De Marco [ID](#)⁵⁷, C. De Martin [ID](#)²⁴, S. De Pasquale [ID](#)²⁹, R. Deb [ID](#)¹³⁵, R. Del Grande [ID](#)⁹⁶, L. Dello Stritto [ID](#)²⁹, W. Deng [ID](#)⁶, P. Dhankher [ID](#)¹⁹, D. Di Bari [ID](#)³², A. Di Mauro [ID](#)³³, B. Diab [ID](#)¹³¹, R.A. Diaz [ID](#)^{143,7}, T. Dietel [ID](#)¹¹⁵, Y. Ding [ID](#)⁶, J. Ditzel [ID](#)⁶⁵, R. Divià [ID](#)³³, D.U. Dixit [ID](#)¹⁹, Ø. Djuvsland²¹, U. Dmitrieva [ID](#)¹⁴², A. Dobrin [ID](#)⁶⁴, B. Dönigus [ID](#)⁶⁵, J.M. Dubinski [ID](#)¹³⁷, A. Dubla [ID](#)⁹⁸, S. Dudi [ID](#)⁹¹, P. Dupieux [ID](#)¹²⁸, M. Durkac¹⁰⁷, N. Dzalaiova¹³, T.M. Eder [ID](#)¹²⁷, R.J. Ehlers [ID](#)⁷⁵, F. Eisenhut [ID](#)⁶⁵, R. Ejima⁹³, D. Elia [ID](#)⁵¹, B. Erasmus [ID](#)¹⁰⁴, F. Ercolessi [ID](#)²⁶, B. Espagnon [ID](#)¹³², G. Eulisse [ID](#)³³, D. Evans [ID](#)¹⁰¹, S. Evdokimov [ID](#)¹⁴², L. Fabbietti [ID](#)⁹⁶, M. Faggin [ID](#)²⁸, J. Faivre [ID](#)⁷⁴, F. Fan [ID](#)⁶, W. Fan [ID](#)⁷⁵, A. Fantoni [ID](#)⁵⁰, M. Fasel [ID](#)⁸⁸, A. Feliciello [ID](#)⁵⁷, G. Feofilov [ID](#)¹⁴², A. Fernández Téllez [ID](#)⁴⁵, L. Ferrandi [ID](#)¹¹¹, M.B. Ferrer [ID](#)³³, A. Ferrero [ID](#)¹³¹, C. Ferrero [ID](#)⁵⁷, A. Ferretti [ID](#)²⁵, V.J.G. Feuillard [ID](#)⁹⁵, V. Filova [ID](#)³⁶, D. Finogeev [ID](#)¹⁴², F.M. Fionda [ID](#)⁵³, E. Flatland³³, F. Flor [ID](#)¹¹⁷, A.N. Flores [ID](#)¹⁰⁹, S. Foertsch [ID](#)⁶⁹, I. Fokin [ID](#)⁹⁵, S. Fokin [ID](#)¹⁴², E. Fragiaco [ID](#)⁵⁸, E. Frajna [ID](#)⁴⁷, U. Fuchs [ID](#)³³, N. Funicello [ID](#)²⁹, C. Furget [ID](#)⁷⁴, A. Furs [ID](#)¹⁴², T. Fusayasu [ID](#)⁹⁹, J.J. Gaardhøje [ID](#)⁸⁴, M. Gagliardi [ID](#)²⁵, A.M. Gago [ID](#)¹⁰², T. Gahlaut⁴⁸, C.D. Galvan [ID](#)¹¹⁰, D.R. Gangadharan [ID](#)¹¹⁷, P. Ganoti [ID](#)⁷⁹, C. Garabatos [ID](#)⁹⁸, T. García Chávez [ID](#)⁴⁵, E. Garcia-Solis [ID](#)⁹, C. Gargiulo [ID](#)³³, P. Gasik [ID](#)⁹⁸, A. Gautam [ID](#)¹¹⁹, M.B. Gay Ducati [ID](#)⁶⁷, M. Germain [ID](#)¹⁰⁴, A. Ghimouz¹²⁶, C. Ghosh¹³⁶, M. Giacalone [ID](#)⁵², G. Gioachin [ID](#)³⁰, P. Giubellino [ID](#)^{98,57}, P. Giubilato [ID](#)²⁸, A.M.C. Glaenger [ID](#)¹³¹, P. Glässel [ID](#)⁹⁵, E. Glimos [ID](#)¹²³, D.J.Q. Goh⁷⁷, V. Gonzalez [ID](#)¹³⁸, P. Gordeev [ID](#)¹⁴², M. Gorgon [ID](#)², K. Goswami [ID](#)⁴⁹, S. Gotovac³⁴, V. Grabski [ID](#)⁶⁸, L.K. Graczykowski [ID](#)¹³⁷, E. Grecka [ID](#)⁸⁷, A. Grelli [ID](#)⁶⁰, C. Grigoras [ID](#)³³, V. Grigoriev [ID](#)¹⁴², S. Grigoryan [ID](#)^{143,1}, F. Grosa [ID](#)³³, J.F. Grosse-Oetringhaus [ID](#)³³, R. Grosso [ID](#)⁹⁸, D. Grund [ID](#)³⁶, N.A. Grunwald⁹⁵, G.G. Guardianio [ID](#)¹¹², R. Guernane [ID](#)⁷⁴, M. Guilbaud [ID](#)¹⁰⁴, K. Gulbrandsen [ID](#)⁸⁴, T. Gündem [ID](#)⁶⁵, T. Gunji [ID](#)¹²⁵, W. Guo [ID](#)⁶, A. Gupta [ID](#)⁹², R. Gupta [ID](#)⁹², R. Gupta [ID](#)⁴⁹, K. Gwizdziel [ID](#)¹³⁷, L. Gyulai [ID](#)⁴⁷, C. Hadjidakis [ID](#)¹³², F.U. Haider [ID](#)⁹², S. Haidlova [ID](#)³⁶, H. Hamagaki [ID](#)⁷⁷, A. Hamdi [ID](#)⁷⁵, Y. Han [ID](#)¹⁴⁰, B.G. Hanley [ID](#)¹³⁸, R. Hannigan [ID](#)¹⁰⁹, J. Hansen [ID](#)⁷⁶, M.R. Haque [ID](#)¹³⁷, J.W. Harris [ID](#)¹³⁹, A. Harton [ID](#)⁹, H. Hassan [ID](#)¹¹⁸, D. Hatzifotiadou [ID](#)⁵², P. Hauer [ID](#)⁴³, L.B. Havener [ID](#)¹³⁹, S.T. Heckel [ID](#)⁹⁶, E. Hellbär [ID](#)⁹⁸, H. Helstrup [ID](#)³⁵, M. Hemmer [ID](#)⁶⁵, T. Herman [ID](#)³⁶, G. Herrera Corral [ID](#)⁸, F. Herrmann¹²⁷, S. Herrmann [ID](#)¹²⁹, K.F. Hetland [ID](#)³⁵, B. Heybeck [ID](#)⁶⁵, H. Hillemanns [ID](#)³³, B. Hippolyte [ID](#)¹³⁰, F.W. Hoffmann [ID](#)⁷¹, B. Hofman [ID](#)⁶⁰, G.H. Hong [ID](#)¹⁴⁰, M. Horst [ID](#)⁹⁶, A. Horzyk [ID](#)², Y. Hou [ID](#)⁶, P. Hristov [ID](#)³³, C. Hughes [ID](#)¹²³, P. Huhn⁶⁵, L.M. Huhta [ID](#)¹¹⁸, T.J. Humanic [ID](#)⁸⁹, A. Hutson [ID](#)¹¹⁷, D. Hutter [ID](#)³⁹, R. Ilkaev¹⁴², H. Ilyas [ID](#)¹⁴, M. Inaba [ID](#)¹²⁶, G.M. Innocenti [ID](#)³³, M. Ippolitov [ID](#)¹⁴², A. Isakov [ID](#)^{85,87}, T. Isidori [ID](#)¹¹⁹, M.S. Islam [ID](#)¹⁰⁰, M. Ivanov¹³, M. Ivanov [ID](#)⁹⁸, V. Ivanov [ID](#)¹⁴², K.E. Iversen [ID](#)⁷⁶, M. Jablonski [ID](#)², B. Jacak [ID](#)⁷⁵, N. Jacazio [ID](#)²⁶, P.M. Jacobs [ID](#)⁷⁵, S. Jadlovská¹⁰⁷, J. Jadlovsky¹⁰⁷, S. Jaelani [ID](#)⁸³, C. Jahnke [ID](#)¹¹¹, M.J. Jakubowska [ID](#)¹³⁷, M.A. Janik [ID](#)¹³⁷, T. Janson⁷¹, S. Ji [ID](#)¹⁷, S. Jia [ID](#)¹⁰, A.A.P. Jimenez [ID](#)⁶⁶, F. Jonas [ID](#)^{88,127}, D.M. Jones [ID](#)¹²⁰, J.M. Jowett [ID](#)^{33,98}, J. Jung [ID](#)⁶⁵, M. Jung [ID](#)⁶⁵, A. Junique [ID](#)³³, A. Jusko [ID](#)¹⁰¹, J. Kaewjai¹⁰⁶, P. Kalinak [ID](#)⁶¹, A.S. Kalteyer [ID](#)⁹⁸, A. Kalweit [ID](#)³³, V. Kaplin [ID](#)¹⁴², A. Karasu Uysal [ID](#)⁷³, D. Karatovic [ID](#)⁹⁰, O. Karavichev [ID](#)¹⁴², T. Karavicheva [ID](#)¹⁴², P. Karczmarczyk [ID](#)¹³⁷, E. Karpechev [ID](#)¹⁴², M.J. Karwowska [ID](#)^{33,137}, U. Keschull [ID](#)⁷¹, R. Keidel [ID](#)¹⁴¹, D.L.D. Keijdener⁶⁰, M. Keil [ID](#)³³, B. Ketzer [ID](#)⁴³, S.S. Khade [ID](#)⁴⁹, A.M. Khan [ID](#)¹²¹, S. Khan [ID](#)¹⁶, A. Khanzadeev [ID](#)¹⁴², Y. Kharlov [ID](#)¹⁴², A. Khatun [ID](#)¹¹⁹, A. Khuntia [ID](#)³⁶, B. Kileng [ID](#)³⁵, B. Kim [ID](#)¹⁰⁵, C. Kim [ID](#)¹⁷, D.J. Kim [ID](#)¹¹⁸, E.J. Kim [ID](#)⁷⁰, J. Kim [ID](#)¹⁴⁰,

J.S. Kim [ID](#)⁴¹, J. Kim [ID](#)⁵⁹, J. Kim [ID](#)⁷⁰, M. Kim [ID](#)¹⁹, S. Kim [ID](#)¹⁸, T. Kim [ID](#)¹⁴⁰, K. Kimura [ID](#)⁹³, S. Kirsch [ID](#)⁶⁵, I. Kisel [ID](#)³⁹, S. Kiselev [ID](#)¹⁴², A. Kisiel [ID](#)¹³⁷, J.P. Kitowski [ID](#)², J.L. Klay [ID](#)⁵, J. Klein [ID](#)³³, S. Klein [ID](#)⁷⁵, C. Klein-Bösing [ID](#)¹²⁷, M. Kleiner [ID](#)⁶⁵, T. Klemenž [ID](#)⁹⁶, A. Kluge [ID](#)³³, A.G. Knospe [ID](#)¹¹⁷, C. Kobdaj [ID](#)¹⁰⁶, T. Kollegger⁹⁸, A. Kondratyev [ID](#)¹⁴³, N. Kondratyeva [ID](#)¹⁴², E. Kondratyuk [ID](#)¹⁴², J. König [ID](#)⁶⁵, S.A. Königstorfer [ID](#)⁹⁶, P.J. Konopka [ID](#)³³, G. Kornakov [ID](#)¹³⁷, M. Korwieser [ID](#)⁹⁶, S.D. Koryciak [ID](#)², A. Kotliarov [ID](#)⁸⁷, V. Kovalenko [ID](#)¹⁴², M. Kowalski [ID](#)¹⁰⁸, V. Kozhuharov [ID](#)³⁷, I. Králik [ID](#)⁶¹, A. Kravčáková [ID](#)³⁸, L. Krcal [ID](#)^{33,39}, M. Krivda [ID](#)^{101,61}, F. Krizek [ID](#)⁸⁷, K. Krizkova Gajdosova [ID](#)³³, M. Kroesen [ID](#)⁹⁵, M. Krüger [ID](#)⁶⁵, D.M. Krupova [ID](#)³⁶, E. Kryshen [ID](#)¹⁴², V. Kučera [ID](#)⁵⁹, C. Kuhn [ID](#)¹³⁰, P.G. Kuijjer [ID](#)⁸⁵, T. Kumaoka¹²⁶, D. Kumar¹³⁶, L. Kumar [ID](#)⁹¹, N. Kumar⁹¹, S. Kumar [ID](#)³², S. Kundu [ID](#)³³, P. Kurashvili [ID](#)⁸⁰, A. Kurepin [ID](#)¹⁴², A.B. Kurepin [ID](#)¹⁴², A. Kuryakin [ID](#)¹⁴², S. Kushpil [ID](#)⁸⁷, V. Kuskov [ID](#)¹⁴², M.J. Kweon [ID](#)⁵⁹, Y. Kwon [ID](#)¹⁴⁰, S.L. La Pointe [ID](#)³⁹, P. La Rocca [ID](#)²⁷, A. Lakrathok¹⁰⁶, M. Lamanna [ID](#)³³, A.R. Landou [ID](#)^{74,116}, R. Langoy [ID](#)¹²², P. Larionov [ID](#)³³, E. Laudi [ID](#)³³, L. Lautner [ID](#)^{33,96}, R. Lavicka [ID](#)¹⁰³, R. Lea [ID](#)^{135,56}, H. Lee [ID](#)¹⁰⁵, I. Legrand [ID](#)⁴⁶, G. Legras [ID](#)¹²⁷, J. Lehrbach [ID](#)³⁹, T.M. Lelek², R.C. Lemmon [ID](#)⁸⁶, I. León Monzón [ID](#)¹¹⁰, M.M. Lesch [ID](#)⁹⁶, E.D. Lesser [ID](#)¹⁹, P. Lévai [ID](#)⁴⁷, X. Li¹⁰, J. Lien [ID](#)¹²², R. Lietava [ID](#)¹⁰¹, I. Likmeta [ID](#)¹¹⁷, B. Lim [ID](#)²⁵, S.H. Lim [ID](#)¹⁷, V. Lindenstruth [ID](#)³⁹, A. Lindner⁴⁶, C. Lippmann [ID](#)⁹⁸, D.H. Liu [ID](#)⁶, J. Liu [ID](#)¹²⁰, G.S.S. Liveraro [ID](#)¹¹², I.M. Lofnes [ID](#)²¹, C. Loizides [ID](#)⁸⁸, S. Lokos [ID](#)¹⁰⁸, J. Lömker [ID](#)⁶⁰, P. Loncar [ID](#)³⁴, X. Lopez [ID](#)¹²⁸, E. López Torres [ID](#)⁷, P. Lu [ID](#)^{98,121}, F.V. Lugo [ID](#)⁶⁸, J.R. Luhder [ID](#)¹²⁷, M. Lunardon [ID](#)²⁸, G. Luparello [ID](#)⁵⁸, Y.G. Ma [ID](#)⁴⁰, M. Mager [ID](#)³³, A. Maire [ID](#)¹³⁰, E.M. Majerz², M.V. Makariev [ID](#)³⁷, M. Malaev [ID](#)¹⁴², G. Malfattore [ID](#)²⁶, N.M. Malik [ID](#)⁹², Q.W. Malik²⁰, S.K. Malik [ID](#)⁹², L. Malinina [ID](#)^{I,VII,143}, D. Mallick [ID](#)^{132,81}, N. Mallick [ID](#)⁴⁹, G. Mandaglio [ID](#)^{31,54}, S.K. Mandal [ID](#)⁸⁰, V. Manko [ID](#)¹⁴², F. Manso [ID](#)¹²⁸, V. Manzari [ID](#)⁵¹, Y. Mao [ID](#)⁶, R.W. Marcjan [ID](#)², G.V. Margagliotti [ID](#)²⁴, A. Margotti [ID](#)⁵², A. Marín [ID](#)⁹⁸, C. Markert [ID](#)¹⁰⁹, P. Martinengo [ID](#)³³, M.I. Martínez [ID](#)⁴⁵, G. Martínez García [ID](#)¹⁰⁴, M.P.P. Martins [ID](#)¹¹¹, S. Masciocchi [ID](#)⁹⁸, M. Masera [ID](#)²⁵, A. Masoni [ID](#)⁵³, L. Massacrier [ID](#)¹³², O. Massen [ID](#)⁶⁰, A. Mastroserio [ID](#)^{133,51}, O. Matonoha [ID](#)⁷⁶, S. Mattiazzo [ID](#)²⁸, A. Matyja [ID](#)¹⁰⁸, C. Mayer [ID](#)¹⁰⁸, A.L. Mazuecos [ID](#)³³, F. Mazzaschi [ID](#)²⁵, M. Mazzilli [ID](#)³³, J.E. Mdhului [ID](#)¹²⁴, Y. Melikyan [ID](#)⁴⁴, A. Menchaca-Rocha [ID](#)⁶⁸, J.E.M. Mendez [ID](#)⁶⁶, E. Meninno [ID](#)¹⁰³, A.S. Menon [ID](#)¹¹⁷, M. Meres [ID](#)¹³, S. Mhlanga^{115,69}, Y. Miake¹²⁶, L. Micheletti [ID](#)³³, D.L. Mihaylov [ID](#)⁹⁶, K. Mikhaylov [ID](#)^{143,142}, A.N. Mishra [ID](#)⁴⁷, D. Miśkowiec [ID](#)⁹⁸, A. Modak [ID](#)⁴, B. Mohanty⁸¹, M. Mohisin Khan [ID](#)^{V,16}, M.A. Molander [ID](#)⁴⁴, S. Monira [ID](#)¹³⁷, C. Mordasini [ID](#)¹¹⁸, D.A. Moreira De Godoy [ID](#)¹²⁷, I. Morozov [ID](#)¹⁴², A. Morsch [ID](#)³³, T. Mrnjavac [ID](#)³³, V. Muccifora [ID](#)⁵⁰, S. Muhuri [ID](#)¹³⁶, J.D. Mulligan [ID](#)⁷⁵, A. Mulliri [ID](#)²³, M.G. Munhoz [ID](#)¹¹¹, R.H. Munzer [ID](#)⁶⁵, H. Murakami [ID](#)¹²⁵, S. Murray [ID](#)¹¹⁵, L. Musa [ID](#)³³, J. Musinsky [ID](#)⁶¹, J.W. Myrcha [ID](#)¹³⁷, B. Naik [ID](#)¹²⁴, A.I. Nambrath [ID](#)¹⁹, B.K. Nandi [ID](#)⁴⁸, R. Nania [ID](#)⁵², E. Nappi [ID](#)⁵¹, A.F. Nassirpour [ID](#)¹⁸, A. Nath [ID](#)⁹⁵, C. Natrass [ID](#)¹²³, M.N. Naydenov [ID](#)³⁷, A. Neagu²⁰, A. Negru¹¹⁴, E. Nekrasova¹⁴², L. Nellen [ID](#)⁶⁶, R. Nepeivoda [ID](#)⁷⁶, S. Nese [ID](#)²⁰, G. Neskovic [ID](#)³⁹, N. Nicassio [ID](#)⁵¹, B.S. Nielsen [ID](#)⁸⁴, E.G. Nielsen [ID](#)⁸⁴, S. Nikolaev [ID](#)¹⁴², S. Nikulin [ID](#)¹⁴², V. Nikulin [ID](#)¹⁴², F. Noferini [ID](#)⁵², S. Noh [ID](#)¹², P. Nomokonov [ID](#)¹⁴³, J. Norman [ID](#)¹²⁰, N. Novitzky [ID](#)⁸⁸, P. Nowakowski [ID](#)¹³⁷, A. Nyanin [ID](#)¹⁴², J. Nystrand [ID](#)²¹, M. Ogino [ID](#)⁷⁷, S. Oh [ID](#)¹⁸, A. Ohlson [ID](#)⁷⁶, V.A. Okorokov [ID](#)¹⁴², J. Oleniacz [ID](#)¹³⁷, A.C. Oliveira Da Silva [ID](#)¹²³, A. Onnerstad [ID](#)¹¹⁸, C. Oppedisano [ID](#)⁵⁷, A. Ortiz Velasquez [ID](#)⁶⁶,

J. Otwinowski [ID](#)¹⁰⁸, M. Oya⁹³, K. Oyama [ID](#)⁷⁷, Y. Pachmayer [ID](#)⁹⁵, S. Padhan [ID](#)⁴⁸,
 D. Pagano [ID](#)^{135,56}, G. Paić [ID](#)⁶⁶, S. Paisano-Guzmán [ID](#)⁴⁵, A. Palasciano [ID](#)⁵¹, S. Panebianco [ID](#)¹³¹,
 H. Park [ID](#)¹²⁶, H. Park [ID](#)¹⁰⁵, J. Park [ID](#)⁵⁹, J.E. Parkkila [ID](#)³³, Y. Patley [ID](#)⁴⁸, R.N. Patra⁹²,
 B. Paul [ID](#)²³, H. Pei [ID](#)⁶, T. Peitzmann [ID](#)⁶⁰, X. Peng [ID](#)¹¹, M. Pennisi [ID](#)²⁵, S. Perciballi [ID](#)²⁵,
 D. Peresunko [ID](#)¹⁴², G.M. Perez [ID](#)⁷, Y. Pestov¹⁴², V. Petrov [ID](#)¹⁴², M. Petrovici [ID](#)⁴⁶,
 R.P. Pezzi [ID](#)^{104,67}, S. Piano [ID](#)⁵⁸, M. Pikna [ID](#)¹³, P. Pillot [ID](#)¹⁰⁴, O. Pinazza [ID](#)^{52,33}, L. Pinsky¹¹⁷,
 C. Pinto [ID](#)⁹⁶, S. Pisano [ID](#)⁵⁰, M. Płoskoń [ID](#)⁷⁵, M. Planinic⁹⁰, F. Pliquet⁶⁵, M.G. Poghosyan [ID](#)⁸⁸,
 B. Polichtchouk [ID](#)¹⁴², S. Politano [ID](#)³⁰, N. Poljak [ID](#)⁹⁰, A. Pop [ID](#)⁴⁶, S. Porteboeuf-Houssais [ID](#)¹²⁸,
 V. Pozdniakov [ID](#)¹⁴³, I.Y. Pozos [ID](#)⁴⁵, K.K. Pradhan [ID](#)⁴⁹, S.K. Prasad [ID](#)⁴, S. Prasad [ID](#)⁴⁹,
 R. Preghenella [ID](#)⁵², F. Prino [ID](#)⁵⁷, C.A. Pruneau [ID](#)¹³⁸, I. Pshenichnov [ID](#)¹⁴², M. Puccio [ID](#)³³,
 S. Pucillo [ID](#)²⁵, Z. Pugelova¹⁰⁷, S. Qiu [ID](#)⁸⁵, L. Quaglia [ID](#)²⁵, S. Ragoni [ID](#)¹⁵, A. Rai [ID](#)¹³⁹,
 A. Rakotozafindrabe [ID](#)¹³¹, L. Ramello [ID](#)^{134,57}, F. Rami [ID](#)¹³⁰, T.A. Rancien⁷⁴, M. Rasa [ID](#)²⁷,
 S.S. Räsänen [ID](#)⁴⁴, R. Rath [ID](#)⁵², M.P. Rauch [ID](#)²¹, I. Ravasenga [ID](#)⁸⁵, K.F. Read [ID](#)^{88,123},
 C. Reckziegel [ID](#)¹¹³, A.R. Redelbach [ID](#)³⁹, K. Redlich [ID](#)^{VI,80}, C.A. Reetz [ID](#)⁹⁸, H.D. Regules-Medel⁴⁵,
 A. Rehman²¹, F. Reidt [ID](#)³³, H.A. Reme-Ness [ID](#)³⁵, Z. Rescakova³⁸, K. Reyers [ID](#)⁹⁵, A. Riabov [ID](#)¹⁴²,
 V. Riabov [ID](#)¹⁴², R. Ricci [ID](#)²⁹, M. Richter [ID](#)²⁰, A.A. Riedel [ID](#)⁹⁶, W. Riegler [ID](#)³³, A.G. Riffero [ID](#)²⁵,
 C. Ristea [ID](#)⁶⁴, M.V. Rodriguez [ID](#)³³, M. Rodríguez Cahuantzi [ID](#)⁴⁵, S.A. Rodríguez Ramírez [ID](#)⁴⁵,
 K. Røed [ID](#)²⁰, R. Rogalev [ID](#)¹⁴², E. Rogochaya [ID](#)¹⁴³, T.S. Rogoschinski [ID](#)⁶⁵, D. Rohr [ID](#)³³,
 D. Röhrich [ID](#)²¹, P.F. Rojas⁴⁵, S. Rojas Torres [ID](#)³⁶, P.S. Rokita [ID](#)¹³⁷, G. Romanenko [ID](#)²⁶,
 F. Ronchetti [ID](#)⁵⁰, A. Rosano [ID](#)^{31,54}, E.D. Rosas⁶⁶, K. Roslon [ID](#)¹³⁷, A. Rossi [ID](#)⁵⁵, A. Roy [ID](#)⁴⁹,
 S. Roy [ID](#)⁴⁸, N. Rubini [ID](#)²⁶, D. Ruggiano [ID](#)¹³⁷, R. Rui [ID](#)²⁴, P.G. Russek [ID](#)², R. Russo [ID](#)⁸⁵,
 A. Rustamov [ID](#)⁸², E. Ryabinkin [ID](#)¹⁴², Y. Ryabov [ID](#)¹⁴², A. Rybicki [ID](#)¹⁰⁸, H. Rytkonen [ID](#)¹¹⁸,
 J. Ryu [ID](#)¹⁷, W. Rzesza [ID](#)¹³⁷, O.A.M. Saarimaki [ID](#)⁴⁴, S. Sadhu [ID](#)³², S. Sadovsky [ID](#)¹⁴², J. Saetre [ID](#)²¹,
 K. Šafařík [ID](#)³⁶, P. Saha⁴², S.K. Saha [ID](#)⁴, S. Saha [ID](#)⁸¹, B. Sahoo [ID](#)⁴⁸, B. Sahoo [ID](#)⁴⁹, R. Sahoo [ID](#)⁴⁹,
 S. Sahoo⁶², D. Sahu [ID](#)⁴⁹, P.K. Sahu [ID](#)⁶², J. Saini [ID](#)¹³⁶, K. Sajdakova³⁸, S. Sakai [ID](#)¹²⁶,
 M.P. Salvan [ID](#)⁹⁸, S. Sambyal [ID](#)⁹², D. Samitz [ID](#)¹⁰³, I. Sanna [ID](#)^{33,96}, T.B. Saramela¹¹¹,
 P. Sarma [ID](#)⁴², V. Sarritzu [ID](#)²³, V.M. Sarti [ID](#)⁹⁶, M.H.P. Sas [ID](#)³³, S. Sawan⁸¹, J. Schambach [ID](#)⁸⁸,
 H.S. Scheid [ID](#)⁶⁵, C. Schiaua [ID](#)⁴⁶, R. Schicker [ID](#)⁹⁵, F. Schlepper [ID](#)⁹⁵, A. Schmah⁹⁸, C. Schmidt [ID](#)⁹⁸,
 H.R. Schmidt⁹⁴, M.O. Schmidt [ID](#)³³, M. Schmidt⁹⁴, N.V. Schmidt [ID](#)⁸⁸, A.R. Schmier [ID](#)¹²³,
 R. Schotter [ID](#)¹³⁰, A. Schröter [ID](#)³⁹, J. Schukraft [ID](#)³³, K. Schweda [ID](#)⁹⁸, G. Scioli [ID](#)²⁶,
 E. Scomparin [ID](#)⁵⁷, J.E. Seger [ID](#)¹⁵, Y. Sekiguchi¹²⁵, D. Sekihata [ID](#)¹²⁵, M. Selina [ID](#)⁸⁵,
 I. Selyuzhenkov [ID](#)⁹⁸, S. Senyukov [ID](#)¹³⁰, J.J. Seo [ID](#)^{95,59}, D. Serebryakov [ID](#)¹⁴², L. Šerkšnytė [ID](#)⁹⁶,
 A. Sevcenco [ID](#)⁶⁴, T.J. Shaba [ID](#)⁶⁹, A. Shabetai [ID](#)¹⁰⁴, R. Shahoyan³³, A. Shangaraev [ID](#)¹⁴²,
 A. Sharma⁹¹, B. Sharma [ID](#)⁹², D. Sharma [ID](#)⁴⁸, H. Sharma [ID](#)⁵⁵, M. Sharma [ID](#)⁹², S. Sharma [ID](#)⁷⁷,
 S. Sharma [ID](#)⁹², U. Sharma [ID](#)⁹², A. Shatat [ID](#)¹³², O. Sheibani¹¹⁷, K. Shigaki [ID](#)⁹³, M. Shimomura⁷⁸,
 J. Shin¹², S. Shirinkin [ID](#)¹⁴², Q. Shou [ID](#)⁴⁰, Y. Sibiriak [ID](#)¹⁴², S. Siddhanta [ID](#)⁵³, T. Siemiarczuk [ID](#)⁸⁰,
 T.F. Silva [ID](#)¹¹¹, D. Silvermyr [ID](#)⁷⁶, T. Simantathammakul¹⁰⁶, R. Simeonov [ID](#)³⁷, B. Singh⁹²,
 B. Singh [ID](#)⁹⁶, K. Singh [ID](#)⁴⁹, R. Singh [ID](#)⁸¹, R. Singh [ID](#)⁹², R. Singh [ID](#)⁴⁹, S. Singh [ID](#)¹⁶,
 V.K. Singh [ID](#)¹³⁶, V. Singhal [ID](#)¹³⁶, T. Sinha [ID](#)¹⁰⁰, B. Sitar [ID](#)¹³, M. Sitta [ID](#)^{134,57}, T.B. Skaali²⁰,
 G. Skorodumovs [ID](#)⁹⁵, M. Slupecki [ID](#)⁴⁴, N. Smirnov [ID](#)¹³⁹, R.J.M. Snellings [ID](#)⁶⁰, E.H. Solheim [ID](#)²⁰,
 J. Song [ID](#)¹⁷, C. Sonnabend [ID](#)^{33,98}, F. Soramel [ID](#)²⁸, A.B. Soto-hernandez [ID](#)⁸⁹, R. Spijkers [ID](#)⁸⁵,
 I. Sputowska [ID](#)¹⁰⁸, J. Staa [ID](#)⁷⁶, J. Stachel [ID](#)⁹⁵, I. Stan [ID](#)⁶⁴, P.J. Steffanic [ID](#)¹²³,
 S.F. Stiefelmaier [ID](#)⁹⁵, D. Stocco [ID](#)¹⁰⁴, I. Storehaug [ID](#)²⁰, P. Stratmann [ID](#)¹²⁷, S. Strazzi [ID](#)²⁶,

A. Sturniolo [ID](#)^{31,54}, C.P. Stylianidis⁸⁵, A.A.P. Suaide [ID](#)¹¹¹, C. Suire [ID](#)¹³², M. Sukhanov [ID](#)¹⁴², M. Suljic [ID](#)³³, R. Sultanov [ID](#)¹⁴², V. Sumberia [ID](#)⁹², S. Sumowidagdo [ID](#)⁸³, S. Swain⁶², I. Szarka [ID](#)¹³, M. Szymkowski [ID](#)¹³⁷, S.F. Taghavi [ID](#)⁹⁶, G. Taillepied [ID](#)⁹⁸, J. Takahashi [ID](#)¹¹², G.J. Tambave [ID](#)⁸¹, S. Tang [ID](#)⁶, Z. Tang [ID](#)¹²¹, J.D. Tapia Takaki [ID](#)¹¹⁹, N. Tapus¹¹⁴, L.A. Tarasovicova [ID](#)¹²⁷, M.G. Tarzila [ID](#)⁴⁶, G.F. Tassielli [ID](#)³², A. Tauro [ID](#)³³, A. Tavira García [ID](#)¹³², G. Tejada Muñoz [ID](#)⁴⁵, A. Telesca [ID](#)³³, L. Terlizzi [ID](#)²⁵, C. Terrevoli [ID](#)¹¹⁷, S. Thakur [ID](#)⁴, D. Thomas [ID](#)¹⁰⁹, A. Tikhonov [ID](#)¹⁴², N. Tiltmann [ID](#)¹²⁷, A.R. Timmins [ID](#)¹¹⁷, M. Tkacik¹⁰⁷, T. Tkacik [ID](#)¹⁰⁷, A. Toia [ID](#)⁶⁵, R. Tokumoto⁹³, K. Tomohiro⁹³, N. Topilskaya [ID](#)¹⁴², M. Toppi [ID](#)⁵⁰, T. Tork [ID](#)¹³², V.V. Torres [ID](#)¹⁰⁴, A.G. Torres Ramos [ID](#)³², A. Trifiró [ID](#)^{31,54}, A.S. Triolo [ID](#)^{33,31,54}, S. Tripathy [ID](#)⁵², T. Tripathy [ID](#)⁴⁸, S. Trogolo [ID](#)³³, V. Trubnikov [ID](#)³, W.H. Trzaska [ID](#)¹¹⁸, T.P. Trzcinski [ID](#)¹³⁷, A. Tumkin [ID](#)¹⁴², R. Turrisi [ID](#)⁵⁵, T.S. Tveter [ID](#)²⁰, K. Ullaland [ID](#)²¹, B. Ulukutlu [ID](#)⁹⁶, A. Uras [ID](#)¹²⁹, G.L. Usai [ID](#)²³, M. Vala³⁸, N. Valle [ID](#)²², L.V.R. van Doremalen⁶⁰, M. van Leeuwen [ID](#)⁸⁵, C.A. van Veen [ID](#)⁹⁵, R.J.G. van Weelden [ID](#)⁸⁵, P. Vande Vyvre [ID](#)³³, D. Varga [ID](#)⁴⁷, Z. Varga [ID](#)⁴⁷, P. Vargas Torres⁶⁶, M. Vasileiou [ID](#)⁷⁹, A. Vasiliev [ID](#)¹⁴², O. Vázquez Doce [ID](#)⁵⁰, O. Vazquez Rueda [ID](#)¹¹⁷, V. Vechernin [ID](#)¹⁴², E. Vercellin [ID](#)²⁵, S. Vergara Limón⁴⁵, R. Verma⁴⁸, L. Vermunt [ID](#)⁹⁸, R. Vértesi [ID](#)⁴⁷, M. Verweij [ID](#)⁶⁰, L. Vickovic³⁴, Z. Vilakazi¹²⁴, O. Villalobos Baillie [ID](#)¹⁰¹, A. Villani [ID](#)²⁴, A. Vinogradov [ID](#)¹⁴², T. Virgili [ID](#)²⁹, M.M.O. Virta [ID](#)¹¹⁸, V. Vislavicius⁷⁶, A. Vodopyanov [ID](#)¹⁴³, B. Volkel [ID](#)³³, M.A. Völkl [ID](#)⁹⁵, K. Voloshin¹⁴², S.A. Voloshin [ID](#)¹³⁸, G. Volpe [ID](#)³², B. von Haller [ID](#)³³, I. Vorobyev [ID](#)⁹⁶, N. Vozniuk [ID](#)¹⁴², J. Vrláková [ID](#)³⁸, J. Wan⁴⁰, C. Wang [ID](#)⁴⁰, D. Wang⁴⁰, Y. Wang [ID](#)⁴⁰, Y. Wang [ID](#)⁶, A. Wegrzynek [ID](#)³³, F.T. Weiglhofer³⁹, S.C. Wenzel [ID](#)³³, J.P. Wessels [ID](#)¹²⁷, J. Wiechula [ID](#)⁶⁵, J. Wikne [ID](#)²⁰, G. Wilk [ID](#)⁸⁰, J. Wilkinson [ID](#)⁹⁸, G.A. Willems [ID](#)¹²⁷, B. Windelband [ID](#)⁹⁵, M. Winn [ID](#)¹³¹, J.R. Wright [ID](#)¹⁰⁹, W. Wu⁴⁰, Y. Wu [ID](#)¹²¹, R. Xu [ID](#)⁶, A. Yadav [ID](#)⁴³, A.K. Yadav [ID](#)¹³⁶, S. Yalcin [ID](#)⁷³, Y. Yamaguchi [ID](#)⁹³, S. Yang²¹, S. Yano [ID](#)⁹³, Z. Yin [ID](#)⁶, I.-K. Yoo [ID](#)¹⁷, J.H. Yoon [ID](#)⁵⁹, H. Yu¹², S. Yuan²¹, A. Yuncu [ID](#)⁹⁵, V. Zaccolo [ID](#)²⁴, C. Zampolli [ID](#)³³, F. Zanone [ID](#)⁹⁵, N. Zardoshti [ID](#)³³, A. Zarochentsev [ID](#)¹⁴², P. Závada [ID](#)⁶³, N. Zaviyalov¹⁴², M. Zhalov [ID](#)¹⁴², B. Zhang [ID](#)⁶, C. Zhang [ID](#)¹³¹, L. Zhang [ID](#)⁴⁰, S. Zhang [ID](#)⁴⁰, X. Zhang [ID](#)⁶, Y. Zhang¹²¹, Z. Zhang [ID](#)⁶, M. Zhao [ID](#)¹⁰, V. Zhrebchevskii [ID](#)¹⁴², Y. Zhi¹⁰, D. Zhou [ID](#)⁶, Y. Zhou [ID](#)⁸⁴, J. Zhu [ID](#)^{55,6}, Y. Zhu⁶, S.C. Zugravel [ID](#)⁵⁷, N. Zurlo [ID](#)^{135,56}

¹ *A.I. Alikhanyan National Science Laboratory (Yerevan Physics Institute) Foundation, Yerevan, Armenia*

² *AGH University of Krakow, Cracow, Poland*

³ *Bogolyubov Institute for Theoretical Physics, National Academy of Sciences of Ukraine, Kiev, Ukraine*

⁴ *Bose Institute, Department of Physics and Centre for Astroparticle Physics and Space Science (CAPSS), Kolkata, India*

⁵ *California Polytechnic State University, San Luis Obispo, California, United States*

⁶ *Central China Normal University, Wuhan, China*

⁷ *Centro de Aplicaciones Tecnológicas y Desarrollo Nuclear (CEADEN), Havana, Cuba*

⁸ *Centro de Investigación y de Estudios Avanzados (CINVESTAV), Mexico City and Mérida, Mexico*

⁹ *Chicago State University, Chicago, Illinois, United States*

¹⁰ *China Institute of Atomic Energy, Beijing, China*

¹¹ *China University of Geosciences, Wuhan, China*

¹² *Chungbuk National University, Cheongju, Republic of Korea*

¹³ *Comenius University Bratislava, Faculty of Mathematics, Physics and Informatics, Bratislava, Slovak Republic*

¹⁴ *COMSATS University Islamabad, Islamabad, Pakistan*

¹⁵ *Creighton University, Omaha, Nebraska, United States*

- ¹⁶ *Department of Physics, Aligarh Muslim University, Aligarh, India*
- ¹⁷ *Department of Physics, Pusan National University, Pusan, Republic of Korea*
- ¹⁸ *Department of Physics, Sejong University, Seoul, Republic of Korea*
- ¹⁹ *Department of Physics, University of California, Berkeley, California, United States*
- ²⁰ *Department of Physics, University of Oslo, Oslo, Norway*
- ²¹ *Department of Physics and Technology, University of Bergen, Bergen, Norway*
- ²² *Dipartimento di Fisica, Università di Pavia, Pavia, Italy*
- ²³ *Dipartimento di Fisica dell'Università and Sezione INFN, Cagliari, Italy*
- ²⁴ *Dipartimento di Fisica dell'Università and Sezione INFN, Trieste, Italy*
- ²⁵ *Dipartimento di Fisica dell'Università and Sezione INFN, Turin, Italy*
- ²⁶ *Dipartimento di Fisica e Astronomia dell'Università and Sezione INFN, Bologna, Italy*
- ²⁷ *Dipartimento di Fisica e Astronomia dell'Università and Sezione INFN, Catania, Italy*
- ²⁸ *Dipartimento di Fisica e Astronomia dell'Università and Sezione INFN, Padova, Italy*
- ²⁹ *Dipartimento di Fisica 'E.R. Caianiello' dell'Università and Gruppo Collegato INFN, Salerno, Italy*
- ³⁰ *Dipartimento DISAT del Politecnico and Sezione INFN, Turin, Italy*
- ³¹ *Dipartimento di Scienze MIFT, Università di Messina, Messina, Italy*
- ³² *Dipartimento Interateneo di Fisica 'M. Merlin' and Sezione INFN, Bari, Italy*
- ³³ *European Organization for Nuclear Research (CERN), Geneva, Switzerland*
- ³⁴ *Faculty of Electrical Engineering, Mechanical Engineering and Naval Architecture, University of Split, Split, Croatia*
- ³⁵ *Faculty of Engineering and Science, Western Norway University of Applied Sciences, Bergen, Norway*
- ³⁶ *Faculty of Nuclear Sciences and Physical Engineering, Czech Technical University in Prague, Prague, Czech Republic*
- ³⁷ *Faculty of Physics, Sofia University, Sofia, Bulgaria*
- ³⁸ *Faculty of Science, P.J. Šafárik University, Košice, Slovak Republic*
- ³⁹ *Frankfurt Institute for Advanced Studies, Johann Wolfgang Goethe-Universität Frankfurt, Frankfurt, Germany*
- ⁴⁰ *Fudan University, Shanghai, China*
- ⁴¹ *Gangneung-Wonju National University, Gangneung, Republic of Korea*
- ⁴² *Gauhati University, Department of Physics, Guwahati, India*
- ⁴³ *Helmholtz-Institut für Strahlen- und Kernphysik, Rheinische Friedrich-Wilhelms-Universität Bonn, Bonn, Germany*
- ⁴⁴ *Helsinki Institute of Physics (HIP), Helsinki, Finland*
- ⁴⁵ *High Energy Physics Group, Universidad Autónoma de Puebla, Puebla, Mexico*
- ⁴⁶ *Horia Hulubei National Institute of Physics and Nuclear Engineering, Bucharest, Romania*
- ⁴⁷ *HUN-REN Wigner Research Centre for Physics, Budapest, Hungary*
- ⁴⁸ *Indian Institute of Technology Bombay (IIT), Mumbai, India*
- ⁴⁹ *Indian Institute of Technology Indore, Indore, India*
- ⁵⁰ *INFN, Laboratori Nazionali di Frascati, Frascati, Italy*
- ⁵¹ *INFN, Sezione di Bari, Bari, Italy*
- ⁵² *INFN, Sezione di Bologna, Bologna, Italy*
- ⁵³ *INFN, Sezione di Cagliari, Cagliari, Italy*
- ⁵⁴ *INFN, Sezione di Catania, Catania, Italy*
- ⁵⁵ *INFN, Sezione di Padova, Padova, Italy*
- ⁵⁶ *INFN, Sezione di Pavia, Pavia, Italy*
- ⁵⁷ *INFN, Sezione di Torino, Turin, Italy*
- ⁵⁸ *INFN, Sezione di Trieste, Trieste, Italy*
- ⁵⁹ *Inha University, Incheon, Republic of Korea*
- ⁶⁰ *Institute for Gravitational and Subatomic Physics (GRASP), Utrecht University/Nikhef, Utrecht, Netherlands*
- ⁶¹ *Institute of Experimental Physics, Slovak Academy of Sciences, Košice, Slovak Republic*
- ⁶² *Institute of Physics, Homi Bhabha National Institute, Bhubaneswar, India*
- ⁶³ *Institute of Physics of the Czech Academy of Sciences, Prague, Czech Republic*

- ⁶⁴ *Institute of Space Science (ISS), Bucharest, Romania*
- ⁶⁵ *Institut für Kernphysik, Johann Wolfgang Goethe-Universität Frankfurt, Frankfurt, Germany*
- ⁶⁶ *Instituto de Ciencias Nucleares, Universidad Nacional Autónoma de México, Mexico City, Mexico*
- ⁶⁷ *Instituto de Física, Universidade Federal do Rio Grande do Sul (UFRGS), Porto Alegre, Brazil*
- ⁶⁸ *Instituto de Física, Universidad Nacional Autónoma de México, Mexico City, Mexico*
- ⁶⁹ *iThemba LABS, National Research Foundation, Somerset West, South Africa*
- ⁷⁰ *Jeonbuk National University, Jeonju, Republic of Korea*
- ⁷¹ *Johann-Wolfgang-Goethe Universität Frankfurt Institut für Informatik, Fachbereich Informatik und Mathematik, Frankfurt, Germany*
- ⁷² *Korea Institute of Science and Technology Information, Daejeon, Republic of Korea*
- ⁷³ *KTO Karatay University, Konya, Turkey*
- ⁷⁴ *Laboratoire de Physique Subatomique et de Cosmologie, Université Grenoble-Alpes, CNRS-IN2P3, Grenoble, France*
- ⁷⁵ *Lawrence Berkeley National Laboratory, Berkeley, California, United States*
- ⁷⁶ *Lund University Department of Physics, Division of Particle Physics, Lund, Sweden*
- ⁷⁷ *Nagasaki Institute of Applied Science, Nagasaki, Japan*
- ⁷⁸ *Nara Women's University (NWU), Nara, Japan*
- ⁷⁹ *National and Kapodistrian University of Athens, School of Science, Department of Physics, Athens, Greece*
- ⁸⁰ *National Centre for Nuclear Research, Warsaw, Poland*
- ⁸¹ *National Institute of Science Education and Research, Homi Bhabha National Institute, Jatni, India*
- ⁸² *National Nuclear Research Center, Baku, Azerbaijan*
- ⁸³ *National Research and Innovation Agency - BRIN, Jakarta, Indonesia*
- ⁸⁴ *Niels Bohr Institute, University of Copenhagen, Copenhagen, Denmark*
- ⁸⁵ *Nikhef, National institute for subatomic physics, Amsterdam, Netherlands*
- ⁸⁶ *Nuclear Physics Group, STFC Daresbury Laboratory, Daresbury, United Kingdom*
- ⁸⁷ *Nuclear Physics Institute of the Czech Academy of Sciences, Husinec-Řež, Czech Republic*
- ⁸⁸ *Oak Ridge National Laboratory, Oak Ridge, Tennessee, United States*
- ⁸⁹ *Ohio State University, Columbus, Ohio, United States*
- ⁹⁰ *Physics department, Faculty of science, University of Zagreb, Zagreb, Croatia*
- ⁹¹ *Physics Department, Panjab University, Chandigarh, India*
- ⁹² *Physics Department, University of Jammu, Jammu, India*
- ⁹³ *Physics Program and International Institute for Sustainability with Knotted Chiral Meta Matter (SKCM²), Hiroshima University, Hiroshima, Japan*
- ⁹⁴ *Physikalisches Institut, Eberhard-Karls-Universität Tübingen, Tübingen, Germany*
- ⁹⁵ *Physikalisches Institut, Ruprecht-Karls-Universität Heidelberg, Heidelberg, Germany*
- ⁹⁶ *Physik Department, Technische Universität München, Munich, Germany*
- ⁹⁷ *Politecnico di Bari and Sezione INFN, Bari, Italy*
- ⁹⁸ *Research Division and ExtreMe Matter Institute EMMI, GSI Helmholtzzentrum für Schwerionenforschung GmbH, Darmstadt, Germany*
- ⁹⁹ *Saga University, Saga, Japan*
- ¹⁰⁰ *Saha Institute of Nuclear Physics, Homi Bhabha National Institute, Kolkata, India*
- ¹⁰¹ *School of Physics and Astronomy, University of Birmingham, Birmingham, United Kingdom*
- ¹⁰² *Sección Física, Departamento de Ciencias, Pontificia Universidad Católica del Perú, Lima, Peru*
- ¹⁰³ *Stefan Meyer Institut für Subatomare Physik (SMI), Vienna, Austria*
- ¹⁰⁴ *SUBATECH, IMT Atlantique, Nantes Université, CNRS-IN2P3, Nantes, France*
- ¹⁰⁵ *Sungkyunkwan University, Suwon City, Republic of Korea*
- ¹⁰⁶ *Suranaree University of Technology, Nakhon Ratchasima, Thailand*
- ¹⁰⁷ *Technical University of Košice, Košice, Slovak Republic*
- ¹⁰⁸ *The Henryk Niewodniczanski Institute of Nuclear Physics, Polish Academy of Sciences, Cracow, Poland*
- ¹⁰⁹ *The University of Texas at Austin, Austin, Texas, United States*
- ¹¹⁰ *Universidad Autónoma de Sinaloa, Culiacán, Mexico*
- ¹¹¹ *Universidade de São Paulo (USP), São Paulo, Brazil*

- ¹¹² *Universidade Estadual de Campinas (UNICAMP), Campinas, Brazil*
- ¹¹³ *Universidade Federal do ABC, Santo Andre, Brazil*
- ¹¹⁴ *Universitatea Nationala de Stiinta si Tehnologie Politehnica Bucuresti, Bucharest, Romania*
- ¹¹⁵ *University of Cape Town, Cape Town, South Africa*
- ¹¹⁶ *University of Derby, Derby, United Kingdom*
- ¹¹⁷ *University of Houston, Houston, Texas, United States*
- ¹¹⁸ *University of Jyväskylä, Jyväskylä, Finland*
- ¹¹⁹ *University of Kansas, Lawrence, Kansas, United States*
- ¹²⁰ *University of Liverpool, Liverpool, United Kingdom*
- ¹²¹ *University of Science and Technology of China, Hefei, China*
- ¹²² *University of South-Eastern Norway, Kongsberg, Norway*
- ¹²³ *University of Tennessee, Knoxville, Tennessee, United States*
- ¹²⁴ *University of the Witwatersrand, Johannesburg, South Africa*
- ¹²⁵ *University of Tokyo, Tokyo, Japan*
- ¹²⁶ *University of Tsukuba, Tsukuba, Japan*
- ¹²⁷ *Universität Münster, Institut für Kernphysik, Münster, Germany*
- ¹²⁸ *Université Clermont Auvergne, CNRS/IN2P3, LPC, Clermont-Ferrand, France*
- ¹²⁹ *Université de Lyon, CNRS/IN2P3, Institut de Physique des 2 Infinis de Lyon, Lyon, France*
- ¹³⁰ *Université de Strasbourg, CNRS, IPHC UMR 7178, F-67000 Strasbourg, France, Strasbourg, France*
- ¹³¹ *Université Paris-Saclay, Centre d'Etudes de Saclay (CEA), IRFU, Département de Physique Nucléaire (DPhN), Saclay, France*
- ¹³² *Université Paris-Saclay, CNRS/IN2P3, IJCLab, Orsay, France*
- ¹³³ *Università degli Studi di Foggia, Foggia, Italy*
- ¹³⁴ *Università del Piemonte Orientale, Vercelli, Italy*
- ¹³⁵ *Università di Brescia, Brescia, Italy*
- ¹³⁶ *Variable Energy Cyclotron Centre, Homi Bhabha National Institute, Kolkata, India*
- ¹³⁷ *Warsaw University of Technology, Warsaw, Poland*
- ¹³⁸ *Wayne State University, Detroit, Michigan, United States*
- ¹³⁹ *Yale University, New Haven, Connecticut, United States*
- ¹⁴⁰ *Yonsei University, Seoul, Republic of Korea*
- ¹⁴¹ *Zentrum für Technologie und Transfer (ZTT), Worms, Germany*
- ¹⁴² *Affiliated with an institute covered by a cooperation agreement with CERN*
- ¹⁴³ *Affiliated with an international laboratory covered by a cooperation agreement with CERN.*

^I *Deceased*

^{II} *Also at: Max-Planck-Institut für Physik, Munich, Germany*

^{III} *Also at: Italian National Agency for New Technologies, Energy and Sustainable Economic Development (ENEA), Bologna, Italy*

^{IV} *Also at: Dipartimento DET del Politecnico di Torino, Turin, Italy*

^V *Also at: Department of Applied Physics, Aligarh Muslim University, Aligarh, India*

^{VI} *Also at: Institute of Theoretical Physics, University of Wrocław, Poland*

^{VII} *Also at: An institution covered by a cooperation agreement with CERN*